SOURCE PROPERTIES OF MICRO-EARTHQUAKES IN EASTERN MARMARA
AND THEIR CONNECTION TO THE STRUCTURE OF THE ÇINARCIK BASIN

by

Birsen Can

B.S., Geophysical Engineering, İstanbul Technical University, 2000

M.S., Geophysics, Boğaziçi University, 2006

Submitted to the Kandilli Observatory and

Earthquake Research Institute in partial fulfillment of

the requirements for the degree of

Doctor of Philosophy

Graduate Program in Geophysics

Boğaziçi University

2019

SOURCE PROPERTIES OF MICRO-EARTHQUAKES IN EASTERN MARMARA
AND THEIR CONNECTION TO THE STRUCTURE OF THE ÇINARCIK BASIN

APPROVED BY:

Prof. Dr. Mustafa Aktar ....
(Thesis Supervisor)

Assoc. Prof. Ali Özgün Konca ....

Assoc. Prof. Onur Tan ....

Prof. Dr. Semih Ergintav ....

Assoc. Prof. Serkan Irmak ....

DATE OF APPROVAL: 04.03.2019

ACKNOWLEDGEMENTS

ABSTRACT

SOURCE PROPERTIES OF MICRO-EARTHQUAKES IN EASTERN MARMARA AND THEIR CONNECTION TO THE STRUCTURE OF THE ÇINARCIK BASIN

This study mainly focuses on the source properties of micro-earthquakes in Eastern Marmara and their connection to the structure of the Çınarcık Basin, in particular. Throughout this study, Prince Islands Real Time Earthquake Monitoring System (PIRES) Arrays data have been used, which is the closest land site locations to the North Anatolian Fault (NAF) in the Marmara Sea. Only a limited number of small magnitude earthquakes occur in the Çınarcık Basin. Therefore, earthquakes only within an epicentral distance of ~20 km to the arrays have been evaluated considering that Signal to Noise Ratio (SNR) decreases abruptly for further distances.

Special methods have been developed and adapted to the PIRES in this study. In this context, advantages of the arrays have been used in all aspects. Array based cross correlation method has been developed for the optimal detection of the small magnitude events which show similarity. Using this method, a systematical search of the foreshocks and aftershocks activities has been performed. This has led to a large improvement of the detection level and revealed large number of earthquake clustering. It became possible to extract many small magnitude events that are buried in the background noise or in the coda of previous events and therefore were missed by the land stations. Since, the main target was to evaluate the performance of the surface arrays against the boreholes, various noise cancelation tools are developed based on the stacking of repetitive observations. These procedures are used for the estimations of the fracture properties of the small events inside the Çınarcık Basin. The fracture properties that have been analyzed are the seismic moment, fracture radius, stress drop, energy and occurrence statistics. Tests are performed to see if the fracture properties are changing in space and time, or show any other characteristic behavior that may be connected to a particular location in the study area.

Variations are observed between the stress drop and location of the events. Similarly, foreshock and aftershock occurrence statistics seems also to vary across the Çınarcık Basin. Since, the present data is rather restricted, it is expected that the interpretations are only preliminary. The results obtained imply that this type of analysis will probably be part of the real time monitoring processes in the future, for the purpose of early warning systems.

ÖZET

DOĞU MARMARA'DAKİ MİKRO DEPREMLERİN KAYNAK PARAMETRELERİ VE ÇINARCIK BASENİ'NİN YAPISIYLA BAĞLANTILARI

Bu çalışma ağırlıklı olarak, Doğu Marmara'daki mikro-depremlerin kaynak parametreleri ve onların özellikle Çınarcık Baseni'nin, yapısıyla bağlantısına odaklanmaktadır. Bu çalışma boyunca, Marmara Denizi'nde Kuzey Anadolu Fayı'na karada en yakın konum olan Prens Adaları Gerçek Zamanlı Deprem Gözlem Sistemi (PIRES) Dizilim verileri kullanılmıştır. Çınarcık Baseni'nde sadece sınırlı sayıda küçük manyetüdlü depremler oluşmaktadır. Bu nedenle, dizilimlere sadece ~20 km uzaklıktaki depremler Sinyal Gürültü Oranının ileri mesafelerde aniden düştüğü dikkate alınarak değerlendirilmiştir.

Bu çalışmada, özel metotlar geliştirilmiş ve PIRES'e adapte edilmiştir. Bu bağlamda, dizilimlerin avantajları tüm yönleriyle kullanılmıştır. Dizime dayalı çapraz ilişki metodu benzerlik gösteren küçük manyetüdlü depremleri en uygun şekilde bulmak için geliştirilmiştir. Bu metodu kullanarak, öncü ve artçı şok aktivitelerini sistematik olarak arama gerçekleştirilmiştir. Bu, algılama seviyesinde büyük bir iyileştirme sağlamıştır ve çok sayıda deprem kümelenmesini ortaya çıkarmıştır. Arka plan gürültüsü ya da önceki depremlere ait koda içinde gömülü kalmış ve bu nedenle karadaki istasyonlar tarafında kaçırılmış çok sayıda küçük manyetüdlü depremi ayıklamak mümkün hale gelmiştir. Ana hedef, yüzey dizilimlerinin kuyulara göre performansını değerlendirmek olduğu için, tekrarlayan gözlemleri yığmaya dayalı çeşitli gürültü kaldırma araçları geliştirilmiştir. Bu yöntemler, Çınarcık Baseni'ndeki küçük depremlerin kırılma özelliklerini değerlendirmek için kullanılmıştır. Analiz edilen kırılma özellikleri, sismik moment, kırık yarıçapı, stres düşümü, enerji ve oluşum istatistiğidir. Kırılma özelliklerinin uzayda ve zamanda değişip değişmediğini ya da herhangi bir karakteristik davranış göstererek bunun çalışma alanında belirli bir konumla bağlantılı olup olmadığını görmek için testler gerçekleştirilmiştir.

Stres düşümü ve depremlerin konumları arasında değişimler gözlenmiştir. Benzer şekilde, ayrıca, öncü ve artçı şok oluşum istatistiklerinin Çınarcık Baseni boyunca değiştiği görülmektedir. Mevcut veri oldukça kısıtlı olduğundan, yorumların sadece başlangıç niteliğinde olduğu varsayılmaktadır. Elde edilen sonuçlar, bu çeşit analizlerin büyük olasılıkla gelecekte erken uyarı sistemleri için gerçek zamanlı gözlem süreçlerinin bir parçası olacağını göstermektedir.

TABLE OF CONTENTS

LIST OF FIGURES

LIST OF TABLES

LIST OF SYMBOLS

A	Normalization constant
b_0	Open circuit damping
c	Wave type (P or S wave)
e	Modulus of elasticity
E	Energy
EC	Transduction (Electrodynamics constant)
f	Frequency
f_0	Lower limit of integration
f_1	Upper limit of integration
f_{ijk}	Natural frequencies of a closed rectangular object
f_m	Upper limit of corner frequency
f_o	Corner frequency
f_c^c	Corner frequency
f_c^m	Corner frequency of the ME
f_c^s	Corner frequency of the SE
Fo	Natural frequency
g	Gravity of acceleration
G	Velocity output sensitivity
h	Damping factor x
i	Index for the normal mode vibrations
j	Index for the normal mode vibrations
k	Index for the normal mode vibrations
lx	Length
ly	Width
lz	Height
m	Gamma
$m(x)$	Mean of the time series x
$m(y)$	Mean of the time series y
Mo	Seismic moment

$\overline{Mo}$	Average seismic moment
p	Period
Q^c	Attenuation coefficient
Q_P	P wave quality factor
Q_S	S wave quality factor
r	Hypocentral distance
r_{xy}	Cross correlation coefficient
R	Ratio
RC	Coil resistance
RL	Damping resistor
R^c	Radiation pattern
R^P	P wave radiation pattern
R^S	S wave radiation pattern
s	Laplace variable
t	Thickness
t^c	Travel time
T	Transfer function
$\dot{u}^c$	Velocity spectrum
u^m	Displacement amplitude of the ME
$\dot{u}_c^m$	Velocity spectrum of the ME
u^s	Displacement amplitude of the SE
$\dot{u}_c^s$	Velocity spectrum of the SE
U	True ground signal
v^c	Wave velocity
v^P	P wave velocity
v^s	S wave velocity
w	Weight
w_0	Frequency
x	Time series x
y	Time series y
Z	Observed signal

ρ Density

σ_B Stress drop

Ω_0^m Seismic moment of the ME

Ω_0^s Seismic moment of the SE

LIST OF ACRONYMS/ABBREVIATIONS

2G	Second Generation
3D	Three Dimensional
3ESPC	GURALP CMG-3ESPC
3ESPCDE	GURALP CMG-3ESPCDE
3G	Third Generation
6TD	GURALP CMG-6TD
A/D	Analog to Digital Converter
AC	Alternating Current
AFAD	Prime Ministry Disaster and Emergency Management Presidency
BASD	Büyükada1
BRGZ	Burgazada
BYZN	Byzantine
CeB	Central Basin
CF-II	Compact Flash II
CMF	Central Marmara Fault
CSPE	Conventional Source Parameter Estimation
DFT	Discrete Fourier Transform
DM24	GURALP CMG-DM24
EAM	Embedded Acquisition Module
EASY	Easy
EDGE	Enhanced Data Rates for GSM Evolution
EDL	Earth Data PR6-24 Portable Field Recorder
EGF	Empirical Green's Function
EW	East West Component
FAP	Discrete Amplitude and Phase Values
FFT	Fast Fourier Transform
FIR	Finite Impulse Response
FUTB	Football Field
GARD	Guard House

GB	Gigabyte
GCF	GURALP Compressed Format
GONAF	Geophysical Borehole Observatory at the North Anatolian Fault
GPS	Global Positioning System
GSM	Global System for Mobile Communications
HYBL	Heybeliada
Hz	Hertz
KNAL	Kınalıada
KRGZ	Büyükada2
L4C	MARK PRODUCTS L4C-3D
LTA	Long Term Average
Mc	Magnitude of Completeness
ME	Master Event
MEGF	Multiple Empirical Green's Function
MMF	Main Marmara Fault
MRTI	Balıkçıada
MSE	Multitaper Spectrum Estimation
MWSR	Multi Window Spectral Ratio Method
NAF	North Anatolian Fault
NAFZ	North Anatolian Fault Zone
NBF	Northern Boundary Fault
NHNM	Global High
NLNM	Global Low
NPTS	Number of Points
NRTH	North Beach
NS	North South Component
OILH	Oil House
PASSCAL	Portable Array Seismic Studies of the Continental Lithosphere
PAZ	Poles and Zeros
PDA	Personal Digital Assistant
PIER	Pier House
PIRES	Prince Islands Real Time Earthquake Monitoring System
PIS	Prince Islands Segment

POWD	Powder Cave
PSD	Power Spectral Density
Q	Attenuation
Q330	QUANTERRA Q330
REFTEK	REFTEK 130-01
RETMC	Regional Earthquake-Tsunami Monitoring Center
RSPE	Reduced Source Parameter Estimation
SAC	Seismic Analysis Code
SAFOD	San Andreas Fault Observatory at Depth
SCREAM	Seismometer Configuration Real-Time Acquisition and Monitoring
SCRP	Sky Scraper
SE	Slave Event
SEISAN	Earthquake Analysis Software
SHTH	S House
SNR	Signal to Noise Ratio
STA	Short Term Average
STA/LTA	Short Term Average/Long Term Average
STS-2	STRECKEISEN STS-2
TB	Terabyte
TCP/IP	Transmission Control Protocol/Internet Protocol
TCXO	Temperature Compensated Crystal Oscillator
UDP/IP	User Datagram Protocol/Internet Protocol
USB	Universal Serial Bus
WGS	World Geodetic System
Z	Vertica

1. INTRODUCTION

The topic of this thesis is source properties of micro-earthquakes in Eastern Marmara and their connection to the structure of the Çınarcık Basin. Therefore, the study area is Eastern Marmara and, in particular, the Çınarcık Basin.

The main goal is to obtain the fracture properties of seismic events in and around the Çınarcık Basin and see whether they have any characteristics that may be connected to a particular location. The fracture properties considered in this study are seismic moment, fracture size, stress drop, energy released and occurrence rate. The analysis tools presented in this thesis can be arranged for routine application in such a way that it will be possible to look whether the fracture properties mentioned are changing in space and time.

The first motivation that has led to focus research particularly in the Çınarcık Basin is the fact that this location is critical for the expected Marmara earthquake (Bohnhoff *et al.*, 2017). Second motivation of this study is the observation of the repeating foreshocks few hours prior to the İzmit Earthquake (17 August 1999 Mw 7.4) that pointed to a slow deformation before the main rupture (Bouchon *et al.*, 2011). This paper has shown the importance of the characteristics of the foreshocks before the nucleation phase of an earthquake. Consequently, there was a motivation to make a more systematical search of the earthquake clusters (foreshocks and aftershocks) in general. The main idea is to compile the behavior of the clusters in normal times in order to be able to differentiate between the normal and abnormal activities in the future. Possible variations of the fracture properties in space (EW, NS and distance to the fault) and in time (number and duration of the foreshocks and aftershocks) are therefore explored in detail.

There were some major difficulties for conducting this study which, at the same time, helped to derive new strategies while trying to overcome them. The first one is that, only a limited number of earthquakes occurred in the Çınarcık Basin during the observation period. Moreover, magnitudes of these earthquakes are small. In addition to these facts,

there are no OBS and borehole data that are open to public. Even this was the case data quality may often be inadequate. For the OBS in particular, the high level of noise in the Marmara Sea and the presence of the thick sediment in the Çınarcık Basin Karabulut *et al.* (2002) which reduces the seismometer coupling lead to important signal degradation. Additionally, since small earthquakes mostly occur in the mid part of the sea, and are at considerable distances from the boreholes that are situated on the land, are still far away to the source region.

The available data that is used throughout this study is the PIRES Arrays data. Although, arrays have many advantages compared to the observations from single stations, PIRES Arrays have a limited observation angle as a disadvantage. Taking also into account that PIRES is a surface array, the atmospheric noise for the small events is a fact that had to be battled for. An additional issue is the noise production due to the concrete boxes that had been built for the protection of the instrumentation. Therefore, one of the significant contributions of this study is the effort to overcome different noise sources both with signal processing and array stacking techniques.

Considering all these mentioned concerns, it is clear that observing small earthquakes is a hard issue and some special methods need to be developed. One essential contribution of this study emerges at this point by providing a performance test for the seismic arrays that are used as a substitute to boreholes. Multiple observations of the same event at different array stations have enabled to use waveform stacking and other statistical tools. Note that the vertical array Geophysical Borehole Observatory at the North Anatolian Fault (GONAF), located close to the PIRES Arrays, do also suffer from the same limitation due to the event distance and does not fully allow use of the array processing. As it is known, GONAF boreholes are vertical arrays which have seismometers at different depths. However, it is reported that array properties of the GONAF is not yet used, instead, all sensors are used as a single station which are buried at a single depth (Malin *et al.*, 2018).

Stacking is used as a high performance method in various areas in this study. At first step, the detection of the events that do not appear in the bulletins of the local agencies is done by this approach. Secondly, the source parameter estimation uses both waveform

stacking and other statistical methods. For the case of the events detected by the local agencies, which will be called Master Event (ME) hereafter, Empirical Green's Function (EGF)s are estimated by stacking. Accordingly, events, which are not detected by the local agencies and only found by the correlation/stacking approach in this study, are called Slave Event (SE).

As it is known, since no information is available about the Attenuation (Q) of the study region, Q is obtained independently using the EGF stacking method for the MEs. This in turn used for the source parameter study of the SEs.

As a new approach, a different methodology has been used for the spectrum estimation of the SEs. Instead of the Discrete Fourier Transform (DFT), Welch Algorithm Welch (1967) has been preferred for the calculation of the spectrums which will be discussed in the following sections.

After outlining the objectives briefly, the topics studied in the thesis are given in the same order as they appear in the text.

Following a short introduction in Chapter 1, problem description, previous studies and methods applied are briefly mentioned in Chapter 2. Chapter 3 includes knowns and unknowns about the Marmara Region from a broader perspective. In this context, highlights from some of the popular studies performed in the Marmara are also mentioned. Chapter 4, which is entitled as "Description of Data", describes the data acquisition issues in general. The reasons for selecting the Çınarcık Basin to install a high number of instrumentations in such a small area are also discussed. Additionally, PIRES Arrays and network are introduced. More detailed information, in particular, technological evolution of the PIRES Arrays, its enlargement within years, information about the station sites, Prince Islands geology, instrumentation, data format, pre-processing and instrument response sections appears in the related part of the Appendix.

Chapter 5 covers the detection and location of the events. In section 5.1, details about the array based waveform cross correlation technique that is adapted from Gibbons and Ringdal (2006) are discussed. The detection uses stations from the two arrays that are ~2

km apart from each other. Cross correlation approach enabled high performance of the technique that allowed seizing of the SEs that are totally missed by all local networks. With the help of this method, various earthquake clusters of different sizes were identified. Moreover, it is observed that some of the clusters are composed of very similar earthquakes. Section 5.2 discusses the details of the location procedure of the MEs. Since, using the advantages of the arrays has been the target, back azimuth information obtained from the FK analysis has been incorporated into the conventional location. Therefore, location problem is modified to solve using more variables than the conventional approach (i.e. back azimuth information in addition to P and S readings). Concepts used in the FK analysis and NORSAR Processing Software EP, Fyen (1989, 2001a,b) in particular, are introduced in this section. Additionally, application of the FK method both in terms of the basic principles and with the application on the real data examples from the PIRES, are given in the Appendix. Major difficulties of dealing with the PIRES Arrays and recipes to overcome, are also given in the same section.

Chapter 6 describes the main processing tools that are used throughout the analysis and therefore composes the backbone of this study. Section 6.1 outlines the pre-processing steps of the source parameter methods, used for both EGF stacking and Reduced Source Parameter Estimation (RSPE) Method cases. Inverting for only two of the source parameters (i.e. seismic moment and attenuation) will be called as RSPE hereafter. Whereas, the conventional approach where three of the source parameters (i.e. corner frequency, seismic moment and attenuation) are obtained simultaneously will be called as Conventional Source Parameter Estimation (CSPE) Method in this study.

The final effects of the pre-processing steps are given in detail and their importance is emphasized by means of examples. Sections 6.2 and 6.3 include the steps where corner frequency, seismic moment and attenuation are obtained. First of all, corner frequency estimated, received as reliably as possible. For this purpose, a stepwise procedure is applied. Since, earthquakes are detected in terms of the sequences, instead of single events, it was possible to use EGF method. Target has been to obtain smoother and more reliable source spectra. Therefore, spectral ratios at all of the arrays stations are stacked. In that sense, once again importance of the arrays comes on the scene. After stacking of the spectral ratios at each sequence, corner frequencies of the MEs are found using inversion,

based on a predetermined spectral model. When compared with the CSPE approach, this method is proven to be more stable.

As soon as obtaining the corner frequencies of the MEs in the sequences, seismic moments and Q were estimated as the second step. In this context, fixing the corner frequencies, seismic moments and attenuation have been searched for using RSPE. Although, spectral analysis is applied individually for each station of the arrays, this time, median values of the moments and attenuations of all of the arrays stations have been calculated. At the end of this technique, attenuation valid for the frequency range of the MEs has been obtained.

For the SEs in the clusters, methods applied gradually become more complex. These are covered in Section 6.4. In spectral estimation, instead of using the technique of DFT, Welch Method, Welch (1967) is preferred. During the inversion of the source parameters, the value of the Q previously obtained from the analysis of the MEs is used. In order to overcome the difficulties encountered due to the small size of the events, the background noise and the multiplicative noise near 80 Hz, variety of techniques are used which are described in detail.

Chapter 7 describes the relative location method used for earthquake clusters, namely the distance of SEs relative to the MEs. The distance is estimated using the well-known cross correlation method.

Chapter 8 analyses the stress drop of earthquakes within a close distance to the PIRES Arrays, which is one of the primary goals of this study. Up to this chapter, most of the effort is given to reliable estimation of the components of stress drop, namely seismic moment and corner frequency. This part of the thesis focuses on whether some kind of variation can be found as the location of the events change in EW and NS directions. The ultimate goal, which is to classify the region in terms of their differences in seismic properties (i.e. seismic moment, fracture radius, stress drop, energy and occurrence rate) is discussed in this chapter.

Seismic energy radiation with respect to seismic moment is discussed in Chapter 9 for the MEs. The critical issue in this context is to find traces of creep like deformation (or slow earthquakes) which are expected to dissipate lower energy than the normal earthquakes.

The last chapter, Chapter 10, discusses the spatial distribution of the number and duration of the earthquakes in the sequences. In this context, once more, an attempt is made to check if the above properties show any variation in the EW and NS directions.

2. PROBLEM DESCRIPTION, PREVIOUS STUDIES AND METHODS APPLIED

In section two, problem description of the study area, previous studies and methods applied throughout the thesis have been briefly handled.

Marmara is one of the two locations on the North Anatolian Fault Zone (NAFZ) that has not been fractured during the last century and therefore it is expected over a 7 magnitude earthquake here. Since, NAFZ passes at a distance of 15 km to 17 million İstanbul, this region is very important. From the seismicity distribution (Figure 2.1), it can be understood more or less, where the fault that will break passes from. In addition to that, seismicity map also shows clearly, in some of the locations earthquakes occur more intensely where else there are some weird locations that earthquakes are observed less.
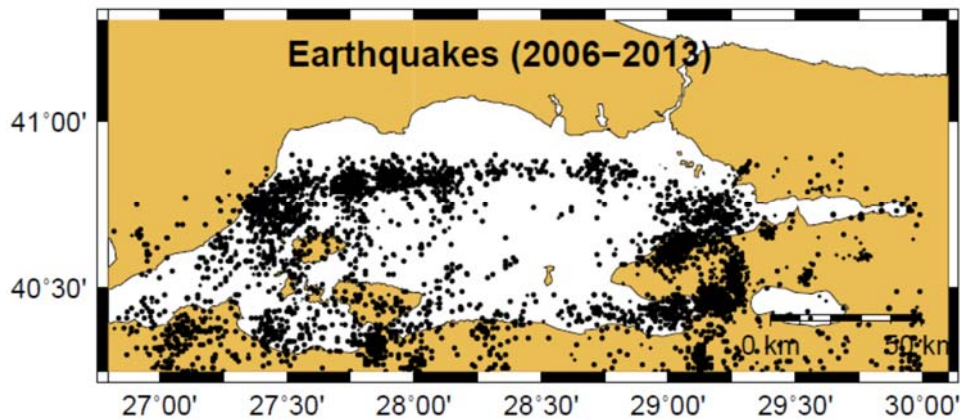
Figure 2.1. Seismicity of the Marmara Region between the years 2006 and 2013.

In spite of the view of the clear distribution of the seismicity, there are still many questions. The most important ones are: First of all, there is a bending on the fault. Therefore, the exact turning point of the bend should be known clearly. In addition to that, how the stress condition is affected nearby the bending should also be understood.

Second one is; there are question marks from the GPS studies. According to the GPS data, there is a big difference between the central part and the Çınarcık Basin. Strain is

observed in the Çınarcık Basin but seismicity is not observed in some of the areas, (Figure 2.1). Because of this reason, aforementioned region is called as "locked" (Bohnhoff *et al.,* 2013) and (Ergintav *et al.,* 2014). On the central, because of the wider aperture of the sea, there is no GPS data close to the fault on the southern part. GPS data that exist are not very well aligned on this part of the fault. Therefore, some researchers prefer not to take into account the GPS velocities measured on the south of the central part. On the other hand, GPS velocities measured on the north are better positioned and they indicate only a very small strain. There are two interpretations of this. Le Pichon *et al.* (2005) claims that, between the northern and southern parts of the fault, there is a difference in rigidity. They propose that, strain is asymmetrical and much of the strain appears on the southern part. In other words, this behavior might correspond to the presence of bi-material interface (Le Pichon *et al.*, 2005). The second interpretation is by Reilinger *et al.* (2006). They claim that absence of strain is because of the creep going on at that location. Since, these two conclusions have totally different consequences for the hazard in İstanbul, it is very important to look for more observations and evidences to clarify this issue.

Lastly, there are also some proposed scenarios about the distribution of the locked and creeping sections along the fault that passes from the Marmara Sea both from the GPS and seismology community. On the Central Marmara Fault (CMF) segment of the Main Marmara Fault (MMF), low level of strain accumulation is observed. Therefore, it is interpreted as the presence of aseismic creep to shallow depths on this fault (Ergintav *et al.,* 2014). In addition to the GPS studies, recent seismological observations such as Schmittbuhl *et al.* (2016) and Bohnhoff *et al.* (2017) have shown the presence of repeating earthquakes on the western Marmara section of the MMF which might be an evidence of creeping. From another point of view, these studies prove the importance of the Prince Islands Segment (PIS) in terms of its being the probable nucleation point of the next Marmara earthquake (Bohnhoff *et al.*, 2017). Particularly, on the PIS that is the same area of interest, strain accumulation has been calculated as 10-15 mm/yr (Ergintav *et al.,* 2014).

When the depth of the seismicity is compared between the different basins in the Marmara Sea, there are lateral variations. For instance; in the Central Basin (CeB), there is high seismicity from surface to ~17 km depth as it has been observed by Schmittbuhl *et al.* (2015). On the other hand; on the PIS in the Çınarcık Basin, seismicity varies between 8

and 14 km and with a locking depth of 10 km. Seismicity is vertically up to the surface at both ends of the basin as observed both by Bohnhoff *et al.* (2013) and Schmittbuhl *et al.* (2015). Bohnhoff *et al.* (2013) have also calculated PIS as a deep seismic gap with 30 km length and 10 km width. Likewise, seismic energy release is low on this part of the fault (Schmittbuhl *et al.,* 2015).

In conclusion; when Marmara Sea has been considered from the general point of view, it is very complex. There are quite heterogeneous materials inside the Marmara in Three Dimensional (3D). One of the reasons of this is the diversity of the materials. For instance; there are materials from Eurasia, Anatolia and also from shallow young deposits. Therefore, constitutive of the materials can be defined as quite various. Moreover, Marmara is also very different in terms of the continental fault and fracture.

There are also debates going on about the exact location of the fault where it passes from, about the geometry of the fault zone and presence of the pull apart structures, etc. In addition to that, asymmetrical basins take place inside the Marmara Sea. There are some locations where earthquakes occur more and there are some locations where creep is observed. On the contrary, there are also some locations where earthquakes occur less and where creep is not observed. Therefore, the question that is trying to be answered in this study is, what kind of information can earthquakes provides that occur in different locations in the Marmara Sea.

Roughly; as first order studies, an idea about the region in terms of the earthquakes and fault mechanisms could be captured. There have been abundant works that have been published in this sense. Such as, Bulut *et al.* (2009), Karabulut *et al.* (2011), Orgulu *et al.* (2011) and Wollin *et al.* (2018), etc.

In terms of the second order and more detailed studies, it can be looked for whether the region could be understood from fracture mechanics or energy dissipation. For detailed and finer analysis, second order studies are most commonly applied at the boreholes rather than surface stations in the world. In the present work, one of the biggest efforts is given to perform second order finer applications using high resolution surface arrays working at high sampling rates. Therefore, this study is essentially focused on the performance of the

seismic arrays as a substitute to boreholes which makes the present practice for studying source parameters, etc.

The above discussions compose the main starting point of the study. Though, as mentioned briefly above, this region has various difficulties. The first problem while doing this work is to detect earthquakes. In this manner, it has been aimed to make an effort to catch SEs. For this purpose, array techniques have been used to lower down the magnitudes of the earthquakes detected. Using the MEs that could be observed ew the land stations as template, similar but smaller events have been searched for with array based cross correlation technique. With this technique, earthquakes including foreshocks and aftershocks that have occurred in this region could be examined. In addition to that, number of earthquakes detected increases and detection threshold decreases compared to using the land stations that are far away. After the detection of earthquakes, more precise locations of the MEs of the clusters have been made using FK analysis in addition to the conventional location methods. On the other hand, SEs in the clusters have been located using cross correlation approaches.

Main target in this study has been to look for, if there is any seismological evidence to support the inferred lateral variations of the rigidity and fault behavior, both on EW and NS directions. In this manner, coherency and consistency have been tried to catch in terms of location and 3D distribution of the differences in stress drop and seismic efficiency in the Çınarcık Basin. Studies such as stress drop and seismic efficiency of the MEs and SEs are mostly accomplished with boreholes. On the other hand, it has been tried to understand whether unknown anomalies can be solved and explained in this region using seismic arrays. It has been attempted to answer whether any relationship can be found between the location and different properties when long term monitoring has been done. Therefore, it has been tried to detect any behavior changes of the seismic activity as well as the physical properties of the earthquakes occurring across these zones. In this context, spectral parameters, stress drop and radiated energy differences of the earthquakes on EW and NS directions are examined.

This study also reveals the general pattern of earthquake clusters, namely how they extend in time and space, etc. The compilation of the behavior of the clusters, if carried

over long period of time, may hopefully serve to develop a classification and a mean for differentiating between any normal and abnormal clusters. This in turn can be used to detect any abnormal cluster which may be a sign of any slow deformation process. This might be a precursor for a large earthquake, just like the one that has been described by Bouchon *et al.* (2011) for the İzmit Earthquake (17 August 1999 Mw 7.4).

In this study, combinations of array and network data have been used. It has been called as PIRES that are on the nearest distance to the fault that passes from the Marmara Sea. All the way through this research, new approaches have been developed appropriate to the problems in detection and estimation of the source parameters of both MEs and SEs and noise cancelation. It has been expected to obtain consistent results if such detailed analysis have been applied and made long term observations.

There are transition zones vertically and laterally where creep and locked zones are side by side in the Marmara Sea. In terms of the PIS, locked patch over creeping base has been identified (Bohnhoff *et al.*, 2013). Therefore, it should also be known very well what it is expected to observe in creeping and locked sections. This is very important in order to predict the potential seismic hazard of the future expected earthquake in the Marmara Sea (Bohnhoff *et al.*, 2017). For instance, most well-known phenomenon about the repeating events is that they might occur in creeping sections. Therefore, other traces of the repeating events, if there are any, have to be known in order to differentiate them clearly.

3. DESCRIPTION OF THE MARMARA REGION

In this section, studies about the Marmara Sea and in particular the Çınarcık Basin that mostly come into prominence will be mentioned. With this part, a quick scan about the known facts and question marks about the study region is aimed to be put forward from a broader perspective.

NAFZ is a 1600 km transform fault. It is considered as a border between the Eurasian and the Anatolian Plates. Although; along most of the NAFZ influence of the strike-slip regime is prominent, probably due to the Hellenic subduction rollback, it converts into the trans-tensional regime in the Easternmost Marmara which at the same time resulted the opening of the Marmara Sea (Şengör *et al.,* 2005). It is thought that, trans-tension still continues thus young pull-aparts in the Eastern Marmara Sea in the Çınarcık Basin are the consequence of this movement (Le Pichon *et al.,* 2001) and (Karabulut *et al.,* 2002).

The NAFZ runs almost in one piece until it branches into mainly two strands called as the northern and the southern NAFZ in the northwestern of Turkey below the Marmara Sea (Le Pichon *et al.,* 2014). Between these two strands, majority of the deformation takes place on the northern strand (Reilinger *et al.,* 2006) and (Ergintav *et al.,* 2014). On the other hand, the southern strand only constitutes %20 of the westward movement of the Anatolia (Ergintav *et al.,* 2014).

During the last century, NAFZ was marked by a series of westward propagating destructive earthquakes Barka (1999) and Pinar *et al*. (2010), along nearly all of its entire length, except the Marmara Sea section (Stein *et al*., 1997). The last of this series of the westward propagating sequence was the 1999 İzmit earthquake (17 August 1999 Mw 7.4) which ruptured nearly 120 km of the eastern segment of the Marmara Sea (Barka *et al*., 2002). The exact limit of the rupture is not known precisely at neither ends. The western limit which has been likely to have extended to the south of the Prince Islands according to Bouchon *et al*. (2002) and Ozalaybey *et al*. (2002), is critical in the sense that it hints the start of the next one in the Marmara Sea. Since, it has passed quite a long time over the last

recorded big event in the Marmara Sea it is a strong indicator that, there is a seismic gap in the seismic cycle threatening İstanbul metropolitan.

Fault plane solutions of the aftershocks during the 1999 İzmit earthquake indicate strike-slip motion along the PIS (Orgulu and Aktar, 2001), (Karabulut *et al*., 2002), (Pinar *et al*., 2003) and (Bohnhoff *et al*., 2006). The distribution of the hypocenters along this segment has shown the presence of a 30 km long seismically quiet patch above 10 km depth (Bohnhoff *et al*., 2013).

The fault structure below the Sea of Marmara is very complex and still unresolved. The two extreme discussions continue between the single strike-slip (Le Pichon *et al.,* 1999 and 2001) and en-echelon faults (Armijo *et al.,* 2002) and (Armijo *et al.,* 2005) which completely results different hazard for the Marmara.

Morphologically there is a strong evidence for the existence of three pull-apart sub-basins in the Marmara Sea aligned along the NAFZ (Le Pichon *et al.,* 2003) and (Armijo *et al.,* 2005). The Easternmost Çınarcık Basin has a wedge shaped structure, bounded by the branches of the NAFZ from its north and south (Bohnhoff *et al*., 2013).

Recent seismological studies have shown that, normal faulting associated with the pull-apart mechanism is likely to have been dominated gradually by dextral strike-slip regime (Le Pichon *et al*., 2001), (Bulut *et al*., 2009) and (Orgulu, 2011). Accordingly, a single catastrophic event which has a potential of rupturing the total length of the Marmara Sea has become a plausible scenario.

4. DESCRIPTION OF DATA

In section four; basically, source of the data used in this study will be introduced. In this manner, purpose of the installation of the seismic arrays and network and their features will be presented.

The inspiration of installing a seismic network in the Marmara Sea was to better understand the physical characteristics of the major fault segments and to improve the local seismicity monitoring. In this context, within a joint project, Boğaziçi University Kandilli Observatory and Earthquake Research Institute Department of Geophysics and Helmholtz Centre Potsdam, GFZ German Research Centre for Geosciences have installed small aperture surface seismic arrays on the two Prince Islands. The project has been named as PIRES and it is designed for permanent operation. PIRES seismic arrays started to operate in 2006. Seismic arrays are located on the two islands, namely Sivriada and Yassıada, at a distance of ~3 km to the Marmara Sea part of the main trend of the NAFZ. This section of the fault is often referred as the Northern Boundary Fault (NBF). The main purpose of choosing these spots as station sites is their being the closest land site locations to the NAFZ, along the total length that passes from the Marmara Sea. The seismic arrays are therefore, ideally located to monitor the low magnitude seismic activity ongoing on the eastern part of the "seismic gap" in the Marmara Sea that is on the south of mega city İstanbul. Furthermore, since the islands are not inhabited and located offshore at ~15 km distance from the city of İstanbul they are less affected by the cultural noise. Both islands have stiff hard rock sites of Devonian graywacke and quartzite formation giving excellent conditions for efficient seismic coupling (Ozgul, 2012).

Locations of the PIRES Arrays stations on Sivriada and Yassıada are shown with red plus signs in the Figures 4.2 and 4.3. Abbreviations of the Sivriada Array stations are: Easy (EASY), North Beach (NRTH), S House (SHTH), Byzantine (BYZN) and Powder Cave (POWD), (Figure 4.2). Abbreviations of the Yassıada Array stations are: Oil House (OILH), Sky Scraper (SCRP), Guard House (GARD), Pier House (PIER) and Football Field (FUTB), (Figure 4.3). These abbreviations will be used for the PIRES Arrays stations in the text hereafter.

Figure 4.1. PIRES seismic arrays: Sivriada Array stations locations.

Figure 4.2. PIRES seismic arrays: Yassıada Array stations locations.

The two islands, therefore the two seismic arrays, are located only ~2 km apart from each other. Each array has five stations distributed in crossed shape configuration and

forming sub-arrays in a star-like layout. They have a maximum aperture of ~300 m limited by the size of the islands and station spacing of ~150 m, (Figures 4.4 and 4.5).
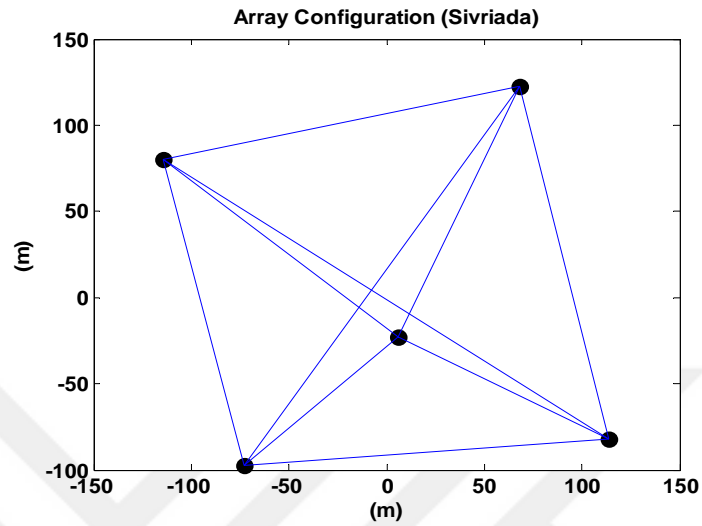
Figure 4.3. Configuration of the PIRES Arrays: Sivriada Array.
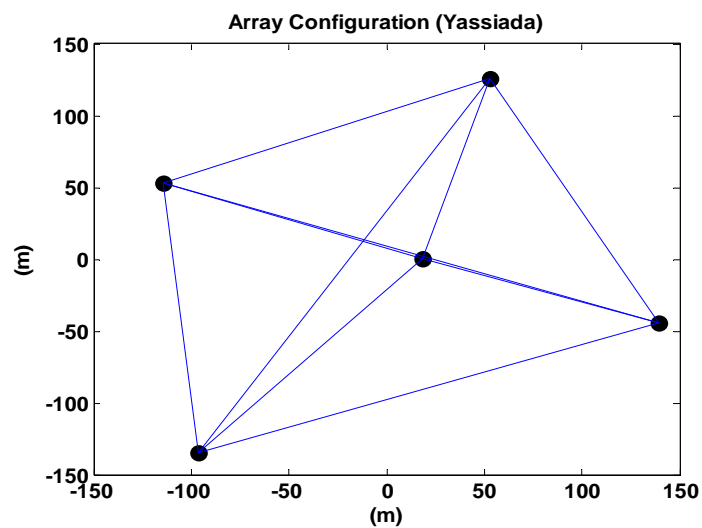
Figure 4.4. Configuration of the PIRES Arrays: Yassıada Array.

Approximate minimum and maximum distances between the arrays stations on Sivriada and Yassıada are as follows:

Table 4.1. Minimum and maximum distances between the PIRES Arrays stations.

Distances between the Array Stations	Sivriada	Yassıada
Minimum Distance	POWD - EASY ~100 m	FUTB - PIER ~125 m
Maximum Distance	BYZN - NRTH ~275 m	GARD - OILH ~295 m

Array stations within hundreds of meters distance, like the case of the PIRES, are mostly appropriate for monitoring local seismicity. Four of the PIRES Arrays stations are located on the outermost edges of the islands making up a circle and one station is in the middle of the islands, (Figures 4.4 and 4.5). Circular array geometry enables to detect earthquakes from all of the azimuths. In addition to that, stations in the middle of the arrays help to increase the signal strength. PIRES Arrays stations locations have been chosen in order to make the resolution of the array as high as possible in a logistically possible extent. This is the best available recording condition for the events occurring ~20 km distance to the arrays.

In addition to the arrays, in order to improve the azimuthal coverage, PIRES network was enlarged to cover the neighboring Prince Islands; Kınalıada, Burgazada, Heybeliada, Büyükada and Balıkçıada reaching finally a total of 16 stations. Abbreviations of the network stations are: Kınalıada (KNAL), Burgazada (BRGZ), Heybeliada (HYBL), Büyükada1 (BASD), Büyükada2 (KRGZ) and Balıkçıada (MRTI). These abbreviations will be used for the PIRES network stations in the text hereafter. Figure 4.6 shows the stations locations on these islands with red pluses. Fault trace passing in front of the islands is drawn from Le Pichon *et al*. (2001). Undoubtedly, adding more stations have improved the locations precisions considerably and allowed more detailed analysis.
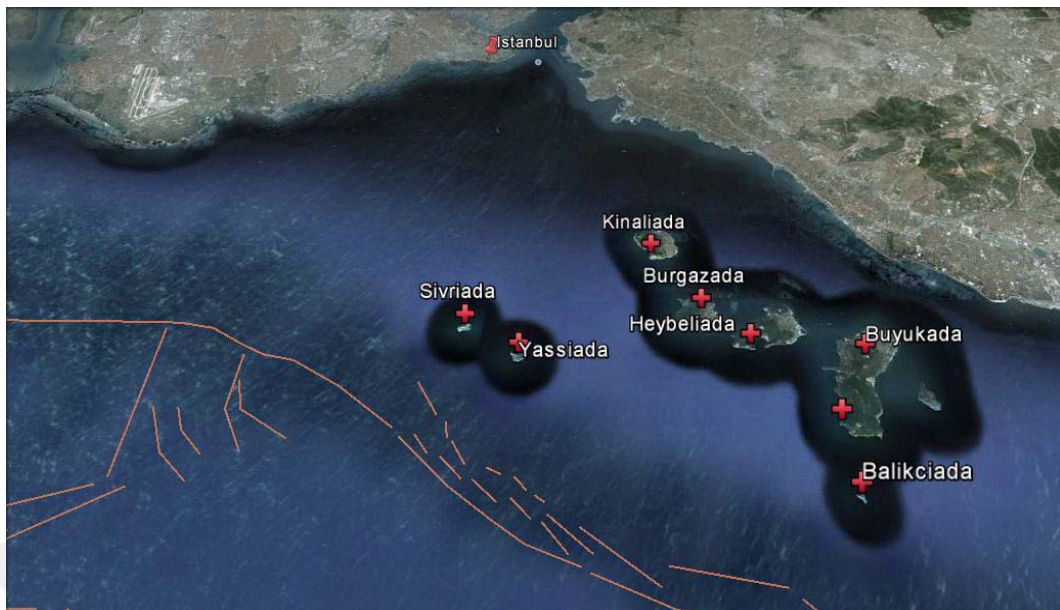
Figure 4.5. PIRES seismic arrays and network stations locations. Fault trace from Le Pichon *et al*. (2001).

Among the PIRES seismic network islands only Balıkçıada is not inhabited, there is population on others. Only one station is located on each of the PIRES seismic network islands, except Büyükada. Since, Büyükada is the biggest island in surface area it has two stations on it. One of the stations is located on the southern west, near the coast, whereas the other one is on the northern part of the island on a higher elevation. These two stations on Büyükada are installed as far as possible from each other in a logistically feasible way. The PIRES seismic network islands are ~5-11 km apart from Yassıada PIRES seismic array and they are within the azimuths between northern east and southern east of it.

Approximate distances of the PIRES network islands with respect to Yassıada are as follows:

Table 4.2. Distances between the PIRES network islands with respect to Yassıada.

Distances between the Islands	Distance (km)
Yassıada and Sivriada	~2 km
Yassıada and Burgazada	~5 km
Yassıada and Kınalıada	~6 km
Yassıada and Heybeliada	~6.5 km
Yassıada and Büyükada	~9.5 km
Yassıada and Balıkçıada	~11 km

Further very detailed information concerning all aspects of the PIRES Arrays and network can be found in the related part of the Appendix.

5. DETECTION AND LOCATION OF EVENTS

Section five that is titled as "Detection and Location of Events" composes of two sub-sections which are "Earthquake Detection Procedure" and "Location by Array Processing", respectively.

5.1. Earthquake Detection Procedure

One of the main purposes of installing seismic arrays on the islands in the Marmara Sea is to lower down the detection threshold below the level which is around M=1.7 between the years 2006 and 2017. Magnitude of completeness (Mc) has been calculated taking into account the Boğaziçi University Kandilli Observatory and Earthquake Research Institute Regional Earthquake-Tsunami Monitoring Center's (RETMC) catalogue, (Figure 5.1). It has been evaluated for a radius of ~20 km considering the latitudes and longitudes of the center stations of the PIRES Arrays (POWD and FUTB) and for cumulative number of earthquakes.
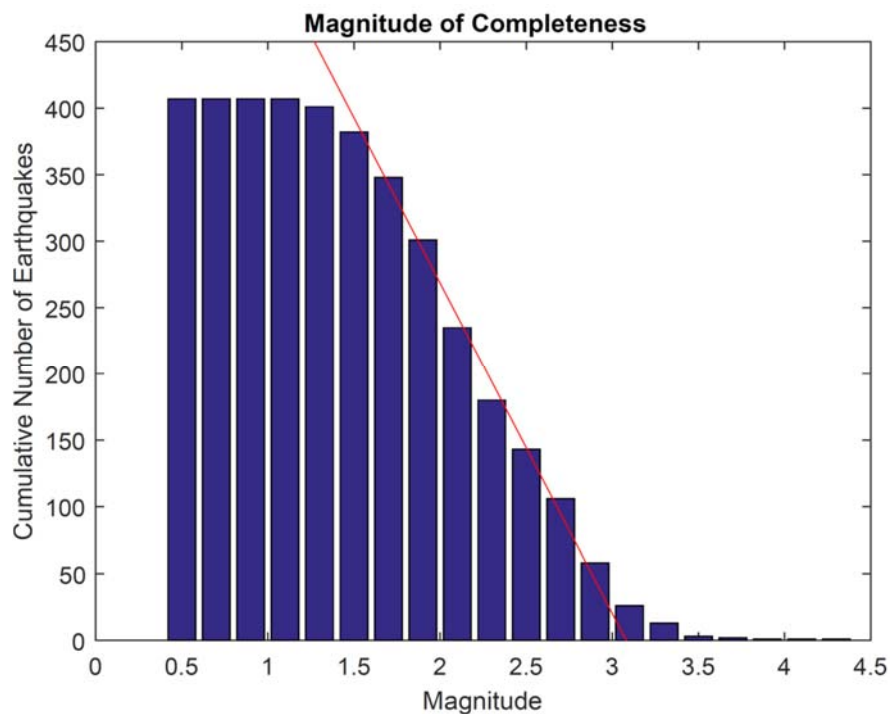
Figure 5.1. Magnitude of completeness (Mc).

There are several methods for instance; maximum curvature, entire magnitude range, etc. used for calculating the Mc but, just a straight line has been fit in order to have an idea about reliably recorded minimum magnitude in the RETMC's catalogue within ~20 km to the PIRES Arrays.

With the PIRES, a special emphasis is given to monitor the NBF close to PIS which is identified as a quiet patch representing a future barrier (Bohnhoff *et al.*, 2013). In this context, main objective of this work is to detect SEs occurring in the seismically low activity area of the Marmara. Therefore, primary purpose is to find SEs in the Marmara close to the PIRES network that were not observed previously by the distant mainland stations of RETMC.

RETMC, like all monitoring centers, try to detect earthquakes using waveforms that are recorded at the stations as it is illustrated in Figure 5.2. The figure shows one hour long waveform (09.08.2011, 19:00-19:59) of the vertical component of the ARMT which is one of the stations of the RETMC located on Armutlu coast. It is the nearest land station of the RETMC with a distance of ~26 km to the hypocenter of a Marmara Sea earthquake (09.08.2011, Md=2.4) indicated with red arrow in Figure 5.2. Earthquake which is shown with blue arrow in Figure 5.2 is Mudanya-Bursa Earthquake (09.08.2011, Md=2.0). ARMT station, although it is on the coast, somehow exemplifies the severe noise conditions of the waveforms recorded at the land stations of the RETMC which is closest from an earthquake occurring in the Marmara Sea (09.08.2011, Md=2.4). Although, a lot of earthquakes occurred in one hour, only a few of them can be barely distinguished clearly from the waveform of the ARMT station, (Figure 5.2). The main reason of this, without doubt, is the long distance of the ARMT station to the hypocenter of the earthquake. The low SNR of a small earthquake (Md=2.4) also has an adverse effect on its amplitude. In addition to that, high level of noise clearly obscures the SEs.
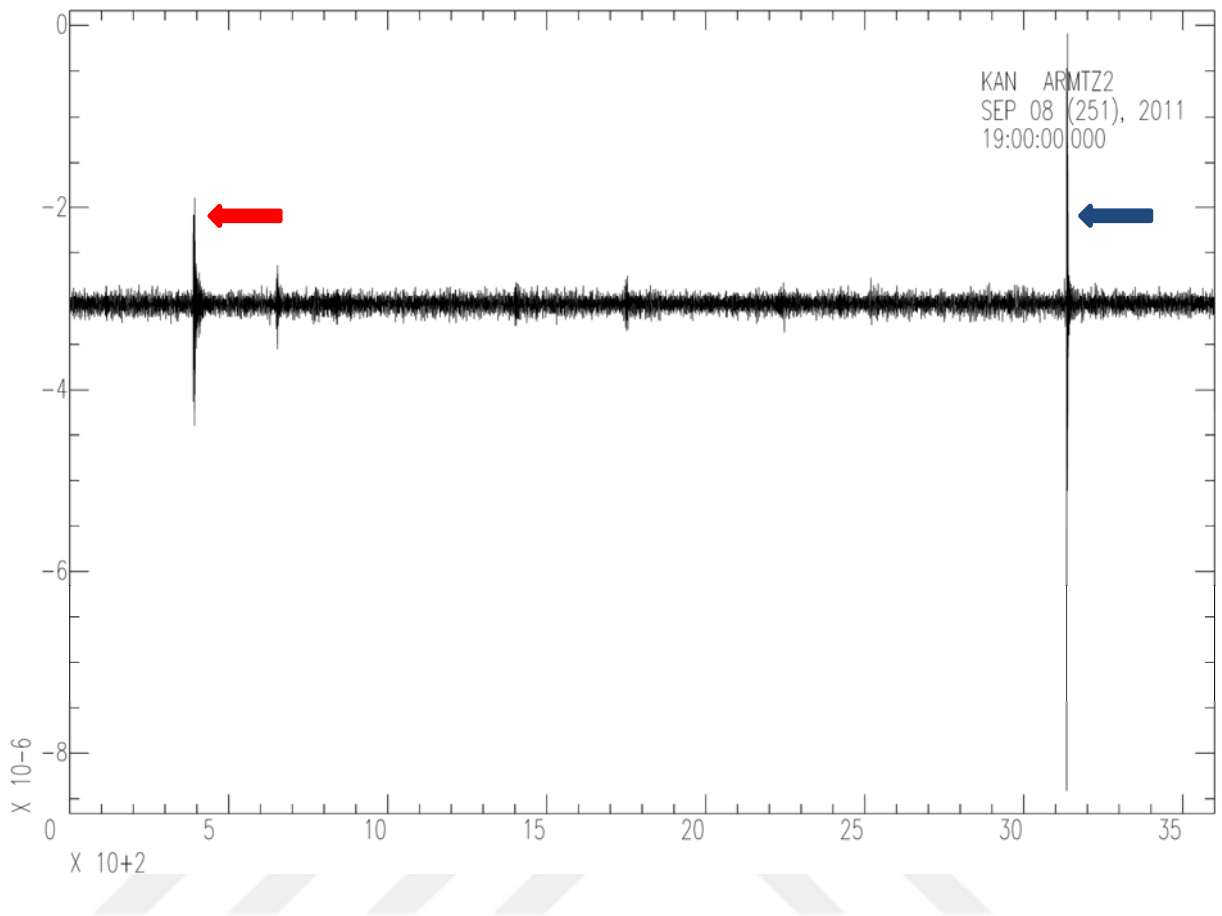
Figure 5.2. One hour long waveform of the vertical component of the ARMT station. Earthquake shown with red arrow is (09.08.2011, Md=2.4) Marmara Sea Earthquake. Earthquake shown with blue arrow is (09.08.2011, Md=2.0) Mudanya-Bursa Earthquake.

Figure 5.3 shows one hour long waveforms (09.08.2011, 19:00-19:59) of the same Marmara Sea earthquake (09.08.2011, Md=2.4) observed at the vertical components of the different stations of the Sivriada Array which are BYZN, NRTH, POWD and SHTH, respectively. The reason of displaying the vertical components of all of the available stations of the Sivriada Array in particular is, some of them are relatively noisier (NRTH and SHTH) than the others (BYZN and POWD) at that particular time of the earthquake occurrence. This figure demonstrates two main ideas. One of them is, although they are all stations closer to the epicenter as compared to the RETMC, earthquake signals are still not obviously differentiated from noisy raw waveforms. Therefore, Figure 5.3 manifests the necessity of a much more powerful method in terms of reducing the noise level. Secondly, despite some of the stations on the islands have a higher noise level than the ARMT which

is on mainland, one could still perceive more earthquakes due to their closer distance (~10 km) to the earthquake generation zone.

In order to compare the noise levels of the stations in Figures 5.2 and 5.3 more quantitatively, waveforms have been multiplied with their corresponding amplification constants and expressed in true velocity. The instrument responses of the seismometers have not been removed but, in order to compare the amplitudes of the different type of instruments more reliably in a visual sense, waveforms have been multiplied with constants. Amplification constants have been calculated by the multiplication of the gain values of the seismometers and digitizers for each station and component of the stations. Finally, velocity seismograms that are in units of counts have been transformed to units of meter/second when multiplied. Seismometer and digitizer gain values of the PIRES stations' and the ARMT station's relevant values have been taken from instrument data sheets and the web site of the RETMC, respectively.
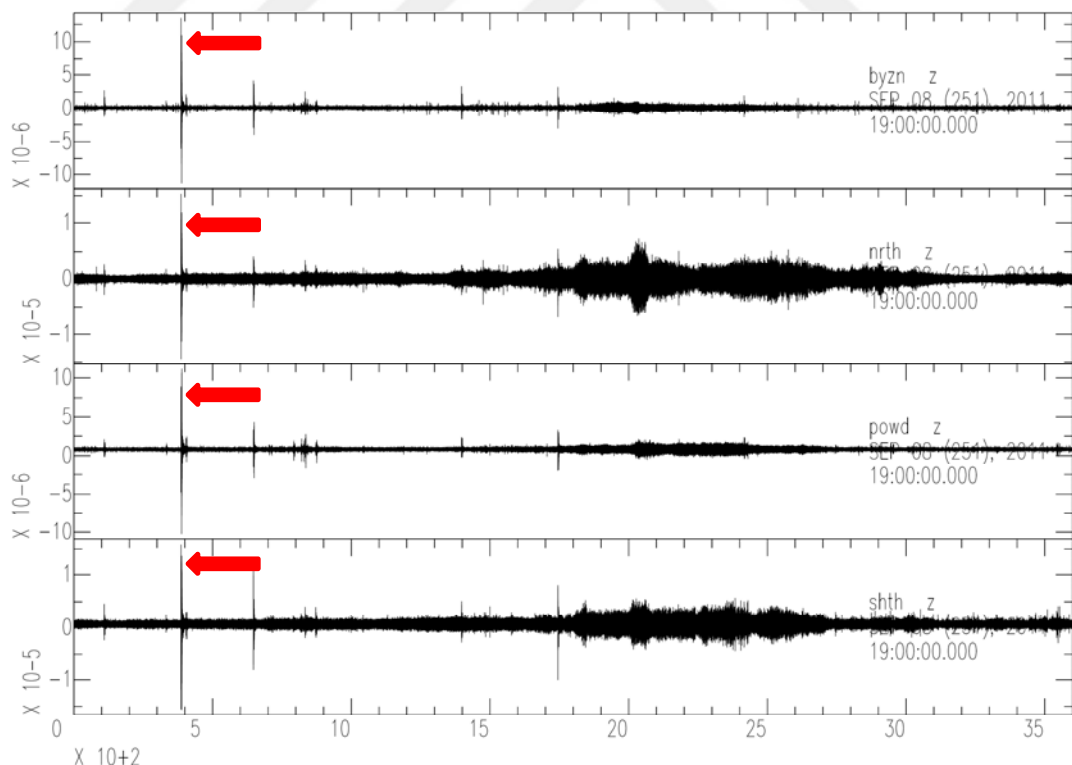
Figure 5.3. One hour long waveforms of the vertical components of the Sivriada Array stations BYZN, NRTH, POWD and SHTH, respectively. Earthquakes shown with red arrows are (09.08.2011, Md=2.4) Marmara Sea Earthquake.

Earthquakes which are shown with red arrows in Figures 5.2 and 5.3 is an event (09.08.2011, Md=2.4) in Marmara Sea that is used as an example. It is clearly seen that at the Sivriada stations (BYZN, NRTH, POWD and SHTH) earthquake has higher amplitudes than the ARMT station since they are closer stations. Other small earthquakes' amplitudes which appear and those could be identified in Figure 5.2 are also relatively small compared to the amplitudes at the Sivriada stations in Figure 5.3. Moreover, among the Marmara Sea earthquake (09.08.2011, Md=2.4), its aftershocks and foreshocks, only one single earthquake could have been located by the RETMC. The only exception is magnitude M=2.0 Mudanya-Bursa earthquake which has occurred at time 19:52. This earthquake, indicated with blue arrow in Figure 5.2, has higher amplitude on the waveform of the ARMT station whereas it has no trace in any of the Sivriada stations because of its being far away to the PIRES stations.

As it has been discussed very briefly above, the fact of this region's producing rare and small events forced to use more powerful techniques in earthquake detection. Henceforward, during a few paragraphs, the technique that has been used in this study will be introduced from a general perspective. Later on, it will be discussed in a more comprehensive manner in terms of way of handling the method used.
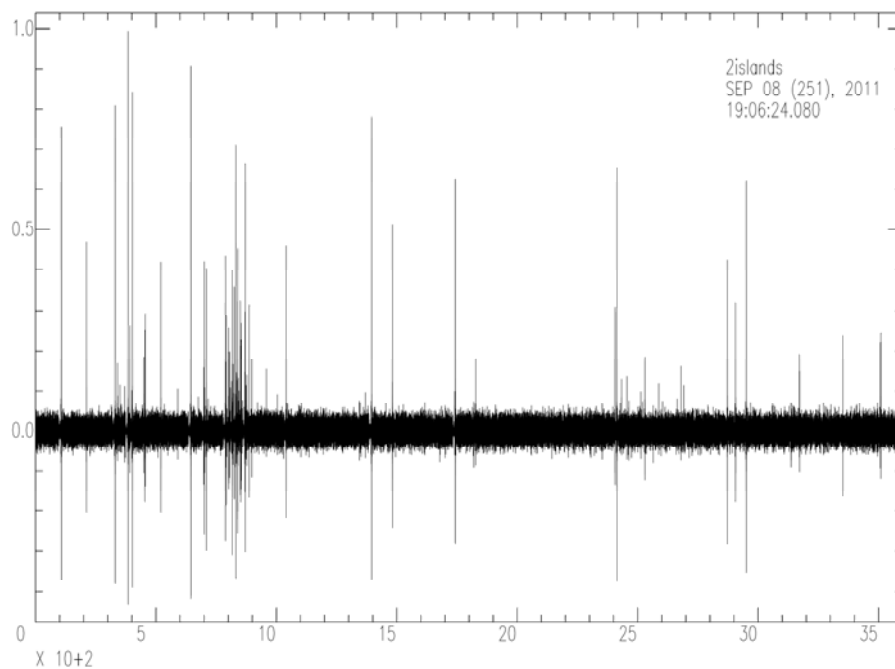
Figure 5.4. Stacked cross correlation traces of all of the stations of the PIRES Arrays.

Figure 5.4 is an example figure of the earthquake detection procedure for the (09.08.2011, Md=2.4) event that has been used in this study in spite of the extensive direct usage of waveforms at monitoring centers. It represents the very last stage of the method which is the stacked cross correlation traces of all of the stations of the PIRES Arrays. Figure 5.4 reveals explicitly the performance of stacking the cross correlation traces over single station waveforms, (Figures 5.2 and 5.3). Signals buried in noise become much more easily detectable with the aforementioned method. Moreover, noise level significantly decreases with stacking compared to the single station waveforms in Figures 5.2 and 5.3. Even the comparison of the PIRES stations, Figure 5.3, with the stacked traces over the two arrays clearly exhibits the improvement, (Figure 5.4). Because of the superior properties of stacking the cross correlation traces, the method mentioned above has been preferred and extensively applied, as will be explained thoroughly during the following passages.

During the search for the small magnitude earthquakes, the intention was to detect similar members of given clusters, instead of finding individual earthquakes. Therefore, a cross correlation based method has been promoted which is best suited for examining the resembling events. Cross correlation measures the degree of similarity between the two time series and this method is highly sensitive to the shape of the waveforms. Because of this feature, false alarms in detecting dissimilar events noticeably decrease.

In the study, earthquake cluster is used to group earthquakes in such a way that in the same group (called a cluster) they are more similar to each other than those in other groups. The earthquake cluster is defined as all events occurring within the window of 15 days from the ME and showing a cross correlation higher than a given threshold with the ME.

The biggest effort of this study has been spent during systematical search with cross correlation procedure, which meant quite a high computational time. One of the drawbacks of the cross correlation based earthquake detection methods is one need to have a good earthquake catalog beforehand in order to use this method effectively. Although, there are several earthquake catalogs open to public, i.e. Prime Ministry Disaster and Emergency

Management Presidency (AFAD) and RETMC, etc. RETMC's catalog has been used as a reference in this study.

Before starting cross correlation, latitudes and longitudes of the stations at the middle of the two arrays, i.e. Sivriada (POWD) and Yassıada (FUTB) and the locations of the earthquakes in the RETMC catalog have been taken. Then, the distances and back-azimuths of all earthquakes in the catalog with respect to both of the stations, (POWD and FUTB), are selected. Finally, earthquakes within an epicentral distance of ~20 km to each of the stations (POWD and FUTB) are used for the cross correlation.
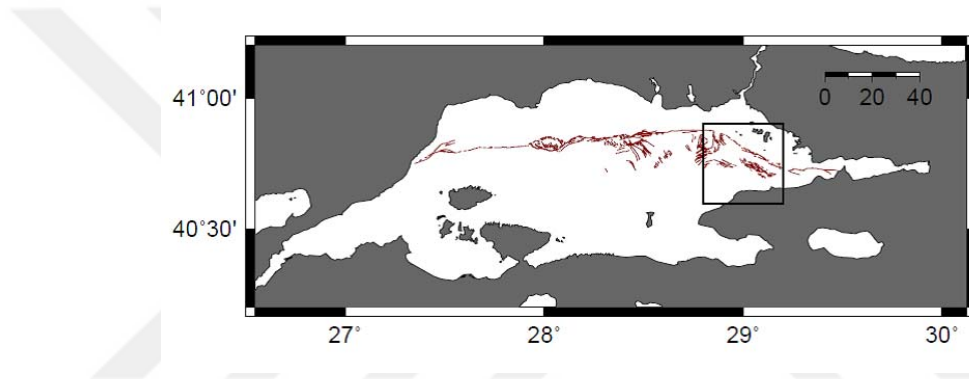
Figure 5.5. Marmara Sea and the study area (Çınarcık Basin).

Figure 5.5 shows the Marmara Sea and the Çınarcık Basin that are monitored by the PIRES Arrays and network stations. Epicentral distance of earthquake searching has been limited within ~20 km to the PIRES Arrays, because quality of the waveforms decreases for SEs going farther away from the arrays. Within ~20 km, earthquakes with a magnitude range of 2.1≤M≤3.3 could have been detected by the RETMC. Therefore, earthquakes that could have been used as template during the search were within this magnitude range. A template event should be chosen as the highest magnitude event in a cluster which will be used as the model to determine others that are undetected. One can visualize that target SEs which are high frequency, already contain all the frequencies of the larger event in smaller amplitude which makes it logical to choose the larger as the template.

Array processing methods have a clear advantage for detecting weak signals (i.e. very small magnitude earthquakes) over conventional earthquake detection methods, i.e. Short Term Average/Long Term Average (STA/LTA) Method. Such techniques' power

comes from delaying and stacking (beam-forming) of the traces from closely spaced instruments. Therefore, this helps to increase the SNR adding up constructively the coherent part of the signal while canceling the incoherent noise (Schweitzer *et al*., 2009) and (Rost and Thomas, 2002). On the other hand, in STA/LTA average values of the absolute amplitude of a seismic signal (STA) is calculated with respect to the average values of the amplitude of seismic noise (LTA) in order to declare an event (Bormann, 2009). For event detection purpose, waveform cross correlation technique adapted from Gibbons and Ringdal (2006) has been used. This method is based on using template events which are then compared systematically to the continuous data in order to reveal similar ones. Cross correlation coefficient has been calculated and used directly to declare the presence of similar events and two waveforms' likeness in this work.

The chosen template is compared to the recorded continuous data calculating a correlation coefficient for each step of the sampling period where a high coefficient points to the possible occurrence of a similar earthquake. The initial sampling period in this study (200 Hz or 500 Hz) has been down-sampled to 100 Hz. There is no need to remove the instrument responses prior the cross correlation. Therefore, raw waveforms have been used directly.

When the template and data are perfectly correlated, correlation coefficient equals to 1. In the opposite case, if they are perfectly anti-correlated, correlation coefficient equals to -1. If they are completely uncorrelated, correlation coefficient equals to 0. In terms of the array traces, if an event is present, all of the correlation coefficients of the array stations will have a maximum at the coincidence time with its corresponding template. Nevertheless, arrival time is fractionally different for each station in a small array like the PIRES. Therefore, an appropriate shifting is needed in order to align the coincidence time of each trace. Finally, all shifted traces are stacked in order to form the final cross correlation trace where all maxima are expected to add up, thus achieving a significant gain. This is a very powerful tool to find the presence of very small aftershocks, foreshocks or repeating events where the signal is buried in the coda of the previous events or in the background noise. Stacking which reduces the noise to a greater extent makes the signal become more visible.

In reality, this method can be applied to any seismic network regardless of whether they are configured as arrays or not. However; when applied to small arrays, seismic traces at array stations resemble each other at a larger extent. Hence, stacking results even a sharper coincident peak, thus leading to a much higher detection performance. In this sense, although there are single stations on different islands in the PIRES network such as; Kınalıada, Burgazada, Heybeliada, Büyükada and Balıkçıada, event detection has been performed using only arrays which are Sivriada and Yassıada. For some unfortunate cases such as malfunctioning of all of the instruments at the same time, cross correlation could not have been performed. Data of some stations have also been ignored during the cross correlation. These are stations which have different sampling rates than the rest because of the failures during the data acquisition configurations.

As it has been mentioned already, during the analysis, the largest magnitude events have been selected as the waveform templates, which are called as MEs. Corresponding waveform templates have been chosen from each available station of the Sivriada and Yassıada Arrays (out of ten stations) and for the vertical components. Figure 5.6 shows the templates for the vertical components of all of the available stations of the Sivriada and Yassıada Arrays for the ME (09.08.2011, Md=2.4).
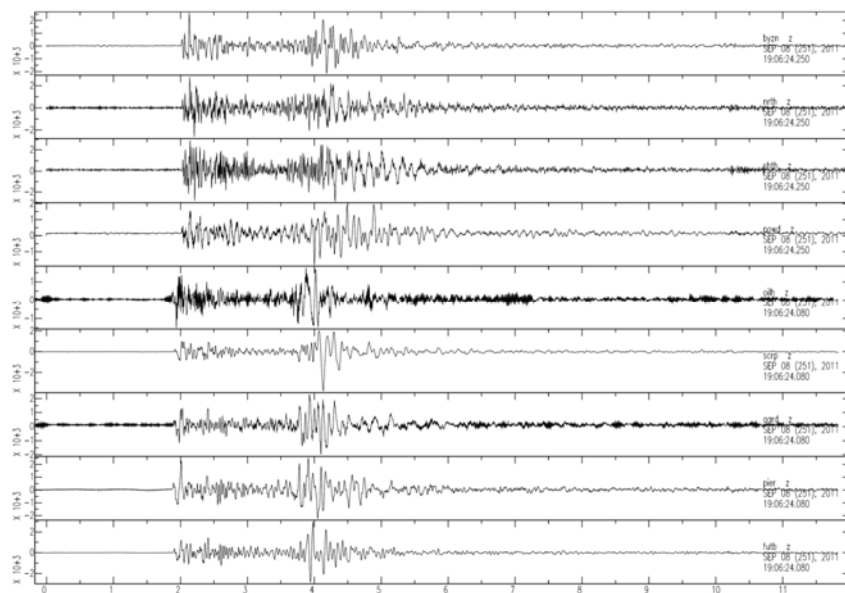
Figure 5.6. Templates of the vertical components of all of the available stations of the Sivriada and Yassıada Arrays for the ME (09.08.2011, Md=2.4).

Before starting the cross correlation, P and S phases of the vertical component of a ME are read and picked in one hour data, for all available stations of the PIRES Arrays using Seismic Analysis Code (SAC). All waveforms have been cut starting from 2 seconds before the P waves and 10 seconds after the S waves in order to form templates for all stations of the vertical components. Considering the window length which is 12 seconds in total, it is quite a long waveform to be included to the cross correlation. In other words, window is chosen long enough so that there is sufficient time for the signal to drop to its pre-event noise level. Note that, phase picks have been only used for cutting the waveforms. They have not been used during the cross correlation procedure.

Figure 5.6 demonstrates templates for all available stations of the Sivriada and Yassıada Arrays, which is a total of nine stations for that period of ME occurrence. They have been cut 2 seconds before the P waves including pre-event noise and 10 seconds after the S waves including coda. Since, earthquakes are recorded at slightly different times at different stations of the seismic arrays, beginning and ending times of the templates are equalized. In this sense, template waveforms have been cut according to the latest starting and earliest ending time of a data to account for difference in length.

Finite Impulse Response (FIR) filter in SAC has been applied when decimating data in order to prevent aliasing effect during down-sampling the signals. Although decimation has unfavorable effect on the waveforms on decreasing the resemblance to the original waveforms, it has been carried on this way taking into account the advantages and disadvantages of the procedure. Before the final step, which is cross correlation, filtering has been applied for the sake of eliminating the noisy parts of the spectrum.

Note that filtering should be used with caution. The optimal filtering parameters (number of poles, number of passes and corner frequencies) may vary significantly for earthquakes of different magnitudes. Moreover, filtering also distorts signals and causes delays, etc. Therefore, decision of the appropriate filter properties has been done according to a small test on data. After considering the pros and cons of different filters on example data, a four-pole bandpass Butterworth filter with passes two and corners at 2 and 20 Hz has been applied for all data. When this filter is applied, filtered waveforms do not much depart

from their original character and they are smoothed eliminating the lower frequencies below 2 Hz and higher frequencies above 20 Hz.

In addition to that, theoretically, for a fixed stress drop of 1 bar (0.1 MPa) magnitude of M=1 earthquake has a corner frequency of 23 Hz and magnitude of M=3 earthquake has a corner frequency of 2.3 Hz (Havskov and Ottemöller, 2009). This output has also been taken into account while deciding the filter higher and lower ends.

Soon after the pre-processing of the waveforms, it has been continued with the cross correlation step where a program written in FORTRAN 77 has been used. Basically, formula 5.1 has been taken into account during the cross correlation where x and y are the two different time series. For the PIRES case, one of them is the template (12 seconds long) and other one is the continuous data (1 hour long). In the formula, r_{xy} is the cross correlation coefficient. Upper part of the division is the cross correlation between x and y whereas lower part is the square root of the auto correlations of x and y. In the Equation 5.1, $m(x)$ and $m(y)$ are the means of the two time series x and y respectively.

$$r_{xy} = \frac{\sum_{i=1}^{n}(x(i)-m(x))(y(i)-m(y))}{\sqrt{\sum_{i=1}^{n}(x(i)-m(x))^2 \sum_{i=1}^{n}(y(i)-m(y))^2}} \tag{5.1}$$

During the cross correlation, template waveform slides all the way to the end of the continuous data until their last points are aligned. Before every step of sliding, where a shorter template waveform comes across with its exact coinciding length of the continuous data, means have to be removed from both of the corresponding data. This procedure is essential especially for the very small magnitude earthquakes where signal is highly contaminated with noise and therefore signal and noise levels are quite comparable with each other. Later on, firstly multiplication is applied at pointwise between the template and continuous data and then addition is performed. This process, where multiplication and addition are applied at each step of the sampling period of the data makes the cross correlation consume long computation time.

The steps of the array based cross correlation method are as follows: First, templates are cross correlated with their corresponding vertical components of the one hour long

continuous waveforms at each station. As a result of this, cross correlation traces for the vertical components of each station have been obtained, (Figure 5.7). Figure 5.7 shows the one hour long correlation traces of available Sivriada Array stations where the last trace is the stack of all of the Sivriada stations (BYZN, NRTH, SHTH and POWD, respectively). The lattermost trace of the Figure 5.7 verifies the power of the correlation based earthquake detection method since there are some sharp peaks suggesting the presence of an event which might be undetected on a single station correlation trace of each station.
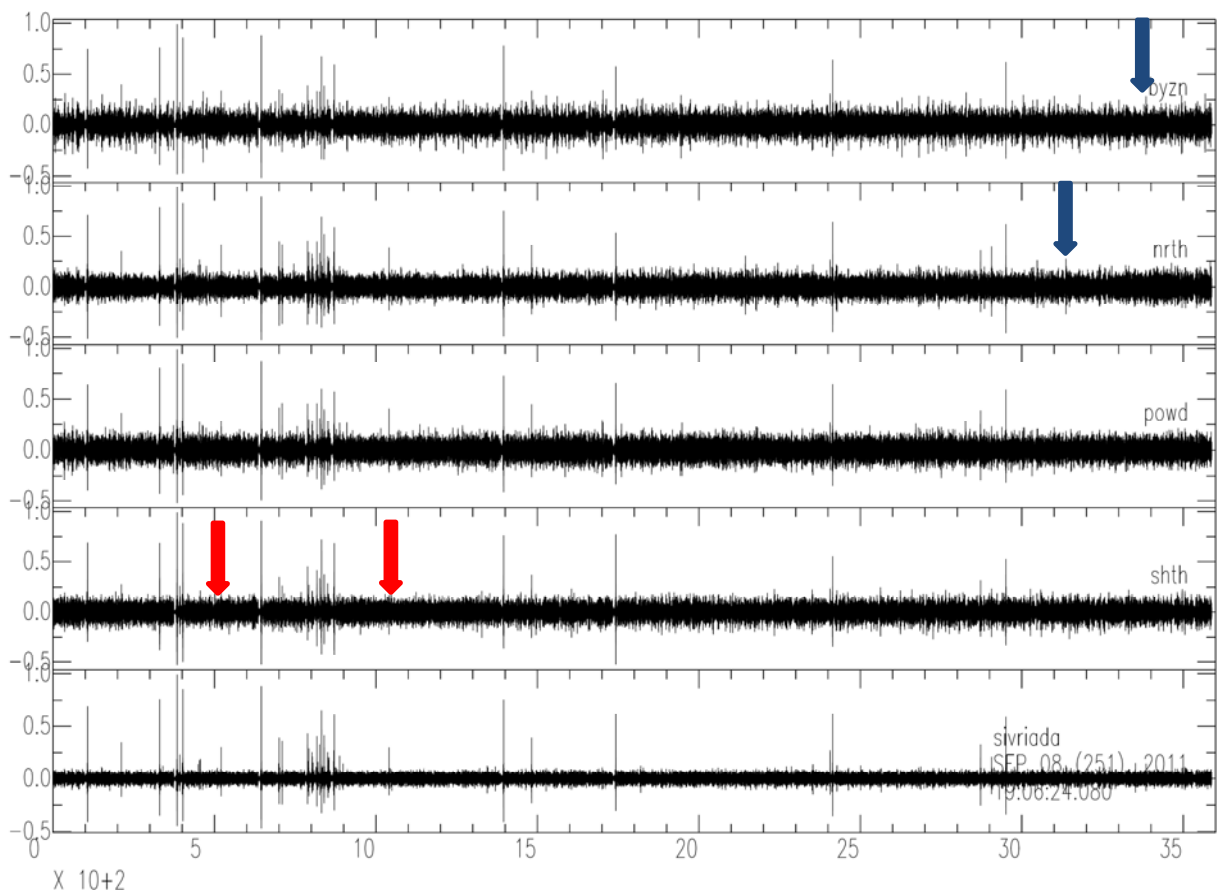
Figure 5.7. Cross correlation traces of the vertical components of the Sivriada Array stations. Last trace is the stack of all Sivriada Array stations. Blue arrows show noises that disappear in the stacked trace. Red arrows show signals that are not detected on single station correlation traces.

For instance, peaks indicated with red arrows are not very well detected on single station correlation traces whereas they become visible in the stacked trace in Figure 5.7.

On the contrary, some peaks which are present on single station correlation traces disappear in the stacked one indicating that they were generated by noise (blue arrows). In other words, this method ensures a real event and crosschecks it on different stations.

Additionally, as it is observed from the Figure 5.7 that, maximum values of y axes are 1 since they are all cross correlation traces. In short, cross correlation traces of the vertical components of all stations of an array have been added up (i.e. Sivriada and Yassıada) separately as in the last traces of the Figures 5.7 and 5.9. Therefore, at the end, one single trace for Sivriada Array and one for Yassıada Array have been obtained, (Figures 5.7 and 5.9). Since, adding the correlation traces makes the amplitude of the trace bigger than one, at the final stage amplitudes have also been divided to the number of stations used for each island. The last traces in Figures 5.7 and 5.9 show the final step where division is applied to the summed traces.
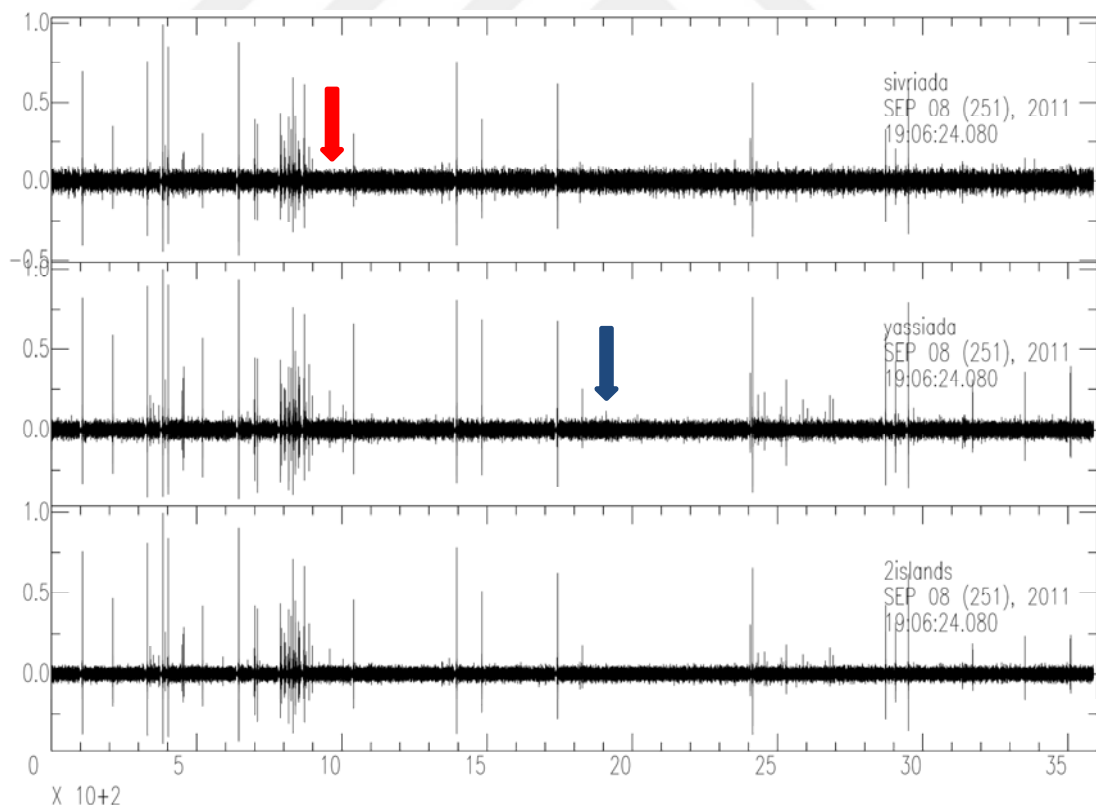
Figure 5.8. Summed cross correlation traces of the Sivriada and Yassıada Arrays. Last trace is the stacked cross correlation trace of the two islands. Blue arrow shows the noise that disappears on the two islands stacked trace. Red arrow shows signal that is not detected on single island correlation trace.

Lastly, cross correlation traces of the Sivriada and Yassıada Arrays have been stacked, (Figures 5.8 and 5.10). The first two traces are summed Sivriada and Yassıada Arrays whereas the last traces in Figure 5.8 and Figure 5.10 are the final summation of the cross correlation traces of the two islands. It is very obvious that, noise level even gets much smaller in the stacked cross correlation trace of the two islands compared to either Sivriada or Yassıada stacks. Moreover, it can be observed that some peaks appear (red arrows) whereas some disappear (blue arrows) in the final stack. Therefore, in order a signal to be declared as a real event it should be present on the two islands stack. Otherwise, it should be considered as noise caused by the local conditions of that island.

In order to examine the performance of the cross correlation based earthquake detection method that has been used, zoomed views of the above figures have also been plotted. Figure 5.9 is the close look to the auto correlation traces of the Sivriada stations. It is 2 seconds before and 2 seconds after the maximum auto correlation peak of the ME. The last trace is the stack of all of the Sivriada stations (BYZN, NRTH, POWD and SHTH, respectively) as it is in Figure 5.7. From the stacked trace of Figure 5.9, the performance of the method can be observed clearly. The noise which is uncorrelated decreases drastically going away from the time of the earthquake compared to the individual auto correlation traces. Whereas, amplitude is maximum at the time of the event indicating that there is a perfect correlation. Since, all of the traces in Figure 5.9 are auto correlation traces, maximum peaks are very narrow and perfect symmetry of the flanks of the peaks can also be apparently observed.
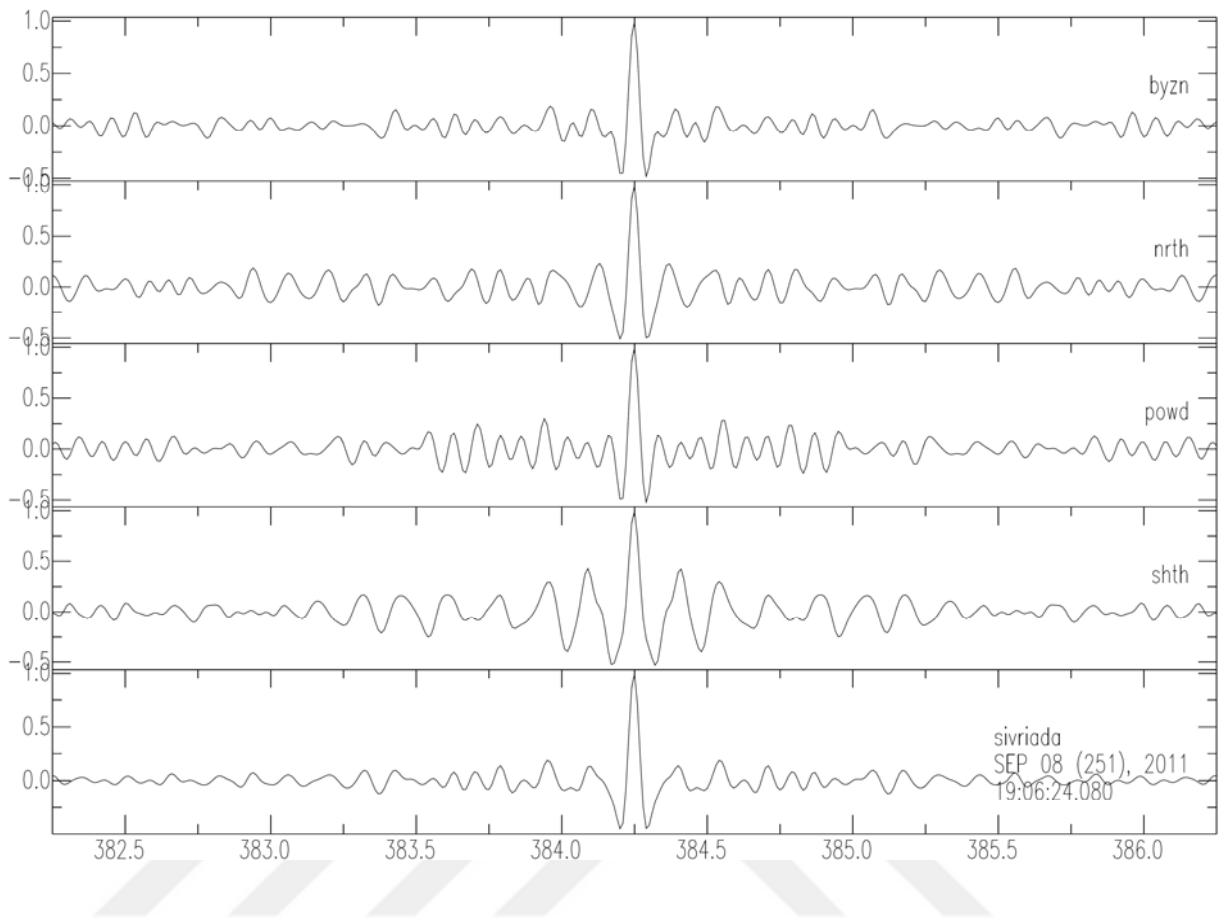
Figure 5.9. Zoomed view of the auto correlation traces of the vertical components of the all of the stations of the Sivriada Array stations and Sivriada stack around the time of the ME.

Immediately after obtaining the stacked traces of the Sivriada and Yassıada Arrays, an appropriate time shift between the summed traces of the two arrays have been applied. Yassıada has been shifted with respect to Sivriada taking into consideration the time of the ME as it is illustrated in the zoomed view in Figure 5.10.
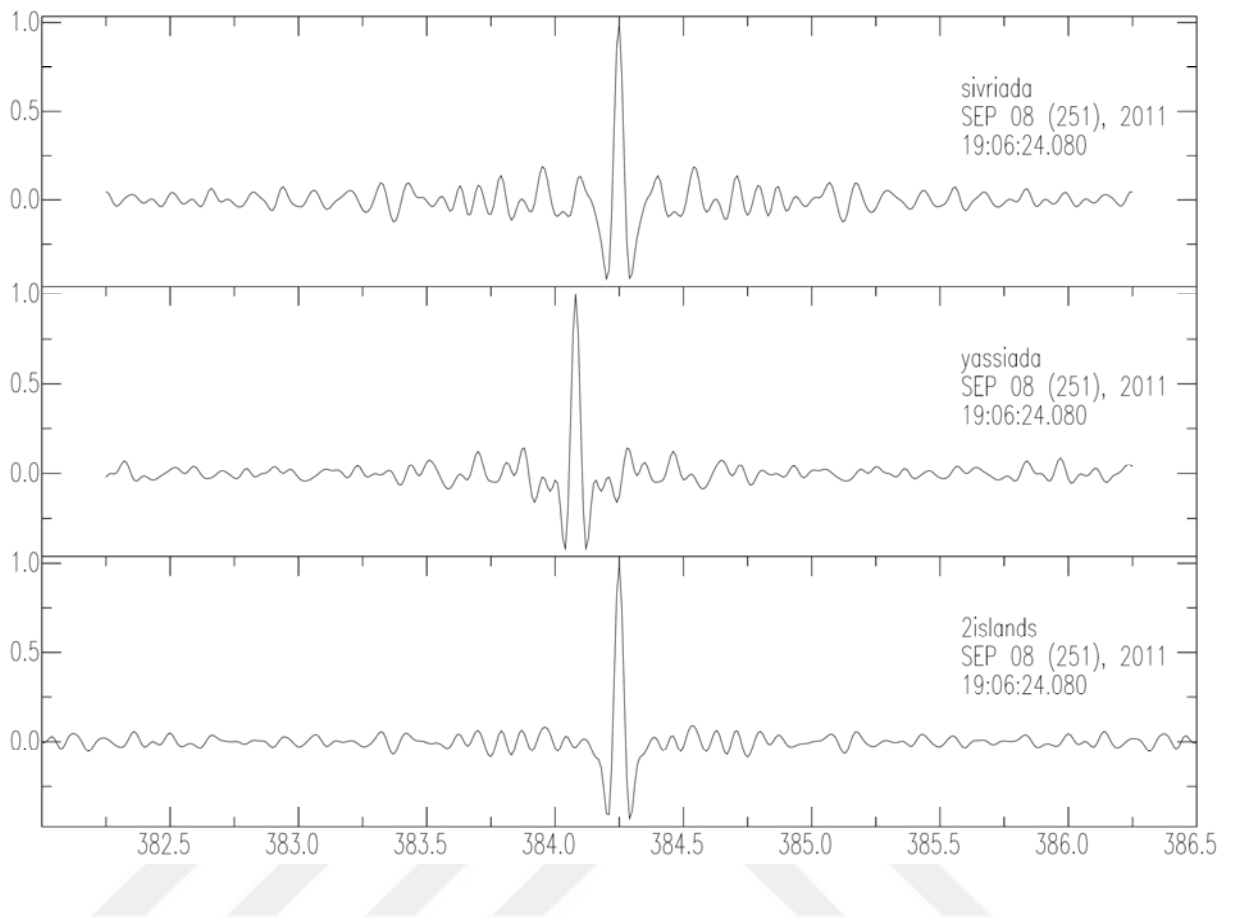
Figure 5.10. Summed cross correlation traces of the Sivriada and Yassıada Arrays before shifting Yassıada with respect to Sivriada. Last trace is the two islands stack.

Yassıada has been cut as the proposed Number of Points (NPTS) and the beginning or ending of the Sivriada or Yassıada traces padded with zeros in order to make the lengths of the cross correlation traces of the two arrays equal in case they are extending beyond the limits.

In addition to that, Sivriada and Yassıada correlation traces have been synchronized in order to equalize their reference times. Figure 5.11 shows zoomed views of the summed cross correlation traces of the Sivriada and Yassıada Arrays stations after aligning Yassıada with respect to Sivriada. As it has been stated previously, alignment is performed according to the time of the ME. Note that, noise level in the last trace of the Figure 5.11 which is the sum of the two arrays, decreases more compared to either stacks of only Sivriada or Yassıada stations.
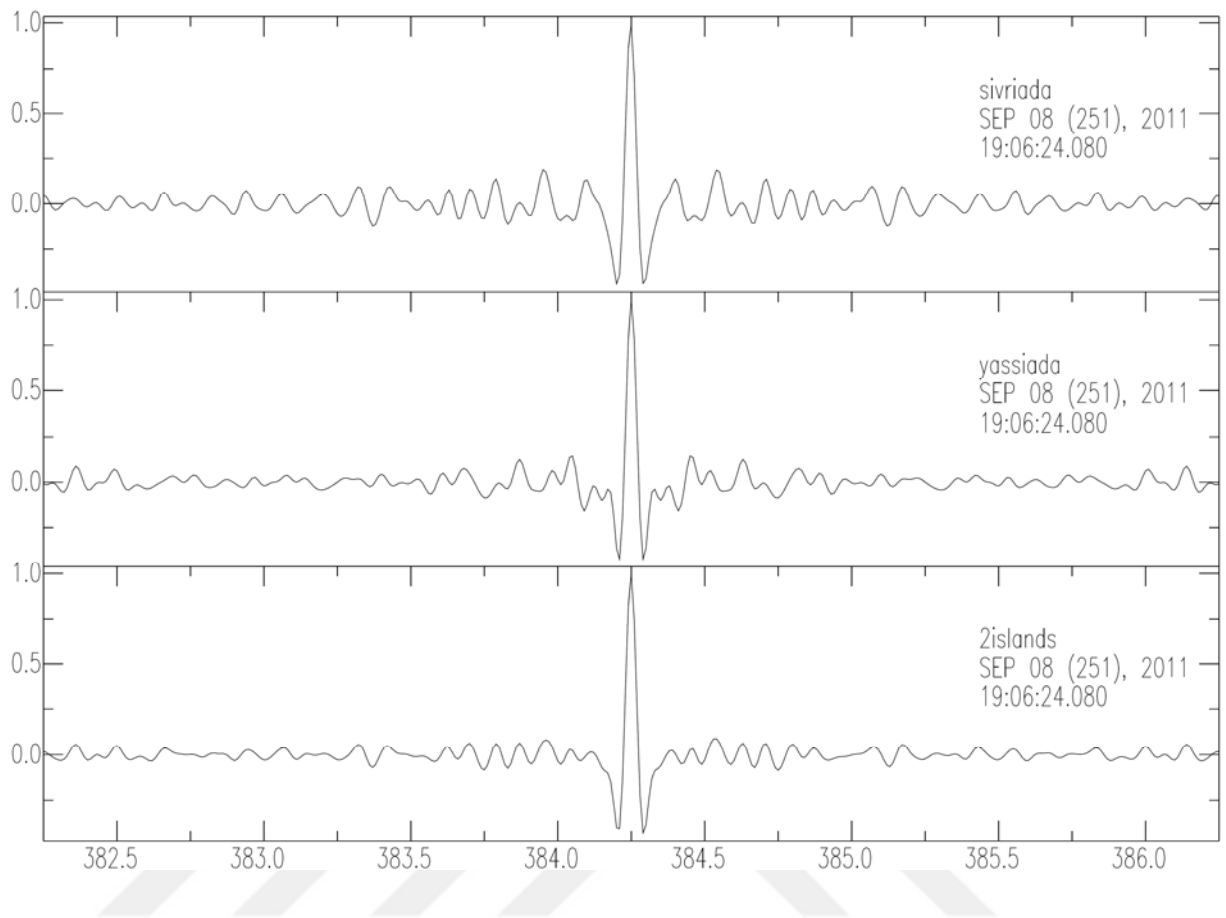
Figure 5.11. Zoomed view of the summed cross correlation traces of the ME at Sivriada and Yassıada Arrays. Last trace is the two islands stack.

Cross correlations have been applied to a time window starting five days before and ten days after a ME detection time. This window can be extended to the expense of computational time. For the intention of observing possible foreshocks, if there are any, correlation has been started five days before the MEs. If the highest magnitude earthquake occurred in this region has been taken into account, time window used for the correlation is supposed to be fairly sufficient to clearly observe both the possible foreshocks and aftershocks. It is quite appropriate to observe the damping of aftershocks both for fairly small and large earthquakes within this window length reliably according to the empirical relation of the modified version of Omori's Law (Utsu, 1961). This relation states that, aftershock rate decreases very fast with time. For instance, according to the Omori's Law, ten days after an earthquake, the probability of a new earthquake will be approximately 1/10 of the first day, when p is equal to 1 (Utsu, 1961). Admittedly, aftershock sequences

follow not only Omori's Law but also Gutenberg-Richter Law. Although, both of the laws have no implication at all about the physical mechanism behind the number of aftershocks of an earthquake, they still help to give a rough idea.

Cross correlation coefficient has been calculated for every increment of evenly spaced samples of continuous data. In this method, an event is declared whenever the cumulative cross correlation value exceeds a given threshold.

In order to summarize the steps and emphasis the performance of the method Figure 5.12 has been plotted. First figure of the Figure 5.12 shows one hour long vertical component of raw data of the station NRTH at the Sivriada PIRES Array. Second figure of 5.12 indicates the corresponding one hour cross correlated trace of NRTH. Third figure of 5.12 is the stacked cross correlation traces of all of the stations of the Sivriada Array. Last figure of 5.12 demonstrates the stacked cross correlation traces of all of the stations of the PIRES Arrays. Comparing the second and last traces in Figure 5.12, one can easily observe that the number of peaks representing the presence of an earthquake in the last figure is much higher. Although, only a few earthquakes can be observed clearly on a raw single station data, number of detected earthquakes increases significantly when using the technique described. ME (indicated with red arrow), foreshocks and aftershocks can also be observed in the last figure of Figure 5.12. Note also that, noise decreases significantly when cross correlation traces of all PIRES Arrays stations have been stacked, (Figure 5.12). In other respects, quite low level of noise also justifies that the uncorrelated signal which is noise cancels very well. Therefore, everything over the noise level supposed to be a signal representing an event.
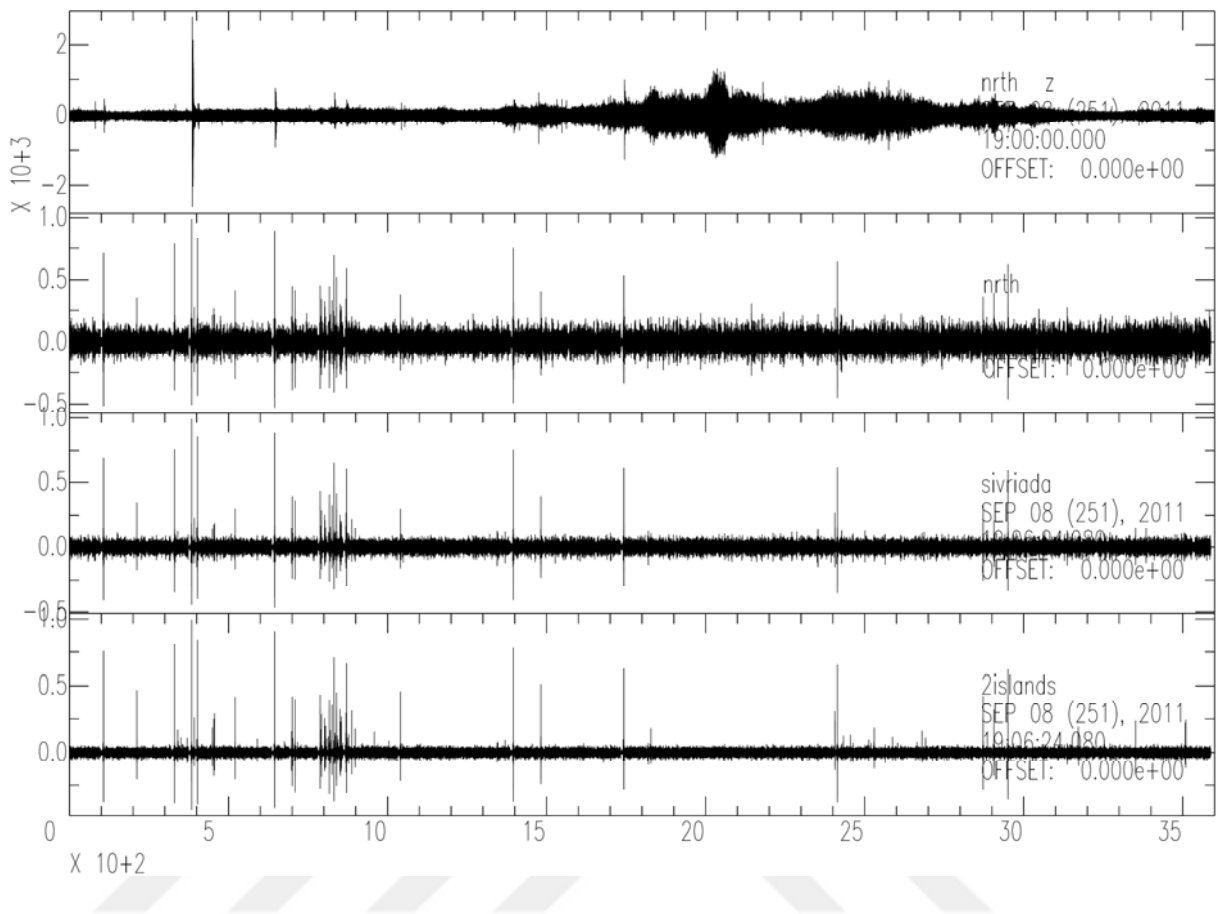
Figure 5.12. One hour long waveform of the vertical component of the Sivriada NRTH station. Cross correlation trace of the vertical component of the Sivriada NRTH station. Stacked cross correlation traces of all of the stations of the Sivriada Array. Stacked cross correlation traces of all of the stations of the PIRES Arrays.

Lastly, Figure 5.13 is an extreme example of the Figure 5.11 showing the zoomed view of the summed cross correlation traces of a small event at the Sivriada and Yassıada Arrays and at the two islands stack. When Figure 5.13 is compared with Figure 5.11 which is the cross correlation traces of the ME, astonishing similarity of the arrival times of the waveforms at Sivriada and Yassıada can be observed. Keeping in mind that the two arrays have been aligned with respect to the ME, it shows that the amount of shift has been valid also for the SE. In addition to that, decrease of the noise level in Figure 5.13 even for a SE has been another benefit of the method. In Figure 5.11 since the ME and its templates have been auto correlated, perfect symmetry of the flanks of the peaks are observed where in

case of a SE (Figure 5.13). Since, ME's templates have been cross correlated with the SE, perfect symmetry of the flanks of the peaks breaks down.
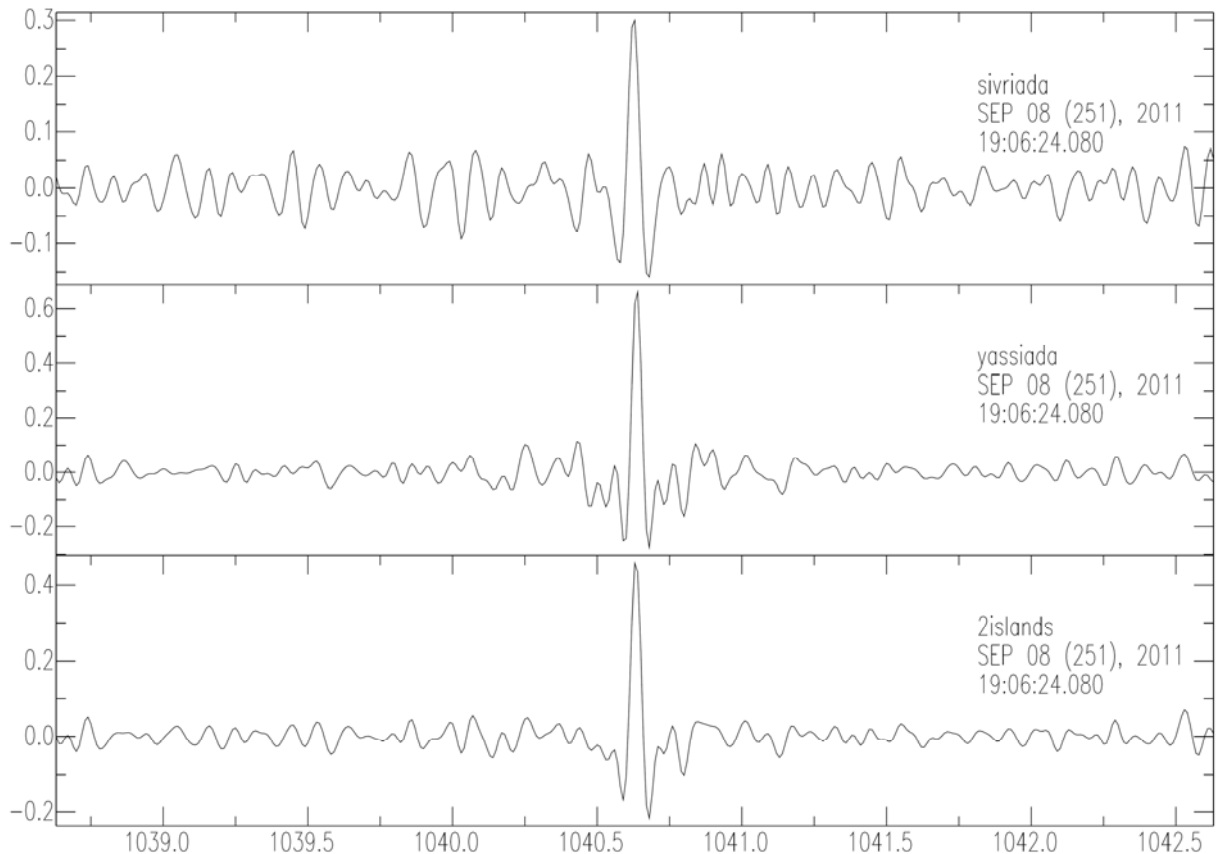
Figure 5.13. Zoomed view of the summed cross correlation traces of a SE at the Sivriada and Yassıada Arrays. Last trace is the two islands stack.

At the final stage, all of the events that have been detected with this method have been cut from the continuous data 0.5 seconds before and 5 seconds after their detection times. Figure 5.14 demonstrates events that have been detected in one hour of vertical component of Yassıada FUTB station. Events are aligned before plotting which brings forward their great similarity of S-P times.
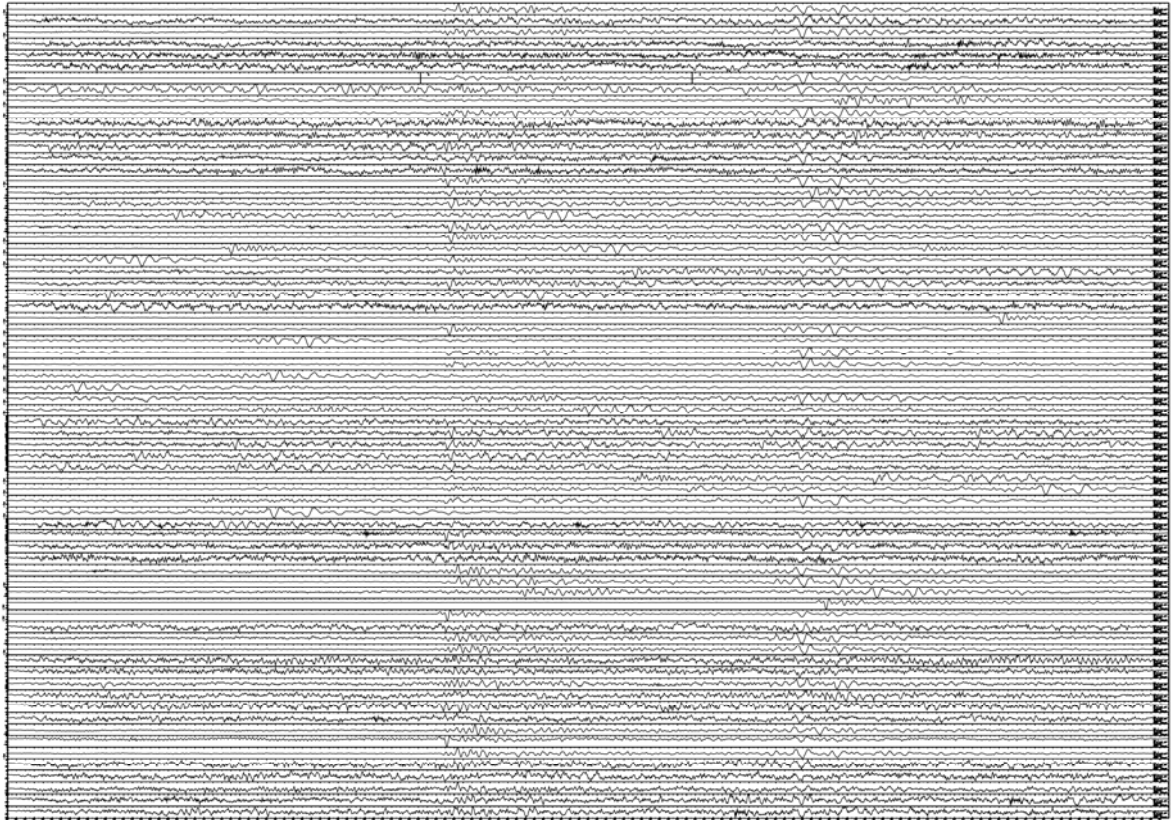
Figure 5.14. Events that have been detected in one hour at Yassıada FUTB station.

According to the Figure 5.14, it can be distinguished very roughly that all of the earthquakes have occurred within a very near distance of each other. Figure 5.14 helped to underline once more that, this type of beam forming approach has led to a very large improvement of the detection level. By using this method, many small magnitude events could have been caught that are buried in the background noise or in the coda of previous events and therefore were normally missed by the land stations of RETMC. This technique helps to lowering the magnitude level that could be detected and therefore improve the Mc for the specific region of the Marmara Sea.

5.2. Location by Array Processing

This study is essentially focused on the performance of the seismic arrays. In this context, arrays have been made use of in terms of earthquake location as well. As it has

been touched previously, the evaluation is based on the study of both MEs and SEs of seismic clusters observed in the Marmara Sea, at ~20 km distance to the PIRES Arrays.

Only the MEs in the clusters were large enough to be detected and located by the local networks. Therefore, these earthquakes have been used as waveform templates for detecting similar SEs. Afterwards, different very precise location methods have been applied both to the MEs in the clusters and SEs forming the clusters. These two different location techniques will be discussed respectively in the following sections.

Locations of the earthquakes that had also been detected by the RETMC have been done using the information from the arrays. In this manner, RETMC stations, PIRES Arrays stations (Sivriada and Yassıada) and the PIRES seismic network stations (Kınalıada, Burgazada, Heybeliada, Büyükada and Balıkçıada) have been used. Later on, P and S phases have been read on the available traces, (Figure 5.15).
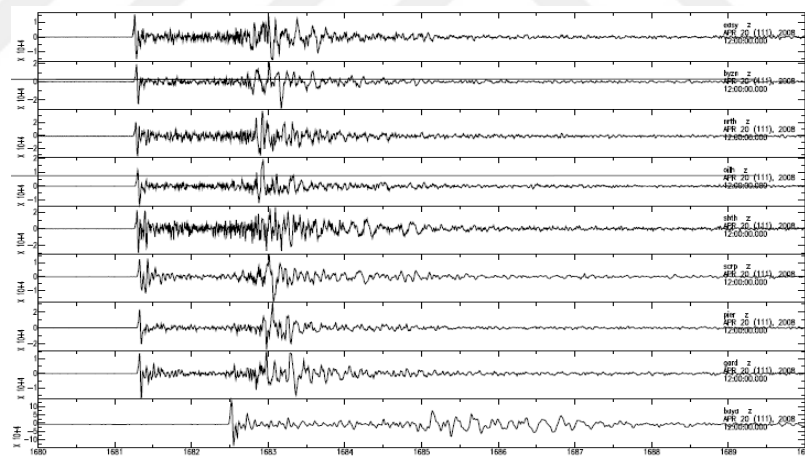
Figure 5.15. Waveforms of an event on the PIRES Arrays (Sivriada and Yassıada) and the PIRES network stations.

Waveforms of the PIRES, (Figure 5.15), show high signal quality of an earthquake that has occurred in the middle of the Marmara Sea, where the land stations of the RETMC are far away. For instance, nearest station ISK is at 23 km away from this earthquake's epicenter. Then, conventional and frequently used hypocenter location program, HYPOCENTER Lienert and Haskov (1995) has been run at high accuracy mode. During

the location processes, 1-D model proposed by Karabulut *et al.* (2011) has been used as the velocity model of the region.

Adding the PIRES Arrays and PIRES network stations clearly improves both the location and depth calculation of the earthquakes. In terms of the earthquakes that are nearer to the PIRES than the land stations, phases can be read more accurately which makes an improvement. Figure 5.16 is an indication of the increased achievement of the location accuracy with the PIRES in terms of the travel time plot. It shows the fits of the P and S phases of this earthquake to the velocity model used.
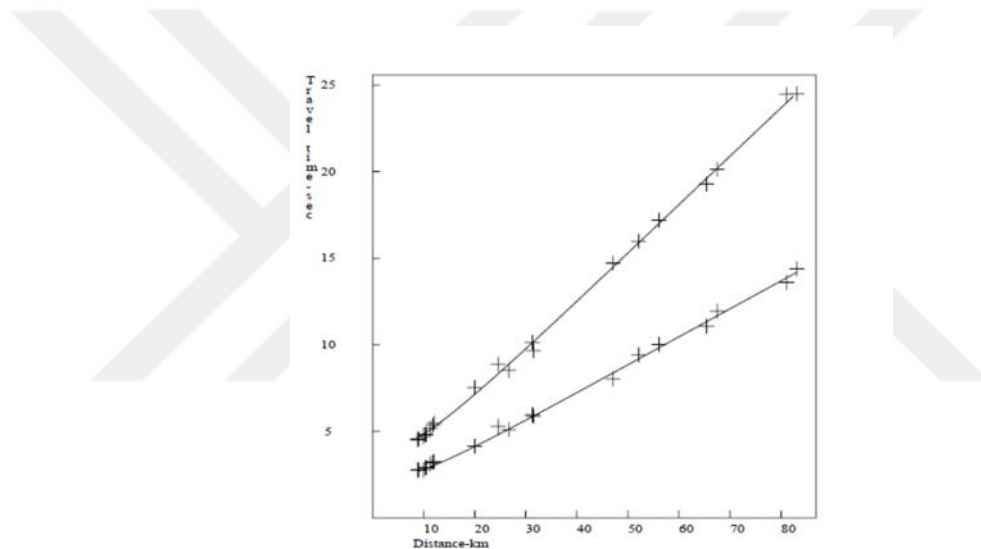
Figure 5.16. Travel time plot of the P and S waves of an event.

In addition to this, in terms of the land stations, S phases cannot be observed very well, which decreases the reliability of the location and depth calculations. Because of this reason, location programs could converge to the local minimum instead of the global minimum during the depth calculations. In this sense, adding the S phases read from nearer distant PIRES Arrays and network stations also help to obtain better depth results.

Besides the above discussions, there are also other advantages of the PIRES. Arrays enabled to incorporate more information, like back azimuth, into conventional location from the FK analysis. The use of arrays and in particular FK analysis, proved to be highly beneficial for finding the locations of the events. In the FK analysis method, first of all

beams which are formed with different slowness vectors are compared in terms of their amplitudes or power. Lastly, apparent velocity and back azimuth combinations giving the highest energy on the beam are found out (Schweitzer *et al*., 2009).

The FK analysis, in other words, slowness analysis, is a standard tool in seismic array processing. The aim is to obtain a coherent spatial sampling of the seismic wave field. All channels are processed together in an array processing (i.e. FK analysis). On the other hand, in a network, phase picking and arrival times of each station are determined separately (Havskov and Alguacil, 2006).

NORSAR Processing Software EP, Fyen (1989, 2001a,b) has been used during the FK analysis which required conversion of data to CSS3.0 format. During the FK analysis, slowness values have been spanned between -0.5 and 0.5 s/km over 401 points, in both EW and NS directions. This gives an equally spaced grid composed of 160801 points which means doing the FK analysis in a very high resolution. The beam power is evaluated for every one of these points. The maximum power in the grid and the slowness vector that corresponds defines the slowness of the plane wave. The power is displayed in terms of dB and with the isolines which decrease from the maximum power. In the plots related to the FK, relative power of the signal is represented with color in the slowness space. Kvaerna and Doornbos (1986) have proposed to use FK technique in such a way that integration is applied over a wide frequency band which is called as either wide band or broadband FK analysis. On the other hand, single frequency wavenumber analysis was used to be applied by Capon (1969a and 1973).

According to many authors Kvaerna and Doornbos (1986), Kvaerna and Ringdal (1986), stability of the wide band FK analysis is much higher than the single frequency FK. Additionally, it has a high SNR within a wide band frequency range. It is the modification of the frequency domain procedure of Capon (1969) in broadband but it provides more stable results than the narrowband estimates (Kvaerna and Ringdal, 1986).

For the FK, Sivriada and Yassıada Arrays are processed separately and back azimuth and slowness values are determined independently for both of them. Only the vertical component waveforms with a short window length (~200-500 ms long) around the P phase

were used in the FK analysis. A bandpass filter (wide band) was applied to reveal the source pulse in a clear fashion. Figure 5.17 is an example of the result of one of the FK analysis of an earthquake (Md=2.4) from Yassıada Array. The black arrow on top of the red area shows the direction of the maximum power.
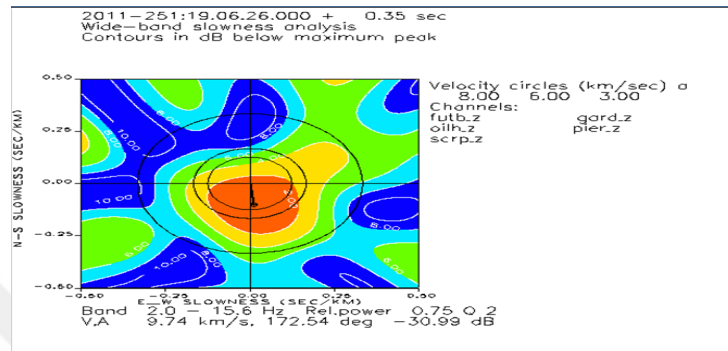
Figure 5.17. FK analysis result of the magnitude 2.4 event at Yassıada Array.

The axes of the Figure 5.17 indicate the apparent slowness in x and y directions and in terms of km-1. The apparent velocity is 9.7 km/s at the maximum power and the back azimuth value is 172 degrees.

Unfortunately, GAP and depth errors increase when locating with only FK analysis with the PIRES. Because, there are only two arrays that are very near to each other (~2 km). On the other hand; origin time error, latitude and longitude errors decrease compared to only using conventional location method. Therefore, events have been located using both the two back azimuth information obtained from the FK analysis of Sivriada and Yassıada, P and S phase readings of arrays and network stations of the PIRES and the RETMC using HYPOCENTER Program, (Lienert and Haskov, 1995). The slowness values obtained from the FK analysis were not included in the solution since it is a local event. The reason is, slowness information is mostly used for the location of the tele-seismic events by the seismology community.

6. SOURCE PARAMETER ESTIMATION

Section six that is titled as "Source Parameter Estimation" composes of four sub-sections which are "Basic Concepts of Source Parameter Estimation", "Source Parameter Estimation of the Master Events: EGF Approach Using Arrays", "Q Estimation: by Product of the Spectral Analysis" and "Source Parameter Estimation of the Slave Events: Using Characteristics of the Previously Analyzed Ray Paths", respectively.

6.1. Basic Concepts of Source Parameter Estimation

Several tips that have to beware of in terms of the source parameter determination will be mentioned in the following paragraphs with some examples and tests. The basic steps that will be discussed will be used during both EGF and CSPE approaches. For instance; choice of window length and window type and their importance will be tackled respectively. The so called pre-processing steps that will be mentioned in detail in this section will be touched with only a few words during the related paragraphs.

One of the important steps during the application of spectral analysis is the choice of window type. In the frequency domain studies like Fourier analysis, where data is cut into small segments, it is important to suppress the ends of the data smoothly. The effect of the Gibbs phenomenon resulting from cutting an infinite time series has to be minimized. This is accomplished by using a window. It has been observed that multiplying data with window or not influences the spectrum estimation. During the source spectrum studies, mostly Tukey Window is used in order to minimize the effects of the Gibbs phenomenon. However, performances of different windows like; Tukey, Chebyshev, Gaussian, Kaiser and Hamming Windows have been tested on data, using their default parameters in MATLAB, (Figure 6.1).
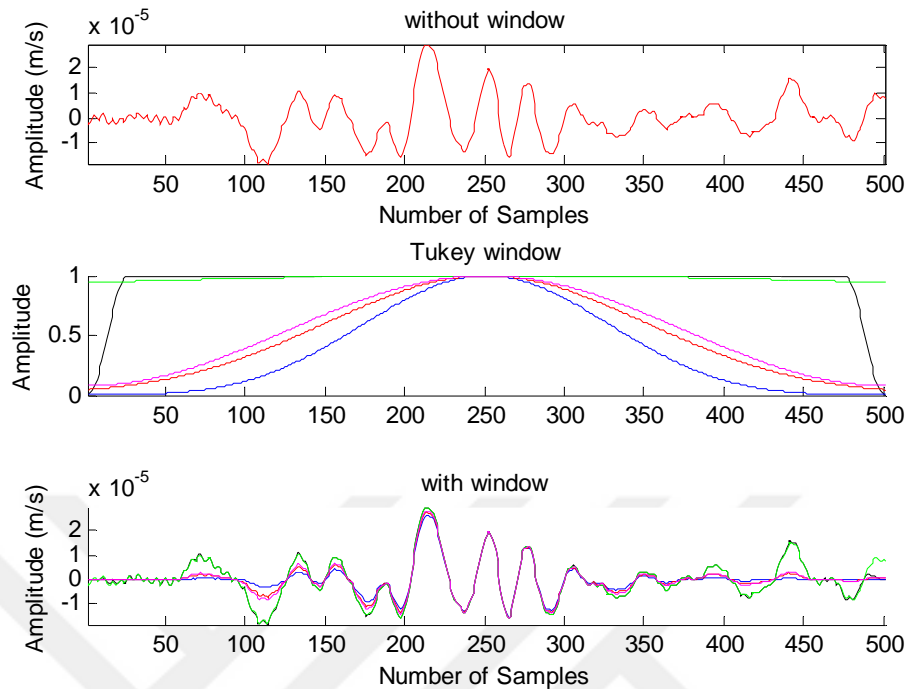
Figure 6.1. Waveform without any window application, different windows and waveform multiplied with windows.

Waveform (red line) on the top of the Figure 6.1 is produced for a number of 500 samples which corresponds to 1 second for a sampling rate of 500 Hz data. The middle of the Figure 6.1 shows different windows with different colors. Finally, the bottom of the Figure 6.1 indicates the resultant waveform obtained by the multiplication of the waveform with different windows. Note that, each waveform is drawn using the corresponding color of windows in the last figure. When the waveform is multiplied with different windows, it can be seen that Gaussian shaped windows suppress both the beginning and the end of the waveform very sharply, modifying the data. Therefore, it has been preferred to use Tukey Window (taper: %10) in this study. Raw data is not supposed to undergo too much change, but instead only the ends are tried to be brought down more slowly. Figure 6.2 is an example of the application of the Tukey Window. When doing EGF, both the ME and the SE seismograms have been multiplied with cosine Tukey Window using ratio of taper as %10 in the time domain. On the other hand, during the CSPE, multiplication is performed only on the processed single waveform using the same window type and ratio.
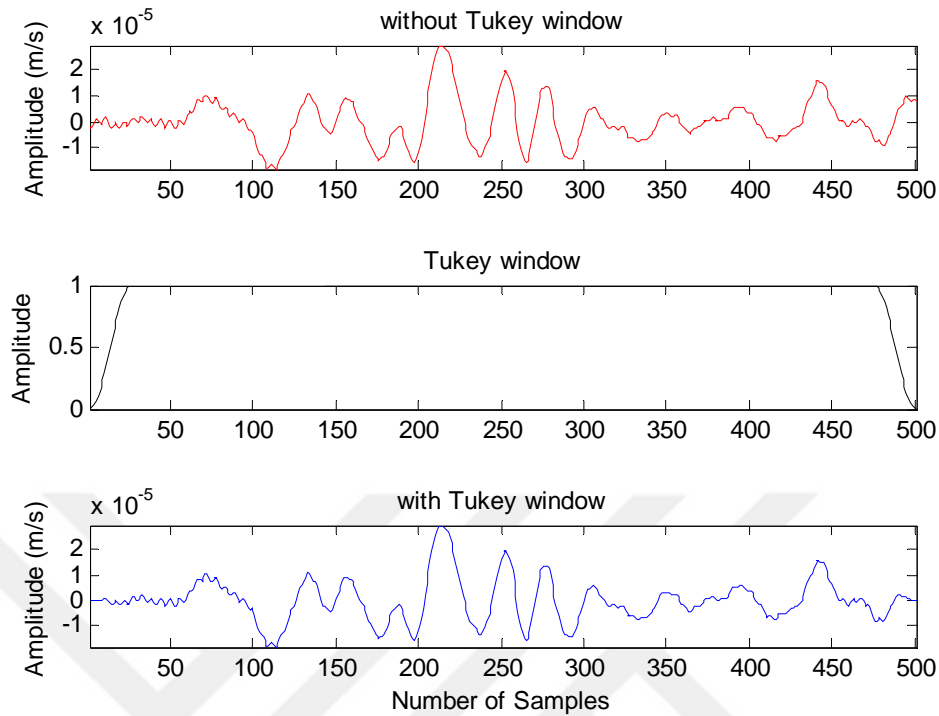
Figure 6.2. Waveform without Tukey Window application, Tukey Window and waveform multiplied with Tukey Window.

Figure 6.2 is produced for the intention of close look at the performance of the Tukey Window. Waveforms (red and blue lines) in Figure 6.2 are also produced for a number of 500 samples which corresponds to 1 second for a sampling rate of 500 Hz data. Raw waveform (not multiplied with Tukey Window), situated at the top of the Figure 6.2 is drawn with red line. In the middle of the figure, shape of the Tukey Window (%10 cosine tapered) can be found (black line). Last figure of 6.2 is the obtained waveform (blue line) after multiplication with the window. Tukey Window has amplitude of 1 showing that it has no effect on the amplitude of the waveform when multiplied. When the waveform is multiplied with the Tukey Window, it can be observed that both the beginning and the end of the waveform are suppressed very smoothly when ratio of taper is %10. Data is not modified much when the ratio of taper is chosen as %10. It is expected that increasing the ratio of taper modifies the data more.

In order to suppress the ends of the data, Tukey Window has been chosen in the previous step. To have an idea about the effect of using the Tukey Window or not, on the

source parameters obtained, another test has been made. In this sense, event 20110908 and one of the PIRES stations, PIER, EW component have been used for the test. Sampling rate of the data is 500 Hz. 0.1 second before the S wave arrival has been cut. Fixing Q to 170, source parameters, moment and corner frequency, have been inverted in the least squares sense. Figures 6.3 and 6.4 show 500 samples of data, 1 second, and the results of the fittings of the theoretical curves to the observed spectra with and without using the Tukey Window, respectively.
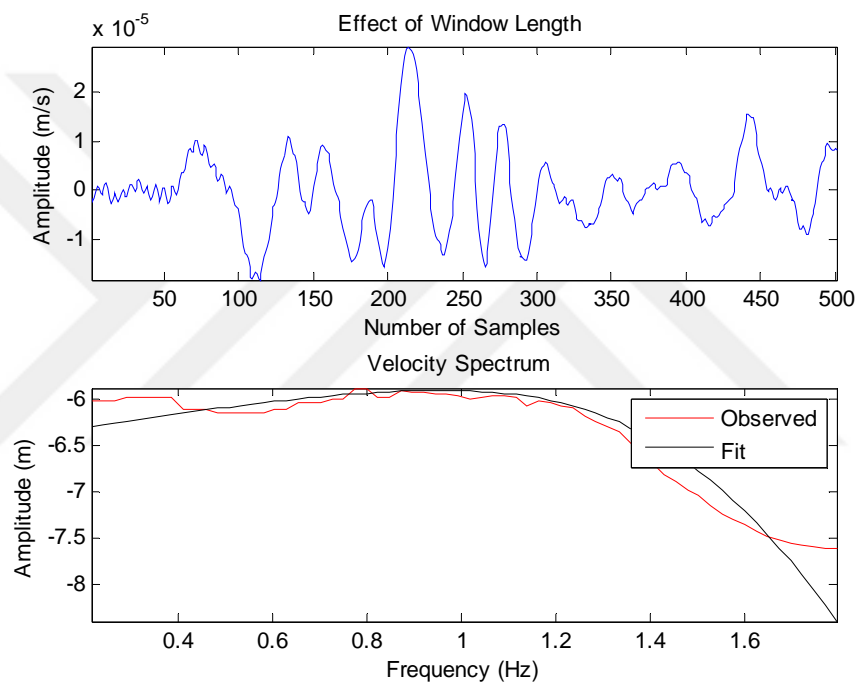
Figure 6.3. 500 samples of data, observed and calculated source spectra without using Tukey Window.
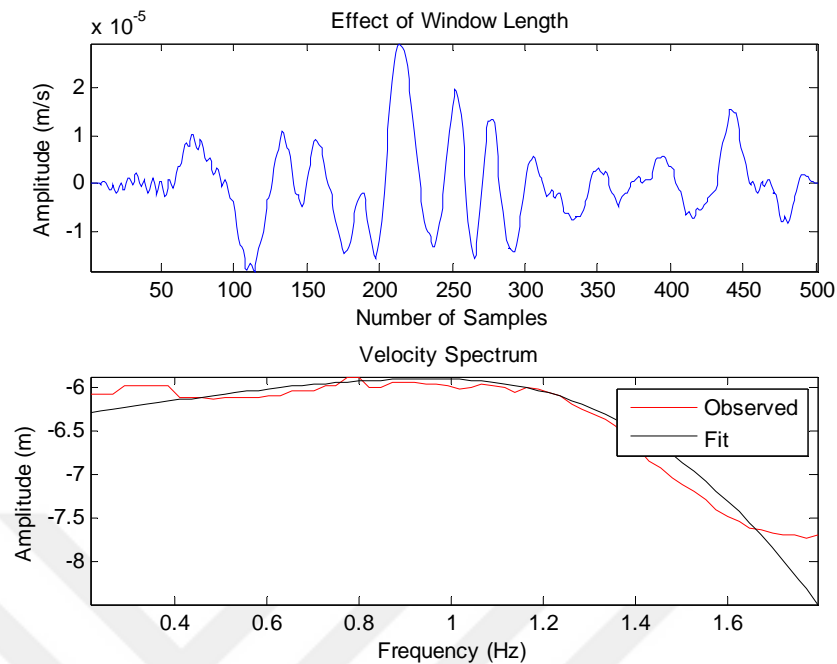
Figure 6.4. 500 samples of data, observed and calculated source spectra with using Tukey Window.

In both figures (6.3 and 6.4), the top figures indicated with blue lines are the waveforms. First waveform in Figure 6.3 is created without multiplication with a window. On the other hand, second one (Figure 6.4) is generated with the multiplication of the Tukey Window. Figures at the bottom of 6.3 and 6.4 show the related observed (red) and calculated (black) source spectra drawn on top of each other. It can be seen from the Figure 6.3 that, when any window is not used, error between the theoretical curve and the observed spectrum gets higher. Therefore, especially corner frequency cannot be determined properly. When the same test is done using a window, error gets lower and theoretical curve fits to the observed spectrum, (Figure 6.4). Therefore, the value of the corner frequency can be determined more reliably.

In the studies, during the calculation of velocity spectra, data is cut into fixed time lengths, whether it is a magnitude 2 or 3 earthquake, etc. Ideally, only direct waves should be used while doing Fast Fourier Transform (FFT) calculation. The main reason of this is,

secondary arrivals or coda waves, etc. effect the results. Therefore, choice of an appropriate time window around the P or S phase is important during FFT.

Small events are the area of interest and various magnitude events in the clusters are analyzed automatically during the EGF in this study. In addition to that; during the RSPE, window length adjustment with respect to the magnitude of an earthquake is not made. Therefore, for the purpose of doing fine analysis, the effect of choosing different lengths of the time windows on the earthquake source parameters determined is also tested. Event 20110908 and one of the PIRES stations, PIER at EW component have been used for the test. Sampling rate of the data is 500 Hz. 0.1 second before the S arrival has been cut. Fixing Q to 170, source parameters, moment and corner frequency, have been inverted in least squares sense with respect to different window lengths. Source parameters have been estimated starting from 200 samples of data and with 100 samples increments up to 1000 samples. This means that data between 0.4 and 2 second have been used, (Figure 6.5).
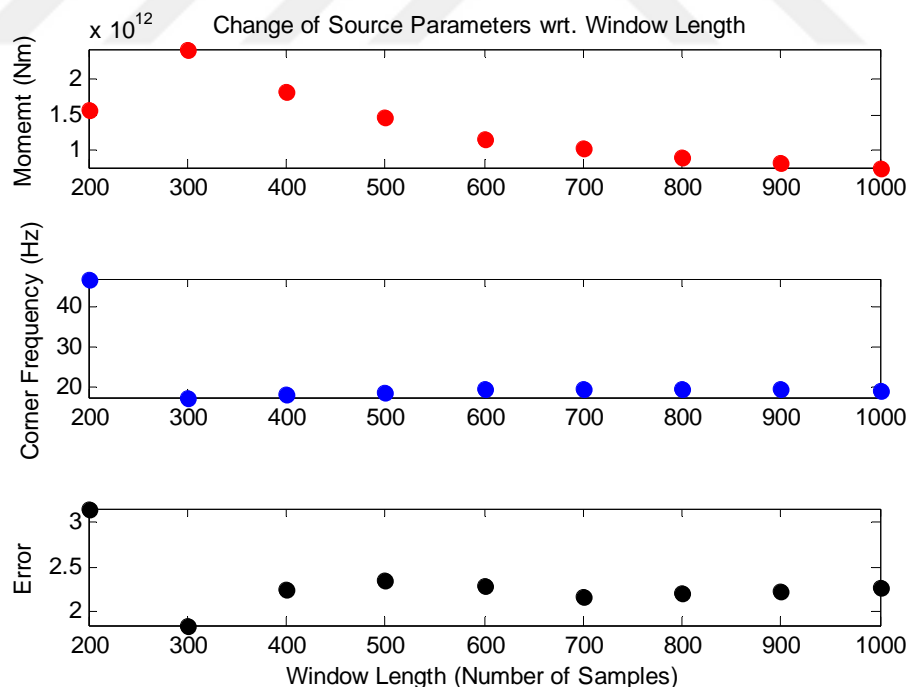
Figure 6.5. Moment, corner frequency and error with respect to different window lengths (number of samples).

Figure 6.5 shows variations of the different source parameters; seismic moment (red dots) and corner frequency (blue dots) and error (black dots) with respect to different window lengths. In the figure, window length is represented in terms of the number of samples. Change of the source parameters; moment and corner frequency and error with respect to different window lengths show that, too short data should not be used. For instance, values of the source parameters obtained for 200 samples scatter more. Moment and corner frequency estimations and error between the observed and theoretical fit to the spectrum become stable after 600 samples, (Figure 6.5).

In addition to the test above, to see whether choosing different window lengths has a significant effect statistically, bootstrap procedure has been used. A test has been made on seismic moment to estimate this fact more quantitatively. The bootstrap method depends on choosing samples randomly from the dataset and then selecting to analyze each sample again replacing them back to the same dataset many times. This means that, a particular sample from the dataset could appear multiple times during bootstrap analysis. At the end, this method enables to obtain the uncertainty of the estimation when applying variety of estimates.
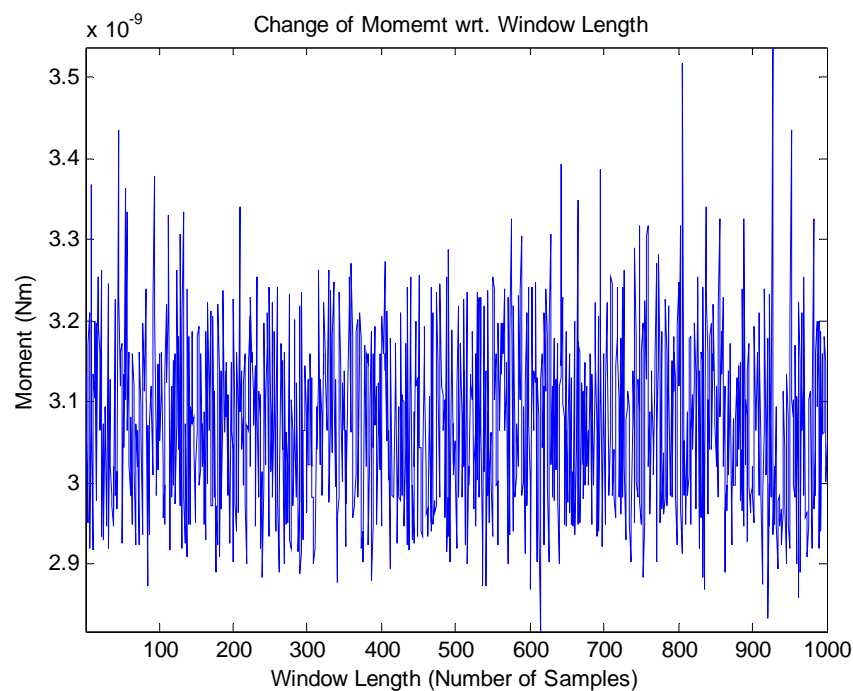
Figure 6.6. Bootstrap analysis of the seismic moment change with respect to different window lengths.

Bootstrap analysis (Figure 6.6), is used to represent the variation of the seismic moment with respect to different window lengths. Window lengths have been changed starting from number of samples as 10 up to 1000 and seismic moments have been evaluated at each increment of the window length. The above bootstrap analysis result (Figure, 6.6), does not show any significant seismic moment change with respect to the different window lengths.

Another necessity in terms of the pre-processing arises from the complexity of the source spectra in the frequency domain. Therefore, some kind of smoothing of the observed spectra in the logarithmic space is needed to be produced so that the curve is not too complex for the nonlinear inversion. During the calculations of the earthquake spectra, the theoretical expressions are expressed in logarithmic scales. On the other hand, estimations based on the curve fitting in spectral domain are biased towards the high frequency end where high numbers of samples are available. Additionally, they are squeezed in a narrow band due to the use of logarithmic x-scale. In order to eliminate this artifact, the spectra have been re-sampled to obtain a linear spacing on the logarithmic x-axis both on the low and high frequency ends (Ide *et al.*, 2003). Linear approximation to log-log spectrum has been applied and each spectral amplitude has been re-sampled at equal intervals of log frequency at $\Delta \log f = 0.025$. For smoothing prior the spectral ratio analysis, moving window of $\Delta \log f = 0.2$ has also been applied. Different values for re-sampling and windows that were used in the literature have been tested and chosen the appropriate ones for the data used in this study.

In addition to these steps, very low and very high frequencies have also been eliminated from all of the spectra where SNR is low. After a quick look at the fitting of the spectra, the number of points to discard from every spectrum has been decided. When the observed and calculated spectra are plotted, values that deviate from the theoretical curve are the points that are eliminated.

In this paragraph, pre-processing steps that are applied in the stage of the spectrum estimation are discussed. These are used during both EGF and RSPE. Application of the methods will be shown on some examples during the related sections. Finally, after

mentioning about all of the pre-processing steps used, the following sections will proceed with the spectral analysis techniques.

6.2. Source Parameter Estimation of the Master Events: EGF Approach Using Arrays

When dealing with the SEs, the estimation of the source parameters from spectrum has some challenges. SE's amplitude is buried in noise more since it has low SNR. The noise level is often comparable to the signal level for a SE. Therefore, it becomes difficult to isolate the source contribution from the background noise. On the other hand, for MEs, SNR is higher compared to the SEs. Because of this reason, MEs and SEs in the clusters were treated differently in this study. The most effective solution found was to make the estimation both sensitive enough to give the details and stable enough to minimize the effect of noise.

In this work, since no detailed information exists about the propagation path and its attenuation properties and since there are co-located of SEs in the clusters, these factors motivated to use EGF. This approach works for the case of co-located events where waveforms show large similarity. It is based on the assumption that the SE can be used as the Green Function of the larger one which is ME.

This method is based on the spectral division of the ME by the SEs in a cluster in the frequency domain, (Equation 6.1). Since both waveforms inherit same disturbances like attenuation, path and site effects, they can all be removed conveniently by spectral division. Similarly, there is also no need to remove instrument response for these types of the frequency domain spectral calculations.

$$\frac{u^m(f_i)}{u^s(f_i)} = \left(\frac{\Omega_0^m}{[1+\left(\frac{f_i}{f_c^m}\right)^4]^{0.5}}\right)\left(\frac{\Omega_0^s}{[1+\left(\frac{f_i}{f_c^s}\right)^4]^{0.5}}\right)^{-1} \tag{6.1}$$

$$log\dot{u}_c^m(f_i) - log\dot{u}_c^s(f_i) = log\Omega_0^m - log\Omega_0^s + \frac{1}{2}log\frac{\left(1+(f_i|f_c^s)^4\right)}{\left(1+(f_i|f_c^m)^4\right)} \qquad (6.2)$$

Theoretical spectral ratio curve is obtained using Boatwright (1978). In Equations (6.1) and (6.2) where;

u^m = displacement amplitude of the ME

u^s = displacement amplitude of the SE

Ω_0^m = moment of the ME

Ω_0^s = moment of the SE

f_c^m = corner frequency of the ME

f_c^s = corner frequency of the SE

c = wave type (P or S wave)

The spectral division of the ME by the SE in a cluster will give true spectrum of the source, where path, site and instrument effects are removed. Moreover, for the PIRES special case, when spectral division is applied multiplicative peculiar narrow noise peak which is located at around 80 Hz also cancels out. Dividing the ME by the SEs at the same station and component enables to obtain smoother and more reliable spectrum even at high frequencies.

Conversely, there are some restrictions for the EGF approach based methods to be used properly. The EGF technique assumes that ME and EGF earthquakes are co-located, have identical source radiation patterns and difference in the corner frequencies of the ME and EGF earthquake is large. This means that SE should be sufficiently smaller in size and duration than the ME so that SE can be treated as an EGF earthquake. SEs in the clusters, therefore EGF earthquakes, should be small enough in magnitude in order to be treated as point sources. ME and EGF earthquake pairs should have similar S to P maximum amplitude ratios showing their source mechanism similarity. On the other hand, using methods such as cross correlation, it is proven that earthquakes in the clusters are co-located, so their path and site effects are identical.

There are various EGF approaches in applications. EGF is applied by Berckhemer (1962), Mueller (1985), Mori and Frankel (1990), Hough (1997) and Abercrombie and Rice (2005) that is based on choosing best EGF pairs between the ME and SEs in a cluster. Extension of the EGF Method is Multiple Empirical Green's Function (MEGF) applied by Hough (1997) and Ide *et al*. (2003) which is based on taking the spectral amplitude ratios between the co-located event pairs' spectra. In addition to the approach of Hough (1997) and Ide *et al*. (2003), who only used single station ratio, Oye *et al*. (2005) has stacked the ratios of all traces and received one stacked ratio for each event of the cluster. The same idea but different method has been applied by Imanishi and Ellsworth (2006) who used more than one number of windows overlapping by half their durations and stacked the spectral ratios over components and stations called as Multi Window Spectral Ratio (MWSR) Method.

Instead of doing spectral ratio analysis at a single station, like Oye *et al*. (2005), ratios for all available traces of the two islands stations have been stacked over components in this study. Therefore, at the end, one stacked ratio has been obtained for each event and component of the cluster.

There are basic ways of combining estimations in situations where more than one station is involved, like the PIRES case of array stations. One of them is to stack all spectra into a single spectrum and then estimate a single set of parameters which is a waveform based stacking method. Stacking of waveforms can be performed either on individual spectra or on spectral ratios. In this study, the ratios have been stacked since there are co-located events. Spectral division of the ME by the SEs at a single station is a quite reliable and stable method. Using the advantage of the PIRES stations being in juxtaposition, this method's stability have been increased more by stacking the spectral ratios at all of the 10 available PIRES stations. Therefore, noise decreased and the spectral ratio became more smooth and stable. In addition to that, like in the spectral ratio analysis, there is also no need for a prior knowledge about attenuation, path and site effects and instrument response during stacking of the spectral ratios which will be called as EGF stacking method hereafter in the study.

In EGF method, spectral division of the ME by the SE in a cluster will give the spectral ratio. It is possible to estimate the relative seismic moment between the ME and SE and corner frequency of the ME and SE in a sequence using spectral ratio method, (Figure 6.7). Nevertheless, it is not possible to obtain the absolute moment of the ME and the SE with the EGF Method.
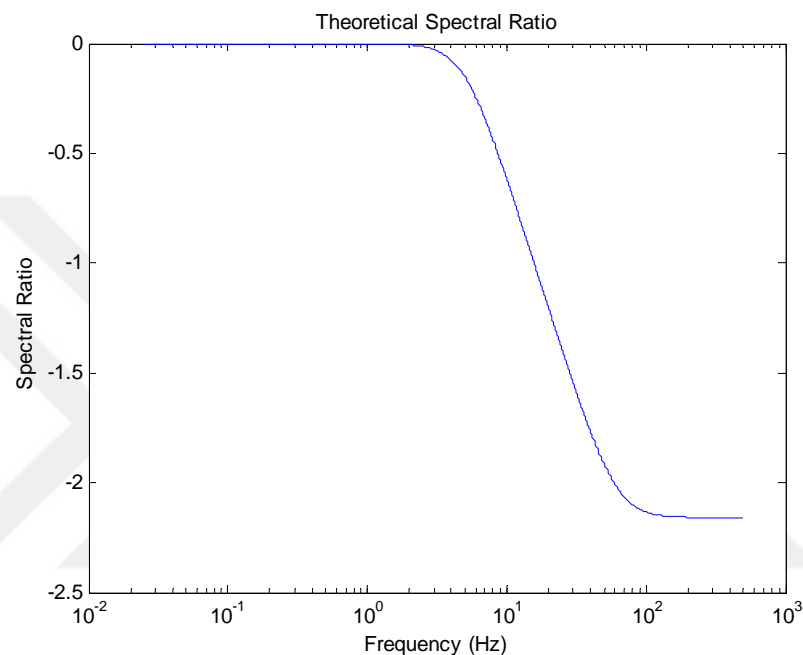
Figure 6.7. Theoretical spectral ratio curve.

The value of the relative seismic moment is located at the low frequency level where the spectrum is flat, crossing y-axis. ME's corner frequency is situated at the corner where the spectrum starts to deviate from flatness and corner frequency of the SE is at the high frequency end at the turning point. They both have the coinciding frequency values at the x-axis. Theoretical spectral ratio curve, Figure 6.7, is produced assuming the corner frequency of a ME as 5 Hz and corner frequency of the SE as 60 Hz. Frequency values varies between 0.025 Hz and 500 Hz with 10 Hz increments. Only after the additional part of the Equation 6.2 is used for the theoretical calculation.

The difference between the corner frequencies of the ME and EGF earthquakes should be large for the corner frequency of the SE to be determined more reliably with spectral ratio method. In order to show this visually, theoretical spectral ratio curve, Figure 6.8, has been produced for a corner frequency of a ME as 5 Hz, corner frequencies of the SEs between 10 Hz and 160 Hz varying with 10 Hz increments. Frequency values change between 0.025 Hz and 500 Hz with 10 Hz increments. After the additional part of the Equation 6.2 is used for the calculation.
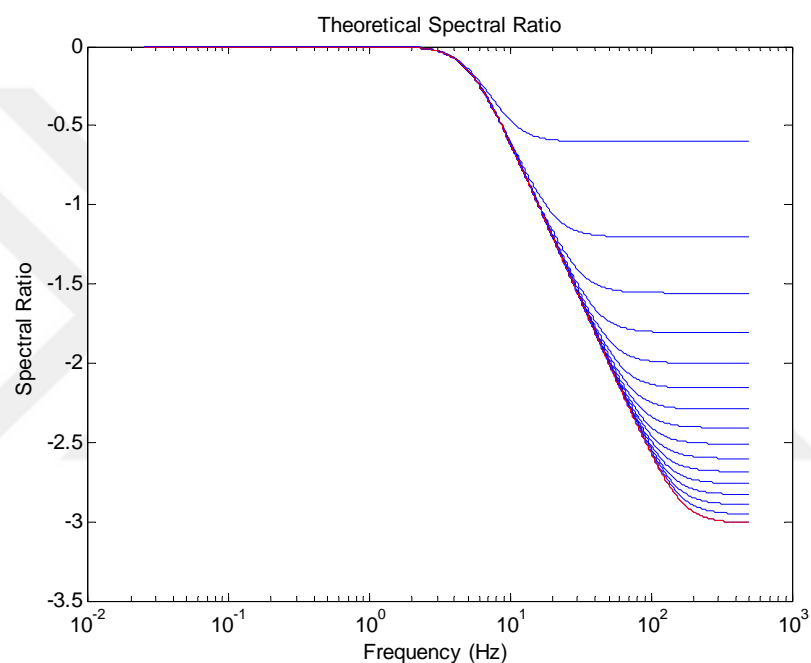
Figure 6.8. Spectral ratio curve showing the theoretical difference between the corner frequencies of the ME and an EGF earthquake.

Figure 6.8 shows that, when the difference between the corner frequencies of the ME and EGF earthquakes gets higher, turning point of the spectrum becomes more pronounced. A sharp turning point enables to obtain the corner frequency of the SE more reliably. Therefore, magnitudes of the EGF earthquakes should be sufficiently smaller than the magnitude of a ME for a reliable spectral ratio analysis. This is especially important for the determination of the corner frequency of SE which is at higher frequency.

Although, corner frequencies of a ME and SEs can be obtained with EGF method, only the corner frequencies of MEs have been taken into account in this study. Since, SNR of the SEs are low compared to the ME at higher frequencies, estimation of the corner frequencies of SEs are affected more from the noise than the ME. In conclusion, it has been considered that the most reliable output of this method is the corner frequency of the ME. In addition to that, since it is not possible to obtain the absolute moment of the ME and the SE with the EGF method, absolute values of the moments will be obtained with another step that will be discussed in the next section in detail.

On the way throughout this study, there were various obstacles that had to be overcome. For instance, small magnitude events with low SNR and narrow peak frequency at ~80 Hz subjected resulting from the normal modes of the concrete boxes. Because of these reasons, seismograms were not rotated to their radial and transversal not to contaminate the possible noise sources to different components. Additionally, in the study, velocity seismograms have been used instead of displacement seismograms. Mean or trend have not been removed and no filter has been applied prior the spectrum calculation. Note that, since ratios will be calculated, there is no need for the instrument response correction.

Until now, an introduction is given about the logic of the EGF method. Starting from this paragraph, steps of the EGF stacking estimation process will be tackled in detail. Firstly, all of the earthquakes of the clusters have been cut, including MEs and SEs, at fixed time lengths. 0.1 second before and 1 second after the S wave arrivals were used as the time window. Therefore, time domain window length used for 500 Hz data in terms of the number of samples is 550, (Figure 6.9). As an example of the application, event 20110908 has been chosen. Velocity seismograms of the ME (red) and one of the SEs (blue) in the cluster at BYZN station and EW component are shown, (Figure 6.9). Time domain window length used is 1.1 second corresponding to number of samples as 550 in Figure 6.9. Note also the very high similarity of the waveforms in the figure.
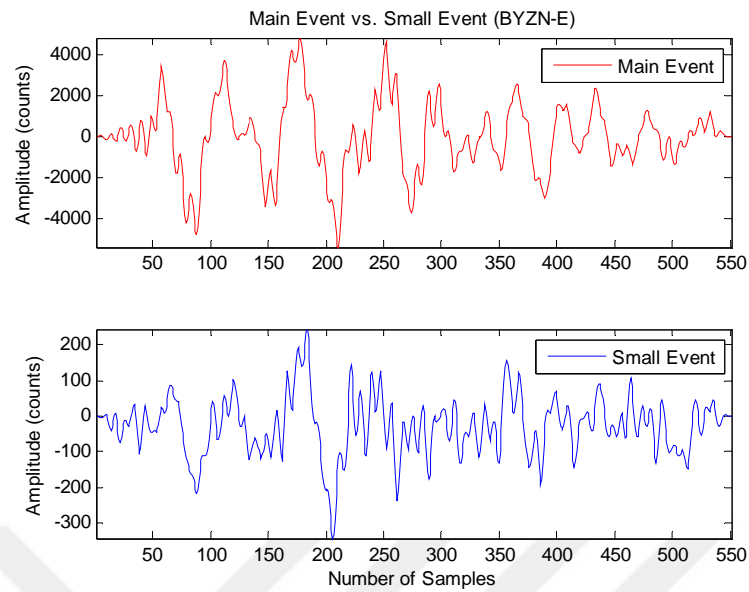
Figure 6.9. Velocity seismograms (without instrument correction) of a ME and a SE at BYZN-EW for the event 20110908.

Next, both the ME and SE seismograms have been multiplied with cosine Tukey Window with %10 taper in the time domain. Then, Fourier amplitudes of EW and NS component velocity seismograms have been calculated separately for all of the earthquakes of the clusters. Finally, spectral ratios have been taken between the ME with respect to all SEs in a cluster, (Figure 6.10). This step has been applied for all of the PIRES stations and for each component (EW and NS) of the S wave seismograms separately.
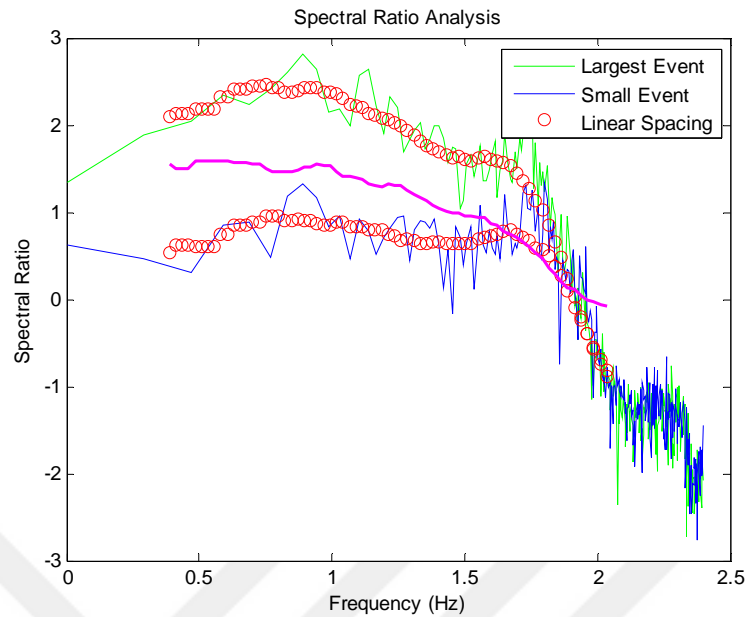
Figure 6.10. Observed spectra of the ME and SE, their re-sampled linear spaced spectra and their spectral ratio.

In Figure 6.10, green line shows the observed spectrum of the ME whereas blue line shows the observed spectrum of the SE. Spectral ratio is indicated with pink line in the figure. It is obtained from the result of the division of the ME spectrum with the SE spectrum. Red circles on top of the observed spectra of the ME and the SE are the re-sampling result of the spectra at equal intervals, (Figure 6.10). As discussed in detail in section 6.1, re-sampling of the logarithmic x-axis has been applied for the purpose of balancing the low and high frequency parts of the spectrum in linear spacing fashion (Ide *et al.*, 2003). At the same time, spectra become much simpler with the help of the linear approximation and re-sampling procedures. Optimum parameter used for the linear approximation is $\Delta \log f = 0.025$. Secondly, for smoothing prior the spectral ratio analysis, moving window of $\Delta \log f = 0.2$ has been used. Lastly, elimination of the low SNR values from the lower part of the spectra and very high values from the higher end of the spectra has been also performed for all of the spectra of a cluster. For instance, out of 100 points of data, only 78 points have been used throwing 17 points from the beginning and 5 points from the end of 20110908 cluster earthquakes, (Figure 6.10). Steps of both linear

approximation and elimination of very low and very high values are applied both to the ME and SEs, (Figure 6.10).

Figure 6.11 expresses the calculation of the ratio step in a more clear fashion. First, velocity spectra of the ME and all SEs have been calculated for each station and component (EW and NS) in a cluster, (Figure 6.11). Next, spectral ratios have been calculated between all combinations of the ME with respect to all SEs in a cluster on every station and with every EW and NS components of the S waves. This has been performed automatically and for each component (EW and NS) separately, (Figure 6.11).
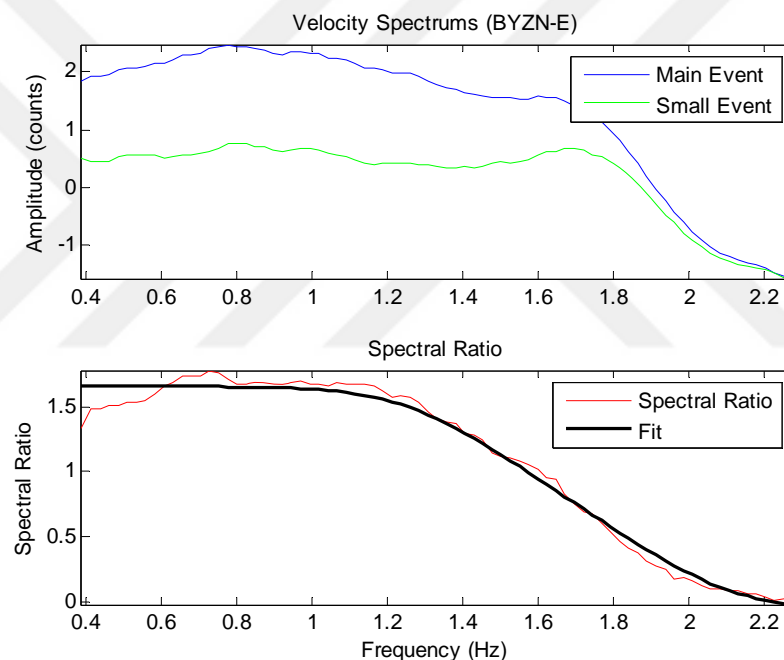
Figure 6.11. Velocity spectra of the ME and SE at BYZN-EW for the event 20110908. Spectral ratio analysis fitting result between the ME and one of the SEs in a cluster.

On the top of the Figure 6.11, blue line shows the source spectrum of the ME and green line shows the source spectrum of the SE. On the below figure of Figure 6.11, red line is the spectral ratio of the ME with respect to one of the SEs at one of the PIRES station (BYZN) at EW component. Ratio is obtained by the division of the two spectra. In the same figure, Figure 6.11, black line represents the theoretical fit to the spectral ratio.

Before proceeding with the step of stacking the spectral ratios of all traces of the two island stations, ratios that too much deviate from the average have been checked. Ratios belonging to these stations with largest deviations have been eliminated. Lastly, spectral ratios have been stacked over all available PIRES Arrays stations and at each component (EW and NS), (Figure 6.12). At the end, one single stacked ratio has been obtained for each event and component of the cluster.
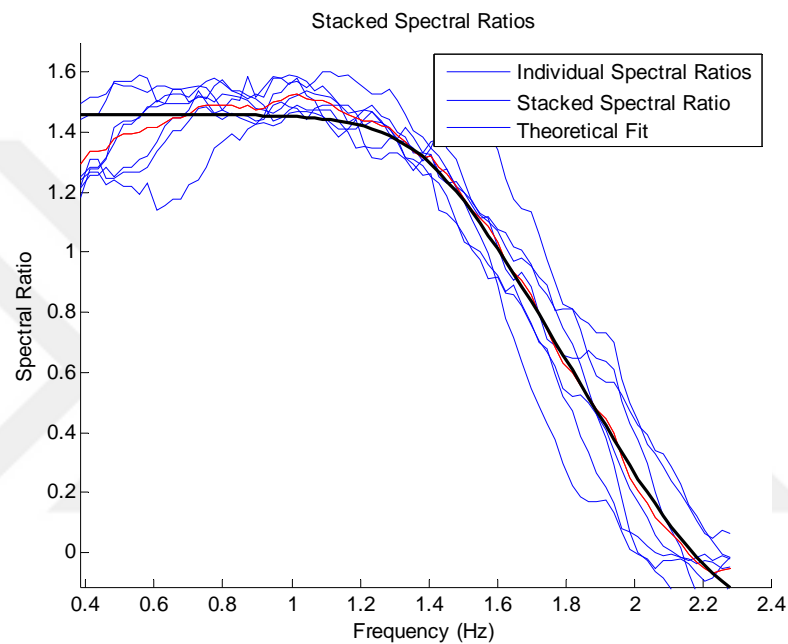
Figure 6.12. Calculated spectral ratio curves for all of the available PIRES stations at EW component for the event 20110908, their stacked ratio and best fitting theoretical curve.

In Figure 6.12, each blue line shows spectral ratio of each combination between the ME with respect to one of the SEs at all of the PIRES Arrays station at EW component. Red line is the result of the stacking of all ratios. As it is seen, stacking the ratios of all traces of the two islands stations over each component had a substantial improvement on estimation of the reliable corner frequencies of the MEs.

As a last step, source parameters have been estimated. In this sense, nonlinear curve fitting in least squares has been used as an inversion method. Initial values have been set to seismic moment ratio as 15, corner frequency of a ME as 10 Hz and corner frequency of a

SE as 50 Hz. Then, the source parameters have been searched for within predefined lower and upper bound values keeping the solution in the defined range. For instance, lower and upper bound values have been chosen between 1 and 20 for moment ratio, between 0.1 and 500 Hz for the corner frequency of a ME and between 0.1 and 500 Hz for the corner frequency of the SE. Then, seismic moment ratio and corner frequency of the ME and the SEs have been searched. Theoretical spectral ratio curve has been produced using the expression based on Boatwright (1978), (Equation 6.2). Starting from the chosen initial values and setting lower and upper bounds for searching, best fit of the nonlinear function to the data in least squares sense has been found. At each iteration, errors between the observed and the theoretical curves have been minimized. The value of the error between the observed and the calculated has been obtained in addition to the source parameters, seismic moment ratio and corner frequency of the ME and the SEs. MATLAB has been used for the nonlinear curve fitting of the observed to the theoretical spectrum in least squares sense. The trust-region-reflective algorithm has been preferred as the optimization method. In this algorithm, nonlinear system of equations cannot be underdetermined; which means, the number of equations must be at least as many as the length of the data.

From all ME and SEs pairs, ME corner frequencies have been found for each event in a cluster and at each component (EW and NS) of the S wave. Then, a large number of samples of the ME corner frequency values have been obtained at the end. Stacking that has been done so far was waveform based. As a second approach of stacking, multiple set of parameters that are found individually from each observed spectrum can be combined into a single set of estimates by taking either the mean, or the median or the percentile, etc.

Same variable, which is the corner frequency of the ME, has been calculated many times during all combinations of the ME and the SEs pairs at two different components (EW and NS). This enabled to calculate the median of the ME corner frequency values over EW and NS components of the S wave separately. Since, some of the stations or some components of the stations may not work very well or some of the waveforms may contain high level of noise, etc. estimating the median helps to obtain more reliable corner frequencies. Calculating median instead of mean (average) has been preferred, during all of the calculations in this study. For the reason that, when the most of the numbers in the data are towards either the low or the high end or when there is one value that is very different

from the others, median calculation is more accurate than the mean. Especially, in a small set of data and under these circumstances, mean value will not be as precise as median value. During the calculation of percentile which is another method of combining estimates into a single set, values are sorted first and then linear interpolation is used. Minimum or maximum values are also removed for the chosen percentage (0 to 100) in percentile. Although, median and percentile methods seem to be compatible in terms of removing the outlier values, decision of the appropriate amount of the percentage is the difficulty in percentile.

At the end, there is an even number of corner frequency observations (one value from EW and one value from NS components) in a sequence. This means that, there is no middle value to pick. Therefore, the mean of the two corner frequency values has been calculated and found out one single corner frequency for each ME in an earthquake cluster. In short, this time, the most reliable output has been tried to be obtained within a number of separate estimates in the sense of statistical consistency.

In order to indicate the distribution of the corner frequencies for each component (EW and NS) and for different clusters, histogram plotting has been chosen in terms of graphical representation, (Figure 6.13). On the histogram, corner frequencies near 0 Hz are the outliers, therefore these values should not be taken into account.
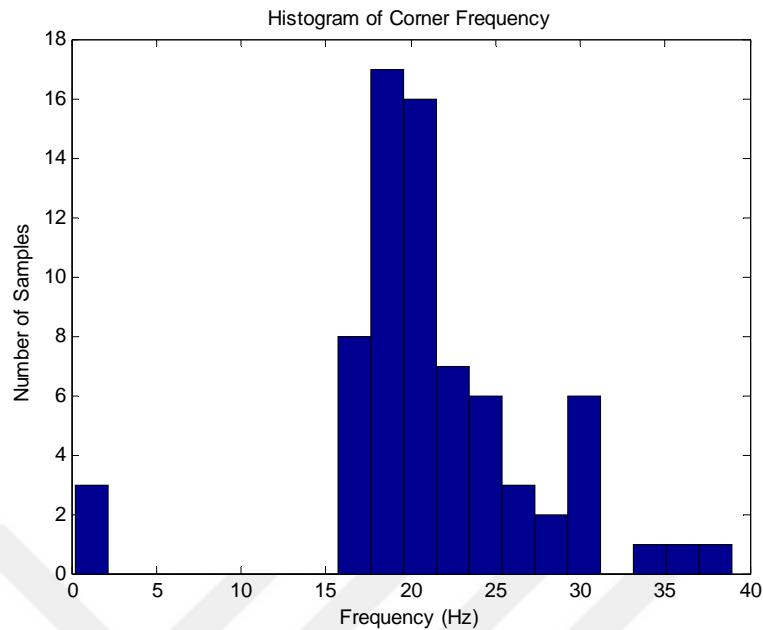
Figure 6.13. Histogram result of the corner frequency of the MEs for the EW component for one of the clusters (20110908).

Using the histogram result of the corner frequency of the MEs for one of the clusters, 20110908 at EW component, (Figure 6.13), results of the different estimations, i.e. mean, median and percentile have been compared. The mean of 20110908 cluster at EW component is 21.8162, median is 20.8671 and percentile is 17.4894 (using %10 percent value). This shows that, for a small set of data where there is scattered data, median should be used for reliable estimation, (Figure 6.13). During the construction of the histograms, first binned, divided the entire range of the estimated corner frequency values into equal size intervals. Then, the number of the corner frequency values has been counted that fall into each interval. Horizontal axis represents the range of the corner frequency values and vertical axis indicates the number of cases, times per unit of the variable on the horizontal axis, i.e. number of samples.

Considering the overall result of the ME corner frequency values for all of the clusters obtained, corner frequency values had increased more than 3 times with stacking of the spectral ratios compared to CSPE. This shows that, due the availability of multiple traces from seismic arrays allowed to compute more stable estimations statistically.

6.3. Q Estimation by the Product of the Spectral Analysis

Spectral analysis is a very useful tool in order to obtain seismic moment and moment magnitude. However, when applying spectral analysis, attenuation correction must be done beforehand. In order to get the correct corner frequency, correction of the spectra for attenuation is very important.

As it has been mentioned in the previous section, relative seismic moments between the MEs and SEs and corner frequency of the MEs and SEs in all of the detected sequences could have been estimated using either the EGF or the EGF stacking methods. However, only the corner frequencies of the MEs of the clusters have been taken as the output of the method that has been described in the previous section. EGF based methods do not supply absolute values of the seismic moments and attenuation cancels with the spectral division. Therefore, seismic moment and attenuation of the MEs in the clusters have been obtained within a second step using RSPE that will be described in this section.

Attenuation has two main effects. Firstly, since it changes the shape of the spectrum, determination of the correct corner frequency is affected severely. Secondly, it changes the level of the spectrum which effects the correct seismic moment estimation (Havskov and Ottemöller, 2009). Moreover, attenuation is frequency dependent therefore it has serious effect especially on the SEs that are at higher frequencies. Since, source spectrum at the receiver is modified by the attenuation, in order to obtain reliable parameters representing the source, it has to be removed. In short, source spectra should be determined with the knowledge of attenuation. If attenuation of the study region is unknown, it has to be estimated. If attenuation information of a region already exists, it might be used. On the other hand, in this study, an attempt has been made in order to find also the attenuation of the study area using spectral analysis. Therefore, a stepwise approach has been developed on the way to obtain parameters; seismic moment, corner frequency and attenuation.

The basic approach for estimating the source parameters, consist of finding the best set of physical parameters that fits a related analytical expression to the recorded seismogram. Although, the basic approach remains the same, methods differ considerably in the choice of the theoretical model, in the way the spectrum estimated, in the number of

unknowns and in the way multiple estimations from various seismograms are brought together. The fitting to an analytical expression can be done either in the time domain or in the frequency domain. In the time domain, the initial pulse of the waveform arrival is used to estimate various parameters. Namely, pulse duration (corner frequency) is linked to the size and area under the pulse to the moment. In the frequency domain, a source model fitting is applied to the observed spectra. In general, frequency domain approach is more widely used. In terms of the frequency domain methods, spectral fitting can be applied either to velocity or displacement spectra.

There are different methodologies used for the spectrum estimation. Most well-known of them is, DFT. For relatively larger events that are called as MEs, the time window is too short to include many cycles of the source frequency. Therefore, conventional Discrete FFT should be used carefully while doing analysis with these events. On the other hand, SNR of the earthquakes in this range is higher compared to the SEs. In this sense, it is possible to isolate the source contribution from the background noise.

The analytical expression relating the source parameters to seismograms are also numerous. In this study, spectral model proposed by Boatwright (1978) have been used to approximate the velocity amplitude spectra of only the MEs, (Equation 6.3). Boatwright (1978) suggested a modified version of the spectral shape of the Brune's Model (Brune, 1970, 1971). Boatwright (1978) assumes w^{-2} fall-off at the high frequencies of the spectra. Therefore, two corner frequencies can be observed on the spectrum with Boatwright (1978) approximation. At the low frequencies, the spectrum is flat where the level is considered proportional to the moment. On the other hand, decay of the spectral level linearly with a slope of -2 at the high frequencies determines the corner frequency.

$$g\left(f; log\, Mo, \frac{1}{Q^c}, f_c^c\right) = log\left(\frac{R^c f}{2\rho(v^c)^3 r}\right) + logMo - \frac{1}{2\,log\left(1+\left(\frac{f}{f_c^c}\right)^4\right)} - \left(\frac{\pi f t^c}{Q^c}\right) loge \qquad (6.3)$$

Where;

Mo = seismic moment

Q^c = attenuation coefficient

f_c^c = corner frequency

R^c = radiation pattern

ρ = density

v^c = wave velocity

r = hypocentral distance

t^c = travel time

c = wave type (P or S wave)

There are several constant values used in Equation 6.3. Commonly used values of these constants in source parameter studies are listed as below.

$v^P = 5.8 \text{ km/s}$

$v^S = 3.3 \text{ km/s}$

$R^P = 2/\sqrt{15}$

$R^S = \sqrt{2/5}$

$\rho = 2700 \text{kg/m}^3$

In this study, while doing RSPE, same values have also been assumed for these variables. In the literature, average radiation pattern correction varies between 0.55 and 0.85. For instance, according to Aki and Richards (2002), average values for the P and S waves are 0.52 and 0.63, respectively. Using the analytical approach for the spectral modeling that has been proposed by Boatwright (1978), the theoretical curve in Figure 6.14 can be obtained indicated with blue circles.
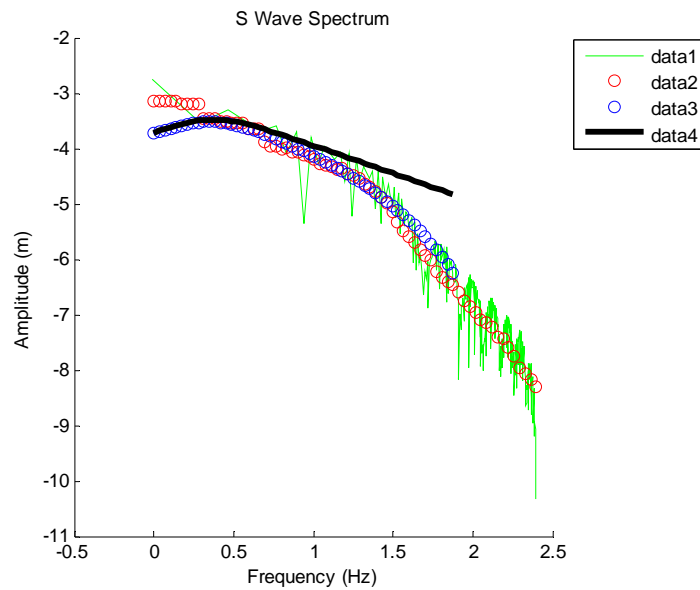
Figure 6.14. The best fitting theoretical curve (blue circles) to the observed spectrum (green). Red circles show linear approximation of log-log spectrum. Q corrected curve (black).

In the Figure 6.14, green line indicates the observed spectrum of a ME, red circles show re-sampling of the spectral amplitudes at equal intervals in log-log spectrum, blue circles form the best fitting theoretical curve to the observed spectrum and black line is the Q corrected spectrum. As it is in the Figure 6.14, seismic moment value is located at the low frequency level at the y-axis. Corner frequency value is at the junction of the horizontal line which represents the moment and the high frequency asymptote where the spectrum starts to fall off with a slope of -2.

For the special case of the PIRES, there is a peculiar narrow noise peak located at around 80 Hz at some stations where the instruments are kept in concrete housings. Noise peak is clearly observed in Figure 6.14 on the observed spectrum drawn with green where logarithm base 10 of 80 Hz corresponds to ~1.9 Hz. Every PIRES Arrays station has its own characteristic value independent of an earthquake. The peak value shows slight variations between ~70-90 Hz for different stations. Therefore, during fitting of the theoretical curve to the observed spectrum it should be away from this noise peak.

In the spectral applications such as CSPE or RSPE, besides the attenuation, instrumental effect should also be known beforehand and should be removed from the spectra. For this reason, instrument responses of the seismograms have been corrected.

Using Boatwright (1978) approximation (Equation 6.3), the absolute values of the seismic moment, corner frequency and attenuation are obtained. However, corner frequencies of the MEs were obtained with the EGF stacking approach and therefore have been fixed during the RSPE. At the end, only, seismic moment and attenuation of the MEs of the clusters have been searched.

Since, the events are small in magnitudes, corner frequencies are expected to be located on the higher end of the spectrum that are affected more from the noise. Consequently, more effective methods are needed for the corner frequencies to be estimated precisely. Seismic moment is estimated from the lower frequency part. Therefore, individual spectral methods are sufficient for accuracy and stability for the moment calculation.

During the application of the method, only the S phases have been used. In case of the S phases, corresponding S wave travel times have been used as in the Equation 6.3. Seismograms have not been rotated to their radial and transversal. Fourier amplitude spectra have been calculated both for the EW and NS component velocity spectra of fixed time lengths, for all of the MEs of the clusters. In this sense, 0.1 second before and 1 second after the S wave arrivals of fixed time lengths have been used. Mean or trend have not been removed and no filter has been applied. Data have been multiplied with cosine tapered Tukey Window using ratio of taper as %10. During the calculations of the velocity amplitude spectra, log-log spectrum have been linearized and spectral amplitudes have been re-sampled in log frequency at $\Delta logf = 0.025$ and at equal intervals. Moving window has been used as $\Delta logf = 0.2$ for smoothing (Ide *et al.*, 2003). Very low and very high values have been thrown away from all of the spectra of a cluster where SNR is low. For instance, out of 100 points of data, only 65 points have been used throwing 5 points from the beginning and 30 points from the end of the 20110908 cluster's ME. Many points have not been used from the end of the spectrum because of the noise peak located at ~80 Hz, (Figure 6.14). In addition to these, steps of the linear approximation and elimination of the

very low and very high values were applied to the MEs observed at all of the PIRES Arrays stations on the EW and NS components separately.

The MEs analyzed are observed from an epicentral distance of 20 km in average. Using nonlinear least squares inversion method, seismic moment, attenuation coefficient and corner frequency can be obtained using Equation 6.3. On the other hand, corner frequency of each ME has been fixed that had been obtained from the previous step and only searched for the best seismic moment and attenuation of the MEs for all of the PIRES stations and components (i.e. EW and NS) individually.

Nonlinear curve fitting in least squares sense has been used as an inversion method. In this manner, best fit of the nonlinear function (Equation 6.3) to the data has been searched. Initial values have been set to seismic moment as 0.5e+12 Nm and attenuation as 50. Only the seismic moment and attenuation have been searched within predefined lower and upper bound values and keeping the solution in this range. For instance, for the moment, lower and upper boundary values have been chosen between 1 Nm and $1x10^{25}$ Nm. In terms of the attenuation, boundaries vary between 50 and 1000. The search begins from the chosen initial values and continues up to the determined upper bounds. Seismic moment and attenuation of the MEs have been searched for using the theoretical expression based on Boatwright (1978), (Equation 6.3). At each iteration, the error between the observed and calculated spectra has been minimized simultaneously. Then, the calculated velocity spectra have been fit to the observed using the same equation. At the end, error between the observed and calculated has been obtained in addition to the source parameters, seismic moment and attenuation of the MEs. MATLAB has been used for the nonlinear curve fitting of the observed to theoretical spectrum in least squares sense. The commonly used trust-region-reflective algorithm has been preferred as the optimization method as in the case of EGF stacking analysis.

From all of the MEs, ME moment and attenuation have been found for each component and station for the S waves. Finally, a large number of the ME moment and attenuation values have been obtained. Since, there are two seismic arrays, there are estimations involving from more than one station. Therefore, at the end, there are multiple estimates of the parameters that have been obtained individually from each spectrum. This

advantage enables to make a statistical choice from the numerous samples obtained from 10 near distance arrays stations. Source parameters; seismic moment and attenuation at all of the 10 available PIRES stations and at different components (EW and NS) make up a collection of 20 samples which can be used to make a stable estimation of the final spectrum. In order to obtain one single value out of a number of measurements, mean, median or percentile, etc. can be used. Thus, median of all ME moment and attenuation values have been calculated over the two arrays stations and over the EW and NS components for the S waves separately. Finally, mean of EW and NS components of the S waves have been estimated in a sequence and found out one single moment and attenuation for each ME and component in an earthquake cluster.

Calculating median instead of mean has been preferred during the calculations. The reason for this is, median is more reliable than the mean in small sets of data since it discards the extreme values. In the present application, source contribution was able to be estimated reliably due to the availability of multiple traces from seismic arrays. Therefore, stability has been improved statistically with the help of using more than one estimations.

Lastly, after the median calculation of all MEs' attenuations, the value of the Q for the S wave is obtained as 170 for the study area within ~20 km to the PIRES. This value is consistent with the results of Bindi *et al*. (2006) and Horasan *et al*. (2004). Such low Q values are also observed in various fault zone areas as well (Ben-Zion *et al*., 2003). Bindi *et al*. (2006), have studied İzmit Earthquake's (Mw=7.4) aftershocks (Ml<4.5). Bindi *et al*. (2006) calculated the frequency dependent attenuation properties of the P and S waves from 1 to 10 Hz and between the distances 10 to 140 km. From 10 to 40 km, the proposed relationships for the quality factors are;

$$Q_S(f) = 17f^{0.80} \quad \text{for} \quad 1 \leq f \leq 10 \text{ Hz}$$
$$Q_P(f) = 56f^{0.25} \quad \text{for } 2.5 \leq f \leq 10 \text{ Hz} \qquad \text{(Bindi } et\ al., 2006)$$

According to these results, there is strong attenuation in the upper crust (Bindi *et al*., 2006).

In conclusion, there are critical points in the RSPE. These are, firstly making a reliable estimate of the spectrum and secondly finding an optimal model to fit the spectrum. The difficulties involved mainly relate to the shortness of the waveform used and also to the level of noise that perturbates the estimation. Signal level is higher than the noise level for the MEs in the clusters. Therefore, amplitude is not very much buried in noise over a sufficient level. Additionally, making use of the high number of stations available, estimates from single stations are combined in a statistical meaningful fashion such that a single reliable estimation could have been obtained from the data.

6.4. Source Parameter Estimation of the Slave Events: Using Characteristics of the Previously Analyzed Ray Paths

The estimation of the source parameters from spectrum offers a challenge when dealing with the SEs with low SNR. In this situation, the spectral ratio method cannot be applied since the events are already too small to be de-convolved by even SEs. Furthermore, the noise level is often comparable to the signal level which consequently makes it difficult to isolate the source contribution from the background noise.

In the present application, source contribution was able to be estimated reliably due to the availability of the multiple traces from the seismic arrays which allowed an efficient noise canceling procedure. Additionally, in order to improve the estimation process, special tools and procedures have been applied that will be described in this section.

There are different methodologies used for the spectrum estimation. Most well-known is, DFT. A recently developed technique, Multitaper Spectrum Estimation (MSE) has been used by Thomson (1982), Park *et al*. (1987) and Prieto *et al*. (2009). On the other hand, modified periodogram spectral estimation method called as Welch Algorithm, Welch (1967) has been proposed for the spectrum estimation in this study.

For the SEs, estimating the spectrum, there is a totally different difficulty. In this case, time window is large enough to include many cycles. However, amplitude is too low such that it is buried in noise. The solution is, to make estimation sensitive enough to give

the details, but stable enough to minimize the effect of noise. For this purpose, Welch Method, Welch (1967) has been used which first divides the time window into overlapping segments. Then, stacking of the spectra of all windows takes place for stabilizing the outcome.

The events analyzed are observed from an epicentral distance of 20 km in average. Most of the events' magnitudes lie between $0.5 \leq M \leq 1.5$ which implies a corner frequency within a range of 10-100 Hz. Although, the time window is long, the overlapping intervals available for estimating the spectra are very short therefore limited due to the arrival of the S phases. In reality, this duration becomes even shorter due to the rapid drop of the SNR. Generally, the time durations for the S waves are longer since the existing source receiver geometries do not produce significant surface waves contaminating the S waves. Consequently, as far as the time duration is concerned, the available signals are large enough to make a good estimate of the Fourier spectra in the range of interest. Moreover, S waves are larger in amplitude that means a slower degrading in SNR. Since, the events are small in magnitudes, the corner frequencies are expected to be located on the higher end of the spectra. In other words, a better accuracy and stability needs to be achieved for the high frequency end as compared to the lower frequency part. Therefore, Welch Method, Welch (1967) is found to be ideal for spectrum estimation instead of the DFT.

Welch Method, Welch (1967) is an improved tool for Power Spectral Density (PSD) estimation. In this method, available signal is divided into smaller segments that partially overlap with each other. Then, the spectrum of each sub segment is calculated separately. Lastly, the final spectrum of the entire signal is obtained by taking the average of individual PSD estimates. The spectrum estimated using this method shows less fluctuation than the DFT especially at the high frequency end. The price paid is the fact that, since individual spectra are calculated from smaller time segments, the low frequency coverage is reduced. In practice, there is trade-off between the stability of the estimation and the low frequency coverage. This is optimized in order to produce the best balance for each type of the application. In the present application, it has been found that a reliable estimation can be achieved by dividing the 1.0 second signal into smaller segments of 0.250 second each. The amount of the overlap has been chosen as 80% with adjacent segments. The chosen parameters mean that, the final spectrum is found by averaging the many different spectra.

This provides a sufficient sample space for an improved stability. %10 Tukey type tapering has been used for each individual window prior the Fourier Transform of the velocity spectrum calculations. The value for the Q correction is obtained from the previous steps concerning the MEs. Lastly, in a cluster of earthquakes, only the reliable ones are calculated others are discarded.

In applications concerning the earthquake spectra, the theoretical expressions are best expressed in logarithmic scales. Accordingly, any estimation procedure based on the curve fitting in spectral domain is expected to be biased towards the high frequency end where high numbers of samples are squeezed in a logarithmic way. In most applications, the spectra are resampled to give a linear spacing on the logarithmic axis in order to correct for the bias (Ide *et al.* 2003). When using the Welch approach, Welch (1967), the spectra can be computed at preselected frequencies with linear spacing, thus avoiding the resampling step (Welch, 1967). In the present application, the spectra have been estimated at 120 different frequencies which linearly spaced in the range between 0.5-250 Hz. The spectra are then smoothed by applying a moving average filter of length 5. The velocity amplitude spectrum has been approximated following Boatwright (1978), Equation 6.3.

It has been observed that both the P and S wave spectra were largely contaminated by the background noise at high frequencies. Tests showed that most of the noise was of additive nature and could be removed by simple subtraction. However, it has also been observed that sometimes the background noise was not stationary. It showed rapid variations even during the course of one single event. Just before the S arrival, the signal often contains the trailing end of the P wave arrival. There were also cases where the P wave contained disruptive contributions from the earlier events. Such a situation occurs when there are very short intervals between the events. Consequently, an estimation of the background noise was updated repeatedly using a window of 0.5 second preceding each arrival. The spectral comparison of the source contribution with the background noise allows an estimation of the SNR individually at each spectral point. At this stage, all spectral points have been eliminated from further analysis where SNR was less than 3 dB. In other words, only the spectral points have been selected where signal level is large enough for parameter estimation. This approach is different from the conventional one,

where SNR based elimination is done in frequency domain over the whole signal without considering SNR at individual frequencies.

The spectra are computed at 3 different components (Z, EW and NS) from 10 different stations available in the arrays. Finally, this gives a collection of up to 30 samples which can be used to make a more stable estimation of the final spectrum. For each spectral point, the median of the samples is chosen as the final estimate at this frequency. Median has been preferred instead of the mean in order to reduce the disruptive effect of any abnormal value that may deviate from the mainstream. The procedure described above allows a statistically stable estimation of the spectra of the P and S waves, as well as the background noise that proceeds at each arrival. At this stage, a new SNR spectrum is obtained for each individual event, this time based on the median of the spectral samples. This spectral SNR is used as a kind of weighting function when fitting the theoretical curve to the data. In other words, fitting procedure has been forced to pay more emphasis to those spectral points where the SNR is high and conversely. The choice of this type of weighting is somehow arbitrary. However, it has been observed that modifying the weighting function or removing it totally did not affect the estimation results significantly. Figure 6.16 illustrates the estimation processes described above. The figure on the left hand side shows the background noise spectra. It is estimated for the noise window before the P wave arrival. Thin blue lines are the estimations for every component of every station. The median based average noise spectrum is also shown (bold black lines). The figures in the middle and at the right hand side show the P and S wave spectra respectively in the same manner. The best fitting theoretical curves are shown on the same figures using red bold lines.
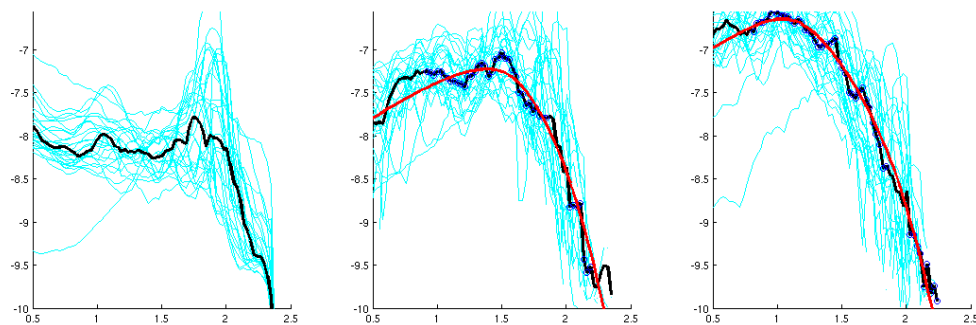
Figure 6.15. Welch type spectra (blue), Welch (1967), computed at each station and component for P and S wave and noise where median values are shown in red.

Note that, although the waveform is short and noisy, the final estimations of the spectra are remarkably smooth and stable. This type of detailed analysis shows interesting properties that are usually unidentified in the conventional approach.

In case of the multiplicative noise near 80 Hz that is produced by the presence of concrete boxes, an iterative approach has been developed to find the best fitting model. Before fitting, weighting has been applied to the data such that the parts of the spectrum that deviates from the model are less influenced by the data. This is done by reducing the cost function at these problematic intervals. The new fit at each step ignores the larger deviations even more (Figure 6.16).
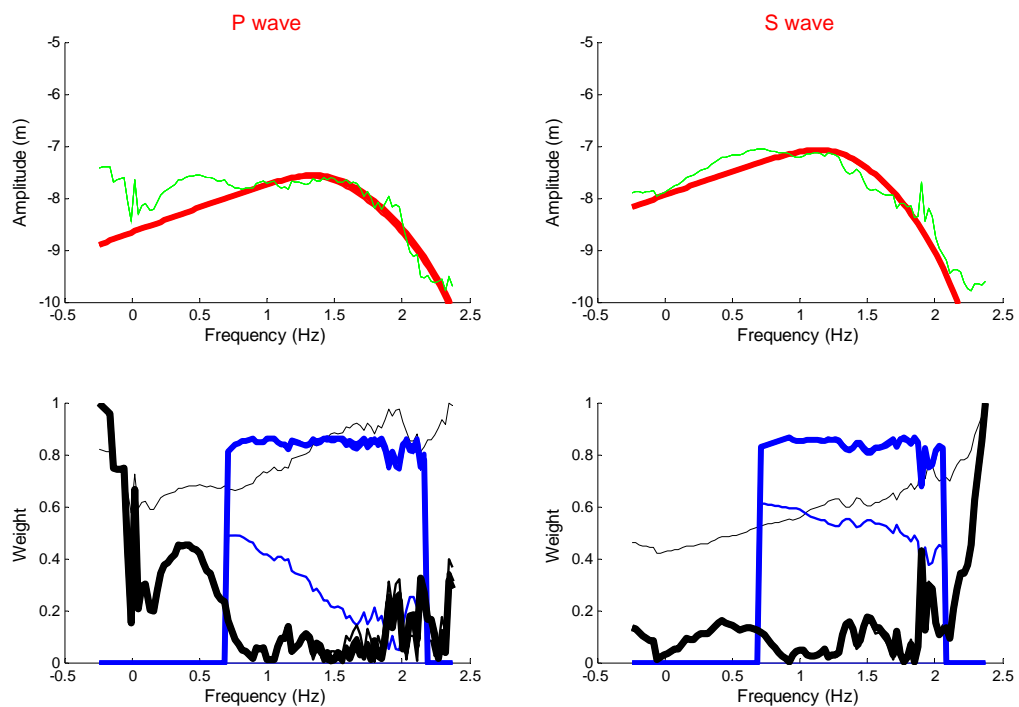
Figure 6.16. Iterative weighting procedure of data.

In the Figure 6.16, on the top line, the observed spectra and the final theoretical fits to the spectra for the P and S waves are presented in green and red, respectively. At the same figures, two consecutive values of the weighting function are plotted in dark and light blue, respectively. The consecutive changes in noise are plotted in light black and dark

black, respectively. In general, 2 or 3 steps of iterations are enough to reach a stable solution.
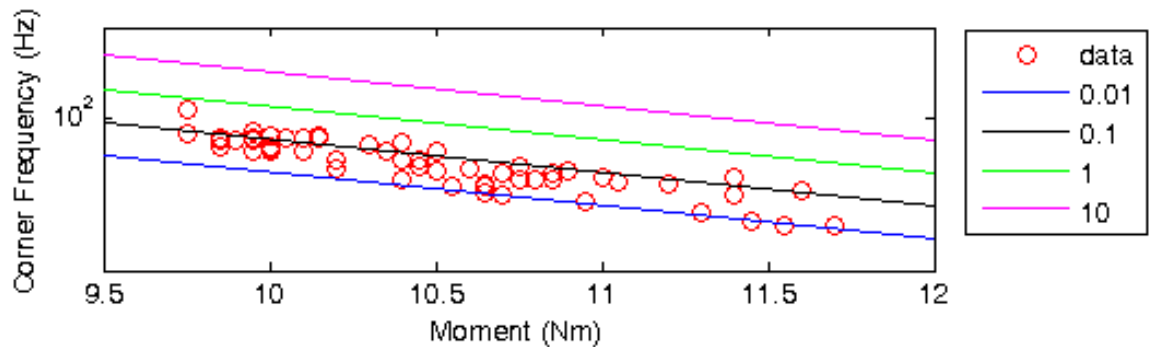
Figure 6.17. Stress drop in co-located events within a cluster.

Figure 6.17 is the result of the application of the procedure mentioned. It presents stress drop values in one of the co-located events within a cluster. Event sizes are between the magnitudes 0.5 and 2.4. When the figure is examined, it is observed that low stress drops vary on the order of 0.01 MPa and 0.1 MPa. Taking into account that, this cluster is one of the clusters consisting of very similar earthquake occurrences, the result of the low stress drops is quite meaningful. Since, earthquakes in the aforementioned cluster are "burst type" there was probably no sufficient time in order to build the stress up in a very short period of time. As a result of this phenomenon, earthquakes occurred with low stress drops.

7. RELATIVE LOCATION IN THE CLUSTERS

In case of the MEs, SNR is high and phase arrivals can be read at all stations from different azimuths. Therefore, conventional earthquake location, earthquake location by array processing (FK analysis) or conventional location together with the FK analysis works well for such events. On the other hand, higher frequency SEs can only be detected at closer stations and moreover, their phase arrivals cannot be easily distinguished. Stations of the RETMC that are on the land are far away to detect such small magnitude events in the Marmara region.

In case of the PIRES, although stations are on the islands nearer than the local networks, the majority of the earthquake activities in the Marmara Sea, in the Çınarcık Basin, occur south of the PIRES. Unfortunately, PIRES Arrays and network stations that are situated on the islands can only monitor earthquakes from a narrow azimuth. Therefore, azimuthal coverage is very restricted for the SEs occurring in the Marmara Sea for the PIRES. Under these circumstances, a relative earthquake location approach has to be used.

Basically, in the relative earthquake location methods, SEs in the sequences are located relatively to the MEs, since they are co-located. In fact, relative earthquake location between the events is a more accurate method than the absolute location methods since it uses cross correlation. The cross correlation measures the similarity between the signals. In case of the similarity, it enables to determine the relative arrival times of the events with more accuracy.

In the present application, the closer stations to the events are the two seismic arrays that are on the islands; Sivriada and Yassıada. Therefore, data recorded at these stations are used during the calculations. The MEs, of which the hypocenters are accurately determined by the RETMC, are used as the MEs for locating the SEs in each sequence.

The processing steps of the application are as follows: first, only the ME's P and S phases have been accurately picked on the Z components of the PIRES Arrays stations, since they are representative for the SEs in the sequences. On the other hand, phase arrival

readings of the SEs for both P and S waves are done relative to the reference event (ME) by cross correlating the waveforms.

As soon as the MEs are cross correlated with respect to the SEs in the clusters, with the help of the cross correlation, S-P time delays are determined. The maximum amplitude of the cross correlation function determines the relative times at the same stations where the ME and SEs are similar to each other.

Another pre-processing step of the application is the decision of the appropriate window length that is used during filtering. The cross correlation window length was chosen to correspond about twice the duration of the source pulse of the SEs. In this study, both the ME and SEs have been filtered by a filter which is adjusted to the pulse duration of the SE. Bandpass FIR filter have been used in the range of 6-30 Hz during the estimation of the differential times. Lastly, the spatial spreading of the event clusters was found by averaging the distance of each individual event to the ME in the cluster.

In terms of the hypocenter inversion program classical hypoDD, Waldhauser and Ellsworth (2000), have not been used. In case of the SEs detected, the azimuth coverage is too constrained for the PIRES. For the hypoDD program to be used efficiently, a good azimuthal coverage around the hypocenter of an earthquake is essential. Therefore, instead, a simple 3D grid exhaustive search has been used for locating the SE with respect to the ME in the least squares sense. Since, most of the arrays stations are located at a distance of ~20 km from the clusters, depth resolution for the inversion is not very well constrained. Therefore, a weighting mechanism has been used for the inversion, which allowed three times more emphasis to the horizontal direction in comparison to the vertical one. The results of the locations of all sequences are shown in Figure 7.1.
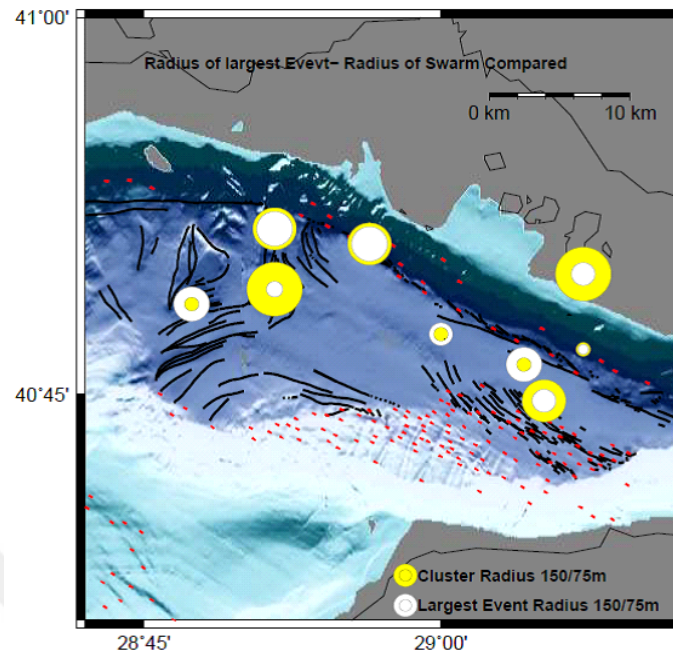
Figure 7.1. Radius of the largest event (white) compared to the cluster radius (yellow).

On the Figure 7.1, yellow circles indicate radius of the clusters and white circles indicate radius (corner frequency) of the MEs in the clusters found by the source parameter estimation study.

These two radii have been compared plotting them on top of each other. If the radii of the clusters are comparable to the radii of the MEs in the sequences, this might be the indication of slipping of the same exact location on the fault plane.

Observations show that, some clusters have sizes comparable to the sizes of the MEs. Therefore, events in these clusters are co-located. Earthquakes in some of these sequences are very identical and highly correlated. Their very similar waveforms also prove this phenomenon. This is a very strong evidence that some earthquakes might have occurred at the same location on the fault and have the same focal mechanisms. According to the Figure 7.1, especially near the main fault, some very similar earthquakes might have occurred. In the opposite case, when going away from the main fault, off the fault, radii of the clusters with respect to the radii of the MEs in the clusters decrease.

8. ESTIMATION OF THE STRESS DROP AND ITS VARIATION IN SPACE

The other property of the source parameters besides the seismic moment, corner frequency and attenuation that have been examined closely in this study is namely, stress drop of the earthquakes.

Stress drop is a physical property of the seismic source. It is considered as the difference of the stress before and after an earthquake. Stress drop is basically used in order to understand the earthquake physics, seismic source scaling and local stress level of the crust (Imanishi *et al.*, 2004). In terms of the small earthquakes, it helps to explain whether the future large events are predicable (Imanishi *et al.*, 2004).

There is an ongoing debate between the scientists whether the stress drop increases with increasing magnitude or not. This behavior of the stress drop, especially for the small magnitude earthquakes, is still not fully understood. From a more practical aspect, stress drop of the earthquakes are very important for the seismic hazard studies while computing the ground motion equations.

In this sense, how the stress drop arises after an earthquake in different parts of the study region will be searched thoroughly in this study. For this purpose, stress drop values of the MEs have been compared that scattered within ~20 km to the PIRES Arrays.

Basically, estimating stress drop consists of fitting a theoretical model to the frequency spectrum of the source. This model, once fitted, gives both the size of the fracture (corner frequency) and the seismic moment released. These two parameters finally give the value of the stress drop.

In this study, stress drops of the earthquakes have been calculated using Brune's approach (Brune, 1970), Equation 8.1.

$$\sigma_B = 7/16(\ \overline{Mo}(\frac{2\pi f_c^s}{2.34 v^s})^3) \qquad (8.1)$$

where; f_c^s is the S wave corner frequency, v^s is the S wave velocity ($v^s = 3.3\ km/s$) and $\overline{Mo}$ is the average seismic moment of the S waves.

There are difficulties involved in estimating the stress drops of high frequency small events accurately. Moment, in the Equation 8.1, is estimated from the low frequency part of the spectrum. Therefore, attenuation effects the moment calculations less. In this manner, it is more stable and reliable. On the other hand, corner frequency is calculated from the high frequency part of the spectrum. Because of this reason, it is severely affected from the attenuation and path effects. These facts make the corner frequency estimations harder. Moreover, stress drop estimation is dependent on the cube of the corner frequency which increases the uncertainty in the stress drop measurements. Whereas, moment is linearly proportional with the stress drop. Since, stress drop is more dependent on the corner frequency than the moment, more effort is needed to obtain the corner frequency reliably than the moment. Therefore, obtaining the corner frequency correctly is more important than the moment.

Reliable corner frequency calculation also requires good quality data with high frequency content because bandwidth limitations produces false cut offs at high frequencies (Viegas *et al.*, 2010). Therefore, in order to estimate the corner frequencies of the small earthquakes, high sampling rates are needed. Since, the PIRES data have been sampled with high rates, i.e. 200 Hz or 500 Hz, this necessity is ensured in this study.

Stress drop results also depend on the source model chosen. For instance, Brune (1970) and Madariaga (1976) circular source models that are used to estimate the S wave stress drops of micro earthquakes differ by factors of 1.2 and 0.71, respectively (Prejean *et al.*, 2001). On the other hand, results of the stress drops are 0.3 and 1.9 times the Sato and Hirasawa Models (Imanishi *et al.*, 2004). Therefore, while comparing the results of the different stress drop studies, it should be taken into account that different models might have different consequences.

Q of the study region has been already calculated in the previous section as 170. In this section, stress drops of the MEs have been computed. Fixing the attenuation value to 170, only the corner frequencies and moments of the MEs that have occurred within ~20 km distance to the PIRES Arrays have been searched. Pre-processing steps that have been applied during the computation of the source parameters are similar as described previously.

These steps are as follows: Prior the individual spectral application, instrumental corrections have been applied to all spectra. Seismograms have not been rotated to their radial and transversal components. Fourier amplitude spectra of the EW and NS component of the S wave velocity spectra have been calculated. FFT have been estimated starting from 0.1 second before and 1 second after the S wave arrivals of fixed time lengths. Data have been multiplied with cosine tapered Tukey Window with %10 taper. Mean, trend or filtering has not been applied before the spectrum calculations. Linear approximation and moving window analysis have been done to log-log spectra.

The analytical expression used was the spectral model proposed by Boatwright (1978). The velocity amplitude spectra have been approximated to the theoretical model of Boatwright (1978). The value of the constants in the Equation (6.3) of Boatwright (1978) have been used exactly the same as in the previous section. Then, Boatwright (1978) theoretical source model has been fit to the observed spectra. Since, the events used (i.e. MEs) are relatively larger magnitude compared to the SEs, SNR is higher. Therefore, RSPE Method has been applied to these earthquakes.

MATLAB has been used for the inversion to obtain the source parameters. Algorithm preferred was trust-region-reflective algorithm which is a nonlinear curve fitting tool in least squares sense. Fixing Q to 170, only searched for the seismic moments and corner frequencies of the MEs. The chosen lower and upper bound values for the moment were between 1 Nm and $1x10^{25}$ Nm and corner frequency values lied between 50 Hz and 1000 Hz.

First of all; source parameters, moment and corner frequency, have been received individually from the two seismic arrays stations. Figure 8.1 shows the result of the corner frequency and seismic moment relationship of the MEs.
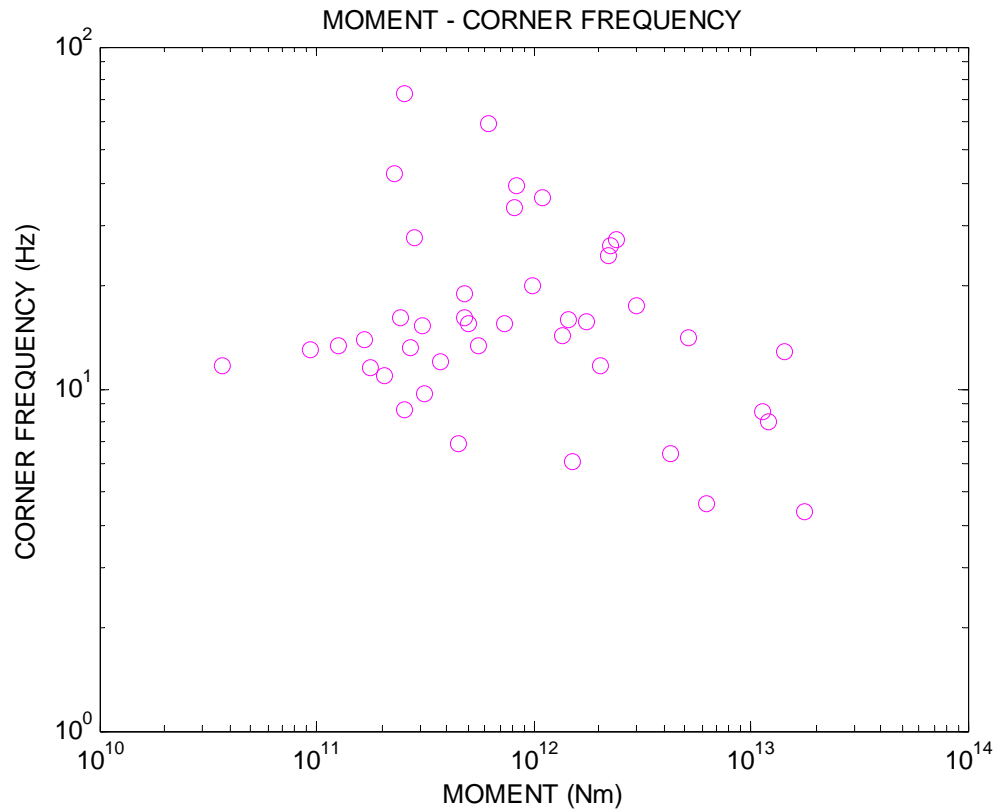
Figure 8.1. Seismic moment-corner frequency of the MEs.

Then, stress drops have been estimated for each of these individual collections of data at different stations and components (EW and NS). Lastly, statistical median of the stress drops have been computed at arrays stations for the EW and NS components of the S waves. Finally, mean of the EW and NS component stress drops have been estimated for all of the MEs. Figure 8.2 indicates the seismic moment and stress drop distribution of the MEs. According to the figure, although there is a linear dependency of the seismic moment to stress drop, there are also some outliers.
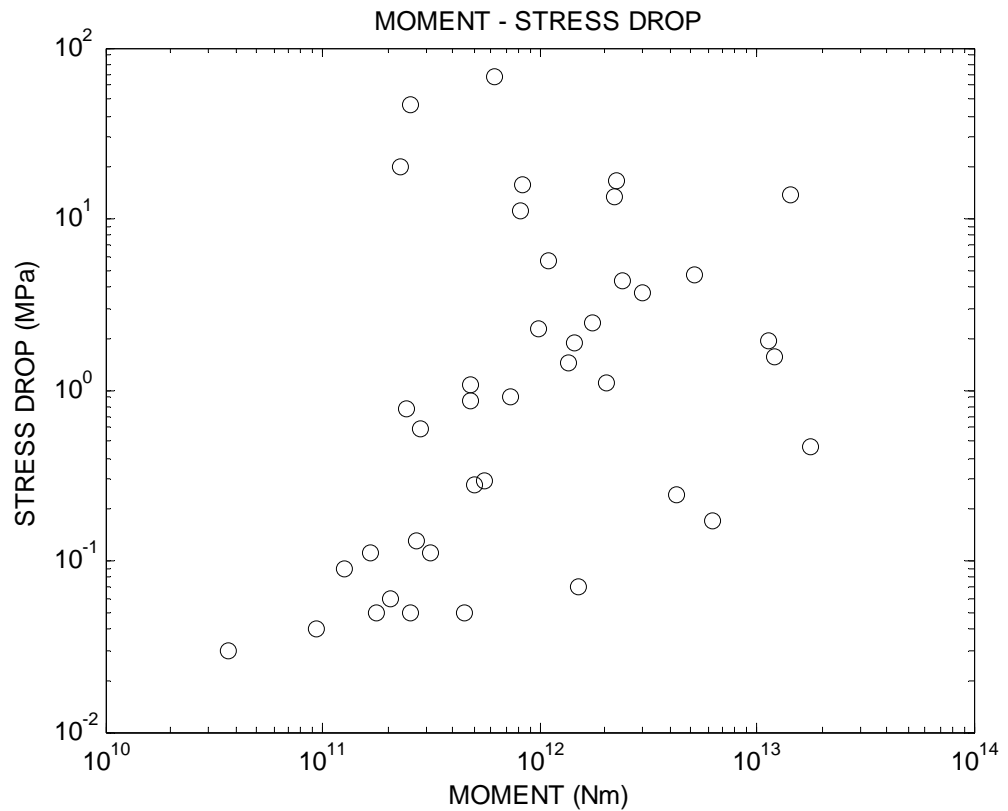
Figure 8.2. Seismic moment-stress drop of the MEs.

The result of the distribution of the stress drop values is shown in Figure 8.3. Stress drop results vary between 0.01 MPa and 44 MPa. Mostly, high stress drops are observed on the west, on the central part. Where else, earthquakes on the Çınarcık Basin generally have smaller stress drop values. Possible explanations of the observations might be as follows. Earthquakes on the west look like they are not easily triggered. Therefore, either strain is accumulated longer or rigidity of the central part is higher. For this reason, when the earthquakes in this region occur, they happen as a sudden burst with higher stress drops. This may point to a more rigid block with less significant fracturing and less significant fluid influence.
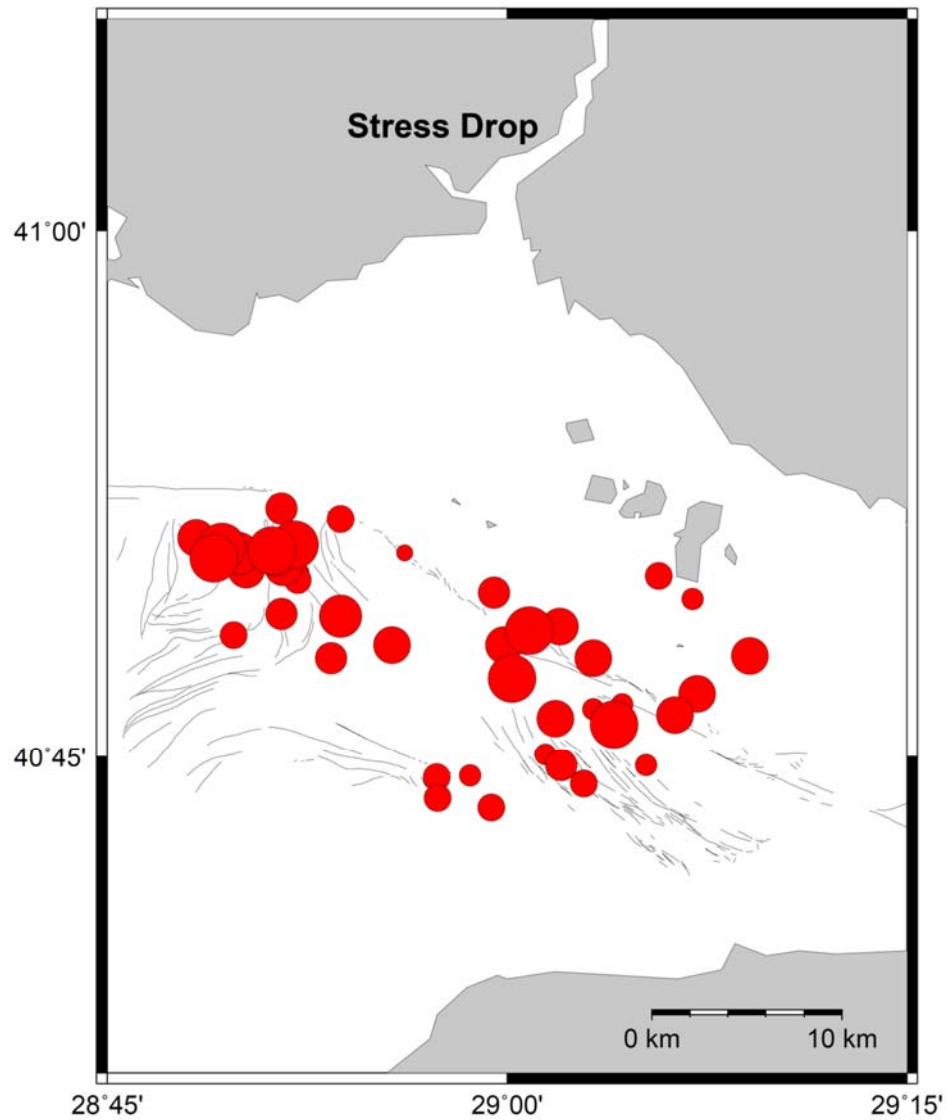
Figure 8.3. Stress drop results of the MEs.

In terms of the activity on the east, on the east end of the Çınarcık Basin, situation is just the opposite of the western part. Earthquakes in this region are generally low stress drop events except a few outliers. Small stress drops can be related to the high damaged zone with low friction. This may be more likely to be related to a fluid activity in a more intensively cracked environment. In other words, a complex network of faulting structure might be interacting mutually. This whole picture describes a highly fractured and less rigid environment. Additionally, there are some locations on the main fault with lower stress drops.

9. ELASTIC ENERGY DISSIPATION AND SEISMIC EFFICIENCY

Seismic energy radiated from the MEs has also been calculated in this study. These earthquakes occurred within a radius of ~20 km to the PIRES Arrays. In this context, since seismic energy is a function of the seismic moment and corner frequency, first of all, source spectra of the MEs have been estimated. Secondly, velocity spectra have been squared and integrated. In terms of the pre-processing step, instrument responses have been removed beforehand. During the energy calculations, EW, NS and Z component energies have been summed up for the P and S waves in order to obtain total energy radiated from an earthquake.

In this sense, Boatwright and Fletcher (1984) approach has been applied in order to calculate the radiated energy (Equation 9.1).

$$E = 4\pi\rho v^c r^2 x2 \int_{f_0}^{f_1} \left| \dot{u}^{\cdot c}(f) exp(\frac{\pi f t^c}{Q^c}) \right|^2 df \qquad (9.1)$$

Where;

ρ = density

v^c = velocity

r = distance

f_0 = lower limit of integration

f_1 = upper limit of integration

$\dot{u}^{\cdot c}$ = velocity spectrum

f = frequency

t^c = travel time

Q^c = attenuation

In order to accomplish such studies, integration should be done at all frequencies and over the entire focal area. Data are sampled at high frequencies, 200 Hz or 500 Hz at the PIRES stations. But still, limited bandwidth of the instruments effect reliable energy

calculations. In addition to that, unfortunately, only a small percent (~%20) of the energy can be carried by the frequencies smaller than the corner frequency (Ide and Beroza, 2001). It is clear that, most of the energy radiation occurs at high frequencies. Therefore, there is an underestimation problem in energy calculations. Moreover, signal should be above noise where the energy calculations are performed. Therefore, radiated seismic energy calculations have been corrected to reach the theoretical energy release using the Equation 9.3. In this sense, Omega square model of Boatwright (1978) has been used for the velocity spectrum estimations, (Equation 9.2).

$$\dot{u}(f) \approx M_o f / \sqrt{1 + (f/f_0)}^4 \tag{9.2}$$

Where; M_o is moment, f_0 is corner frequency and f is the frequency. Then, the ratio R, between the estimated and true energy based on Boatwright (1978) will be as in Equation 9.3;

$$R(f_m, f_o) = \frac{1}{2\pi} \left\{ log \frac{1 - \frac{\sqrt{2}f_m}{f_0} + (\frac{f_m}{f_0})^2}{1 + \frac{\sqrt{2}f_m}{f_0} + (\frac{f_m}{f_0})^2} + 2(arctan\left(1 + \frac{\sqrt{2}f_m}{f_0}\right) - arctan\left(1 - \frac{\sqrt{2}f_m}{f_0}\right)) \right\} \tag{9.3}$$

Where; f_m is the upper limit of the corner frequency and f_o is the corner frequency. The ratio R shows the amount of the adjustment value accounting for the radiated seismic energy, (Ide and Beroza, 2001).

Figure 9.1 shows the seismic moment and radiated energy results of the MEs. When the figure is examined, it is observed that, seismic moment almost linearly increases with the radiated energy.
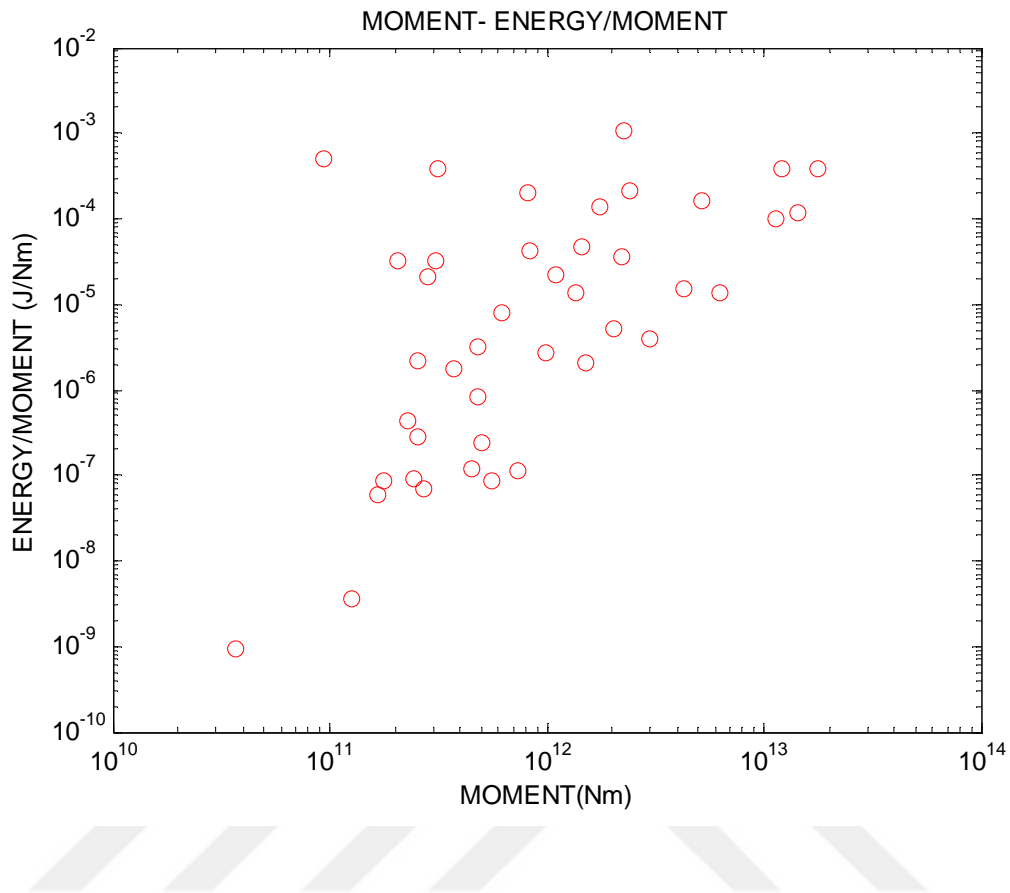
Figure 9.1. Seismic moment-radiated energy results of the MEs.

Figure 9.2 shows the result of radiated energy versus seismic moment of the MEs. Although there are a few exceptions, energy per moment on the main fault trace is lower compared to off the main fault.

While interpreting the results of the radiated energy studies, as it might be expected, if an earthquake is a creep like deformation or if it is a slow earthquake, energy radiation will be low. On the contrary, for the earthquakes with more typical rupture velocities, high frequency radiation will occur. Accordingly, much more energy will be radiated from such kind of earthquakes. Under the light of this information, there might be some locations on the main fault that are producing earthquakes different from typical earthquakes.
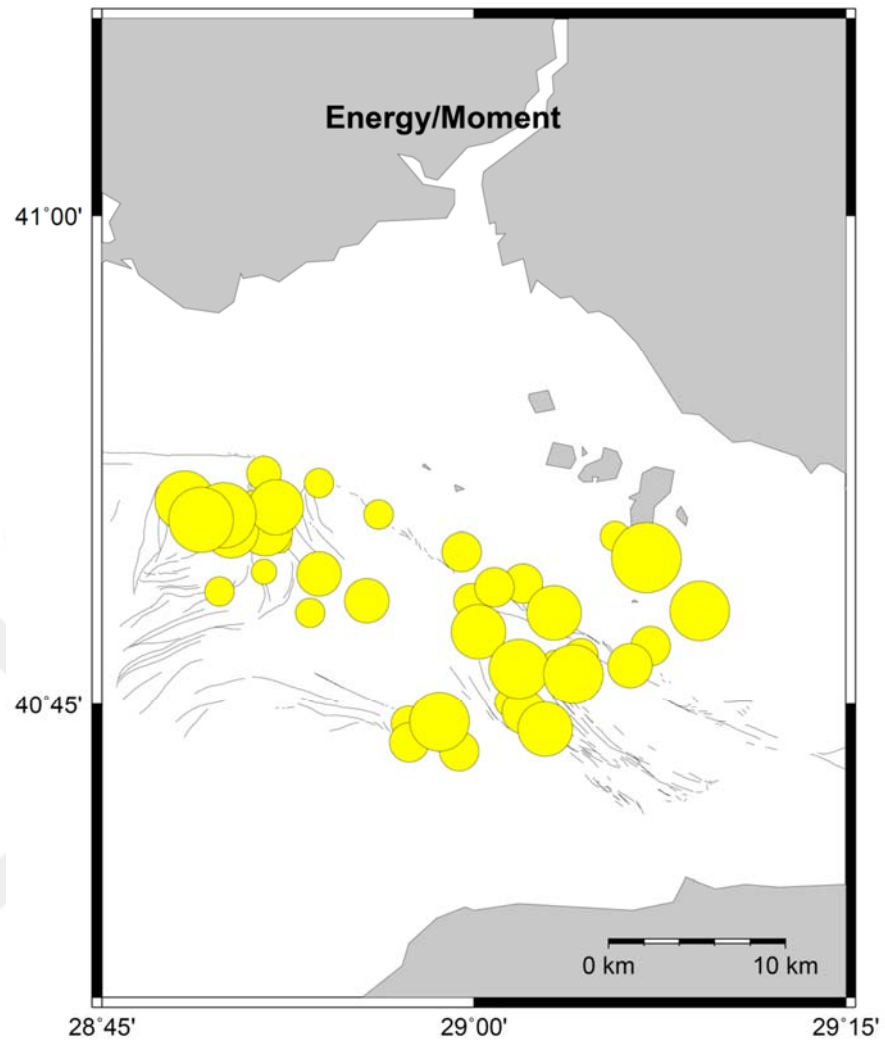
Figure 9.2. Radiated energy/seismic moment results of the MEs.

10. COMPARISON OF AFTERSHOCK AND FORESHOCK ACTIVITIES

In this section, the study region has been tried to be evaluated from a statistical point of view. Within this context, effort has been put forward for an attempt of making classification in the EW and NS directions in the Çınarcık Basin in terms of statistics. Spatial distribution of the number and duration of the earthquakes in the sequences (foreshocks and aftershocks) are evaluated in Section 10 in this respect.

As it has been stated in the previous sections, using the power of array detection technique (stacking of cross correlation coefficients on array stations) which uses the advantages of array processing, foreshocks and aftershocks sequences of earthquakes could have been examined. Once the earthquake clusters have been detected, curiosity whether different parts of the Çınarcık Basin exhibits different earthquake concentrations or not was the driving force in this study.

Foreshocks were thought to be occurring infrequent compared to the aftershocks. Therefore, they used to be less frequently studied. Recently, importance of the foreshocks has arisen with the study of Bouchon *et al*. (2011). Afterwards, many studies have been performed including laboratory experiments in order to understand the foreshocks from various aspects (i.e. mechanisms and physics behind the initiation of foreshocks, etc.). Thus, it is believed that foreshocks might play an important role during nucleation phase of a larger earthquake. Additionally, they might be used as an alarm before a bigger earthquake if they have been figured out comprehensively. Because of the reasons mentioned, besides aftershocks, foreshocks have also been evaluated from the perspective of the statistics in this study.

One of the probable reason of the foreshocks' being less studied is, far away distant stations are not capable of detecting very small earthquakes (i.e. foreshocks) therefore they were missed. With this study; along with the aftershocks, foreshocks have also been searched for going back within huge amount of the data collected. Therefore, one of the

contributions of this study was to reveal very small foreshocks within the high noise waveforms using the performance of the arrays and array based cross correlation detection.

When the distribution of the foreshocks and aftershocks processes are examined spatially, differences on the EW and NS directions can be observed. The first figure (Figure 10.1) shows spatial variation of the number of earthquakes recorded during the foreshock and aftershock activities. Here, distribution of the frequency of the foreshocks and aftershocks in spatial extension has been determined. This evaluation has been applied by counting the number of the earthquakes in each sequence before the beginning of the initiation of the ME (foreshock) and after the ME (aftershock).
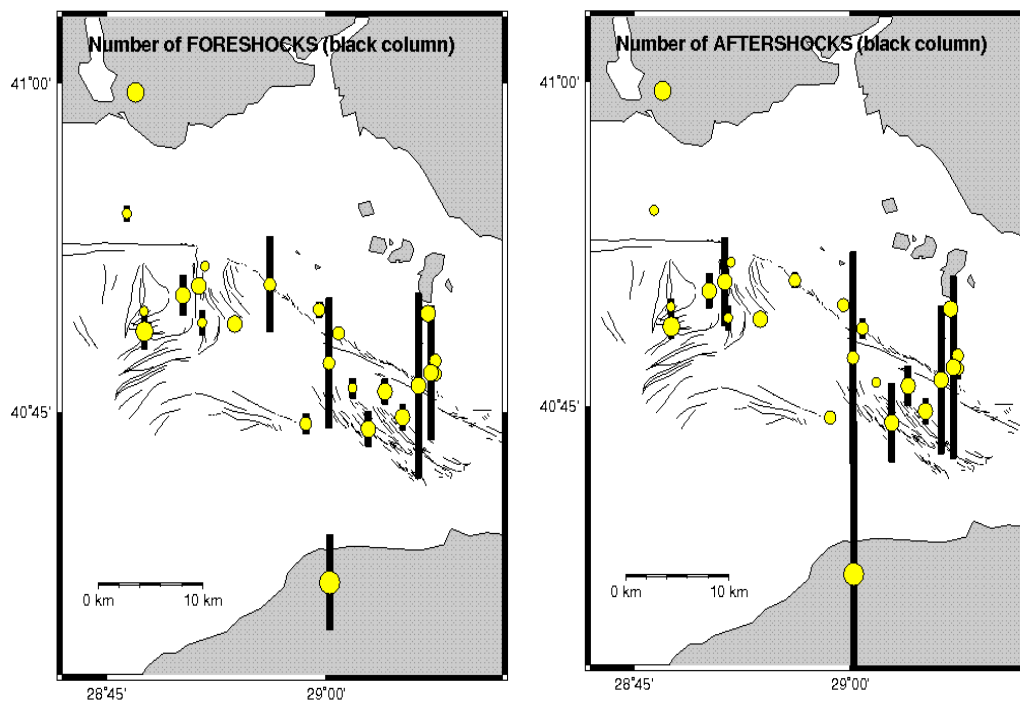
Figure 10.1. Spatial variation of the number of earthquakes recorded in the foreshocks and aftershocks sequences.

Since, the magnitudes of the ME detected by the local network is limited, it is possible to compare such earthquake sequences in terms of Gutenberg-Richter law. On the plots (Figure 10.1 and Figure 10.2), yellow circles indicate the locations of the MEs. Black columns show the number of earthquakes recorded in terms of the foreshock (figure on the

left hand side) or aftershock (figure on the right hand side) sequences (Figure 10.1). The heights of the black columns correspond to the numbers in the sequences where comparatively higher columns indicate presence of more earthquakes in a sequence.

If the Figure 10.1 is inspected in detail, variations between the different earthquake sequences are observed. It can be noticed immediately that, both the foreshock and aftershock activities are more intense in the east on the Çınarcık Basin compared to the central part in the west.

The second observation is that, events that have the most intense activity are the ones closer to the main fault. Clusters on or nearer to the smaller fault branches compose sequences with lesser foreshocks or aftershocks. Note here that, the single event on the northwest is located on the inferred rigid block. This is the event with magnitude 3.8 and seismic signal with no single foreshock and aftershock (Figure 10.1). This shows the striking difference between the north (no foreshock and aftershock) and south (a number of foreshocks and aftershocks) of the region in terms of rigidity, etc.

The second figure (Figure 10.2) makes a comparison of the foreshock and aftershock duration times. Durations of the foreshock sequences have been computed using the elapsed time between the first and last event occurrence before the ME. Meanwhile, durations of the aftershock sequences have been computed using the elapsed time between the first and last event occurrence after the ME.
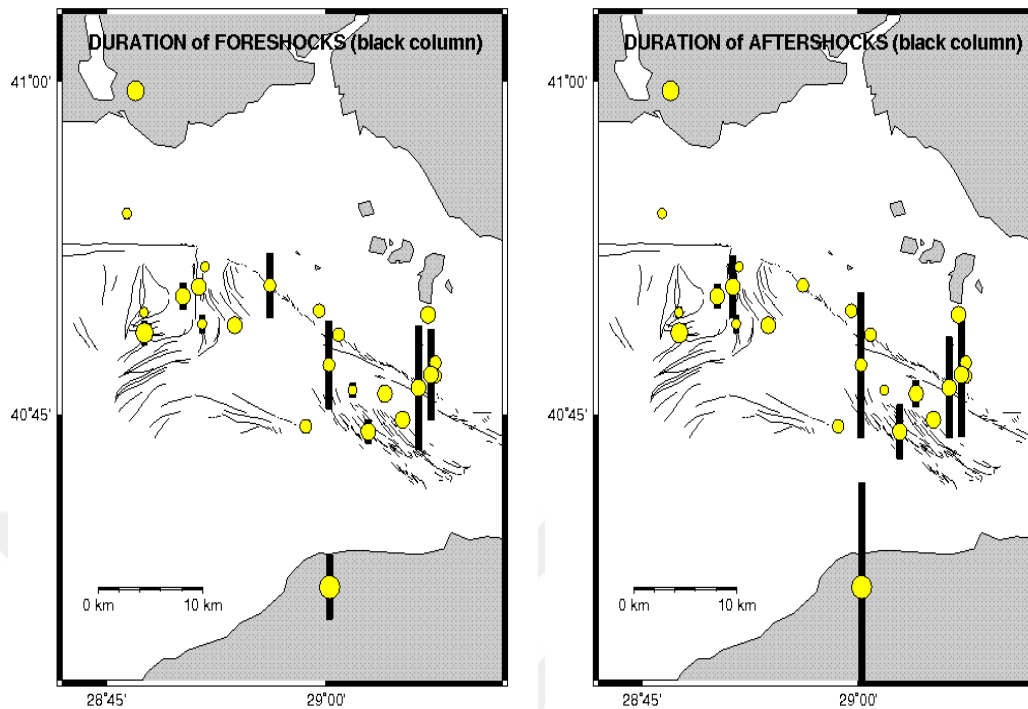
Figure 10.2. Spatial variation of the duration of the earthquakes recorded in the foreshocks and aftershocks sequences.

On the plot (Figure 10.2) like in Figure 10.1, yellow circles indicate the locations of the MEs. Black columns show the duration of the earthquakes recorded in terms of foreshock (figure on the left hand side) or aftershock (figure on the right hand side) sequences, (Figure 10.2). The heights of the black columns correspond to the durations in the sequences.

Once again, difference between the east and west of the region is observed in terms of the decay rate of the foreshock and aftershock duration times. On the east, both foreshock and aftershock sequences last in longer duration. Therefore, both of the activities die down gradually. On the contrary, on the west their duration is shorter in time. In other words, foreshock and aftershock duration fades more quickly.

In addition to that; also, the largest durations occur on the locations which are closer to the main fault. Whereas, as the same behavior observed in terms of the number of earthquakes, durations are shorter near or on the small fault branches.

Briefly stating; on the east, in other words, on the segments which correspond to the Çınarcık Basin, earthquake clusters include higher number of events (foreshocks and aftershocks) extending over a longer time period. In contrast; on the west, number of events is lower occurring in shorter time. It can be concluded that, sequences at different parts of the Çınarcık Basin have quite different properties. The dissimilar behavior of the eastern and western sides of the region might indicate material or stress field differences.

On the east, earthquakes are occurring or triggered more easily and as a result last longer compared to the west. In this case, earthquake generation relates to a deformation transient and has a longer characteristic time. Therefore, this corresponds to a slow process such as fluid migration with a long wavelength pore pressure transient. On the west, once the sequences of earthquakes occur, the rate of the decrease of activity is quicker with time.

Aftershocks lie within or near the area affected by the strain of the ME and induced by the stress changes and frictional properties of the fault zone caused by the ME (Stein and Liu, 2009).They are also the adjustments of the crust around the fault plane after a ME. Therefore, while interpreting the different behaviors of the study region these should be taken into account. For instance, if the durations last longer it means crust's rearrangements after the ME continuous longer.

Secondly, both the number and duration of the earthquakes are higher nearby the main fault. One of the possible explanation for this is the main fault's being more mature than the small branches inside the Çınarcık Basin producing more earthquakes.

Another output of this study is; it exhibits in contrast to the belief that foreshocks are rare compared to the aftershocks, results do not support this. Probably, foreshocks have not been detected either because of the earthquake detection performance of the stations not

being sufficient for high frequency small earthquakes (i.e. distance of the earthquakes to the stations) or appropriate techniques' not being applied.

Secondly, there seems not much difference between the foreshocks and aftershocks in terms of the statistics. For instance, their behaviors are quite similar in number and durations at different parts of the Çınarcık Basin. Additionally, distances of the foreshocks and aftershocks to the main fault or smaller faults also look like each other. Therefore, it seems that, both the foreshocks and aftershocks display the same kind of patterns in the study area.

11. CONCLUSIONS

Detailed analysis of the source properties of small magnitude earthquakes has become an interesting part of the borehole studies in recent years. In particular, this provides a rich source of information about the fracture properties inside the fault zones. Pioneering work on this line was initiated at the fault zone drill sites like San Andreas Fault Observatory at Depth (SAFOD). Nevertheless, borehole technology is very expensive. Therefore, it is not very easy to drill high number of boreholes. In addition to that, logistically it is hard to drill boreholes everywhere. Moreover, in case of the shallow boreholes, SNR might not be as high as expected. Because of these reasons, PIRES Arrays are implemented as an alternative to boreholes, for studying the Marmara Branch of NAFZ, at the shortest distance possible from the fault. This work is an attempt to use surface array data from the PIRES as a substitute to boreholes.

The main purpose is to estimate and classify source properties of small events occurring inside the fault zone. In this context, a number of new approaches are developed and adapted to the special case of the Marmara. In order to detect very small magnitude earthquakes, instead of using frequently used conventional methods, array based waveform cross correlation tools were developed, based on the earlier techniques used by Gibbons and Ringdal (2006). The detection parameters are optimized for the PIRES case where stations are distributed into two arrays that are ~2 km distant from each other. Stacking has been utilized as a high performance method in various areas in this study. For instance, stacking the cross correlation coefficient traces over the two near distant arrays not only increased the performance of the technique, it additionally allowed to catch small magnitude earthquakes that were missed by other networks. With the help of the method, a large number of new earthquake clusters were identified. Analysis of these previously unknown clusters is also seems to contain very similar earthquakes.

Each cluster is studied in detail by the systematical search of the aftershocks, as well as foreshocks which are often omitted in many earlier surveys. Foreshocks contain very important information regarding the nucleation phase of a large earthquake. Therefore, in addition to the aftershocks, foreshocks have also been evaluated in terms of the occurrence

statistics, stress drop and seismic efficiency, etc. As it is very well known, earthquakes can only be entitled as foreshocks after their similarity with the main shock is proved. This requires data processing before the main event. Although, it is thought that foreshocks are infrequent, results show that the situation is quite opposite. The probable reason of this belief might be missing the very small events because of the low capability of the stations, high level of noise or distances of the stations to the earthquake source, etc. In this sense, PIRES Arrays which work at high sampling rates proves to be most suitable for high detection performance.

The power of the arrays has been used in various applications in this study. For instance, the back azimuth information obtained from the FK analysis is incorporated into the conventional location procedure. Therefore, the location problem was solved using more variables (i.e. P and S readings and back azimuth) improving the stability and the convergence. In order to obtain back azimuth via FK, NORSAR Processing Software EP, Fyen (1989, 2001a,b) has been used.

New methods are also introduced for the source parameter estimation of small events. The first goal is to estimate the corner frequency reliably. Since, the corner frequency is situated at the high frequency end of the spectrum, attenuation, path and site effects and decreasing SNR at higher frequencies have negative effects for the estimation. However, this is the critical parameter that should be obtained the most accurately because it appears as the third power in the stress drop expression. Therefore, a new stepwise procedure has been implemented instead of estimating all of the source parameters simultaneously in a single step. In this sense, the new approach determines the corner frequency, first and then in the second stage more stable parameters (seismic moment and attenuation) are estimated.

Since, sequences of the earthquakes have been detected, this allowed to use EGF method. Advantages of the EGF are attenuation, path and site effects cancellations which are the hardest parameters to determine. However, instead of using the standard EGF approach, a new type of EGF stacking is applied. Despite the fact that conventional EGF could easily be applied, it is not found as much satisfactory as EGF stacking method. In this sense, classical EGF technique has been modified for the PIRES case. In this manner,

spectral ratios at all of the arrays stations have been stacked. Since, the target is to obtain a smoother and a more reliable source spectrum, this approach proved to reach these requirements even closer. The application of stacking the spectral ratios at 10 arrays stations has undoubtedly increased the stability and reliability of the estimations. Therefore, spectral ratios have been stacked at each sequence and found the corner frequencies of the MEs using inversion. When compared with the CSPE, this method has proven to be more reliable. Values of the corner frequencies have increased (almost three times in some cases) both with the usage of stacking the spectral ratios and step wise procedure. Although, spectral analysis is applied individually for each station of the arrays, this time median values of the moments and attenuations of all of the arrays stations have been calculated. Therefore, when a station does not work properly or an earthquake is recorded with high local noise level, etc. it was possible to eliminate such artifacts with this kind of an approach.

At the end of applying this technique, Q value (i.e.170) was obtained with an independent approach. Therefore, it should be considered as noteworthy. There are not many attenuation studies in the Marmara Sea. Therefore, from this point of view, an attempt to obtain Q is an important effort. The value of the Q acquired was very low. When the Q is compared with other small number of attenuation studies in the Marmara that have been performed using different techniques, the result found can be considered as quite compatible. Moreover, in some other regions of the world where highly attenuated fault zones appear, similar low values of Qs are obtained.

During the inversion of the source parameters of the SEs, Q value which was obtained for the MEs was considered as fixed. Therefore, inversion was run only in order to obtain corner frequency and seismic moment for the SEs. For such events in the clusters, more sophisticated methods were needed because of the reasons mentioned so far.

Without hesitation, one of the primary goals of this study was to obtain stress drops of the earthquakes within ~20 km to the PIRES Arrays. Ensuring all of the necessities, such as stable and reliable estimation of the corner frequency and seismic moment, stress drops of the MEs are obtained. Afterwards, it has been examined whether some kind of different behavior both in EW and NS directions exits in the study area or not. At the end,

the main aim was to classify the region in terms of the observed differences. A difference in NS direction might verify the presence of bi-material approach inferred by Le Pichon *et al*. (2005). When the results of the stress drop of the MEs are investigated, higher stress drops are observed on the west compared to the east. Therefore, eastern and western parts of the region might be different in terms of the rigidity or other physical properties. West of the Çınarcık Basin appears to be more rigid than the east. Rigidity of a region can be explained with the degree of fracturing, cracking and damage in a zone, amount of fluid entry or level of friction. Therefore, all of these definitions remind that east of the basin is highly fractured, cracked and damaged than the west. Therefore, entry of fluid is easier because of fracturing which also lowers the friction. All of these parameters help to create appropriate conditions for lower stress drops and more easily triggered higher number of earthquakes in a region. In short, the results should be interpreted under the light of this information.

Seismic energy radiation with respect to seismic moment was also considered in this study. The most critical point in the energy radiation is to detect any deformation that resembles creep or slow earthquakes which would dissipate lower energy than the typical earthquakes. In typical earthquakes, rupture velocities and friction are higher than the creeping and slow events. Therefore, such earthquakes fracture abruptly and dissipate out higher seismic energy. There are some particular locations on the main fault where lower seismic energy radiation is calculated coinciding with lower stress drops. However it is yet too early to claim a systematic variation of the energy release for a particular location.

Lastly, spatial distribution of the number and duration of earthquakes in the sequences were also evaluated in order to make classification in the EW and NS directions in the Çınarcık Basin as well. It is clearly observed that, the east of the Çınarcık Basin has both higher number of foreshock and aftershock activities and longer durations than the west. It is clear that, under stress, weak and less resistant environments produce higher number of small events, (Aktar *et al*., 2004). This interpretation is also compatible with the result of the stress drops. Since, earthquake activity is higher and cluster durations are longer on the east, as expected, stress drops are lower in this region. Intuitively, one can claim that in situations where the earthquakes occur easily and activity continue for longer time, there is no time available for substantial strain accumulation. This is also true for

burst type earthquakes. In that case also, since the required time for accumulation of strain is not sufficient, lower stress drops are expected.

The tools presented in this study may in future be part of a continuous monitoring system that helps to estimate the state of a fault zone in a real time manner. At present time, only earthquake number and sizes are used to detect an anomaly inside a hazard zone, such as ETAS In the future, it is possible that real time detection of any cascade and slow slip processes may help to declare early warning and alarm announcements. In this context, the work in this thesis is a preliminary and experimental step for the application of such future systems.

REFERENCES

Abercrombie, R. and J. Rice, "Can Observations of Earthquake Scaling Constrain Slip Weakening ?", *Geophys. J. Int.*, vol. 162, pp. 406-424, 2005.

Aki, K. and P.G. Richards, *Quantitative Seismology*, 2nd edn., Sausalito, California, University Science Books, 2002.

Aktar, M., S. Ozalaybey, M. Ergin, H. Karabulut, M.P. Bouin, C. Tapırdamaz, F. Bicmen, A.Yoruk and M. Bouchon, "Spatial Variation of Aftershock Activity across the Rupture Zone of the 17 August 1999 İzmit Earthquake, Turkey", *Tectonophysics*, vol. 391, pp. 325-334, 2004.

Armijo, R., B. Meyer, S. Navarro, G. King and A. Barka, "Asymmetric Slip Partitioning in the Sea of Marmara Pull-apart: A Clue to Propagation Processes of the North Anatolian Fault?", *Terra Nova*, vol. 14, Issue: 2, pp. 80-86, 2002.

Armijo, R., N. Pondard, B. Meyer, G. Uçarkuş, B. Mercier de Lépinay, J. Malavieille, S. Dominguez, M. Gustcher, S. Schmidt, C. Beck, N. Çağatay, Z. Çakır, C. İmren, K. Eriş, B. Natalin, S. Özalaybey, L. Tolun, I. Lefèvre, L. Seeber, L. Gasperini, C. Rangin, Ö. Emre and K. Sarıkavak, "Submarine Fault Scarps in the Sea of Marmara Pull Apart (North Anatolian Fault): Implications for Seismic Hazard in İstanbul", *Geochem. Geophys. Geosyst.*, vol. 6, Q06009, 2005.

Arnold, C., *Earthquake Effects on Buildings,* Risk Management Series Designing for Earthquakes, A Manual for Architects FEMA 454, 2006.

Barka, A., "The 17 August İzmit Earthquake", *Science*, 285, pp. 1858-1859, 1999.

Barka, A., H. S. Akyüz, E. Altunel, G. Sunal, Z. Çakir, A. Dikbas, B. Yerli, R. Armijo, B. Meyer, J. B. de Chabalier, T. K. Rockwell, J. R. Dolan, R. D. Hartleb, T. E. Dawson, S. A. Christofferson, A. Tucker, T. E. Fumal, R. M. Langridge, H. D. Stenner, W. R. Lettis, J.

Bachhuber and W. D. Page, "The Surface Rupture and Slip Distribution of the 17 August 1999 İzmit Earthquake (M 7.4), North Anatolian Fault", *Bull. Seismol. Soc. Am.*, vol. 92, no.1, pp. 43-60, 2002.

Ben Menahem, A., "Radiation of Seismic Surface Waves from Finite Moving Sources", *Bull. Seismol. Soc. Am.*, vol. 51, pp. 401-435, 1961.

Ben Menahem, A, "Radiation of Seismic Body Waves from Finite Moving Sources", *J. Geophys. Res.*, vol. 67, pp. 345-350, 1962.

Ben-Zion, Y., Z. Peng, D. Okaya, L. Seeber, J.G. Armbruster, N. Ozer, A.J. Michael, S. Baris and M. Aktar, "A Shallow Fault Zone Structure Illuminated by Trapped Waves in the Karadere-Duzce Branch of the North Anatolian Fault, Western Turkey", *Geophys. J. Int.*, vol. 152, pp. 699-717, 2003.

Berckhemer, H., "Die Ausdehnung der Bruchfiiche i'm Erdbebenherd und ihr Einfiuss auf das seismische Wellenspektrum", Getlands, Beitr. *Geophys.*, vol. 71, pp. 5-26, 1962.

Bindi, D., S. Parolai, H. Grosser, C. Milkereit and S. Karakisa, "Crustal Attenuation Characteristics in Northwestern Turkey in the Range from 1 to 10 Hz"*, Bull. Seismol. Soc. Am.*, vol. 96, no.1, pp. 200-214, 2006.

Blevins, R. D, *Fluid Systems,* Formulas for Natural Frequency and Mode Shape, Van Nostrand Reinhold, New York, Chapter 13, 1984.

Boatwright, J., "Detailed Spectral Analysis of Two Small New York State Earthquakes", *Bull. Seismol. Soc. Am.*, vol. 68, pp. 1117-1131, 1978.

Boatwright, J. and J. B. Fletcher, "The Partition of Radiated Energy Between P and S Waves"*, Bull. Seismol. Soc. Am.*, vol. 74, no. 2, pp. 361-376, 1984.

Bohnhoff, M., H. Grosser and G. Dresen, "Strain Partitioning and Stress Rotation at the North Anatolian Fault Zone from Aftershock Focal Mechanisms of the 1999 İzmit Mw = 7.4 Earthquake", *Geophys. J. Int.*, vol. 166, pp. 373-385, 2006.

Bohnhoff, M., F. Bulut, G. Dresen, P. Malin, T. Eken and M. Aktar, "An Earthquake Gap South of İstanbul", *Nat. Commun.*, 4:1999, pp. 1-6, 2013.

Bohnhoff, M., C. Wollin, D. Domigall, L. Küperkoch, P. Martínez-Garzón,G. Kwiatek, G. Dresen and P.E. Malin,"Repeating Marmara Sea Earthquakes: Indication for Fault Creep"*, Geophys. J. Int*, vol. 210, Issue: 1, pp. 332-339, 2017.

Bormann, P., *New Manual of Seismological Observatory Practice (NMSOP-1)*, IASPEI, GFZ German Research Centre for Geosciences, Potsdam, 2009.

Bouchon, M., M. N. Toksoz, H. Karabulut, M.P. Bouin, M. Dietrich, M. Aktar and M. Edie, "Space and Time Evolution of Rupture and Faulting During the 1999 İzmit (Turkey) Earthquake", *Bull. Seismol. Soc. Am.*, vol. 92, pp. 256-266, 2002.

Bouchon, M., H. Karabulut, M. Aktar, S. Ozalaybey, J. Schmittbuhl and M.P. Bouin, "Extended Nucleation of the 1999 Mw 7.6 İzmit Earthquake", *Science*, vol. 331, Issue: 6019, pp. 877-880, 2011.

Brune, J. N., "Tectonic Stress and the Spectra of Seismic Shear Waves from Earthquakes", *J. Geophys. Res.,*vol. 75, pp. 4997-5009, 1970.

Brune, J.N., Correction [to "Tectonic Stress and the Spectra of Seismic Shear Waves from Earthquakes"], *J. Geophys. Res.*, vol. 76, p. 5002, 1971.

Bulut, F., M. Bohnhoff, W. L. Ellsworth, M. Aktar and G. Dresen, "Microseismicity at the North Anatolian Fault in the Sea of Marmara Offshore İstanbul", *J. Geophys. Res.*, vol. 114, B09302.4, 2009.

Burridge, R. and L. Knopoff, "Body Force Equivalents for Seismic Dislocations", *Bull. Seismol. Soc. Am.*, vol. 54, pp. 1875-1878, 1964.

Capon, J., "High Resolution Frequency Wavenumber Spectrum Analysis", *In Proc. IEEE*, vol. 57, pp. 1408-1418, 1969.

Capon, J., "Signal Processing and Frequency Wavenumber Spectrum Analysis for a Large Aperture Seismic Array", *Methods Comput. Phy.,* vol. 13, pp. 1-59, 1973.

Carpenter, P.J. and A.R. Sanford, "Apparent Q for Upper Crustal Rocks of the Central Rio Grande Rift", *J. Geophys. Res*, vol. 90, Issue: B10, pp. 8661-8674, 1985.

Ergintav, S., R. E. Reilinger, R. Çakmak, M. Floyd, Z. Cakir, U. Doğan, R. W. King, S. McClusky and H. Özener, "İstanbul's Earthquake Hot Spots: Geodetic Constraints on Strain Accumulation Along Faults in the Marmara Seismic Gap", *Geophys. Res. Lett.*, vol. 41, pp. 5783-5788, 2014.

Fyen, J., *Event Processor Program Package*, NORSAR Sci. Rep., 2-88/89, pp. 117-123, 1989.

Fyen, J., *NORSAR Seismic Data Processing – User Guide and Command Reference*, NORSAR (contribution 748), Kjeller, Norway, 2001a.

Fyen, J., *NORSAR Seismic Detection Processing – User Guide and Command Reference*, NORSAR (contribution 731), Kjeller, Norway, 2001b.

Gibbons, S.J. and F. Ringdal, "The Detection of Low Magnitude Seismic Events Using Array Based Waveform Correlation", *Geophys. J. Int.*, vol.165, pp. 149-166, 2006.

Haskell, N.A., "Total Energy Spectral Density of Elastic Wave Radiation from Propagating Faults", *Bull. Seismol. Soc. Am.*, vol. 54, pp. 1811-1841, 1964.

Haskell, N.A., "Total Energy Spectral Density of Elastic Wave Radiation from Propagating Faults, Part II", *Bull. Seismol. Soc. Am.*, vol. 56, pp. 1811-1841, 1966.

Haskell, N. A., "Total Energy and Energy Spectral Density of Elastic Wave Radiation from Propagating Faults, II. A Statistical Source Model", *Bull. Seismol. Soc. Am.*, vol. 56, pp. 125-140, 1966.

Havskov, J. and G. Alguacil, *Instrumentation in Earthquake Seismology*, 2006.

Havskov, J. and L. Ottemöller, *Processing Earthquake Data*, 2009.

Horasan, G. and A. Boztepe-Güney, "S Wave Attenuation in the Sea of Marmara, Turkey"*, Physics of the Earth and Planetary Interiors*, vol. 142, Issues: 3-4, pp. 215-224, 2004.

Hough, S. E., "Empirical Green's Function Analysis: Taking the Next Step", *J. Geophys. Res.*, vol. 102, pp. 5369-5384, 1997.

Ide, S. and G. C. Beroza, "Does Apparent Stress Vary with Earthquake Size?"*, Geophys. Res. Lett*, vol. 28, pp. 3349-3352, 2001.

Ide, S., G. Beroza, S. Prejean and W.L. Ellsworth, "Apparent Break in Earthquake Scaling due to Path and Site Effects on Deep Borehole Recordings", *J. Geophys. Res.*, vol. 108, p. 2271, 2003.

Imanishi, K., W.L. Ellsworth and S.G. Prejean, "Earthquake Source Parameters Determined by the SAFOD Pilot Hole Seismic Array", *Geophys. Res. Lett.*, vol. 31, L12S09, 2004.

Imanishi, K. and W. Ellsworth, "Source Scaling Relationships of Microearthquakes at Parkfield, CA, Determined Using the SAFOD Pilot Hole Seismic Array", *Earthquakes: Radiated Energy and the Physics of Faulting, Geophys. Monogr. Ser.*, vol. 170, edited by R. Abercrombie et al., pp. 81-90, AGU, Washington, D. C. 2006.

Karabulut, H., M.P. Bouin, M. Bouchon, M. Dietrich, C. Cornou and M. Aktar, "The Seismicity in the Eastern Marmara Sea after the 17 August 1999 İzmit Earthquake", *Bull. Seismol. Soc. Am.*, vol. 92, pp. 387-393, 2002.

Karabulut, H., J. Schmittbuhl, S. Özalaybey, O. Lengliné, A. Kömeç-Mutlu, V. Durand, M. Bouchon, G. Daniel and M.P. Bouin, "Evolution of the Seismicity in the Eastern Marmara Sea a Decade before and after the 17 August 1999 İzmit Earthquake", *Tectonophysics*, vol. 510, Issues: 1-2, pp. 17-27, 2011.

Kostrov, B., "Self Similar Problems of Propagation of Shear Cracks", *Journal of Applied Mathematics and Mechanics*, vol. 28, pp. 1077-1087, 1964.

Kvaerna, T. and D. Doornbos, *An Integrated Approach to Slowness Analysis with Arrays and Tree Component Stations*, NORSAR Semiannual Technical Summary, 1 October 1985-31 March 1986, NORSAR, Kjeller, Norway, Scientific Report, No. 2-85/86, 1986.

Kvamme, L. and J. Havskov, "Q in Southern Norway", *Bull. Seismol. Soc. Am.*, vol. 57, pp. 1575-1588, 1989.

Le Pichon, X., A. M. C. Sengor, E. Demirbag, C. Rangin, C. Imren, R. Armijo, N. Gorur, N. Cagatay, B. Mercier de Lépinay, B. Meyer, R. Saatcilar and B. Tok, "The Active Main Marmara Fault", *Earth Planet Sci. Lett.*, vol. 192, pp. 595-616, 2001.

Le Pichon, X., N. Chamot-Rooke, C. Rangin and A. M. C. Şengör, "The North Anatolian Fault in the Sea of Marmara", *J. Geophys. Res.*, vol. 108, no. B4, p. 2179, 2003.

Le Pichon, X. and Kremeer, "Asymmetry in Elastic Properties and the Evolution of Large Continental Strike Slip Faults", *J. Geophys. Res*, vol. 110, Issue: B3, B03405, 2005.

Le Pichon, X., C. Imren, C. Rangin, A. M. C. Şengör and M. Siyako, "The South Marmara Fault", *International Journal of Earth Sciences*, vol. 103, Issue: 1, pp. 219-231, 2014.

Lienert, B. R. and J. Havskov, "HYPOCENTER 3.2, A Computer Program for Locating Earthquakes Locally, Regionally and Globally", *Seismol. Res. Lett.*, vol. 66, pp. 26-36, 1995.

Lin, B. C., I. G. Tadjbakhsh, A. S. Papageorgiou and G. Ahmadi, "Response of Base Isolated Buildings to Random Excitations Described by the Clough-Penzien Spectral Model", *Earthquake Engineering and Structural Dynamics*, vol. 18, Issue: 1, pp. 49-62, 1989.

Madariaga, R., "Dynamics of an Expanding Circular Fault", *Bull. Seismol. Soc. Am,.* vol. 66, pp. 639-666, 1976.

Madariaga, R., *Seismic Source Theory*, Earthquake Seismology, H. Kanamori, ed., Tretatise of Geophysics, Academic Press, Chapter 2, vol. 4, 2007.

Malin, P. E., M. Bohnhoff, F. Blumle, G. Dresen, P. Martínez-Garzón, M. Nurlu, U. Ceken, F. T. Kadirioglu, R. F. Kartal, T. Kılıc and K. Yanık, "Microearthquakes Preceding a M4.2 Earthquake Ofshore İstanbul", *Scientific Reports*, vol. 8, Article , Number: 16176, 2018.

Maruyama, T., "On the Force Equivalents of Dynamical Elastic Dislocations with Reference to the Earthquake Mechanism", *Bulletin of the Earthquake Research Institute*, vol. 41, pp. 467-486, 1963.

Mori, J. and A. Frankel, "Source Parameters for Small Events Associated with the 1986 North Palm Springs, California, Earthquake Determined Using Empirical Green's Functions", *Bull. Seismol. Soc. Am.*, vol. 80, pp. 278-295, 1990.

Mueller, C. S., "Source Pulse Enhancement by Deconvolution of an Empirical Green's Function", *Geophys. Res. Lett.*, vol. 12, pp. 33-36, 1985.

Mueller, C. S. and E. Cranswick, "Source Parameters from Locally Recorded Aftershocks of the 9 January 1982 Miramichi, New Brunswick Earthquake", *Bull. Seismol. Soc. Am.*, vol. 75, pp. 337-360, 1985.

Nakano, H., "Notes on the Nature of the Forces which Give Rise to the Earthquake Motions", *Seismological Bulletin of Central Metrological Observatory of Japan*, vol. 1, pp. 92-120, 1923.

Omori, F., *On the Aftershocks of Earthquake*, J. Coll. Sci. Imp. Univ. Tokyo, vol. 7, pp. 111-200, 1894.

Orgulu , G. and M. Aktar, "Regional Moment Tensor Inversion for Strong Aftershocks of the August 17, İzmit Earthquake (Mw = 7.4)", *Geophys. Res. Lett.*, vol. 28, pp. 371-374, 2001.

Orgulu, G., "Seismicity and Source Parameters for Small Scale Earthquakes along the Splays of the North Anatolian Fault (NAF) in the Marmara Sea", *Geophys. J. Int.*, vol. 184, pp. 385-404, 2011.

Oye, V., H. Bungum and M. Roth, "Source Parameters and Scaling Relations for Mining Related Seismicity within the Pyhäsalmi Oremine, Finland", *Bull. Seismol. Soc. Am.*, vol. 95, Issue: 3, pp. 1011-1026, 2005.

Ozalaybey, S., M. Ergin, M. Aktar, C. Tapirdamaz, F. Bicman and A. Yoruk, "The 1999 İzmit Earthquake Sequence in Turkey: Seismological and Tectonic Aspects", *Bull. Seismol. Soc. Am.*, vol. 92, pp. 376-386, 2002.

Ozgul, N., "Stratigraphy and Some Structural Features of the İstanbul Palaeozoic", *Turkish J. Earth Sci.*, vol. 21, pp. 817-866, 2012.

Park, J., C. Lindberg and F. Vernon, "Multitaper Spectral Analysis of High Frequency Seismograms", *J. Geophys. Res.*, vol. 92, 12, pp. 675-684, 1987.

Peterson, J., *Observations and Modelling of Background Seismic Noise*, Open-file report 93-322, U. S. Geological Survey, Albuquerque, New Mexico, 1993.

Pinar, A., K. Kuge and Y. Honkura, "Moment Tensor Inversion of Recent Small to Moderate Sized Earthquakes: Implications for Seismic Hazard and Active Tectonics beneath the Sea of Marmara", *Geophys. J. Int.*, vol. 153, pp. 133-145, 2003.

Pinar, A., S. B. Üçer, Y. Honkura, N. Sezgin, A. Ito, Ş. Barış, D. Kalafat, M. Matsushima, and S. Horiuchi, "Spatial Variation of the Stress Field along the Fault Rupture Zone of the 1999 İzmit Earthquake", *Earth Planets Space*, vol. 62, pp. 237-256, 2010.

Prejean, S.G. and W.L. Ellsworth, "Observations of Earthquake Source Parameters and Attenuation at 2 km Depth in the Long Valley Caldera, Eastern California", *Bull. Seismol. Soc. Am.*, vol. 91, pp. 165-177, 2001.

Prieto, G. A., R. L. Parker, F. L. Vernon, P. M. Shearer and D. J. Thomson, *Uncertainties in Earthquake Source Spectrum Estimation Using Empirical Green Functions*, Earthquakes: Radiated Energy and the Physics of Faulting, vol. 170, pp. 69-74, 2006.

Prieto, G., R. Parker and F. Vernon, "A Fortran 90 Library for Multitaper Spectrum Analysis", *Comput. Geosci.*, vol. 35, pp. 1701-1710, 2009.

Reilinger, R., S. McClusky, P. Vernant, S. Lawrence, S. Ergintav, R. Cakmak, H. Ozener, F. Kadirov, I. Guliev, R. Stepanyan, M. Nadariya, G. Hahubia, S. Mahmoud, K. Sakr, A. ArRajehi, D. Paradissis, A. Al-Aydrus, M. Prilepin, T. Guseva, E. Evren, A. Dmitrotsa, S. V. Filikov, F. Gomez, R. Al-Ghazzi and G. Karam, "GPS Constraints on Continental Deformation in the Africa-Arabia-Eurasia Continental Collision Zone and Implications for the Dynamics of Plate Interactions", *J. Geophys. Res.*, vol. 111, Issue: B5, Article Number: B05411, 2006.

Rost, S. and C. Thomas, "Array Seismology: Methods and Applications", *Rev. Geophys.*, vol. 40, Issue: 3, p. 1008, 2002.

Sammis, C. G. and J. R. Rice, "Repeating Earthquakes as Low Stress Drop Events at a Border between Locked and Creeping Fault Patches", *Bull. Seismol. Soc. Am.*, vol. 91, Issue: 3, pp. 532-537, 2001.

Sato, T. and T. Hirasawa, "Body Wave Spectra from Propagating Shear Cracks", *J. Phys. Earth*, vol. 21, pp. 415-431, 1973.

Savage, J.C., "Radiation from a Realistic Model of Faulting", *Bull. Seismol. Soc. Am.*, vol. 56, pp. 577-592, 1966.

Scherbaum, F., *Of Poles and Zeros*, Fundamentals of Digital Seismology, 1996.

Schmittbuhl, J., H. Karabulut, O. Lengliné and M. Bouchon, "Seismicity Distribution and Locking Depth along the Main Marmara Fault, Turkey", *Geochemistry, Geophysics, Geosystems*, vol. 17, pp. 954-965, 2015.

Schmittbuhl, J., H. Karabulut, O. Lengliné and M. Bouchon, "Long-Lasting Seismic Repeaters in the Central Basin of the Main Marmara Fault", *Geophys. Res. Lett.,* vol. 43, Issue: 18, pp. 9527-9534, 2016.

Schweitzer, J., J. Fyen, S. Mykkeltveit, S. J. Gibbons, M. Pirli, D. Kühn and T. Kværna*, Chapter 9, Seismic Arrays*, New Manual of Seismological Observatory Practice (NMSOP-1), IASPEI, GFZ German Research Centre for Geosciences, Potsdam, Bormann, P. (Ed.), 2009.

Scream 4.5, *Seismic Monitoring Software User Guide*, MAN-SWA-0001, Designed and Manufactured by GURALP Systems Limited 3 Midas House, Calleva Park Aldermaston RG7 8EA England

Sengor, A. M. C., O. Tuysuz, C. Imren, M. Sakınc, H. Eyidogan, N. Gorur, X. Le Pichon and C. Rangin, "The North Anatolian Fault: A new look", *Ann. Rev. Earth Planet. Sci.*, 33, pp. 37-112, 2005.

Sengor, A. M. C., C. Grall, C. Imren, X. Le Pichon, N. Görür, P. Henry, H. Karabulut and M. Siyako, "The Geometry of the North Anatolian Transform Fault in the Sea of Marmara and its Temporal Evolution: Implications for the Development of Intracontinental Transform Faults", *Canadian Journal of Earth Sciences,* vol. 51, Issue: 3, pp. 222-242, 2014.

Stein, R. S., A. Barka and J. H. Dieterich, "Progressive Failure of the North Anatolian Fault since 1939 by Earthquake Stress Triggering", *Geophys. J. Int*., vol. 128, pp. 594-604, 1997.

Stein, S. and M. Liu, "Long Aftershock Sequences within Continents and Implications for Earthquake Hazard Assessment", *Nature*, vol. 462, Issue: 7269, pp. 87-89, 2009.

Templeton, D. C., R. M. Nadeau and R. Bürgmann, "Behavior of Repeating Earthquake Sequences in Central California and the Implications for Subsurface Fault Creep", *Bull. Seismol. Soc. Am*., vol. 98, no. 1, pp. 52-65, 2008.

Thomson, D. J., "Spectrum Estimation and Harmonic Analysis", *in Proceedings of the IEEE*, vol. 70, pp. 1055-1096, 1982.

Trnkoczy, A., "Understanding and Parameter Setting of STA/LTA Trigger Algorithm", Bormann, P. (Ed.), New Manual of Seismological Observatory Practice 2 (NMSOP-2), Potsdam Deutsches GeoForschungsZentrum GFZ, pp. 1-20, 2012.

Utsu, T., "A Statistical Study on the Occurrence of Aftershocks", *Geophys. Mag*., vol. 30, pp. 521-605, 1961.

Viegas, G., L. G. Baise and R. E. Abercrombie, "Regional Wave Propagation in New England and New York", *Bull. Seismol. Soc. Am*., vol. 100, no. 5A, pp. 2196-2218, 2010.

Waldhauser, F. and W. L. Ellsworth, "A Double Difference Earthquake Location Algorithm: Method and Application to the Northern Hayward Fault", *Bull. Seismol. Soc. Am*., vol. 90, pp. 1353-1368, 2000.

Waldhauser, F., *HypoDD, A Program to Compute Double Difference Hypocenter Locations*, Tech. Rep. Open File Report, 01-113, U.S. Geological Survey, 2001.

Welch, P.D, "The Use of Fast Fourier Transform for the Estimation of Power Spectra: A Method Based on Time Averaging Over Short, Modified Periodograms", *IEEE Trans. Audio Electroacoustics*, vol. AU-15, pp. 70-73, 1967.

Wollin, C., M. Bohnhoff, P. Martínez-Garzón, L. Küperkoc, C. Raub, "A unified Earthquake Catalogue for the Sea of Marmara Region, Turkey, Based on Automatized Phase Picking and Travel Time Inversion Seismotectonic Implications", *Tectonophysics*, vol. 747, pp. 416-444, 2018.

APPENDIX

Appendix composes of six sections which are "Data", "Instrumentation", "Data Format and Pre-Processing", "Calculating Instrument Response", "Analysis of the Possible Source for the High Frequency Spurious Spectral Peaks" and "Application of FK to the PIRES Data", respectively.

APPENDIX A: DATA

The first part of the Appendix will start with brief information concerning the geology of the PIRES sites. Section will continue with the evaluation of the noise level of one of the PIRES stations as an example. Finally, it will end up with a view from real-time spectrogram of the PIRES.

In the following part of this section, in order to have an idea about the geology of the PIRES Arrays and network islands, a short summary will be given based on the study of Ozgul (2012). According to this study, Kınalıada, Burgazada, most of Heybeliada and the northern Büyükada are composed of Kınalıada Formation. It is mostly Middle-Late Ordovician aged and consists of feldspathic type sandstone and siltstone. Kınalıada Formation is divided into Gülsuyu and Manastır Tepe Members.

Aydos Formation's outcrops exist on the southern Büyükada. It mostly consists of quartzites. It is aged between Upper Ordovisian to Lower Silurian. Denizli Koyu Formation outcrops can be traced on the southwestern of Büyükada. It consists of limestone, clayey limestone, nodular limestone and lydites and also has shale intercalations. It is aged between Middle-Late Devonian to Early Carboniferous, (Ozgul, 2012).

Figure A1 shows geological map of the Prince Islands (Kınalıada, Burgazada, Heybeliada and Büyükada). Palaeozoic stratigraphic units of the Prince Islands that are drawn with different colors in the geological map, (Figure A1), are explained in Table A1 in terms of formation, member, symbol and age. Sivriada that does not appear in Figure A1, mostly consists of Kınalıada Formation and altered dasidic volcanits called as Ozan Tepe Volcanits. Gülsuyu and Manastır Tepe Members of Kınalıada Formation are also traced on Sivriada determined from the borehole drill, (Ozgul, 2014).
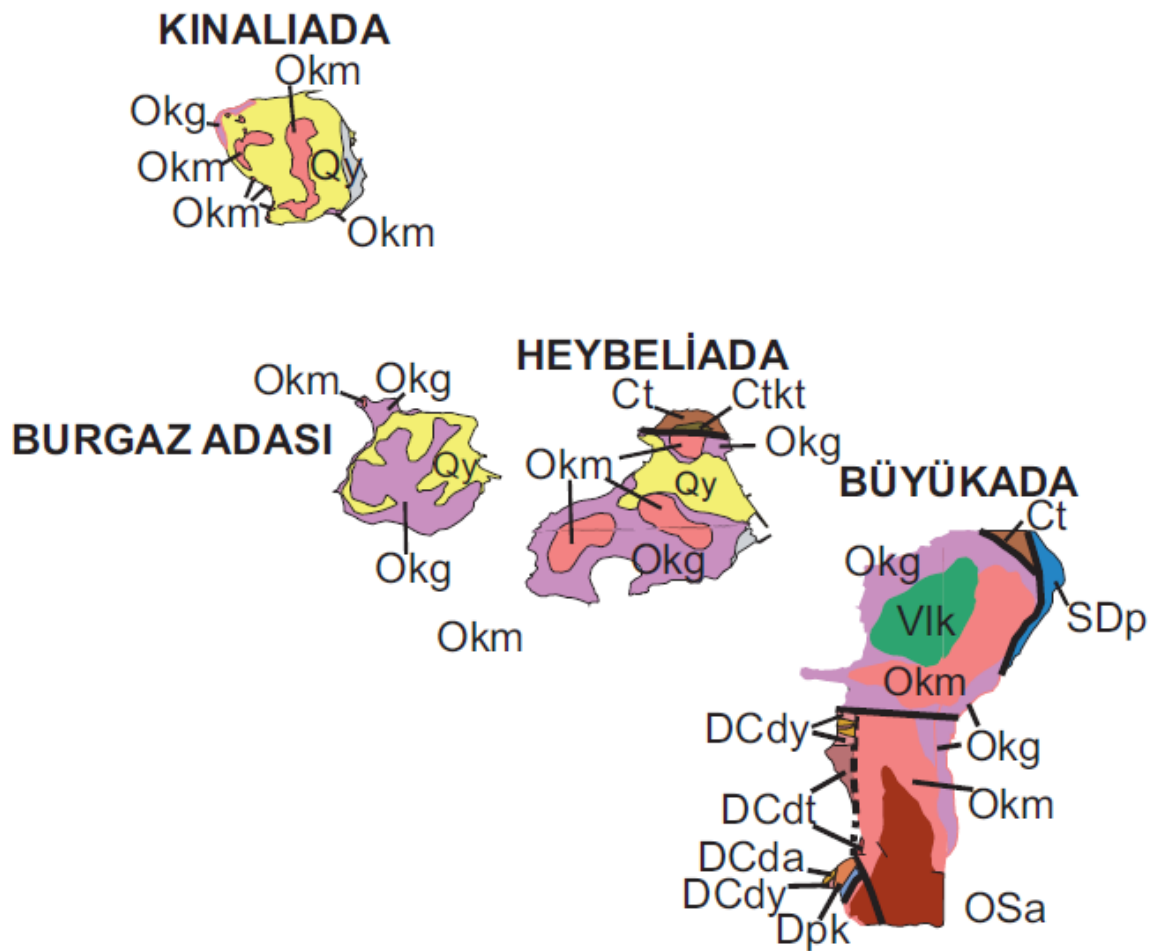
Figure A1. Geological map of the Prince Islands, (Ozgul, 2012).

Table A1. Palaeozoic stratigraphic units of the Prince Islands, (Ozgul, 2012).

FORMATION	MEMBER	SYMBOL	AGE
Trakya	undifferentiated	Ct	Early Carboniferous
Trakya	Kartaltepe	Ctkt	Early Carboniferous
Denizli Koyu	Ayineburnu	DCda	Late Devonian Early Carboniferous
Denizli Koyu	Tuzla	DCdt	Middle-Late Devonian
Denizli Koyu	Yorukali	DCdy	Middle-Late Devonian
Pendik	Kartal	Dpk	Middle Devonian
Kınalıada	Gülsuyu	Okg	Middle-Late Ordovician
Kınalıada	Manastır Tepe	Okm	Middle-Late Ordovician
Aydos	undifferentiated	OSa	Late Ordovician Early Silurian
Superficial Deposits		Qy	Pleistocene
Pelitli	undifferentiated	SDp	Late Silurian Early Devonian
Volcanics		Vlk	Cretaceous

After a brief introduction about the geology of the PIRES Arrays and network islands, in order to have an idea about the noise level of the PIRES surface stations, power density acceleration spectrum is calculated for one of the stations, MRTI, (Figure A2). Seismograms are always obscured by noise because of micro-seismic noise, environmental noise, etc. Especially, surface stations are affected more from the noise compared to the boreholes. Therefore, background noise has unfavorable effect on the surface station data. Noteworthy, noise is much more severe on the high frequency SEs like the case of this study's area of interest.

In order to have an idea about the noise level of seismic stations, power density spectrum which is a kind of spectral analysis is used. Peterson curve is the standard way of calculating the noise level at a seismic station. It is produced between global high (NHNM) and global low (NLNM) noise models, (Peterson, 1993). These curves represent cumulative power spectral densities of ground acceleration within upper and lower bounds

for the periods of both noisy and quiet at 75 stations from all over the world (Havskov and Alguacil, 2006).
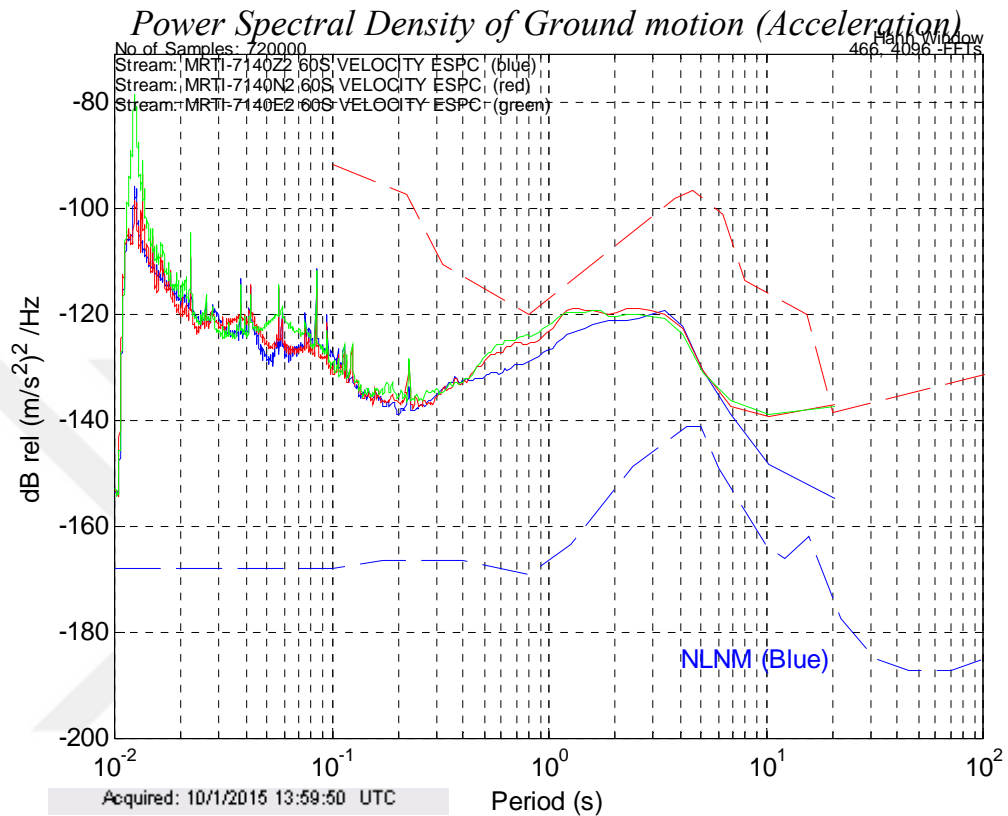
Figure A1. The Peterson noise curves shown with dashed lines and spectral level of noise for MRTI station.

Power density acceleration spectrum (Figure A2) is calculated for MRTI station during day time (at 14:00) and for the first day of October when the noise level is expected to be high. The noise spectra are shown for 3 components (EW, NS and Z) of MRTI. Spectrum is produced using Seismometer Configuration, Real-Time Acquisition and Monitoring (SCREAM) Program and for one hour raw GURALP Compressed Format (GCF) file. Spectrum is represented in terms of period (seconds) in the x axis and dB at the y axis. Blue dashed line shows the global low noise model (NLNM) and red dashed line shows the global high noise model (NHNM). In between these dashed lines, different colors show different components of MRTI, i.e. Z with blue, EW component with red and NS component with green. Note that noise level of MRTI station lies in between the low

and high noise models. In addition to that, noise level of vertical (Z) component is generally a bit lower than the other components. For all of the three components, noise level is higher between ~1 and ~10 seconds and at ~0.01 seconds.

Using real-time monitoring of the PIRES data, it has been possible to track transitions of boats nearby the islands or detect high decibel noise on the islands, i.e. noise of construction, etc. Real time spectral analysis of incoming data could have been performed using SCREAM software and such noise sources could have been observed.

Spectrograms shown in Figure A3 have been produced for one hour raw data for different stations (OILH, BRGZ, SHTH, HYBL, SCRP, PIER, EASY, MRTI and FUTB) at the EW components. The vertical axis of the spectrum is linear. Spectrogram size has been chosen as 512 and it has been presented between the Nyquist frequency (100 Hz) of the instruments at the top and 0 Hz at the bottom, (Figure A3).
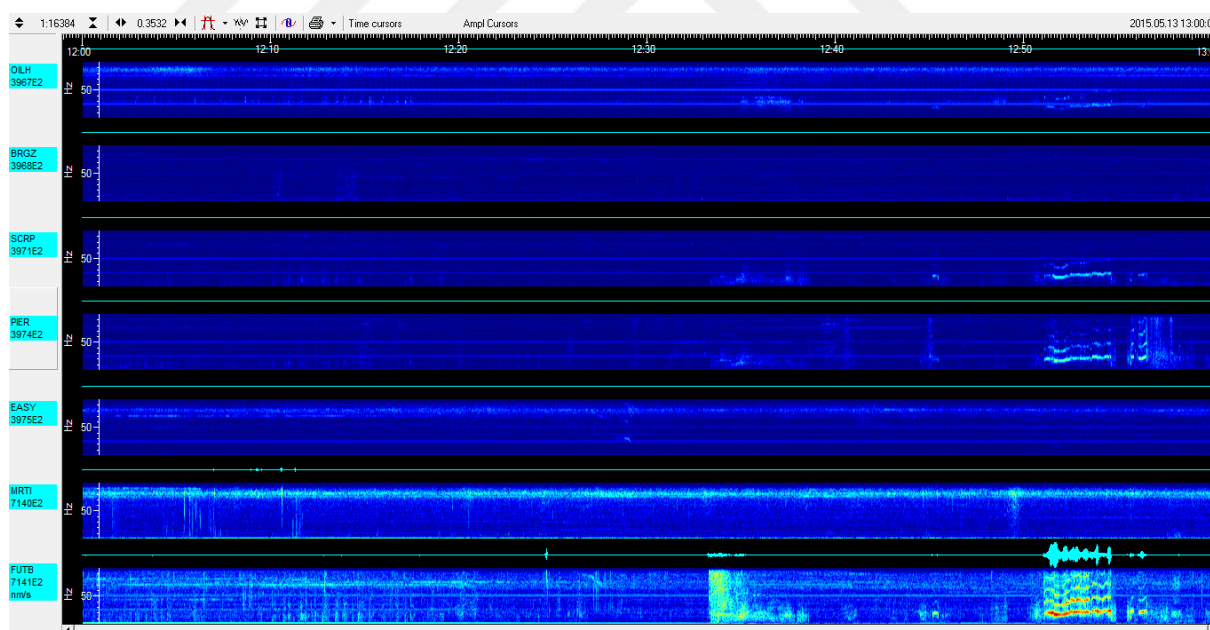
Figure A2. Real time spectrograms of the PIRES Arrays and seismic network stations at the EW components.

From the Figure A3, it can be observed that, very high level of noise occurs several times in one hour data. The noise continues for a while. Two of the noise levels are higher

than the rest of them and all of the noises occur near FUTB station on Yassıada. Noises occur at very high decibels so that they have been even detected by other stations of Yassıada such as SCRP, PIER and OILH. Moreover, multiples of the noises are also apparently observed on the real time spectrogram of the PIRES stations. Most probably, these noises have arisen during the destruction of the building near FUTB station.

APPENDIX B: INSTRUMENTATION

In the Appendix; relevant to instrumentation section, infrastructure and technology that have been used throughout the PIRES Project will be introduced in detail. Additionally, PIRES seismic network and its evolution in chronological order will be handled as well.

Sivriada and Yassıada Islands are inhabited. Therefore, both for long term operation and in order to protect the stations and the instrumentations from vandalism, concrete boxes have been constructed on these islands. These are very firm and heavy rectangular shaped concrete housings on the surface. They are built in summer 2006 before the operation of the PIRES. Dimensions of these boxes are shown in Figure B1.

Basically; cement, sand, gravel and water have been used for the construction. Iron profiles are added both inside the edges of the boxes and concrete lids. Additional usage of iron besides concrete makes the station housings more rigid, (Figure B2). In addition to that, extra lids made up of entirely iron are also used to cover the top of the boxes that are placed below the concrete uppermost lids, (Figure B2). Concrete housings have been constructed with similar dimensions using similar portions and properties of concrete, etc. at every PIRES Arrays stations.
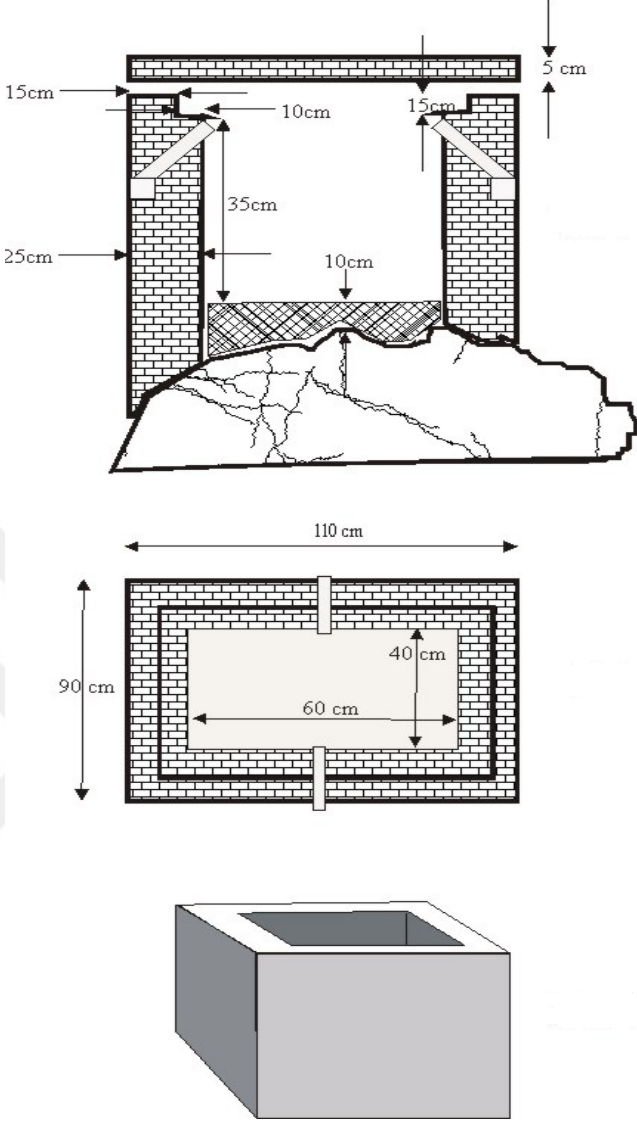
Figure B1. Sketch of the PIRES Arrays stations housings on Sivriada and Yassıada Islands.

Figure B2. Photo of the PIRES Arrays stations housings on Sivriada and Yassıada Islands.

During the test period of online data transmission, second housings have been constructed next to the two of the PIRES Arrays stations, FUTB and POWD. The distances between the two boxes are only ~20 cm. These second housings that have been constructed later have slightly smaller dimensions, (Figure B3). They are lighter and constructed from galvanized sheet, (Figure B4). Since, these boxes are built from different materials, their properties like rigidity, elasticity modulus, gamma and weight, etc. differ from the previous station housings.
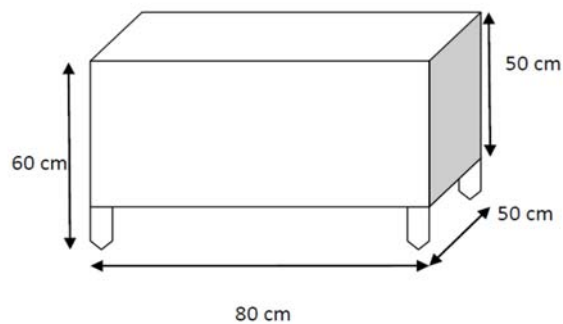
Figure B3. Sketch of the second housings next to the two of the PIRES Arrays stations (POWD and FUTB) on Sivriada and Yassıada Islands.

Figure B4. Photo of the second housings next to the two of the PIRES Arrays stations (POWD and FUTB) on Sivriada and Yassıada Islands.

On the contrary; on KNAL, BRGZ, HYBL, BASD, KRGZ and MRTI where there are single stations rather than arrays, instrumentations have been buried under the soil in plain ground. On BRGZ and HYBL, seismometers have been directly buried under the soil whereas digitizers and batteries have been placed inside the iron or galvanized boxes and then they have been buried all together. On MRTI, the arrangement of the system used to be exactly the same with BRGZ and HYBL stations. Later on, organization on MRTI has been changed. On KNAL, BASD and KRGZ and afterwards on MRTI; all of the instrumentations including; seismometers, digitizers and batteries that are placed inside the galvanized boxes are buried under the soil in plain ground.

PIRES Arrays and network stations consist of a recorder, a seismometer, a GPS receiver, battery and solar panel, (Figure B5). 12 volt battery is used at the PIRES Arrays and network stations. In case of insufficient energy, energy problems or during winter;

either the number of batteries has been increased to two or the ampere-hour of the batteries has been increased from 60 Ah to 100 Ah.

Figure B5. Photo of the PIRES Arrays and network stations' instrumentations.

PIRES Arrays and network stations run on solar panels. Solar panels supply energy for charging the batteries. In order to provide energy to the batteries in winter or during night time sufficiently and for long term without having power problems, either two solar panels have been used instead of one or the power of the solar panels has been increased from 40 Watt to 60 or 65 Watt.

All of the different instrumentations used at the PIRES stations have their own GPS receivers. Synchronization of the GPS of all PIRES instruments work in continuous mode and according to map datum WGS84. In order to maintain accurate timing for a long time, all instruments use high precision and stable Temperature Compensated Crystal Oscillator (TCXO). Other electrical and electronic equipment used in all of the stations are converter between solar panel and battery (regulator), low voltage disconnect, etc.

When the online data transmission period has started, The Global System for Mobile Communications (GSM) antenna and modem have also been added to the stations. At the beginning, data has been received via Second Generation (2G) Wireless Telephone Technology then the system has been upgraded.

Later on, data have been received either via Enhanced Data Rates for GSM Evolution (EDGE) or Third Generation (3G) Mobile Telecommunications Technology which have higher frequency bands and higher data transmission rates. EDGE is considered as a pre 3G technology. In this sense, different modems; GlobesurferIII+, ER75i, UR5i or Cloudgate have been used at different times at the PIRES stations.

Last two elements composing the instrumentation are seismometers and digitizers. First of all, information regarding the seismometers and then the digitizers will be presented in this part.

Table B1 summarizes and gives information about the PIRES Arrays and network stations' installations or removal dates, types of the instrumentations installed and date of the events that take place, i.e. sampling rate changes, online data transmission, etc.

Table B1. Installed or removed PIRES Arrays and network stations with respect to date.

DATE (Month Day Year)	STATION	DIGITIZER	SEISMOMETER
09.26.2006	FUTB	EARTH DATA LOGGER	MARK PRODUCTS L4C-3D
09.26.2006	GARD	EARTH DATA LOGGER	MARK PRODUCTS L4C-3D
09.26.2006	SCRP	EARTH DATA LOGGER	MARK PRODUCTS L4C-3D

09.27.2006	SHTH	EARTH DATA LOGGER	MARK PRODUCTS L4C-3D
09.28.2006	BYZN	EARTH DATA LOGGER	MARK PRODUCTS L4C-3D
09.29.2006	EASY	EARTH DATA LOGGER	MARK PRODUCTS L4C-3D
09.29.2006	POWD	EARTH DATA LOGGER	GURALP CMG 3ESPC
09.29.2006	NRTH	EARTH DATA LOGGER	MARK PRODUCTS L4C-3D
10.04.2006	PIER	EARTH DATA LOGGER	GURALP CMG 3ESPC
10.04.2006	OILH	EARTH DATA LOGGER	MARK PRODUCTS L4C-3D
02.07.2007	FUTB, POWD	REMOVED	REMOVED
02.07.2007	GARD	EARTH DATA LOGGER	MARK PRODUCTS L4C-3D
02.07.2007	SCRP	EARTH DATA LOGGER	MARK PRODUCTS L4C-3D
02.07.2007	BYZN	EARTH DATA LOGGER	MARK PRODUCTS L4C-3D
02.07.2007	PIER	EARTH DATA LOGGER	MARK PRODUCTS L4C-3D

02.07.2007	SHTH	EARTH DATA LOGGER	MARK PRODUCTS L4C-3D
02.07.2007	NRTH	EARTH DATA LOGGER	MARK PRODUCTS L4C-3D
02.07.2007	EASY	EARTH DATA LOGGER	MARK PRODUCTS L4C-3D
02.07.2007	OILH	EARTH DATA LOGGER	MARK PRODUCTS L4C-3D
11.07.2007	POWD	QUANTERRA	STS-2
04.30.2008	BRGZ	EARTH DATA LOGGER	MARK PRODUCTS L4C-3D
05.25.2009	MRTI	EARTH DATA LOGGER	MARK PRODUCTS L4C-3D
05.27.2009	POWD	REMOVED	REMOVED
10.07.2009	MRTI	REFTEK 130	MARK PRODUCTS L4C-3D
10.20.2009	BRGZ	REFTEK 130	MARK PRODUCTS L4C-3D
11.12.2010	FUTB	EARTH DATA LOGGER	MARK PRODUCTS L4C-3D
12.23.2010	SAMPLING RATE INCREASED to 500 Hz from 200 Hz		

04.13.2011	POWD	EARTH DATA LOGGER	MARK PRODUCTS L4C-3D
04.22.2011	HYBL	REFTEK 130	MARK PRODUCTS L4C-3D
02.20.2012	MRTI	GURALP CMG 3ESPCDE	GURALP CMG 3ESPCDE
02.20.2012	POWD	GURALP CMG 3ESPCDE	GURALP CMG 3ESPCDE
02.20.2012	FUTB	GURALP CMG 3ESPCDE	GURALP CMG 3ESPCDE
05.15.2012	BASD	GURALP CMG 6TD	GURALP CMG 6TD
05.16.2012	KRGZ	GURALP CMG 6TD	GURALP CMG 6TD
05.17.2012	KNAL	GURALP CMG 6TD	GURALP CMG 6TD
10.15.2012	EASY	GURALP CMG DAS U	MARK PRODUCTS L4C-3D
10.15.2012	BYZN	GURALP CMG DAS U	MARK PRODUCTS L4C-3D
10.15.2012	NRTH	GURALP CMG DAS U	MARK PRODUCTS L4C-3D

10.15.2012	SHTH	GURALP CMG DAS U	MARK PRODUCTS L4C-3D
10.15.2012	GARD	GURALP CMG DAS U	MARK PRODUCTS L4C-3D
10.16.2012	PIER	GURALP CMG DAS U	MARK PRODUCTS L4C-3D
10.16.2012	SCRP	GURALP CMG DAS U	MARK PRODUCTS L4C-3D
10.16.2012	BRGZ	GURALP CMG DAS U	MARK PRODUCTS L4C-3D
10.16.2012	HYBL	GURALP CMG DAS U	MARK PRODUCTS L4C-3D
10.17.2012	OILH	GURALP CMG DAS U	MARK PRODUCTS L4C-3D
02.20.2014	SAMPLING RATE DECREASED to 200 Hz		
10.09.2014	HYBL	GURALP CMG DAS U	MARK PRODUCTS L4C-3D
06.24.2015	FUTB, GARD, SCRP, PIER	REMOVED	REMOVED
11.26.2015	BASD	REMOVED	REMOVED
11.26.2015	KNAL	GURALP CMG 6TD	GURALP CMG 6TD
12.08.2016	HYBL	GURALP CMG DAS U	MARK PRODUCTS L4C-3D

01.23.2017	KNAL	GURALP CMG DAS U	MARK PRODUCTS L4C-3D
02.03.2017	KRGZ	GURALP CMG DAS U	MARK PRODUCTS L4C-3D
09.07.2017	NRTH	GURALP CMG DAS U	MARK PRODUCTS L4C-3D

PIRES Arrays stations went into operation in 2006 with short period stations equipped with MARK PRODUCTS L4C-3D (L4C). It is a three component short period seismometer (geophone) of 1 Hz natural frequency. It has a simple moving coil and a suspended mass.

L4C, which was at the center of Yassıada at FUTB station, was removed in February 2007 because of the security problems. In November 2010, it was installed back again, (Table B1). L4C-3D, which was at the center of Sivriada at POWD station, was replaced with STS-2 in November 2007. Then, in May 2009, STS-2 was also removed because of the channel problem. In April 2011, station POWD was installed back with short period L4C seismometer, (Table B1). Lately, stations at the middle of the PIRES Arrays, POWD and FUTB, were replaced with broadband seismometers.

PIRES seismic network stations; BRGZ, HYBL and MRTI also work with L4C seismometers, (Table B1). With the initiation of the online data transmission period, L4C was dismantled from MRTI and a broadband seismometer has been deployed instead (Table B1).

During November 2007 and May 2009, there was STRECKEISEN STS-2 (STS-2) very broadband sensor at the middle of Sivriada Array, at the station POWD. STS-2 is a force balance three component triaxial seismometer with 120 seconds period having 3 inertial pendulums.

On the PIRES seismic network stations: KNAL, BASD and KRGZ stations, there were 6TD semi broadband of 30 seconds period triaxial seismometers, (Table B1). They are three component force balance digital seismometers with integrated digitizers. They have 24-bit built-in digitizers and 2 Gigabyte (GB) of internal Flash memory.

When the data transmission became online, MRTI and stations at the middle of the PIRES Arrays (FUTB and POWD) are equipped with three component triaxial broadband GURALP CMG-3ESPCDE (3ESPCDE) seismometers, (Table B1). These instruments are 60 seconds period force balance seismometers having nonlinear electronic feedback. The 3ESPCDE is the combination of CMG-3ESP weak motion instrument, an integrated 24-bit built-in CMG-DM24 digitizer and an Embedded Acquisition Module (CMG-EAM) used for data recording and communication. They have Universal Serial Bus (USB) data storage of 16 GB. Mass locking, mass unlocking and centering can be performed remotely and automatically with these instruments. In conclusion, GURALP seismometers have more complex circuitry than the L4C.

Recorders that were used at the PIRES Arrays were Earth Data PR6-24 Portable Field Recorder (EDL). The EDL is a digital recording system for standalone use with 24-bit resolution. Data is stored on hard disk. They have one hard disk with 36 GB data capacity. EDLs that had been used were 3 or 6 channels. Stations on BRGZ and MRTI were also equipped with EDL, (Table B1).

STS-2 on Sivriada Array, at the station POWD, ran with QUANTERRA Q330 (Q330) recorder between November 2007 and May 2009, (Table B1). Q330 is also a 24-bit resolution Analog to Digital Converter (A/D) instrument. It is a 3 channels broadband and high resolution seismic system.

EDL recorders of BRGZ and MRTI stations were replaced with REFTEK 130-01 (REFTEK). On the other hand, HYBL station equipped with REFTEK beginning with its installation period, (Table B1). REFTEK has 3 channels with 24-bit resolution. Two removable Compact Flash II (CF-II) data storage devices of 16 GB were used in REFTEK for storing large amounts of data in the field. They have totally 32 GB of data capacity.

Setup, control and status monitoring was accomplished with a Personal Digital Assistant (PDA) with the REFTEKs.

When the data transmission became online, EDL and REFTEK digital recording systems were replaced with GURALP CMG-DM24 (DM24) digitizers. Recorders on BRGZ, HYBL and outermost four of the PIRES Arrays stations started to work with GURALP digitizers, (Table B1). It is a digital recorder that has a dynamic range of 24-bit resolution with 3 channels. They can perform data recording, communication and control. Total data storage is 16 GB and supplied on portable USB.

All of the PIRES seismic stations have worked with very high sampling rates during its operation. PIRES started collecting data with a sampling rate of 200 Hz in July 2006 beginning from its installation period till December 2010. Then, the sampling rate was increased from 200 Hz to 500 Hz at all of the PIRES stations in December 2010, in order to improve the sensitivity of locations and perform finer and more detailed analysis.

After working with 500 Hz for two years between December 2010 and February 2014, sampling rate was decreased back to 200 Hz. During the presence of the STS-2, between November 2007 and May 2009 on Sivriada (POWD) station, data were collected at various sampling rates at the same time at this station, for instance 20 Hz and 100 Hz. KNAL, BASD and KRGZ stations worked at sampling rate of 100 Hz because of their limited size of hard disk capacity when working with GURALP CMG6TD (6TD) semi broadband of 30 seconds period seismometers.

Data have been collected with continuous recording at all of the PIRES Arrays and network stations. The PIRES data have been recovered offline by periodic exchange of hard disks beginning from the array installation period. After a short test period, the data transmission became online. Afterwards, offline data collection has been done for only the stations that had online data transmission problems. When the data transmission became online, data started to flow both to Boğaziçi University Kandilli Observatory and Earthquake Research Institute Department of Geophysics and Helmholtz Centre Potsdam, GFZ German Research Centre for Geosciences simultaneously.

Starting from the online data transmission date, SCREAM seismic monitoring software application on Windows has been started to be used. It has been designed and manufactured by GURALP Systems and have been used for real-time acquisition and monitoring of the PIRES data. Then, recording, monitoring and transmitting data streams in GCF have been done in real-time. Data have been received using combinations of both User Datagram Protocol/Internet Protocol (UDP/IP) and Transmission Control Protocol/Internet Protocol (TCP/IP) file transfer protocols. UDP/IP does not give any guarantee of successful data deliver or receive. Therefore, it is not a very reliable service in that sense. On the other hand, basically UDP/IP has been used, because aim was receiving packets on time instead of waiting for the delayed packets. For the recovery of missing data, TCP/IP application has been used. When a block of data with a gap is received, it connects to the server over TCP/IP. In TCP/IP, transmission of every block is guaranteed and error check of delivery of a stream is performed. Digitizers could be configured and instruments could be controlled either over the network or on the field. Also, data streams' status, positions of the masses and GPS timing of every instrument could be monitored via network (Scream 4.5 Manual).

Table B2. Raw data collected with respect to year.

YEAR	RAW DATA COMPRESSED (GB)
2006	OFFLINE: 52.9 GB
2007	OFFLINE: 200.4 GB
2008	OFFLINE: 266 GB
2009	OFFLINE: 261.6 GB
2010	OFFLINE: 259.1 GB
2011	OFFLINE: 524.7 GB
2012	OFFLINE: 552.8 GB ONLINE: 348.2 GB+OFFLINE: 271.4 GB
2013	ONLINE: 539.0 GB+OFFLINE: 267.4 GB
2014	ONLINE: 359.9 GB+OFFLINE: 207.3 GB
2015 (FIRST 6 MONTHS)	ONLINE: 140.9 GB+OFFLINE: 086.2 GB
TOTAL AMOUNT of DATA	**4338.8 GB**

In conclusion, starting from 2006, PIRES has passed from various cycles. Table B2 provides insight in terms of the data stored. Table B2 indicates the amount of raw and compressed online and offline data collected with respect to year in terms of GB. According to the Table B2, amount of the data collected has increased considerably by the years both with the installation of new stations and increasing the sampling rate from 200 Hz to 500 Hz, (Table B2).

APPENDIX C: DATA FORMAT AND PRE-PROCESSING

In appendix C, titles basically mentioned are; different data formats used at the PIRES Arrays and network stations, how they have been uniformed and pre-processing procedures applied before the data have been made ready.

PIRES Arrays are two small aperture seismic arrays and distances between the stations are less than 150 m. In order to do a very sensitive study in terms of local earthquake location and array processing, one needs to have very precise latitude, longitude and elevation of the seismic stations. Because of this reason, synchronization of the Global Positioning System (GPS), providing location and time information of all of the instruments at the PIRES Arrays and network, work in continuous mode rather than cycled mode. All of the PIRES instruments' GPS work according to map datum WGS84. It is a World Geodetic System (WGS) standard for reference surface (datum) and reference coordinate system used by the GPS. Therefore, there was no need to make any conversion at the station coordinates between the different map datums that have been provided by the different type of the instruments.

Using one year long log files of the PIRES stations, containing seasonal and day/night variations of the location information, Figure C1, median values of the stations coordinates have been calculated. Then, these more accurate latitude, longitude and elevation information have been used during earthquake location and FK analysis, etc. Median has been preferred instead of mean during all of the calculations.

Median is calculated arranging all of the values from lowest to highest and then picking the middle one. When most of the numbers composing the data are either towards the lower or the higher end or when there is a value that is very different from the others (outlier), because of the measurement errors, etc., median calculation is more accurate. Especially, in a small set of data, the mean (average) value will not be as precise as median value.

Figure C1 shows the number of measurements with respect to latitude (blue), longitude (red) and elevation (black) in one year of Yassıada PIER station. Median values for latitude (blue), longitude (red) and elevation (black) out of 8000 observations are calculated for PIER, (Figure C1). This procedure was applied to all of the PIRES Arrays and network stations. There can be seen fluctuations in location information that might be because of the decrease in the number of satellites, signal strength, etc. in Figure C1. The reason for that is, accuracy of the GPS calculating the position changes from time to time. By calculating the medians of the stations coordinates; latitude, longitude and elevation, more reliable values are aimed to be found. At the end, stations coordinates have also been calculated for different programs; for instance SAC, Earthquake Analysis Software (SEISAN), etc. that use different conventions, i.e. degrees, degrees minutes, etc.
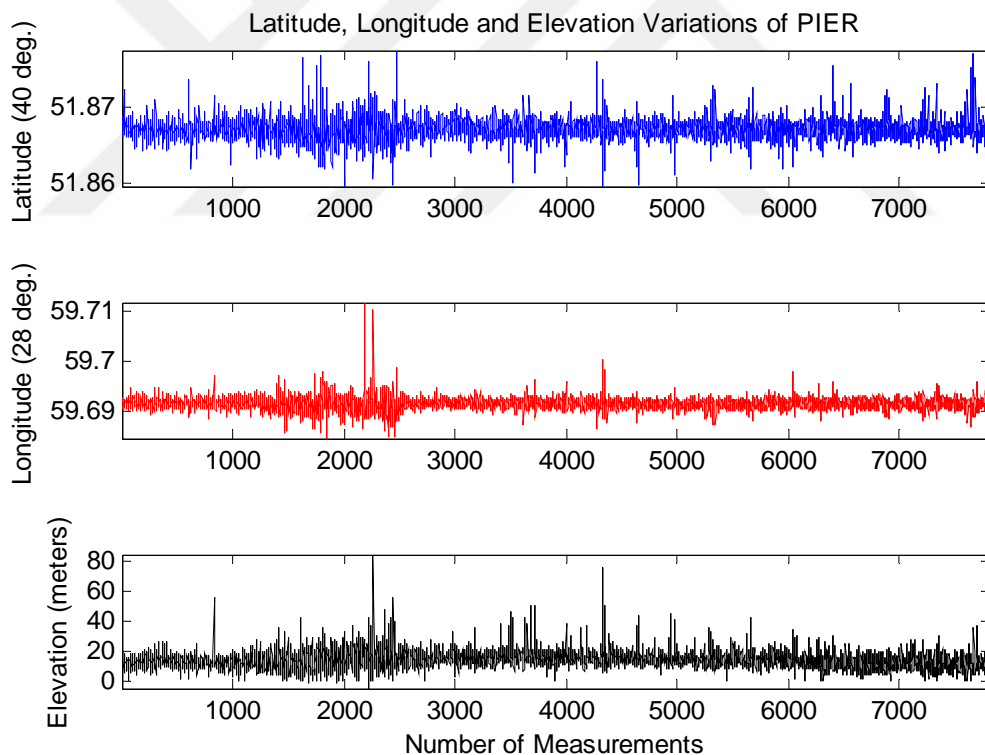

Figure C1. One year of latitude, longitude and elevation variations of Yassıada PIER station.

On the PIRES Arrays stations, there were short period L4C seismometers with EDL recorders. Therefore, data were collected in MiniSEED compressed (Steim-1) format from

these stations. Stations BRGZ on Burgazada and MRTI on Balıkçıada had also the same instrument configurations for a short period of time. At the POWD station on Sivriada, three component broadband STS-2 seismometer and Q330 recorder worked together for a short period of time. Therefore, there was another version of MiniSEED formatted data at the POWD station, which is MiniSEED compressed (Steim-2). Later on, at the PIRES network stations, MRTI, BRGZ and HYBL, short period L4C seismometers were connected to REFTEK recorders. Accordingly, data format on these stations had been in REFTEK Portable Array Seismic Studies of the Continental Lithosphere (PASSCAL) compressed (Steim-2) recording format. When the online data transmission began, data were started to be collected in GCF from all of the PIRES Arrays and network stations. Starting from the beginning of the PIRES Project, data have been collected in continuous mode in all of these different data formats. During the pre-processing of the PIRES raw data, first of all, these different data formats have been converted i.e. MiniSEED, REFTEK and GCF to SAC format. Various data format conversion programs have been used for this purpose to convert data to SAC format.

30 minutes long data were used to be collected from the PIRES Arrays and network stations. However, starting from 2009, one hour long data have been started to be collected from these stations. Therefore, 30 minutes long data that have been collected between 2006 and 2009 have been merged in order to make them one hour. On the other hand, one day long traces from POWD station that had STS-2, have been broken down to one hour. REFTEK formatted data from MRTI, BRGZ and HYBL stations start from the beginning of the data logger (DAS) recording time. These data have been merged in such a way to make them one hour long as well. With the initiation of the online data transmission period, one hour long GCF formatted data have been started to be collected. Offline data that have been collected inside the instruments during the break down of online transmission were one single file for three components. They are also compressed GCF formatted files of one hour long. In order to use such GCF data, files have been first uncompressed for every component using utility of the SCREAM Program. In conclusion, various data lengths have been made one hour long SAC data.

In addition to that, different instruments have different header information in default. In order to provide consistency between different header variables, identical SAC header

variables have been entered in terms of SAC convention. For instance; station name, channel name, component azimuth (degrees, clockwise from north), component incident angle (degrees from vertical), event latitude (degrees, north positive), event longitude (degrees, east positive) and event elevation (meters), etc.

In conclusion, during pre-processing of the PIRES raw data; all of these different data formats, different length of data, different header information, etc. have been made uniform. Different filenames and file directory structures have been also changed to a standard convention.

APPENDIX D: CALCULATING INSTRUMENT RESPONSE

In this section of the Appendix, preparation of instrument response and the PIRES special case in this sense will be discussed in detail. A seismogram is the convolution of the source effect, site effect and instrument effect. Therefore, a seismogram does not represent true ground motion. When the purpose is obtaining true ground motion, like in earthquake source studies, instrument responses have to be removed from the signals. Making a correction for the instrument response means performing deconvolution which is a kind of spectral division process.

The general form of the transfer function, T, in Laplace form (in terms of Laplace variable, s) is Scherbaum (1996);

$$T(s) = \frac{Z(s)}{U(s)} \tag{D1}$$

where, Z is the signal observed and U is the true ground signal. Equation D1 can also be written as in Equation D2;

$$\frac{Z(s)}{U(s)} = G * A * T(s) \tag{D2}$$

where;

$G =$ velocity output sensitivity (gain constant) of instrument
$A =$ normalization constant to make the magnitude of $A * T(s)$ unity
(A is calculated at normalizing frequency value)

$T(s)$ in Equation D1 can be expressed as in Equation D3 in open form, (Scherbaum, 1996).

$$T(s) = \frac{-s^2}{s^2 + 2hw_0 s + w_0^2} \tag{D3}$$

where;

h = damping factor

w_0= frequency

Using Equation D3, poles can be obtained from the roots of the denominator of the polynomial and zeros from the numerator of the polynomial. In short; transfer function is computed using poles, zeros and normalization constant. Normalization constant is used to make the height of the flat part of the modulus of the transfer function unity.

In order to calculate the instrument response, one needs to have information about the sensor and the digitizer which are the two most important components that take part in the calculations. Constants that are related to the sensor are sensor free period, damping and generator constant. Relevant constant for the digitizer is digitizer sensitivity. At the end, all of these values compose the instrument response.

Actually, dealing with instrument response is a bit complicated. Difficulty arises from the fact that, there is not one single standard way of expressing response information. There are various methods in order to represent it and many different conventions can be used. Examples to the different representations of instrument responses can be given as, for instance; Poles and Zeros (PAZ), Discrete Amplitude and Phase Values (FAP), polynomials, filter coefficients, etc. In addition to that, different international waveform formats, i.e. SEED, GSE, etc. also give response information in different ways. Moreover, different processing systems use different instrument response formats. For example; SAC and SEISAN both use GSE format and their own formats. Some data formats include response information with the data such as, SEISAN and GSE whereas SAC does not. In addition to the different instrument response conventions, response can be given in terms of velocity, displacement or acceleration (Havskov and Alguacil, 2006).

In terms of the PIRES stations case, pole zero files have been prepared based on SAC convention. SAC pole zero files are prepared using poles, zeroes and a constant. Values of poles, zeros and constant and comment lines in the SAC files are written in free format. Below shows an example pole zero file representation in SAC. According to SAC

pole zero file format; poles, zeros and normalization constant should be expressed in *radian/second*. Pole zero files are prepared for the case of displacement in SAC and after the removal of the instrument response, output will be displacement in units of *nanometers*.

ZEROS 2

0.0   0.0

0.0   0.0

POLES 5

-0.0740   -0.0740

-0.0740   0.0740

-1.0053e+003 0.0

-502.6548   0.0

-1.1310e+003 0.0

CONSTANT 1.0473e+018

Constant is a kind of scaling factor that is used in SAC pole zero files and it is calculated as in Equation D4.

$$Constant = (A) \times (Sensor\ Gain) \times (Digitizer\ Gain) \qquad (D4)$$

Constant value should also be multiplied with (2π) in order to prepare displacement response instead of velocity in SAC.

Under the light of the given information above, instrument response files of the PIRES Arrays and network stations for each of the three components have been prepared. Most of the PIRES Arrays and network stations have worked with natural frequency of 1 Hz short period three component seismometers, entitled as L4C. L4C seismometers are connected to various digitizers at different stations; for instance EDL, REFTEK or DM24. First of all, calculations in terms of the L4C sensor (i.e. obtaining poles, zeros and sensor gain) is handled in order to remove the effect of the instruments. Then, the digitizer gain has been included in terms of the different type of digitizers.

Using Equation D5, poles can be obtained from the roots of the denominator of the polynomial. Polynomial generating the poles of the transfer function is;

$$s^2 + 2hw_0s + w_0^2 \qquad (D5)$$

where;

$$w_0\ (frequency) = 2\pi Fo \qquad (D6)$$

$$h\ (total\ damping) = b_0 + \frac{1.1\ RC}{RC+RL} \qquad (D7)$$

where; b_0 is the open circuit damping, RC is coil resistance, RL is damping resistor in order to generate damping of 0.7. If Fo (natural frequency) and h (total damping) are given, the denominator of the transfer function, therefore the poles of a seismometer in s domain (Laplace variable) will be as in Equation D8. The roots (poles) of the polynomial can be found using the relationship D8.

$$p = \left[1 \quad 2\left(b_0 \quad + \left(\frac{1.1 \times RC}{RC+RL}\right)\right)(2\pi F_0) \quad (2\pi F_0)^2\right] \qquad (D8)$$

Implementing the units of all variables into Equation D8, poles can be got in units of (*radian/second*). 2 poles are obtained from the denominator of the transfer function. Using Equation D3, zeros can be obtained from the roots of the numerator of the polynomial.

When the above calculations are applied, units of poles and zeros will be in omega format, (*radian/second*), which is also the unit used in the pole zero file representation in SAC. After obtaining poles and zeros of a L4C sensor, calculations in terms of sensor gain (amplification constant) of L4C will be discussed next, (Equation D9). Seismometer gain is the second component of the constant value used in SAC, (Equation D9).

$$Amplification\ constant = (EC/2.54)(RL/(RC + RL)) \qquad (D9)$$

EC = Transduction (Electrodynamics constant)

1 inch $= 2.54\ cm$

Inserting the units of constants into Equation D9, finally amplification constant is obtained in units of $Volts/(cm/sec)$.

Using the results of the computations above (poles, zeros and amplification constant), amplitude and phase response plots of one of the PIRES Arrays station, FUTB, at Z component can be obtained as in Figure D1.
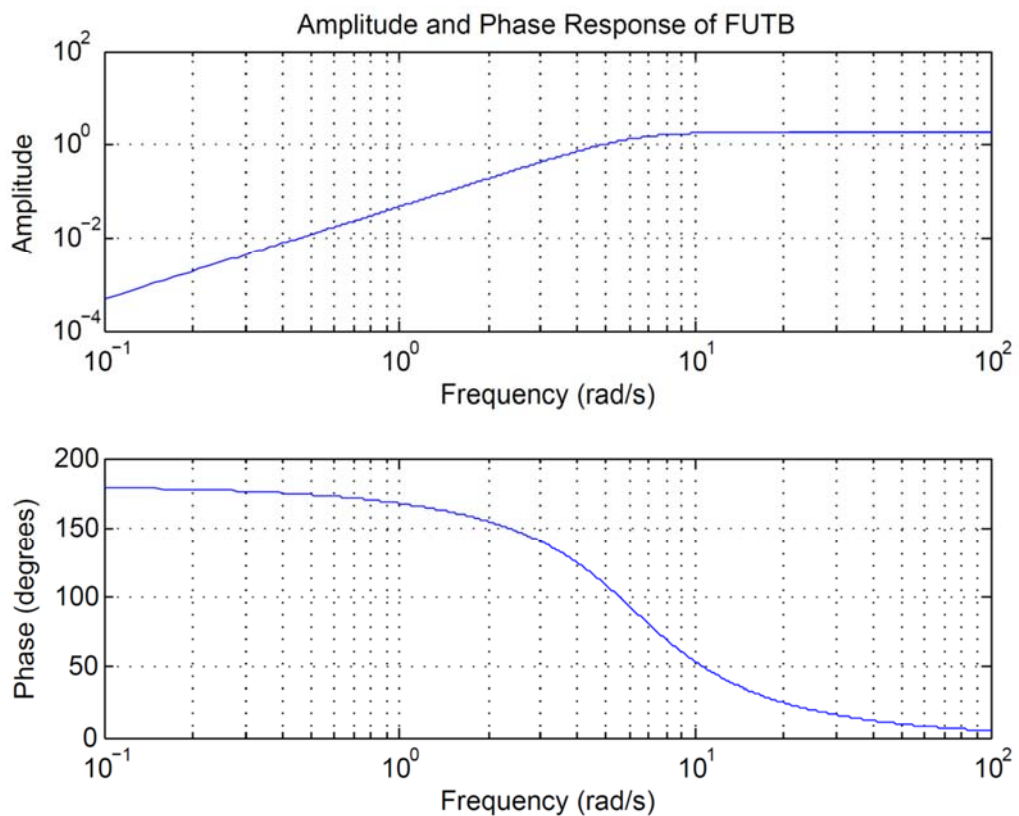

Figure D1. Amplitude and phase responses of one of the PIRES Arrays station, FUTB, at Z component.

Since, instrument response plots, Figure D1, is drawn using poles, zeros and amplification constant, amplitude is higher than 1. According to the amplitude response plot, L4C seismometer passes between ~8 and ~100 (*radian/second*) effectively.

Secondly, calculations in terms of the different combinations of L4C with aforementioned digitizers will be mentioned, EDL, REFTEK and DM24. Digitizer gain will be the last component in order to generate the constant value of SAC, (Equation D4).

In principle; constant in SAC pole zero file is prepared as in Equation D4. Therefore, in order to calculate the value of the constant in SAC, parameters for each sensor and the recorder have to be figured out. Normalization constant, A can be taken as 1 for L4C-3D seismometers. Sensor gain value is equal to the amplification constant (sensitivity of the seismometer) that has been obtained in the previous steps in $Volts/m/sec$. Other important component forming the constant in SAC is related to the digitizer which is the sensitivity of the digitizer. It is a value that converts $Volts$ to $counts$. Therefore, digitizer gain of the recorder is in $Counts/Volts$.

PIRES seismic network stations: KNAL, BASD and KRGZ, have 6TD 30 second period semi broadband seismometers. They are three component force balance digital seismometers with built-in digitizers. When working with GURALP seismometers or combinations of GURALP seismometers and GURALP digitizers; it should be kept in mind that GURALP manuals express poles, zeros and A value in units of $Hertz$ (Hz) instead of $radian/second$. On the other hand, SAC pole zero files should be in $radian/second$. In order to remove the instrument response for the case of SAC, if poles and zeros are in (Hz), they should be converted to $omega$ ($radian$).

To convert poles and zeros to $radian/second$, each pole and zero should be multiplied with (2π). If A value is also given in (Hz), it should also be converted to omega ($radian$). To get A in $radian/second$, it should be multiplied by $(2\pi)^{(NP-NZ)}$ where both NP and NZ are the number of poles and zeros.

A is the normalization constant which scales the amplitude of the transfer function to unity. Without the normalization constant, amplitude response of the poles and zeros will not be equal to unity. Therefore, normalizing factor A should also be calculated according to this convention.

Using the poles, zeros and amplification constant calculated, amplitude response of one of the PIRES network station, KNAL at Z component on Kınalıada, is drawn as in Figure D2. There is a semi broadband of 30 seconds period 6TD at KNAL.
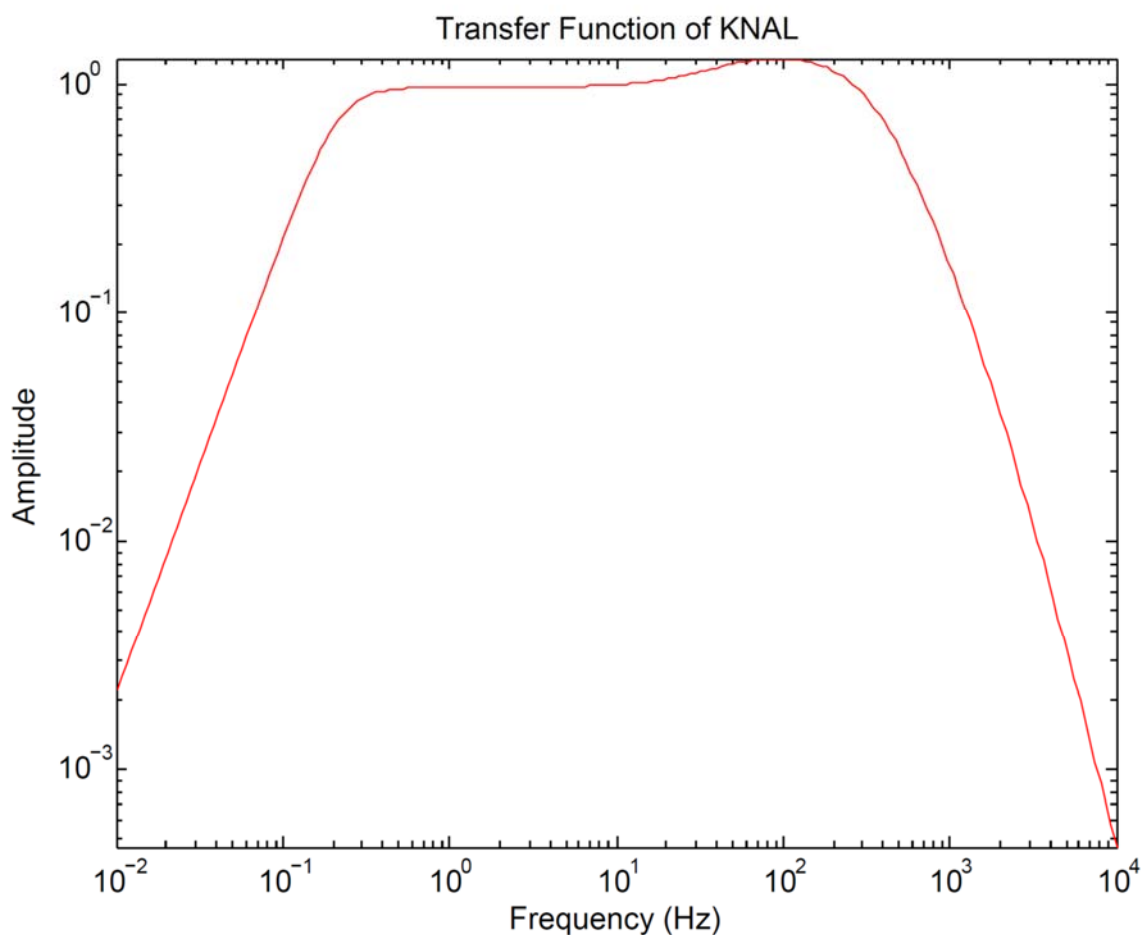

Figure D2. Amplitude response of one of the PIRES semi broadband station KNAL at Z component on Kınalıada.

Note that, between ~0.3 and ~100 Hz, amplitude of the transfer function is 1. On the other hand, outside these frequencies, amplitude decreases.

When the data transmission has become online, MRTI and stations in the middle of the PIRES Arrays (FUTB and POWD) are equipped with three component broadband 3ESPCDE seismometers. These instruments are 60 second period broadband

seismometers. The 3ESPCDE is the combination of CMG-3ESP weak motion instrument, an integrated 24-bit built-in CMG-DM24 digitizer and a CMG-EAM.

Also, in case of 3ESPCDE since poles, zeros and the normalizing factor A are given in units of *Hertz*, in order to convert *Hertz* to *radian/second* each pole, zero and A should be multiplied with (2π).

When calculating the velocity response of the seismometer, attention should be paid whether to multiply it with 2 or not. This depends on the type of the connection between the seismometer and the digitizer. When the GURALP digitizers are mounted on the top of the sensor, velocity response is not multiplied with 2, but when the seismometer have a separate stand-alone digitizer, velocity response has to be multiplied with 2. Therefore, velocity response must be multiplied with 2 when the sensor outputs are differential.

Figure D3, shows the transfer function of 3ESPCDE at FUTB station and Z component on Yassıada. At the plot, the flat part of the amplitude response (plateau) is equal to 1.
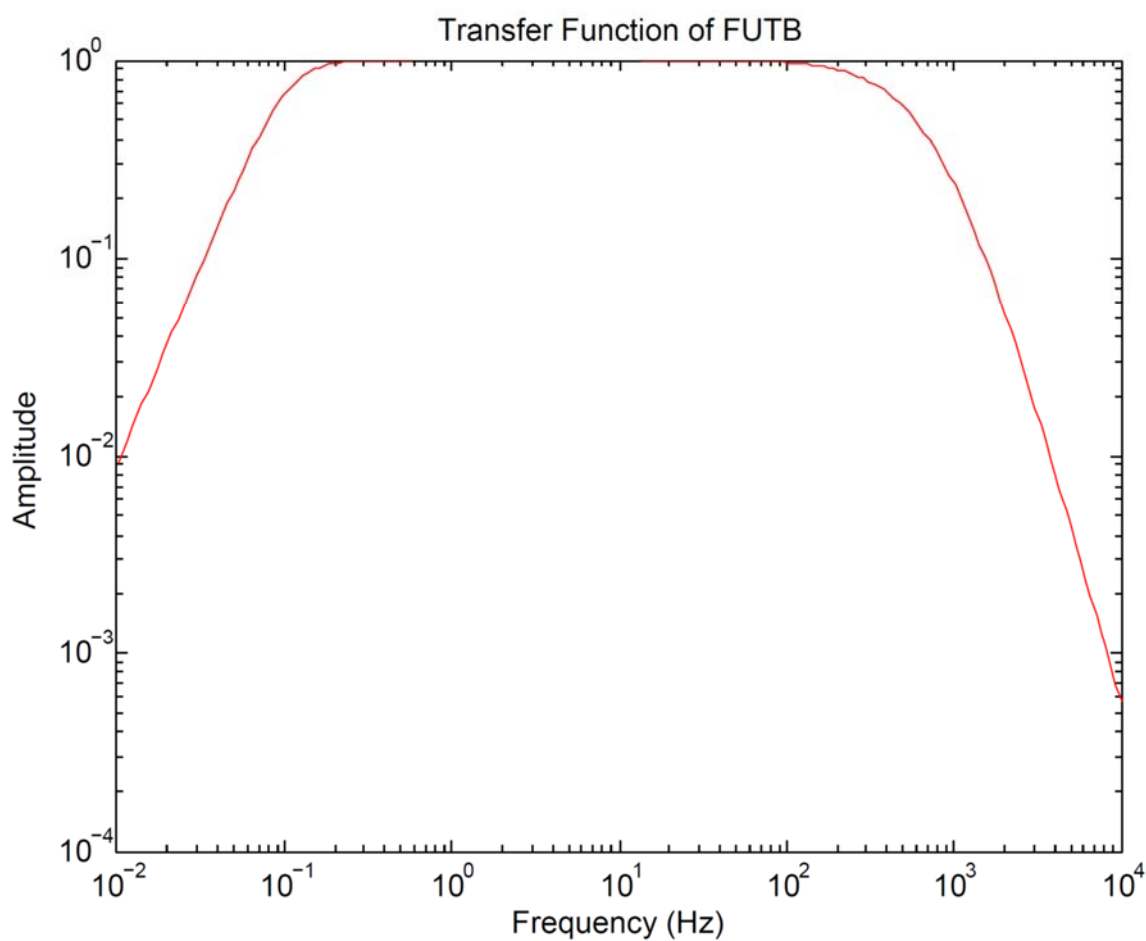
Figure D3. Amplitude response of one of the PIRES broadband station, FUTB, at Z component on Yassıada.

According to the amplitude response plot of 3ESPCDE, seismometer can measure between 0.2 and 100 Hz effectively. Also, amplitude of the transfer function is 1 in this frequency range. On the other hand, outside these frequency values, amplitude decreases.

APPENDIX E: ANALYSIS OF THE POSSIBLE SOURCE FOR THE HIGH FREQUENCY SPURIOU SPECTRAL PEAKS

A close inspection of spectral analysis of the raw data showed a particular behavior that has been studied in more detail in this section. A peculiar narrow peak has been observed located at around 80 Hz in the majority of the estimates. The exact location of the peak shows slight variations between ~70-90 Hz for different PIRES Arrays stations.

Since, it is very important to obtain reliable spectra especially at high frequencies for small magnitude earthquakes it has been found critical to analyze such noise sources in detail. During spectral application of model fitting to the observed source spectrum, the spurious narrow peak becomes dominant and forces the theoretical model to fit that peak artificially. Even when using EGF, where spectral division is performed between the ME and aftershocks and/or foreshocks recorded at each station, the perturbing effect is still present. Furthermore, in this situation since a spectral division is involved, the presence of a spurious peak in the divisor makes the outcome worst. Because; this time, spectral ratio includes uncertainties as a function of the uncertainties of the spectra of the ME and SE. Therefore, at the end of the spectral division, the relative uncertainties in the spectral ratio are larger than both the ME and SE spectrum (Prieto *et al.,* 2013). According to Prieto *et al.* (2013), facing such a phenomenon might be due to the instability of the deconvolution process or dividing the two noisy spectra. Eventually; it has been concluded that, the best way to eliminate the perturbing effect of the peak is to know better the source where it originates so that more appropriate tools can be developed to get rid of it.

From this point of view, in order to understand the general character of the peak, whether it is additive or multiplicative noise and to be sure about the physical source where it is generated, several tests have been made. If it is an additive noise then, it is simply added to the signal. Whereas, the term multiplicative refers to the noise that is convolved (multiplied) with the signal. Additive noise does not depend on the power (strength) of the signal. This means; whatever the signal's power, noise is directly added as it is, without any change. On the other hand, multiplicative noise depends on the power of the signal. Therefore, noise increases with respect to the signal's power. Different types of noise

characters, additive or multiplicative, also induce necessity of different methods for the removal of undesirable noise from the signal. As one might think, it is harder to remove multiplicative noise than the additive. Although, additive noise can be simply subtracted from the signal, eliminating noise with multiplicative character needs more sophisticated methods.

In this manner; first of all, different type of digitizers and seismometers have been compared for the same earthquake at the same component of the different stations. During the tests, it has been tried to verify whether these instruments produce similar peak or not. The instrument responses have not been removed during all of the tests that will be explained in this section. On the other hand, in order to compare the amplitudes of the different type of the instruments more reliably, waveforms have been multiplied with constants. Constants have been calculated by the multiplication of the gain values of the seismometers and digitizers for each station and component. Finally, velocity seismograms that are in units of counts have become velocity in units of meter/second after the multiplication. More detailed information about calculating the instrument response has been given in Appendix D.

80 Hz noise peaks have been encountered during the spectral analysis of the raw data. Therefore; in order to study them in detail, spectra of the earthquakes have been produced using FFT Algorithm for the waveforms including pre-event noise, P and S waves and their codas in order to find the frequency components of the signals in the frequency domain. Before the calculations of the FFTs, waveforms are multiplied with cosine tapered Tukey Window (ratio of taper: %10) in order to minimize the effect of the Gibbs phenomenon. Filtering has not been applied prior the FFTs. On the other hand, mean has been removed before the FFT processing. There was no need for the removal of trend for the waveforms that have been used. MATLAB programming language is used throughout all of the computations in this section.

Firstly, different types of digitizers have been compared. Figure E1, shows comparison of spectra for two different digitizers that were used throughout the array, namely EDL and DM24. The EW components of the waveforms for the event 20121019 (Ml=3.8, back azimuth of 302.4^0 and distance of 33.6 km to Sivriada) are shown at

Yassıada FUTB station which uses EDL digitizer and at Sivriada EASY station which uses GURALP digitizer. Both of the digital recorders have a dynamic range of 24-bit resolution. EDL and GURALP digitizers are connected to 1 Hz L4C short period three component seismometers. Data at the two stations have a sampling rate of 500 Hz. Total length of the waveforms used at both of the stations are ~16 second including 4 second of pre-event noise. S-P time of this event is ~4.4 second. Waveforms (blue) and their corresponding FFT spectra (red) in logarithmic scale, frequency (Hz) versus amplitude (meter), are plotted one under the other, (Figure E1). FFTs are calculated for the whole waveforms including pre-event noise, P and S phases and their codas. Even when using different digitizers, the same sharp narrow peak at around 80 Hz both with the EDL and GURALP digitizers are observed shown with red arrows, (Figure E1). This result rules out the possibility of electro-mechanical noise generation related to any particular digitizer such as hard disk operation or other.
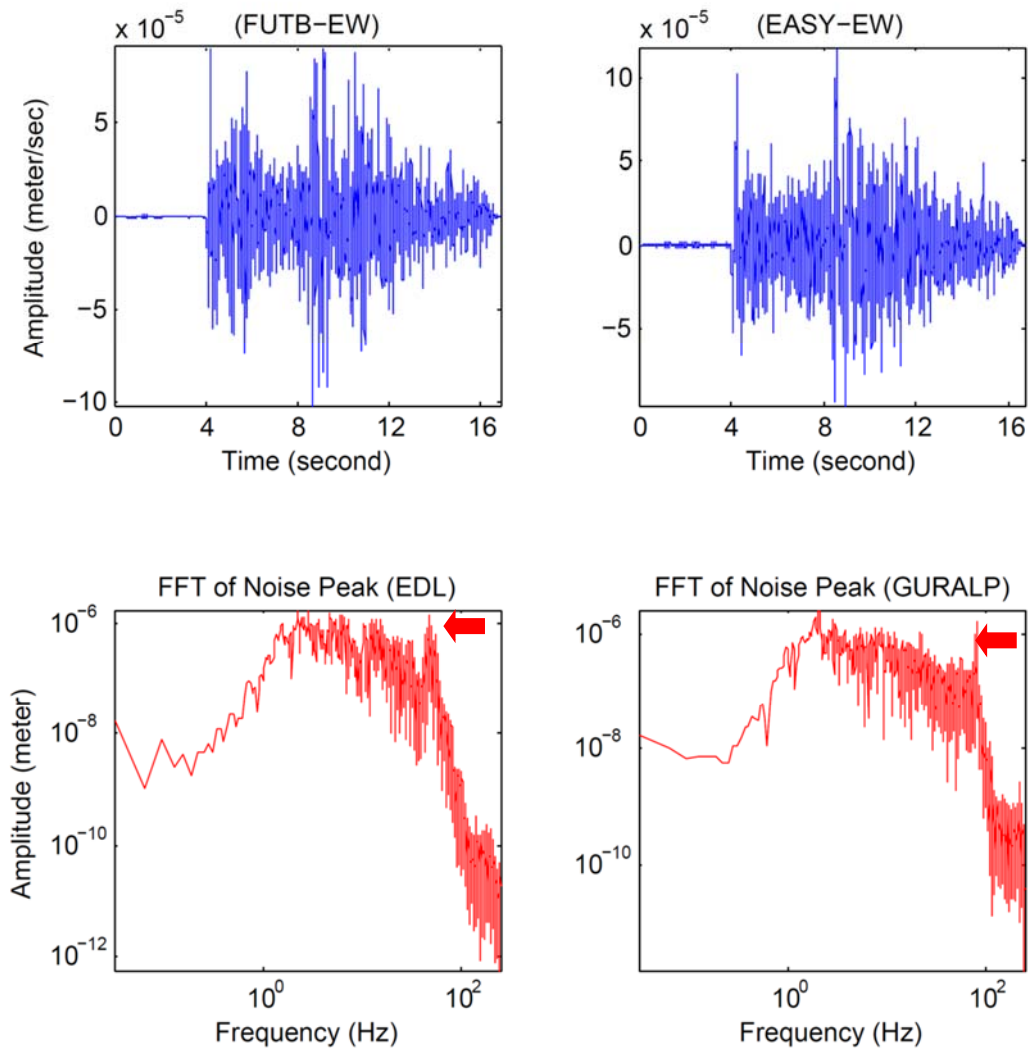
Figure E1. Waveforms of the event 20121019 at FUTB station and EW component with EDL digitizer and at EASY station and EW component with GURALP digitizer and their corresponding FFT spectra. Red arrows show noise peak at 80 Hz.

Secondly; different type of seismometers have been compared, GURALP CMG-3ESPC (3ESPC) and L4C. Figure E2 shows comparison of the spectra of two different seismometers, GURALP and L4C, for the event 20121019 (Ml=3.8, back azimuth of 302.4^0, distance of 33.6 km to Sivriada) at Yassıada FUTB station with GURALP seismometer and at Sivriada EASY station with L4C seismometer for the EW components. Seismometers at both of the stations are connected to DM24 digitizers. Since, the digitizers are same at both stations, different type of seismometers can be reliably compared. This

situation was vise-versa in the previous test. Sampling rates of the data at FUTB and EASY stations are 500 Hz. Pre-event noise window lengths used are 4 second before the P phases. FFTs are calculated for the total of ~16 second of waveforms including pre-event noise, P and S phases with ~4.4 S-P time and their codas. Waveforms (blue) and their corresponding FFT spectra (red) in logarithmic scale, frequency (Hz) versus amplitude (meter), are plotted together, (Figure E2). GURALP is a three component broadband seismometer of 60 second with nonlinear electronic feedback but L4C is a short period three component electro-mechanical system seismometer of 1 Hz natural frequency. Therefore, L4C has a simple moving coil and a suspended mass. On the contrary, GURALP has a more complex circuitry. By chance for a short period, two stations were next to each other at some of the PIRES Arrays stations, POWD and FUTB, with two different instrumentations. Because of this reason, these stations have the same station names, FUTB, in this and the previous examples.
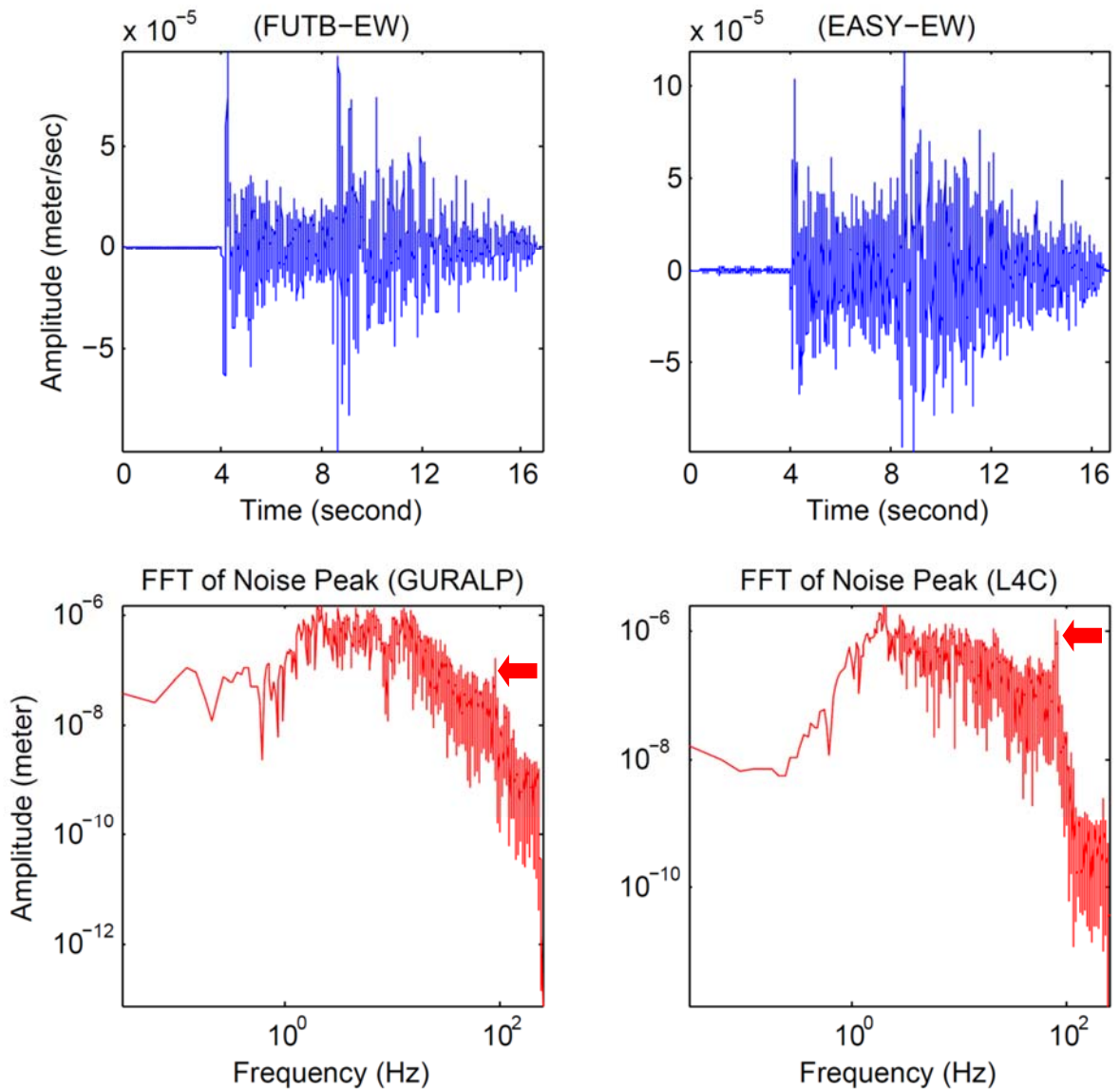
Figure E2. Waveforms of the event 20121019 at FUTB station and EW component with GURALP seismometer and at EASY station and EW component with L4C seismometer and their corresponding FFT spectra. Red arrows show noise peak at 80 Hz.

From the comparison of waveform spectra recorded at two different seismometers, again, the aforementioned sharp narrow peaks (shown with red arrows in Figure E2) are observed at around 80 Hz both with GURALP and L4C seismometers. Note however that the shape of the peaks are not similar, giving a more narrow one on the broadband sensor. Also, at low frequency, broadband seismometer (GURALP) and short period seismometer

(L4C) have quite different spectra. On the other hand, in Figure E1, spectra resemble each other, where two spectra have been compared recorded with the same type of seismometers (1Hz L4C) but different digitizers. It is also worth noting that, only the amplitudes of the waveforms are corrected in this and previous example. In conclusion, it is clear from the above two tests that neither the digitizers nor the seismometers produce this narrow peak at ~80 Hz since the noise exits in any case. Other electrical and electronic equipment used at the stations, such as converter between solar panel and battery, low voltage disconnect, etc. are also same. Therefore, they cannot be held responsible. Also; power line frequency, the frequency of the oscillation of Alternating Current (AC), is 50 Hz which is far below 80 Hz. Although; overtones are observed during the contamination of power line frequency, electrical or electronic noise, they are not multiplicative noises. Accordingly, the amplitude of noise does not increase with respect to the increase in signal power. Therefore; if it is possible to differentiate the character of 80 Hz noise peak in this sense, abovementioned noise sources will also be eliminated.

At first glance, results of these first observations direct to suspect the concrete boxes that are the only common features at these different sites. Therefore, succeeding experiments will be based on understanding the effect of the PIRES housing structures on the occurrence of 80 Hz noise peak. In order to examine the existence of noise and its behavior in more detail, spectrogram plots have been produced that show the time variations of the spectrum of frequencies (i.e. spectrogram) while the pre-event noise, seismic waves (P and S) and coda hit the station. Spectrogram is the 3D time-frequency (time versus frequency versus amplitude) representation of a signal. It gives information about how the frequency spectrum changes over time. In Figures E3 and E4, both the FFT spectra and spectrograms of the earthquakes for the whole waveform have been produced including the pre-event noise, P wave window, S wave window and P and S wave codas. Waveforms have been multiplied with %10 cosine tapered Tukey Window for the elimination of the effect of the Gibbs phenomenon. Filtering has not been applied prior both the FFTs and spectrograms. On the other hand, mean has been removed both before the FFT and spectrogram processing. Since, any trend has not been observed there was no need for the removal of trend from the waveforms.

In the spectrogram plots, Figures E3 and E4, horizontal axes are time, vertical axes are frequency and third dimensions represented by color are the amplitude of a particular frequency. During the spectrogram calculations, most frequently FFT is used. In the general approach, basically time domain data is split into overlapping smaller segments. Then, FFT of the magnitude of the frequency spectrum of each segment is calculated. On the other hand; instead of the most well-known usage of the spectrogram calculation, PSD estimate of each segment has been created and plotted in the figures. PSD simply corresponds to calculating the square of the FFT of each segment of the signal. Therefore; with the application of PSD, distribution of the power (energy) is obtained with the spectrograms. The length of the input signal used to calculate the FFT is 6001 samples of data. Then, data is divided into smaller segments. Each segment overlaps with the neighboring segment over a number of 500 samples. After that, the segments are windowed using a length of 512 points cosine-tapered Tukey Window with a ratio of taper as %10.

With the Figures E3 and E4; now, both the FFT spectra of the seismograms and their corresponding spectrograms recorded at two different stations are compared, EASY on Sivriada and HYBL on Heybeliada at EW components. All of the instrumentations at EASY are installed in a concrete box whereas at HYBL in plain ground. Event 20121019 (Ml=3.8, back azimuth of 302.4^0, distance of 33.6 km to Sivriada) is used for this test. L4C short period (1 Hz) seismometers are connected to DM24 digitizers at both sites. The only difference of these two stations is the place where they are situated. Both stations have sampling rates of 500 Hz and total of ~12 second of data (~8 second before and ~4 second after the S wave arrival) are used for this test. Waveforms (blue), their corresponding FFT spectra (red) in logarithmic scale, frequency (Hz) versus amplitude (meter), are plotted together with spectrograms, (Figures E3 and E4). Waveforms are multiplied with constants obtained by the gain values of the seismometers and digitizers. In Figures E3 and E4, frequency axes of spectrograms are plotted in linear fashion. Upper limits of the y-axes of the spectrograms are plotted up to 250 Hz which are the Nyquist Frequencies of the data used. Both FFTs and spectrograms are calculated for the whole waveforms including pre-event noise, P and S phases and codas. As it can be seen in Figure E3, pre-event noise, P and S waves and coda can be tracked in the spectrogram plot that their arrival times coincide with the seismogram above it. First spectrogram, Figure E3, is from EASY station

where a concrete box was used to protect the instrumentations. At this first spectrogram plot, before the arrival of seismic signal (pre-event noise), there is already a noise peak that is shown with red arrow on the figure. Noise peak's presence during the arrival of pre-event noise can be easily identified with light red color at around 80 Hz, (Figure E3). Its occurrence can be considered because of the oscillation of the box triggered by the environmental noise. As soon as the P wave arrives, noise peak's intensity increases at around 80 Hz. Therefore, light red color becomes darker in the plot. Then, dark red color continues with the arrival of S wave and diminishes with coda. The FFT plot of this whole seismogram, in the middle, also shows a noise peak coinciding with the same frequency value of 80 Hz indicated with red arrow, (Figure E3).
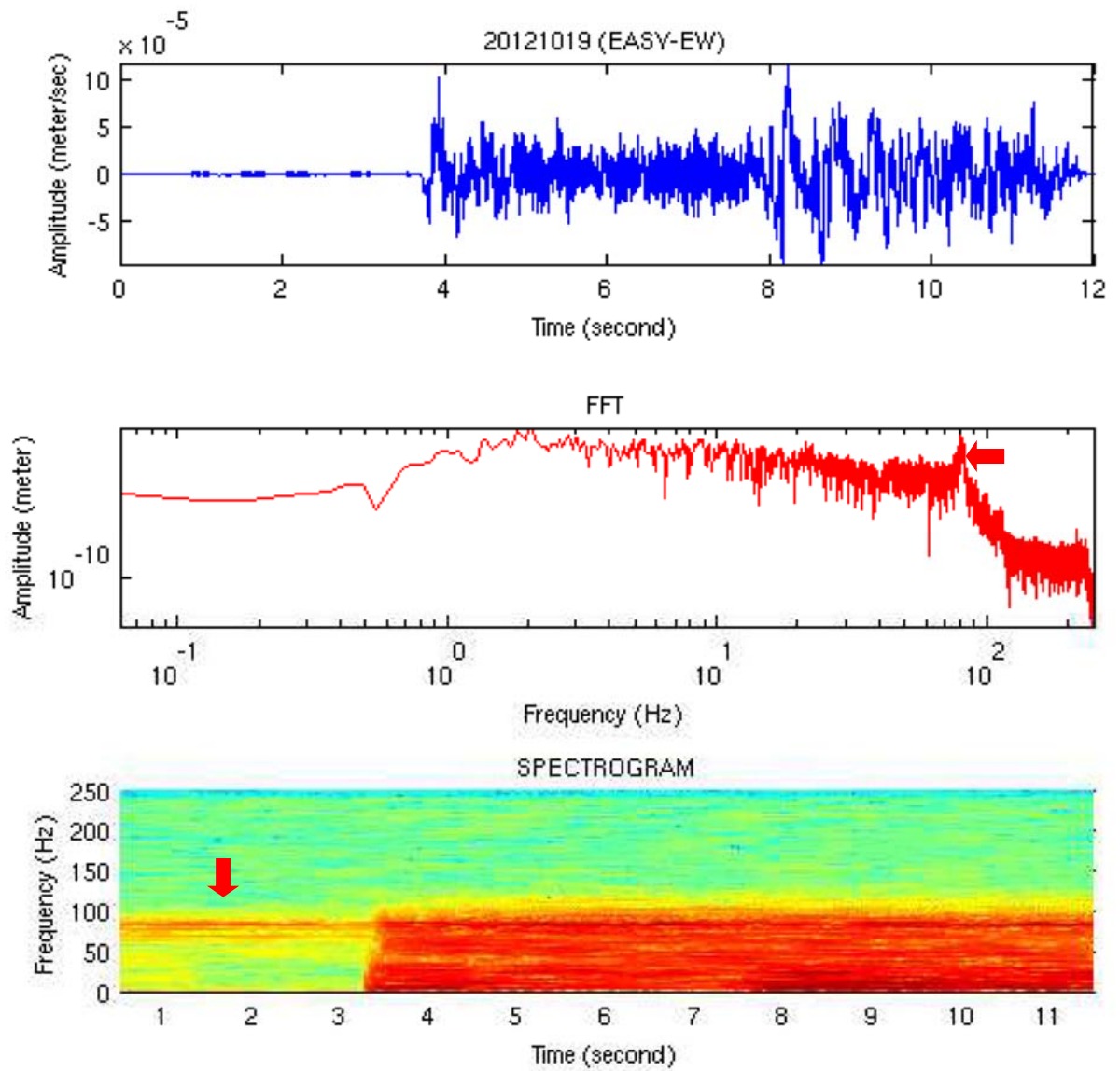
Figure E3. Waveform, FFT spectrum and spectrogram of the event 20121019 at EASY station and EW component. Red arrows show noise peak at 80 Hz.
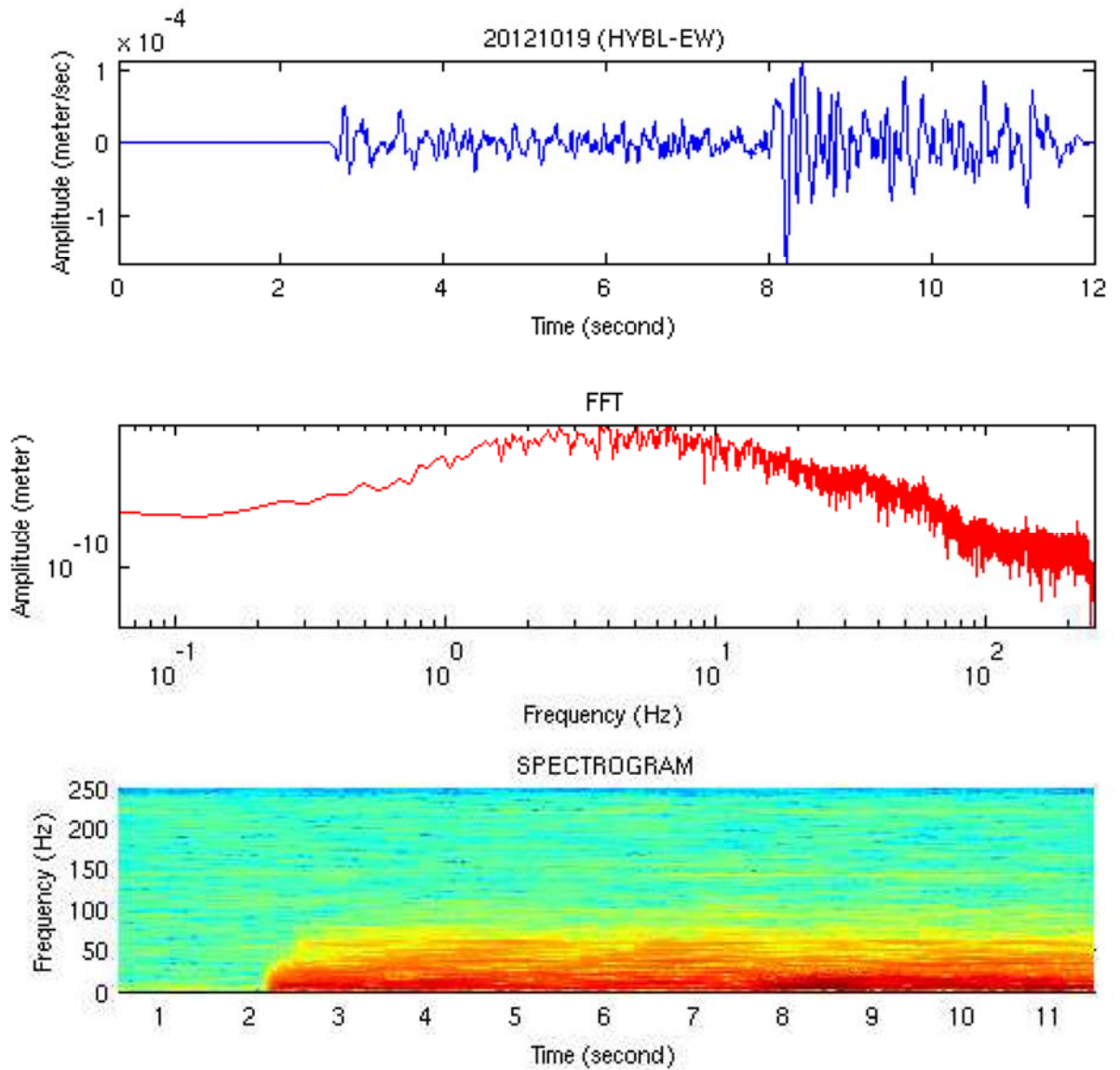
Figure E4. Waveform, FFT spectrum and spectrogram of the event 20121019 at HYBL station and EW component.

Spectrogram in Figure E4 shows the EW component of the same event, 20121019, at HYBL station, where no concrete box structure is used for protecting the instrumentations. There is no sign of any noise peak at around 80 Hz either at the FFT spectrum or at the spectrogram. Moreover, different than the spectrogram in Figure E3, any trace of 80 Hz cannot be tracked during the pre-event noise in Figure E4. Like HYBL on Heybeliada, stations BRGZ on Burgazada and MRTI on Balıkçıada are other two cases where a

concrete box does not exist for the seismometers and no noise peak is observed. Digitizers and other equipment are placed inside the galvanized boxes before they are buried at these stations. All of the instrumentations at KNAL station on Kınalıada and BASD and KRGZ stations on Büyükada are also buried under plain ground. But, since the sampling rates of these stations are only 100 Hz, they do not have sufficient Nyquist Frequency to observe a peak that occurs at around 80 Hz. As a result of the first order observations, it can be concluded that the peak is generated by the box in passive way, in other words by the excitation of the normal mode of the concrete box structure.

Next, it has been looked into the peak frequency near 80 Hz in a more detailed fashion. In this context, to identify the amplitude variations at various frequency components, FFTs of the different portions of the seismograms have been calculated separately. Then, zoomed only into the frequency values at around ~70-90 Hz where the noise peak is observed. Finally, results have been plotted using linear axes, x axis being frequency and y axis being amplitude.

First of all, a test has been made for the case whether the noise is the same for all of the three different components, EW (blue), NS (black) and Z (red), at a single station for the same earthquake. Event 20121019 (Ml=3.8, back azimuth of 302.4^0 and distance of 33.6 km to Sivriada) at Sivriada EASY station has been used. Total of ~10 second of 500 Hz data starting from the S phase arrival is considered. Then, it has been focused at small portions of the FFTs, between 70 and 90 Hz, in order to observe the amplitude variations more clearly. The FFTs are plotted linear x axis being frequency and linear y axis being amplitude. Since, only EASY station has been used for this test, waveform has not been multiplied by the gain values of the seismometer (L4C) and the digitizer (GURALP). Therefore, amplitudes are compared relatively. The result of this test shows that the value of the peak frequency does not differ from one component to other. For instance, the values of the noise peaks at EW, NS and Z components of EASY station are observed at ~81 Hz indicated with red arrows, (Figure E5). This additionally confirms that the peak frequency has a characteristic value for a given earthquake and station for all of its components. Second observation of this test is, amplitudes of the noise peak at the horizontal components (EW and NS) are much higher than the vertical component (Z) for the S phase.
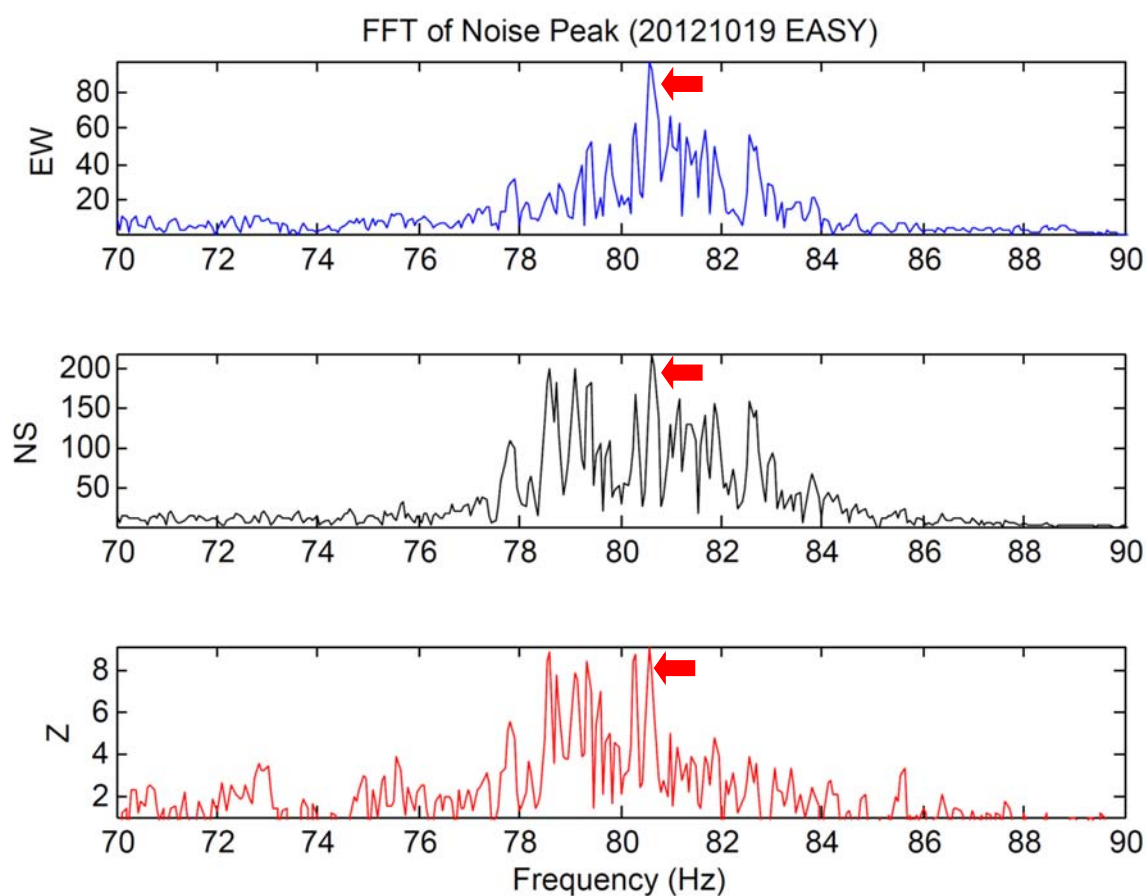
Figure E5. FFTs of noise peaks of the event 20121019 at EW, NS and Z components at
EASY station. Red arrows show the peaks at 80 Hz.

As a continuation of the previous test, it has been tried to understand the behavior of
the peak frequency near 80 Hz in terms of the different phases of seismic signal. For this
purpose, FFTs of the different portions of the seismogram have been calculated. For a
selected earthquake, spectra have been plotted separately for ~4 second of the pre-event
noise (red), ~4 second of the P-wave portion (blue), ~4 second of the S-wave portion
(black) and ~4 second of the coda (green), (Figure E6). At the top of the spectra of the
different phases, whole waveform takes place which of its portions are drawn with the
same corresponding colors of the FFTs. As a result, total of ~16 second of 500 Hz data is
used. All of the FFTs of the different phases are displayed in four rows of the figures in E6.
Amplitude effect has been rounded by not taking small window portions nearby the higher

amplitude P or S phases. Results have been plotted using linear x and y axes, as frequency versus amplitude. Event 20121019 (Ml=3.8, back azimuth of 302.4^0, distance of 33.6 km to Sivriada) is used at EASY station and EW component. S-P time of this event is approximately 4 second. In addition to that, since only EASY station has been used for this test, amplitudes of the waveform have not been multiplied with a constant obtained by the gain values of the seismometer (L4C) and the digitizer (GURALP). Therefore, comparisons of the amplitudes are performed relatively. The FFT results of the different phases are plotted only between 70 and 90 Hz and zoomed only around these frequency values where the noise peak is observed. It can be clearly seen from the Figure E6 that the noise peak is observed exactly at the same frequency value for all of the different portions (pre-event noise, P and S wave and coda) of the waveform which is ~81 Hz and shown with red arrows.
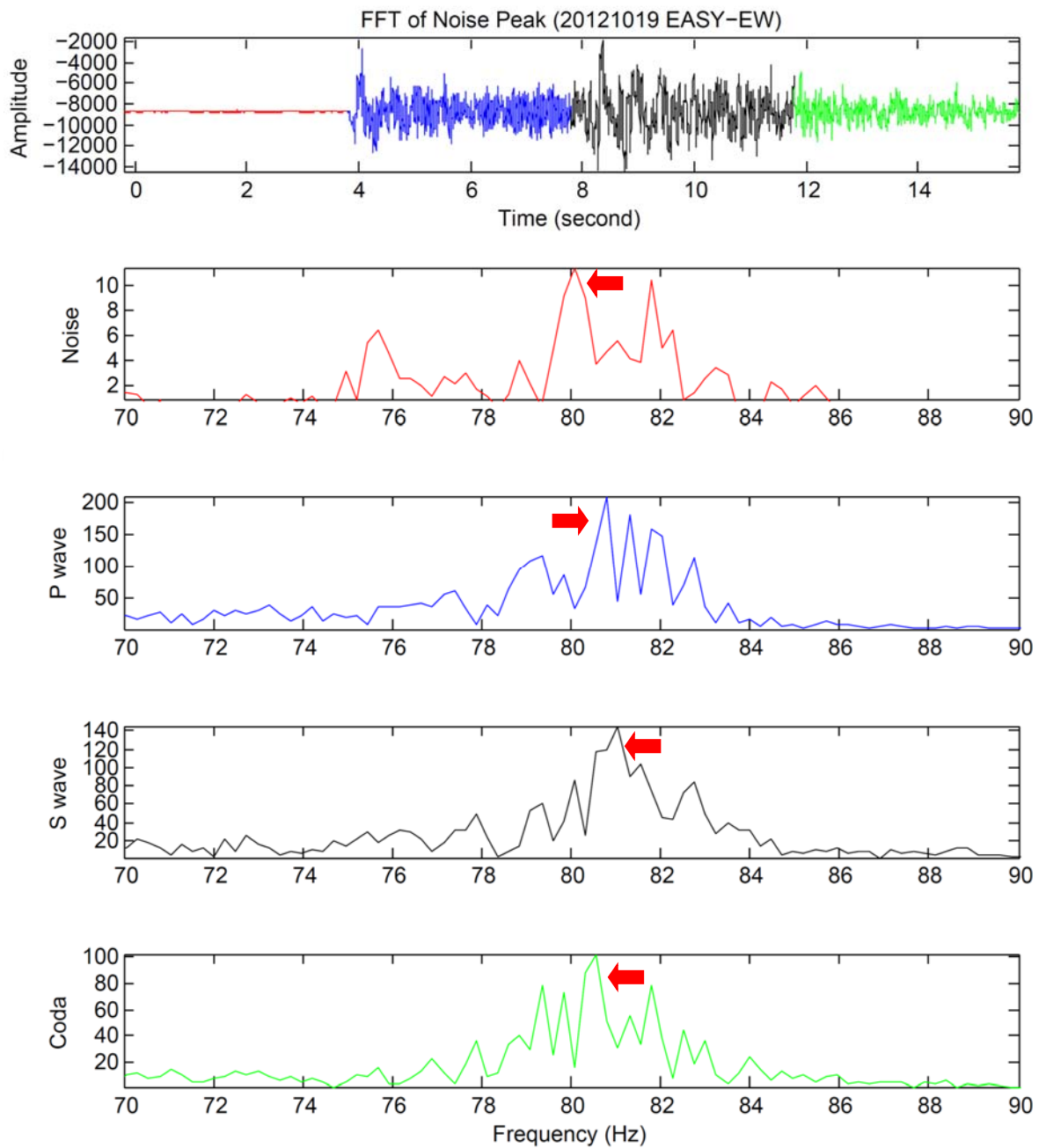
Figure E6. FFTs of the pre-event noise, P and S wave and coda of the event 20121019 at EASY station and EW component and corresponding waveform. Red arrows show the peaks at ~80 Hz.

This observation also proves that peak frequency is a characteristic value for a given earthquake, station and component independent of the phase. Additionally, because of this reason, even before an earthquake, under only environmental noise i.e. wind, boats and microseisms, etc. concrete box oscillates with the same peak frequency value. In this manner, this test is also a verification of the result of the spectrogram where the trace of 80 Hz noise peak could have been tracked on the pre-event noise section. On the other hand, P wave has a higher amplitude than the S wave and amplitude decreases when the S wave impinges. Moreover, P wave has much more higher amplitude than the pre-event noise and coda. When the earthquake signal diminishes, noise level starts to decrease to its initial level. In Figure E6, it is observed that noise peak is affected more with the P wave arrival than the S wave having higher amplitude. In general, P wave has smaller amplitude and higher frequency content. On the other hand, S wave has larger amplitude and lower frequency content. Particles move back and forth in P wave. But, they move up and down in S wave and shake more than the P wave. Since, large window portions have been used nearby the P and S phases including codas, multiples, etc. amplitudes have been rounded in such a way that exactly the opposite result has been obtained. In conclusion, since the noise peak at ~80 Hz is convolved with environmental noise, P and S waves and coda, the amplitudes of the noise peaks increase with the arrival of the seismic waves, i.e. P or S wave and decrease with the pre-event noise and coda. Therefore, the amplitudes of the noise peaks show variations proportional to the strength of the signal or noise. Because of this reason, analysis showed that noise peak has a multiplicative character rather than additive.

Also, a test has been made to investigate whether every station has its own characteristic normal mode frequency value which is independent of the recorded earthquake. For this purpose, peak frequency values of the P and S waves of the two different stations of the same components have been compared for a specific earthquake, (Figure E7). The noise peak is shown for the NS components separately for the P (blue) and the S (black) waves at EASY and SHTH stations that are both on Sivriada. Event used is 20121019 (Ml=3.8, back azimuth of 302.4^0, distance of 33.6 km to Sivriada). 4.4 second (S-P time) after the P and S wave arrivals corresponding total of 8.8 second of data have been used at both stations. Sampling rates are 500 Hz for EASY and SHTH. Only short windows of FFTs between 70 and 100 Hz are presented in Figure E7. Both stations have

L4C short period (1 Hz) seismometers connected to DM24 digitizers. Since, there are same instrumentations (both seismometers and digitizers) at these stations waveforms have not been multiplied by the gain values of the seismometers and the digitizers for this test. Therefore, amplitude comparisons of the FFTs are made relatively. It has been observed that; although same earthquake, same instrumentations and same components are used, the exact frequency value of the noise peak is not the same for the two stations (~79 Hz for EASY and ~92 Hz for SHTH, indicated with red arrows) that are on the same island (Sivriada). This means that every station has a characteristic normal mode value independent of an earthquake. Since, at every PIRES Arrays station, concrete housings are constructed with similar dimensions using similar portions and properties of concrete, etc., peak frequency values of all of the stations should be ideally similar. On the other hand, there are small deviations between the arrays stations and they oscillate at slightly different frequencies. It is also striking that, frequency values of the noise peaks of the P and S waves do not show any variation for each station. In addition to that, noise peak at every station has a characteristic shape. Some stations have broader noise peak shape some have sharper one. For instance, Figure E7 shows the difference of the shapes of the noise peaks at EASY and SHTH stations. Note that; conversely, the noise peaks nearly preserve their forms at the same stations for the P and S phases. But, no test has been done to investigate the mechanism controlling the shape or small differences in peak frequency values at different stations. This might occur because of the ground and box coupling or local ground conditions under stations, etc. Another feature that it is observed is, amplitudes of both the P and S waves at EASY station and at NS component are higher compared to the same component of SHTH. Therefore, this characteristic is immediately seen on the FFT plots. The FFTs of both the P and S waves are higher in amplitude at EASY station than SHTH.
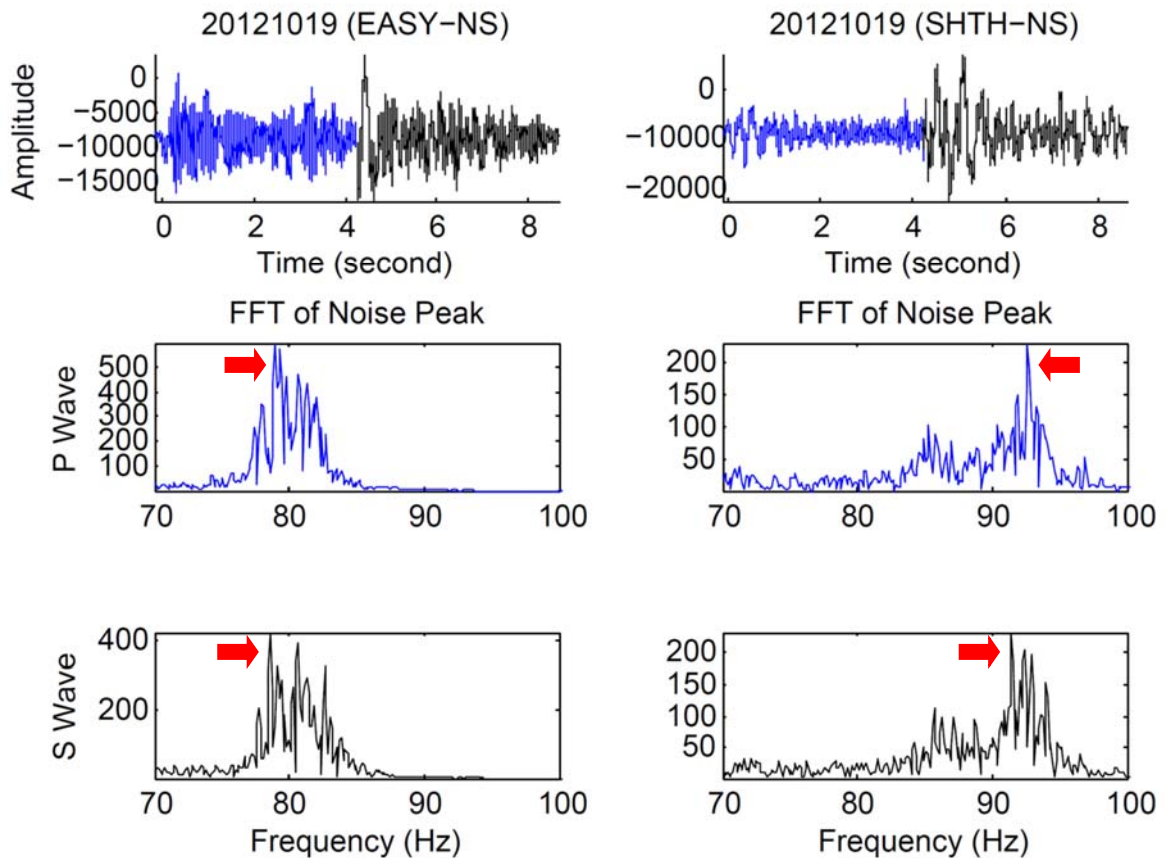
Figure E7. FFTs of noise peaks of the P and S waves of the event 20121019 at EASY and
SHTH stations and at NS components. Red arrows show the noise peaks.

For a given station, oscillation frequency of different earthquakes have also been
compared which have different magnitudes, back azimuths and distances to one of the
island i.e. Sivriada. As a first example of this test, two earthquakes (20130714 Ml=3.1,
back azimuth of 177.3^0, distance of 16.8 km to Sivriada and 20121019 Ml=3.8, back
azimuth of 302.4^0, distance of 33.6 km to Sivriada) have been selected and made a
comparison between the NS components of the same station which is EASY. 4.4 second
(S-P time) after the P (blue) and S (black) wave arrivals have been used corresponding
total of 8.8 second of data for the event 20121019. On the other hand, 2.6 second (S-P
time) after the P (blue) and S (black) wave arrivals have been used corresponding total of
5.2 second of data for 20130714 since it is a smaller magnitude event. Sampling rates of
both of the events are 500 Hz and FFTs only between 70 and 90 Hz are zoomed. Since,
intention is to observe the impact of the different earthquakes at the same station and

components, waveforms have not been multiplied by the gain values of the seismometers and the digitizers for this and the following example. Peak frequency values of the P and S waves are at ~79 Hz (shown with red arrows) both for the events 20121019 and 20130714, (Figure E8). No significant change has been observed at the peak frequency value for a given station and component for different earthquake occurrences that have different magnitudes, back azimuths and distances. Also, peak frequency value does not change for different phases (i.e. P and S).
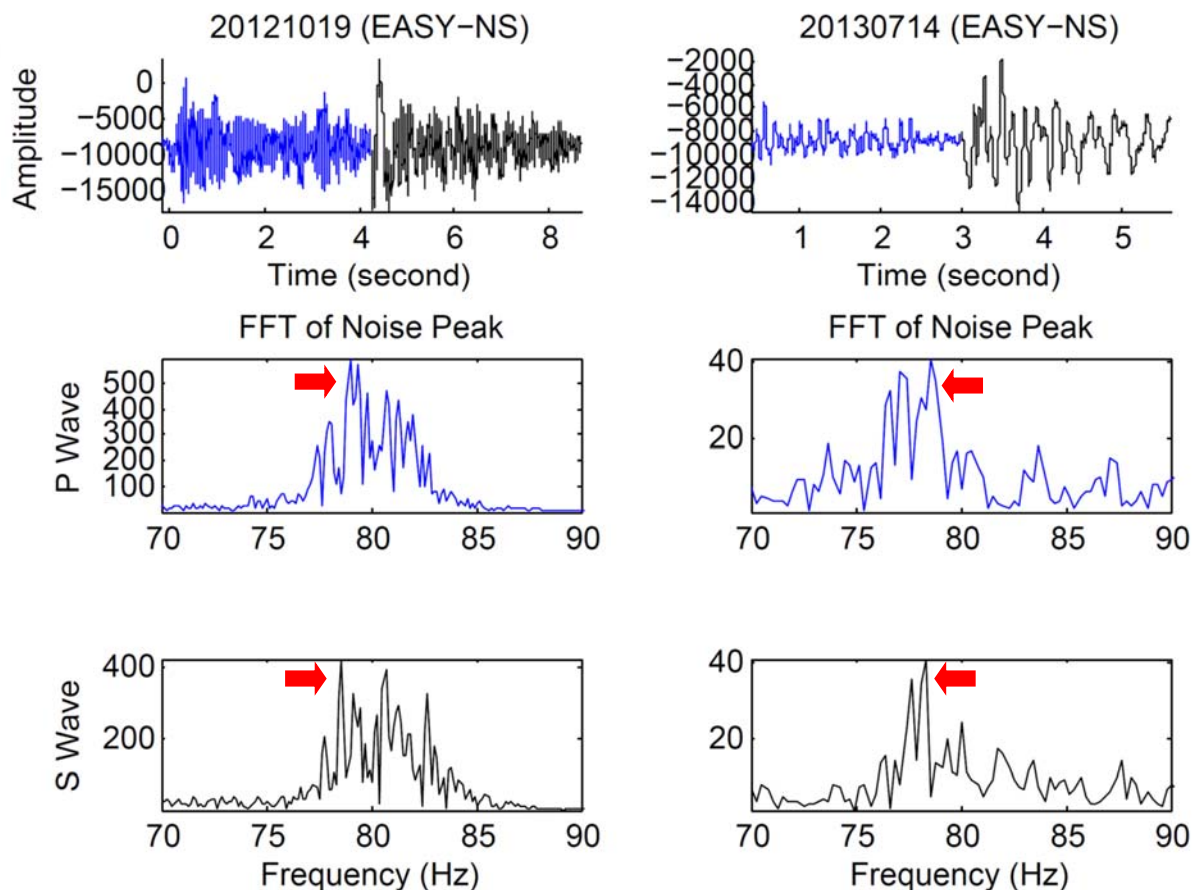

Figure E8. FFTs of noise peaks of the P and S waves for the events 20121019 and 20130714 at EASY station and at NS component. Red arrows show the noise peaks.

As a second example of this test, another comparison has been made taking the same event, 20130714, as a reference and compared it with the event 20130725 at the same station and component. As in the previous test, comparison is made between EASY station

on Sivriada and at NS components. 20130725 is Ml magnitude 2.1 event at the back azimuth of 182.3 degrees and at a distance of 10.4 km to Sivriada. 2.6 second (S-P time) have been used after the P (blue) and S (black) wave arrivals corresponding total of 5.2 second of data for 20130714 and 2.0 second (S-P time) after the P (blue) and S (black) wave arrivals corresponding total of 4.0 second of data for the event 20130725. Sampling rates of both of the events are 500 Hz and FFTs between 70 and 90 Hz are presented. Peak frequency values for the P and S waves are at ~79 Hz (indicated with red arrows) both for the events 20130725 and 20130714, Figure E9, which is exactly the same value with the previous test obtained for the earthquakes with different magnitudes, back azimuths and distances to Sivriada.
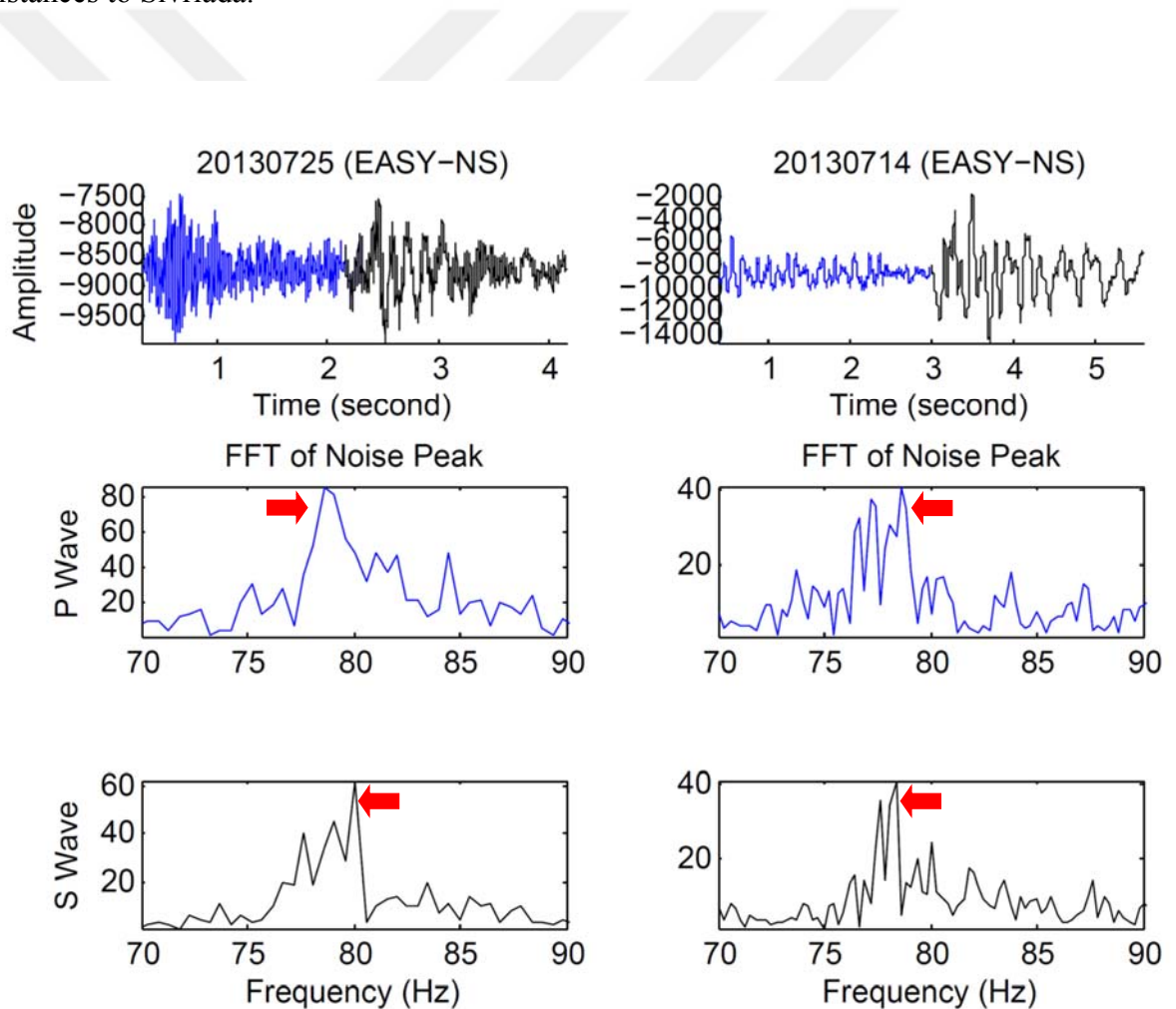

Figure E9. FFTs of noise peaks of the P and S waves for the events 20130725 and 20130714 at EASY station and at NS components. Red arrows show the noise peaks.

It has been also observed from the last test that, peak frequency value does not change for a given station, component and phase for different earthquake occurrences. This also verifies that the noise peak is generated independent of the source and possibly determined by the normal oscillation of the container structure. Normally, every building or construction has a specific peak frequency value depending on its properties such as; its structural system, its construction materials, its contents, its geometric proportions and its height (Arnold, 2006). Therefore, PIRES concrete box structures should also have one specific normal mode frequency value. In addition to this, especially, these last two examples have also verified that the noise peak that has been observed at ~80 Hz has a multiplicative character, since its amplitude increases with the magnitude of the earthquake. For instance, 20130725 is Ml magnitude 2.1 event whereas 20130714 is Ml magnitude 3.1 event and biggest earthquake 20121019 is Ml magnitude 3.8 event. When the P and S wave amplitudes of different magnitude earthquakes are compared, Figures E8 and E9, a direct correlation of an increase in amplitudes of the P and S waves with the magnitudes of earthquakes is observed. Note that, as the earthquake magnitude increases, the amplitude of the noise peak increases. Therefore, concrete box oscillating at higher amplitude with a larger magnitude earthquake is an additional confirmation that 80 Hz narrow noise peak is multiplicative.

Surprisingly, at FUTB (Yassıada) and POWD (Sivriada) stations, where two boxes were next to each other for a short period of time, two noise peaks exist on the spectra at slightly different peak frequency values. For this test, event 20121019 (Ml=3.8, back azimuth of 302.4^0, distance of 33.6 km to Sivriada) at FUTB and POWD stations and at EW components are used. At each station, 4 second before the P wave arrival and corresponding to a total of ~16 second long data are displayed. Sampling rates of the stations are 500 Hz. At both of the stations, DM24 digitizers are connected to 3ESPC 60 second broadband seismometers. Waveforms at both of the stations have been multiplied by the constants obtained by the multiplication of the gain values of the seismometers and the digitizers. Two boxes were next to each other at these locations where they had slightly different dimensions. They are also built from different materials. Therefore, their properties like; rigidity, elasticity modulus, gamma and weight, etc. differ. The one with smaller dimensions, Figure B4, is less rigid and lighter in weight compared to the box in Figure B2 shown in section B. It is probable that, the value of the peak frequency depends

on these properties. Since, the distance between these two boxes is only ~20 cm, the oscillations of both of them have an effect on the other. Therefore, this enables to observe two noise peaks next to each other on the spectra. Locations of the two noise peaks on the spectra (red) of FUTB and POWD stations are indicated with red arrows in Figure E10. Related corresponding waveforms (blue) are also presented at the top of the spectra in the same figure, (Figure E10). Since, the digitizers and seismometers (broadband) are similar type at FUTB and POWD stations, FTTs also look identical. The only difference of these two stations is, POWD is located in a small cave.
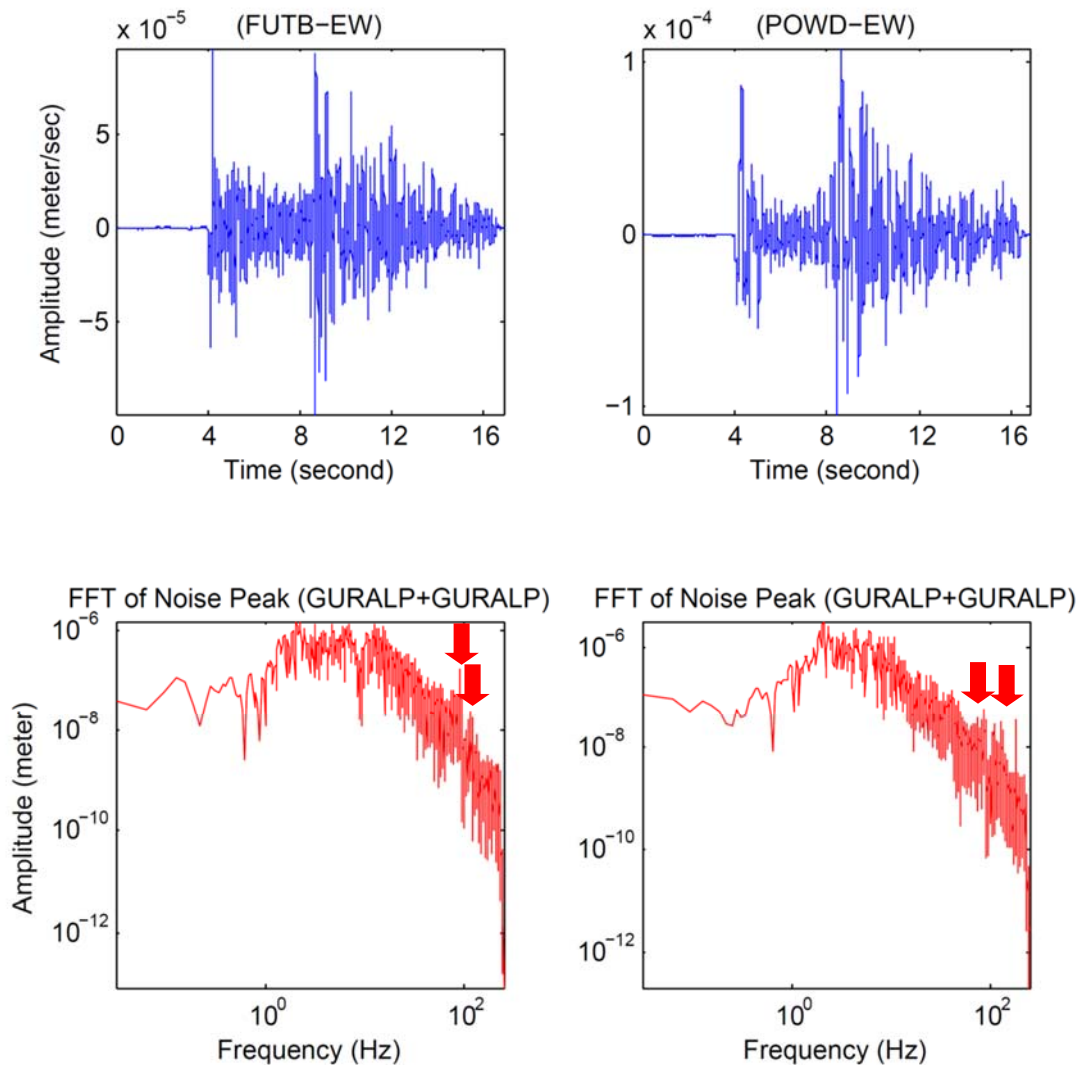

Figure E10. FFTs of noise peaks of the event 20121019 at FUTB and POWD stations and at EW components. Red arrows show the noise peaks.

Since, FFTs have been calculated for long (16 second) portions of waveforms, in order to differentiate the peaks more clearly also it is zoomed into the frequency values at around ~70-95 Hz where two noise peaks are observed next to each other. FFTs of the P (blue) and S (black) phases of the seismograms have been calculated at FUTB and POWD stations and at NS components. Total of ~9 second of data is used for this experiment. Waveforms used are colored in blue and black for the P and S phases in Figure E11, respectively. The results of the FFTs have been plotted linearly x axis being frequency and y axis being amplitude. Waveforms of FUTB and POWD stations have been multiplied by the gain values of the seismometers and the digitizers during zooming into small portion of FFTs in linear fashion. Locations and frequency values of the two noise peaks are indicated with red arrows both for FUTB and POWD stations for the P and S phases in Figure E11. Since, peak frequency values are very near to each other, these frequency values cannot be the multiples that are expected to be produced along with the fundamental modes of the box oscillations. Most probably, two of the noise peaks correspond to the two near distance housing structures at FUTB and POWD stations.
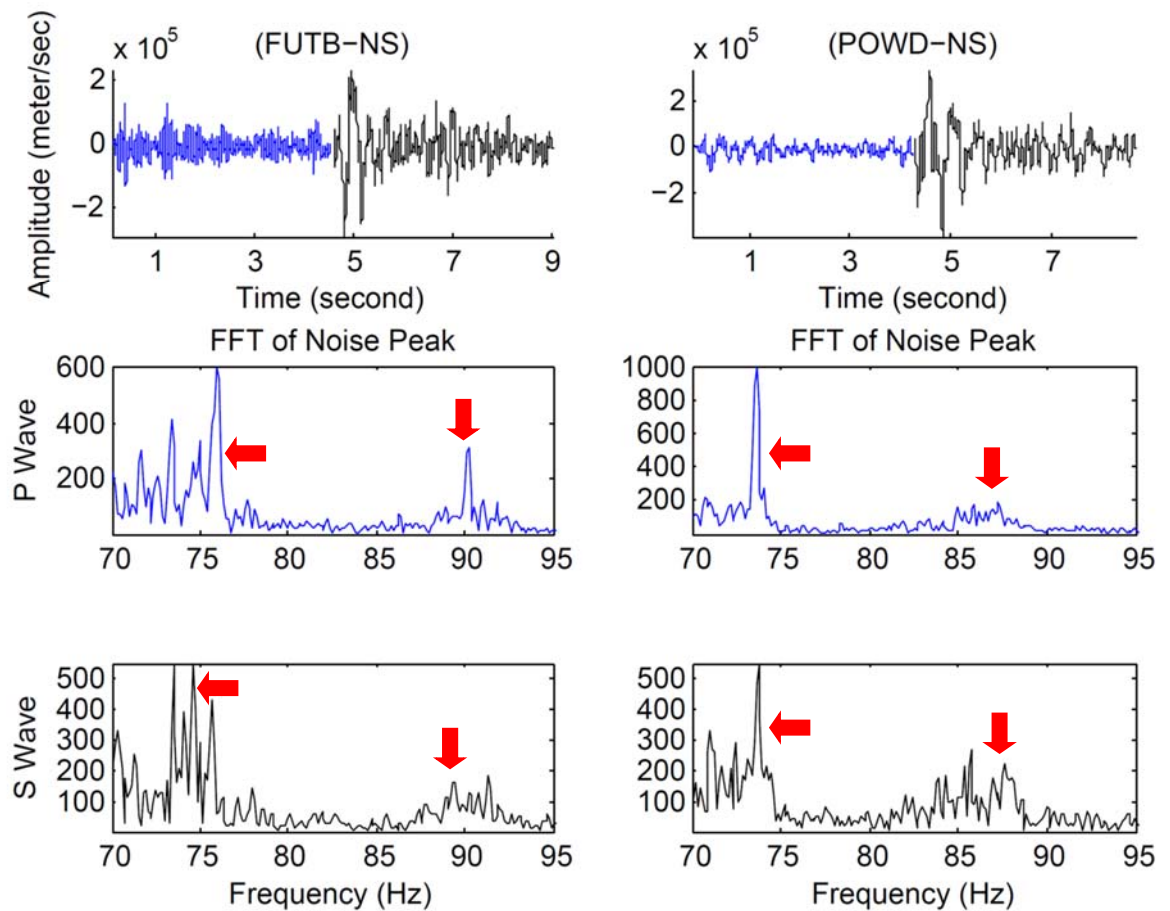
Figure E11. FFTs of noise peaks of the P and S waves for the event 20121019 at FUTB and POWD stations and at NS components. Red arrows show the noise peaks.

The values of the peaks of P and S phases at FUTB station and at NS components are ~75 Hz and ~90 Hz respectively, (Figure E11). On the other hand, peak frequency values of the P and S phases at POWD station and at NS components are ~73 Hz and ~88 Hz respectively, (Figure E11). The values of the noise peak frequencies are marked with red arrows in the figures. Note that, amplitudes of the second peaks decrease at high frequencies because of the decrease of SNR at higher frequencies. This test also confirms the results of the previous tests that have been performed at different stations. Like in the formerly indicated examples, 80 Hz noise peak have been observed at the stations where the instrumentations are placed in concrete housings. Moreover, locations of the noise peak

frequencies do not show much variation between the P and S waves for the same station like in the previous tests.

In addition to the tests that have been done using earthquakes also a ground truth test has been made for crosscheck in order to better understand whether 80 Hz noise peak is created because of concrete structure or not. It has been executed at EASY station by hitting to the walls of the concrete box structure from different directions. The related FFT spectrum has been plotted using an algorithm in SAC, (Figure E12). Seismogram of EASY station and at EW component has been multiplied by the gain values of its seismometer (L4C) and digitizer (GURALP) beforehand. From the figure, it is observed that the oscillation of the box is at exactly 81 Hz, indicated with red arrow, like the tests performed with earthquakes at the same station, EASY, (Figure E12).
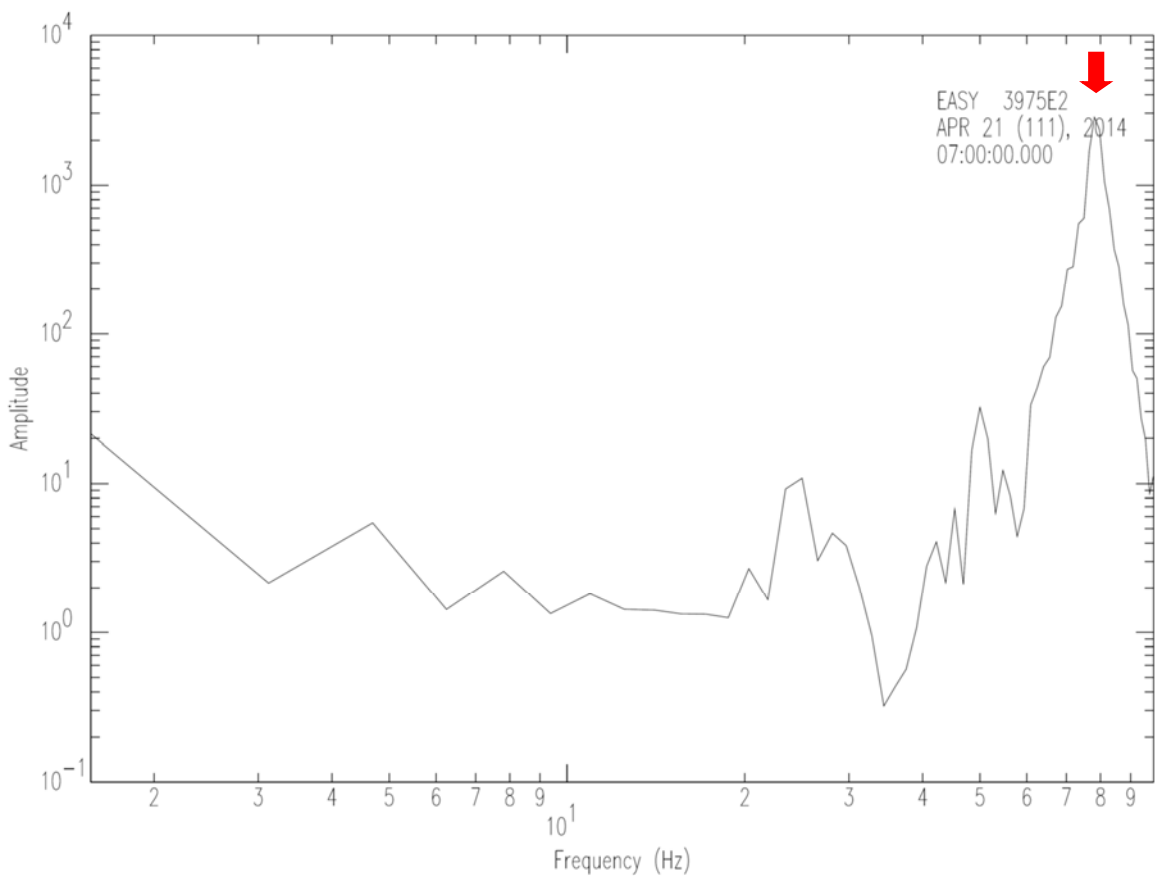

Figure E12. FFT of noise peak at EASY station and EW component. Red arrow show the noise peak at ~80 Hz.

Both the earthquakes and ground truth test have proved clearly that noise peak at ~80 Hz is generated by the normal oscillation of the container. But still, it has been wondered whether travelling of the sound wave inside the empty space or vacuum of the concrete boxes during an earthquake could cause such an effect. The sound has a speed of 343.2 meter per second at 20 °C and under dry air conditions. Therefore, in order to confirm whether vacuum inside the boxes have an effect or not on the production of the noise peak, another ground truth test has been performed at EASY station on Sivriada. This time, in order to prevent the occurrence of vacuum inside the concrete box, it has been filled completely with foam. It is a material used in insulation applications such as; noise insulation, heat insulation, etc. Then, the walls of the concrete box structure have been hit from different directions, i.e. right (blue) and left (red) short sides of the box, front (black) and back (pink) long sides of the box and from the top (green) of the box. Figure E13 shows the FFT results (between 70 and 90 Hz) of hitting from various directions. Only very small portions of time windows (1 second) around the impulses of hitting are used for this experiment. When the figure is examined, it is seen that hitting the box from different directions makes very slight differences on the peak frequency values. Noise peaks are observed at ~80 Hz that are very similar to the results that have been got both with the earthquakes and ground truth test at EASY station. But, there was a very surprising outcome of this test. Right and left short sides of the box have noise peaks at ~79 Hz. Whereas, front and back long sides of the box have noise peaks at ~81 Hz, both shown with red arrows. This might be the indication of longer time spent for traveling at the longer sides of the box. Interestingly, top of the box has noise peak at exactly ~80 Hz which corresponds to the average value of the short and long sides of the concrete box structure. Finally, this experiment points out that 80 Hz noise peak does not occur because of the empty space inside the concrete structure since it has also been witnessed at the box which was completely full.
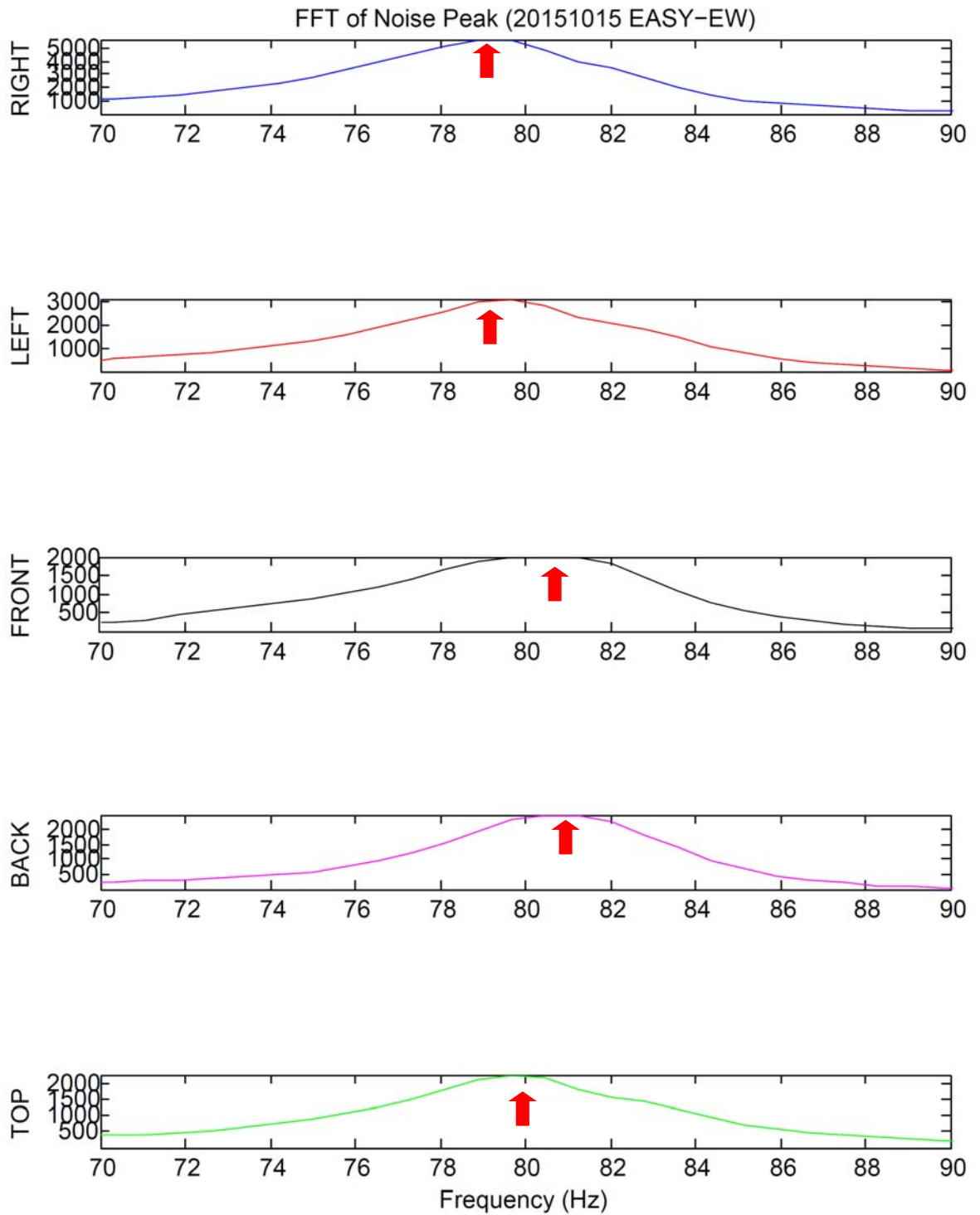
Figure E13. FFTs of noise peaks of different directions of EASY station and at EW component. Concrete box is filled with foam. Red arrows show the noise peaks.

Lastly, it has been tried to determine the values of the natural frequencies of the PIRES boxes from analytical point of view. When the dimensions of a PIRES concrete box has been take into account, (Figure B1), length (lx) of the box is 110 cm, width (ly) of the box is 90 cm, height (lz) of the box is 75 cm and thickness (t) of the walls of the box is 25 cm. Using the values of these dimensions and assuming modulus of elasticity (e) of concrete as 20000 MPa, gamma (m) of concrete as 22 kN/m^3 and gravity of acceleration (g) as 9.81 m/s^2, very crudely the natural frequency of a PIRES concrete box structure has been calculated using the Equation E4.

$lx = 110 \; cm$

$ly = 90 \; cm$

$lz = 75 \; cm$

$t = 25 \; cm$

$e = 20000 \; MPa$

$m = 20 \; kN/m^3$

$g = 9.81 \; m/s^2$

First of all, weight (w) and rigidity (r) are obtained using the Equations E1 and E2. Later on, their values are substituted into the related Equations E3 and E4, respectively to get period (p) and natural frequency (f) of the box.

$$w = ((lx \times ly) - ((lx - 2 \times t) \times (ly - 2 \times t))) \times lz \times m \times 0.000001 \quad (kN) \qquad \text{(E1)}$$

$$r = \left(\left(ly \times \frac{lx^3}{12} \right) - \left((ly - 2 \times t) \times \frac{(lx - 2 \times t)^3}{12} \right) \right) \times \frac{e}{lz^3} \times 10 \quad (kN/m) \qquad \text{(E2)}$$

$$p = (2 \times \pi) \times \left(\sqrt{\left(\frac{\frac{w}{9.81}}{r} \right)} \right) \quad (s) \qquad \text{(E3)}$$

$$f = 1/p \quad (Hz) \qquad \text{(E4)}$$

Using the constants for the modulus of elasticity (e) of concrete as 20000 MPa and gamma (m) of concrete as 22 kN/m^3, a much more higher value than 80 Hz is obtained for the free oscillation frequency of a PIRES concrete box analytically. The probable reasons could be, either the analytical formula used is not the appropriate one or constants taken for the modulus of elasticity (e) and gamma (m) of concrete are not the right values. For instance, Figure E14 has been drawn using elasticity modulus values varying between 500 and 30000 MPa and Figure E15 has been drawn taking the gamma value changing between 10 and 200 kN/m^3. According to the figures, either lower values of elasticity than 500 MPa or higher values of gamma than 180 kN/m^3 could make the natural frequency converge to ~80 Hz.
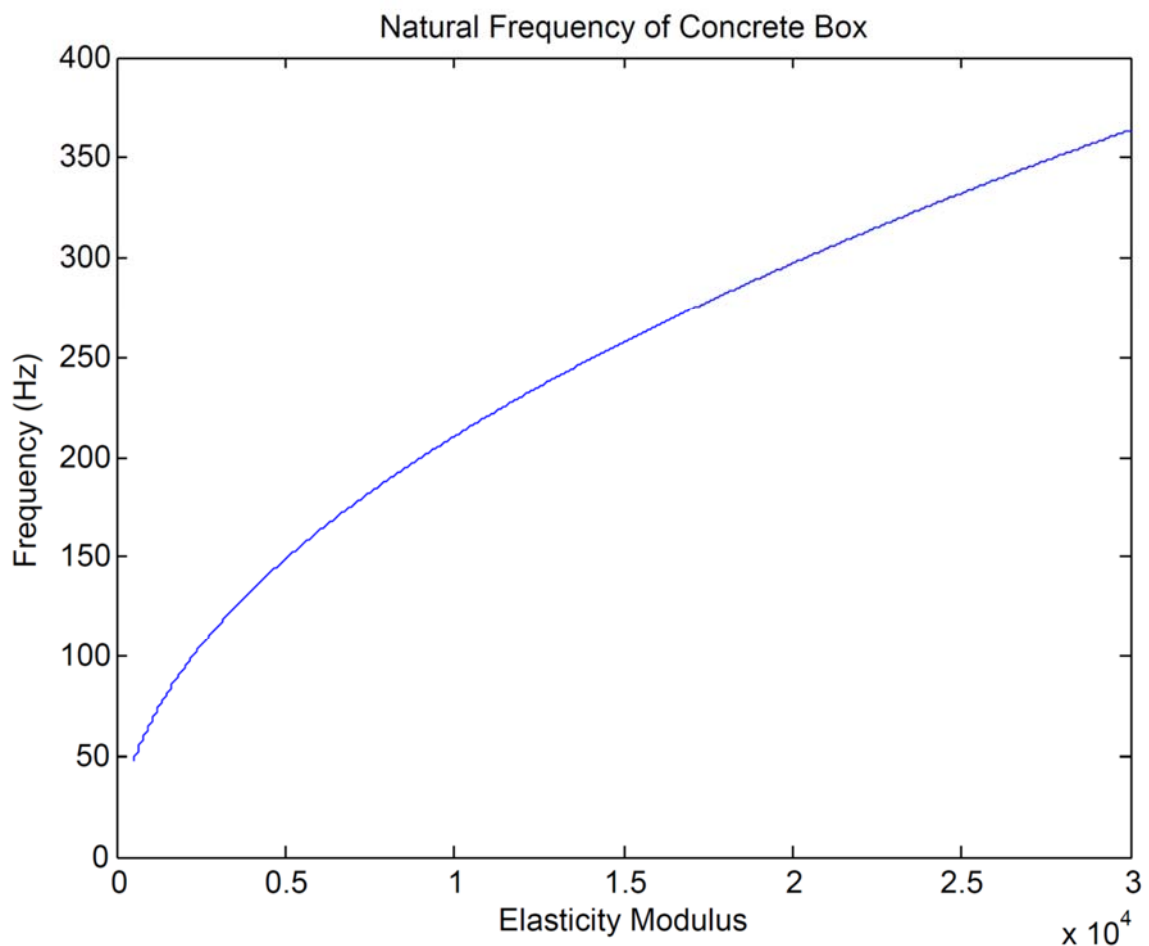

Figure E14. Elasticity modulus with respect to natural frequency.
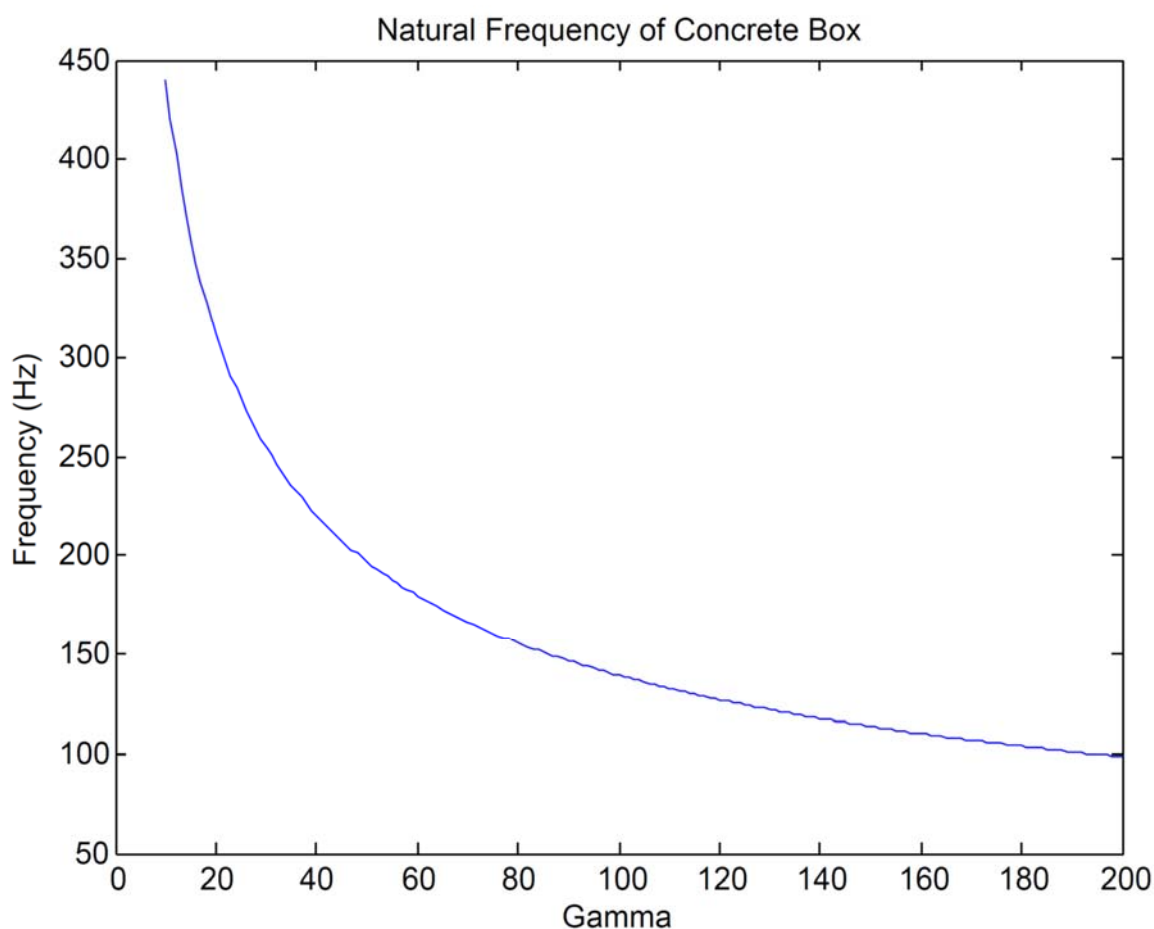
Figure E15. Gamma with respect to natural frequency.

In addition to that, ground and box coupling might play a great role on the normal frequencies of boxes that has not been taken into account during the very simple theoretical computations. Moreover, weight of the iron lids that are used to cover the top of the boxes and their contact with the concrete uppermost lids or their oscillations are not involved in the calculations. Also, iron has been used both inside the boxes and at the edges of concrete uppermost lids that their contributions are not known to the total weight of the boxes exactly.

Secondly; in order to verify the natural frequencies of the PIRES concrete structures for acoustic case, Blevins (1984) analytical solution for a closed rectangular object has been used, (Equation E5). Natural frequencies (in unit of Hz) can be computed following the Equation E5 where, the length (lx) of the box is 1.10 m, width (ly) of the box is 0.90

m, height (lz) of the box is 0.75 m, speed (c) of the sound is 343.2 m/s and i, j, k are the indexes for the normal mode vibrations.

$l_x = 1.10\ m$

$l_y = 0.90\ m$

$lz = 0.75\ m$

$c = 343.2\ m/s$

$$i = j = k = 0,1,2,3$$

$$f_{ijk} = c/2 \left(\sqrt{(i/l_x{}^2) + (j/l_y{}^2) + (k/l_z{}^2)} \right) \qquad (Hz) \qquad (E5)$$

For acoustic case also, a value of 80 Hz cannot be obtained analytically using the Equation E5. Instead, much higher natural frequencies can be obtained. For instance, the lowest value that has been got is 336 Hz for the case of

$$i = j = k = 1$$

Although, the occurrence of 80 noise peak could not be proved with simple analytical solutions such a phenomenon have been observed on some of the spectra that belong to the box structures. It should be kept in mind that, the case of the PIRES boxes could not be mimicked realistically with analytical approaches.

After all of these tests that have been performed, finally the conclusion that has arisen is, noise peak at ~80 Hz is generated by the normal oscillation of the container structure which is built to protect the instruments. In fact, it is totally absent at stations where such structures do not exist. Seismic arrays referred as PIRES on Sivriada and Yassıada Islands in Marmara Sea are inhabited. In order to protect the instrumentations on these islands, very firm and heavy rectangular shaped concrete housings on the surface were constructed in 2006. Dimensions of these boxes are shown in Section B with Figure B1. Basically; cement, sand, gravel and water are used for the construction. Iron profiles are added both inside the edges of the boxes and concrete lids that make the concrete

housings more rigid. In addition to that, extra lids made up of entirely iron are also used to cover the top of the boxes that are placed below the concrete uppermost lids. At the end of 2012, second housings were constructed next to the two of the PIRES Arrays stations, FUTB and POWD, with smaller dimensions and lighter material, (Figure B3). Two stations, within ~20 cm distance and equipped with different instrumentations have worked at the same time for a short period at these locations. On the contrary; on KNAL, BRGZ, HYBL, BASD, KRGZ and MRTI where there are single stations, instrumentations are buried under soil.

After performing many tests, it has been observed that every station has a characteristic noise peak in terms of a frequency value and shape. Moreover, this property does not show much variation with respect to different earthquake occurrences, phases or components. As a secondary outcome; it can be deduced that, 80 Hz noise peak occurs both on Sivriada and Yassıada Islands as in E7 (EASY and SHTH stations and at NS components on Sivriada) and E10 (FUTB and POWD stations and at NS components on Yassıada). Note that, instrumentations (seismometers and digitizers) are also similar for these examples. These two tests help to eliminate any suspicion about the probability of the peak's generation because of the differences in the geometry, structure, topography, etc. of islands. 80 Hz noise peak is observed under both circumstances. Noise peak occurs in any case independent of the island effect.

Finally; a conclusion has been reached that the value of the peak frequency is a characteristic value independent of an earthquake, seismic phase, component, island, etc. Whenever an earthquake signal has the energy that coincidences with the normal mode of the concrete structure resonance occurs. Amplitude of the noise peak increases with the magnitude of an earthquake proving that noise is multiplicative. In fact, every object has a natural or fundamental frequency. It is simply the rate at which an object moves back and forth if it is given a horizontal movement, i.e. earthquake motion, (Arnold, 2006). In the current case, when a box structure is excited with either noise or an earthquake signal, a number of overtones are produced along with the fundamental mode. Such peaks are not observed where the instruments are buried under ground. Another important conclusion that comes out from these analyses is that, housing structures for the instrumentations should be constructed in such a way that the fundamental frequencies of them should be far

away from the dominant earthquake energy (Lin *et al.,* 1989). If these structures have already been constructed then, when doing detailed analysis with high frequency earthquakes, one should be aware of this effect and it should be eliminated. Other important fact is that, very high sampling rate (200 or 500 Hz) of data allowed to catch such a phenomenon.

APPENDIX F: APPLICATION OF FK TO THE PIRES DATA

Sivriada and Yassıada Arrays have only 5 stations on each of them. This fact and some other various reasons put restrictions during the application of the FK. Reliable FK analysis needs some special conditions and requirements. In this section, tackling with the difficulties of the PIRES as an array will be handled with examples. In addition to FK's having some complications in application, PIRES also have its own special difficulties. These cases include;

1) Dissimilarities in amplitudes between the array stations due to the elevation and topography differences underneath the stations
2) Incoherent waveforms in small station spacing
3) Probable local crustal velocity differences underneath the stations

These reasons effect the apparent velocity and back azimuth calculations. For this reason, limited number of stations has to be used for the FK analysis.

NORSAR processing software has been adopted for the PIRES situations. Using an array, wavenumber of the wave that is defined by its wavelength or frequency and its slowness are observed. PIRES Arrays seem to be more stable for the back azimuth calculations even for the lack of stations. On the other hand, slowness measurements are much more effected from these facts which are induced by the PIRES Arrays geometries, (Figures 4.4 and 4.5).

In the array subject, there are a few concepts that should be known in order to evaluate the performance of an array, i.e. PIRES. One of them is the definition of the aperture. It is the largest horizontal distance between the two sensors of the array. Therefore, size of an array is defined by its aperture. For instance PIRES Arrays' apertures are approximately 300 m.

Second important issue before designing an array is the geometry and the number of the seismometers in an array that should be decided according to the intended scientific purposes.

Another drawback is the aliasing effect in arrays. During the observation of the seismic signal's wavefront, spatial sampling of the ground is calculated. Therefore, aliasing might occur in the wavenumber domain due to the spatial sampling (Schweitzer *et al.*, 2009).

Definitions related to constructing an ideal array according to Havskov and Ottemöller (2009) are;

1) Array resolution is defined by the aperture of an array for the small wavenumbers

2) In order to maintain the signal coherency, the size of the array must be as large as possible

3) When the aperture of an array increases, wavenumbers that can be observed decreases

4) Quality of an array as a wavenumber filter is determined by the number of stations

5) More sensors supply improved noise suppression

6) The position of the side lobes of the array and the largest resolvable wavenumber with an array is defined by the distances between the stations

7) The azimuth dependence is defined by the geometry of an array

8) Aliasing can occur in time and space therefore, arrays must be designed taking into account the target dominant phases

9) Small arrays (10-100 m) with high sample rates are used for the local or regional studies

10) Large arrays (1-100 km) are used for tele-seismic studies

When performing FK, a reference is needed so that the rest of the array stations are analyzed with respect to that point. In the seismic arrays, there are more than one seismometer deployed and within these instruments either one of them or some other location close to the array should be assigned as a reference station. The main reason of this is, in the array analysis, relative distances from the reference station to all other array stations are used (Schweitzer *et al.*, 2009).

During beamforming and the FK analysis, for the single array case; POWD on Sivriada and FUTB on Yassıada have been selected as the reference station which are the center stations of the arrays. During the third case; both islands together are unified and treated as one big array. Then, a virtual reference station has been selected between the two arrays. Thus, when there is missing data belonging to the reference stations on Sivriada and Yassıada, that point also becomes a virtual reference station, (Figure F1).
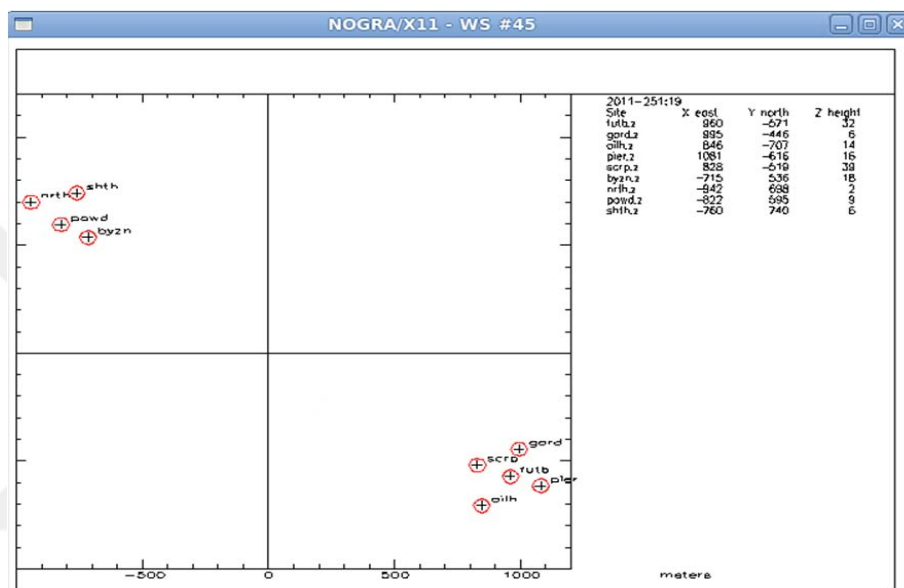
Figure F1. The virtual center of the PIRES Arrays.

Stations indicated with red circles on the right hand side of the Figure F1 represent Yassıada Array. Where else, stations on the left hand side of the Figure F1 compose Sivriada Array. The virtual center in between the PIRES Arrays has the geographic coordinates of 40.87000°N, 28.98200°E. The table on the right of the figure shows the relative coordinates between the stations and the site which is at the center of the array. The elevations of all of the stations are above the sea level and their elevations are in meters.

Mostly, within small distances of the array stations, elevation differences are expected to be very small so that the travel time differences due to the differences in elevation are negligible. Under this condition, it can be assumed that all of the station sites

are in the same horizontal plane. This is one of the cases preferred for the arrays to have a good coherency between the stations (Schweitzer *et al.*, 2009).

Unfortunately, PIRES Arrays do not have the preferred conditions. There are elevation differences between the stations of Sivriada and Yassıada which should be taken into account during the processes of the PIRES. For instance; NRTH station on Sivriada has the lowest elevation with only 2 km. On the other hand, SCRP station that is on Yassıada, has the highest elevation with 37 km. Because of this reason, amplitudes of the waveforms at array stations show significant variations, (Figure F2). Therefore, pre-adjustments are often necessary before applying the FK method. When the large amplitude differences is observed between the different array stations due to the differences in the crust below the stations, like PIRES Arrays, it is recommended either to normalize the amplitudes beforehand or to weight the traces before beamforming (Schweitzer *et al.* 2009).
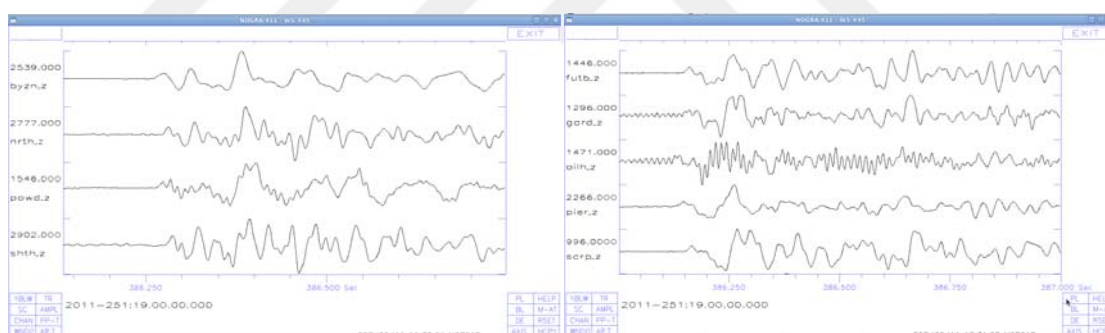

Figure F2. Differences in amplitudes between the stations of two the PIRES Arrays.

As observed in Figure F2, there are differences in amplitudes between the stations of the two PIRES Arrays. For instance, POWD station on Sivriada has amplitude 1546 with the lowest value. Whereas, SHTH station on the same island has amplitude 2902 with the highest value. On Yassıada, SCRP has amplitude 996 with the lowest value whereas PIER has amplitude 2266 with the highest value. Therefore, before the FK analysis, amplitudes are normalized in order to obtain a good amplitude coherency between the stations of arrays. Normalizing the amplitudes also shrinks the main lobe indicated with red color in the centers, (Figure F3).
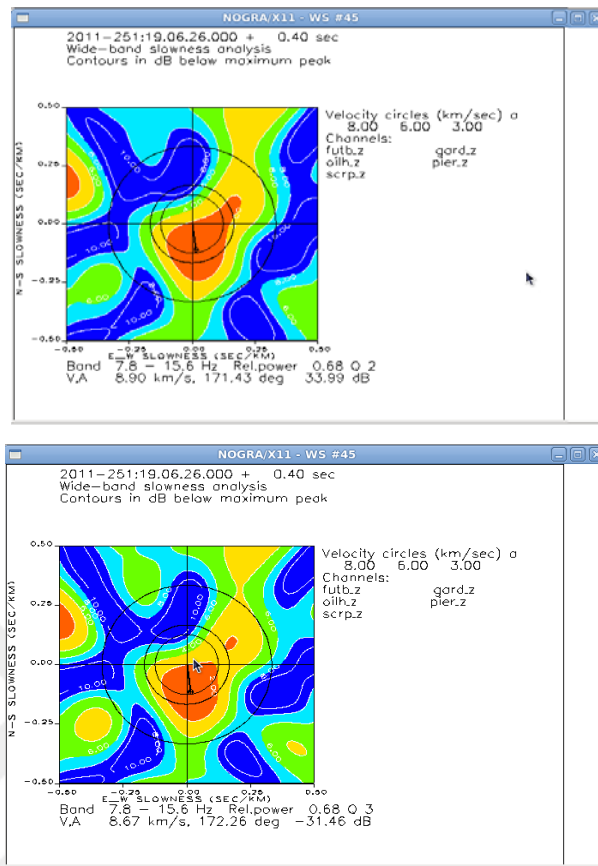
Figure F3. FK results without and with normalization of the amplitudes, respectively.

FK plot on the top has been obtained without normalizing the amplitudes. Whereas; on the bottom figure, amplitudes have been normalized before the FK. During both of the analysis, grid spacing has been taken as 51 by 51 and slowness values are between -0.5 and 0.5 s/km, (Figure F3).

It is also very important to choose an appropriate filter while doing the FK analysis. There is a difference in coherency between the PIRES Arrays stations, as it can be seen in Figure F4. During the FK analysis, it is possible to beamform first and then filter the traces or vice versa, filter the traces first and then beamform (Schweitzer *et al*., 2009). On the other hand, for locally increased noise levels, like the PIRES case, first of all, it is better to filter the traces in order to avoid the leakage of low frequency energy. Since, FK analysis is a tool containing Fourier analysis applications.
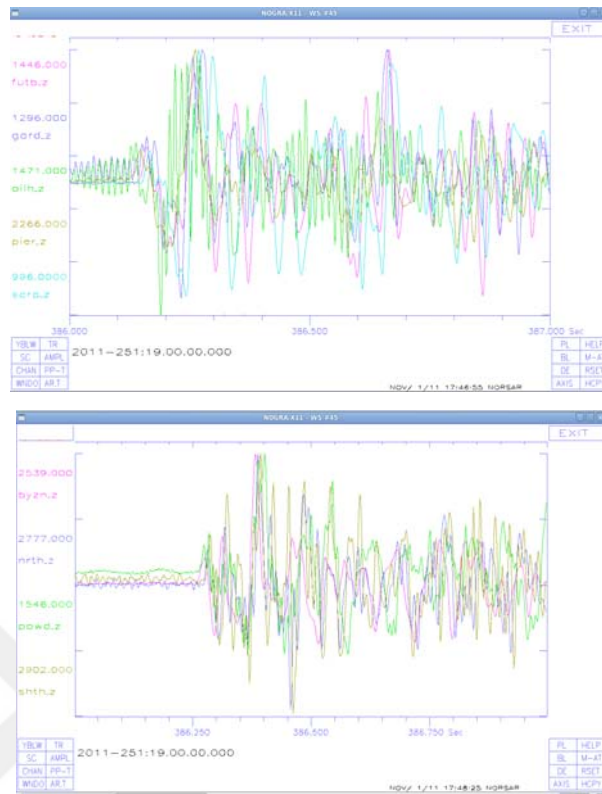
Figure F4. Coherency difference between the stations of the two PIRES Arrays.

Plot on the top of the Figure F4 has been drawn with Sivriada Array stations on top of each other. On the bottom, they are the Yassıada Array stations. Figure F4 clearly indicates the coherency difference between the stations of the two PIRES Arrays when a filter is not used.
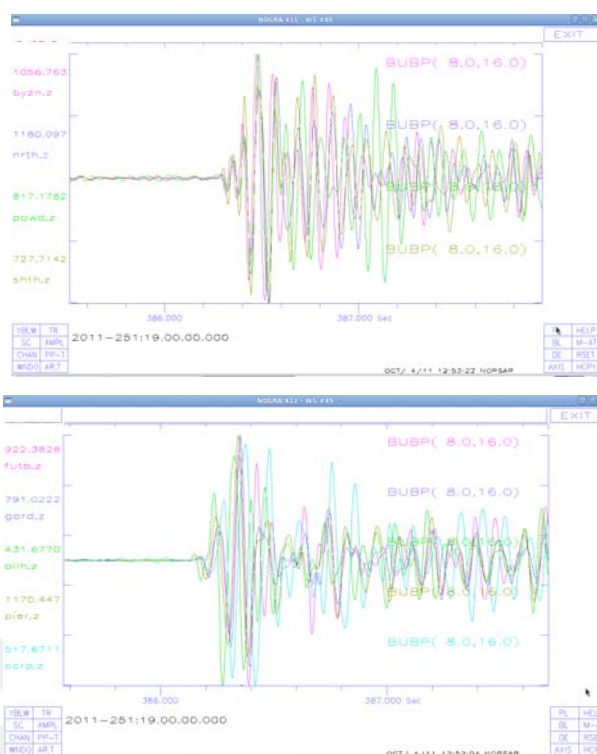
Figure F5. Coherency difference between the stations of the two PIRES Arrays after filtering.

After filtering the seismograms, waveforms resemble each other more, (Figure F5). Data have been filtered using Butterworth bandpass filter between 8 and 16 Hz.

During the FK analysis, an appropriate window length (~200-500 ms long for the PIRES case), has to be chosen around the P phase in such a way that the waveforms look most coherent in that window, (Figure F6). Determination of the choice of window length depends on the intended study, i.e. local, regional or tele-seismic. In terms of local analysis, it should be short. Short windows have to be used because, otherwise coherency is lost drastically.
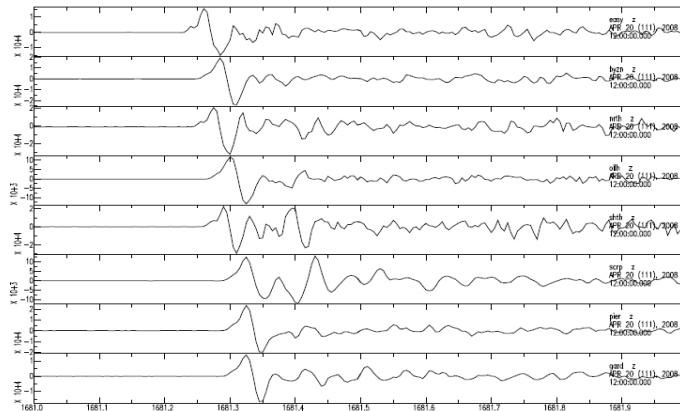
Figure F6. Zoom of the P phases.

Using an appropriate window length is very important for the FK analysis, thus it effects the relative power. Figure F7 shows the FK plots that have been obtained using different window lengths (300 ms, 350 ms and 400 ms), respectively. Amplitudes are also normalized before the FK analysis. Plots are produced for grid spacing of 401 by 401 and slowness values are between -0.5 and 0.5 s/km. Window length of 350 second increases the relative power to 0.71 dB compared to 300 or 400 second as it is seen in Figure F7. Since, during calculations in the frequency domain, it is also important to cut the waveform sufficiently long to avoid unwanted effects of the Fourier analysis.
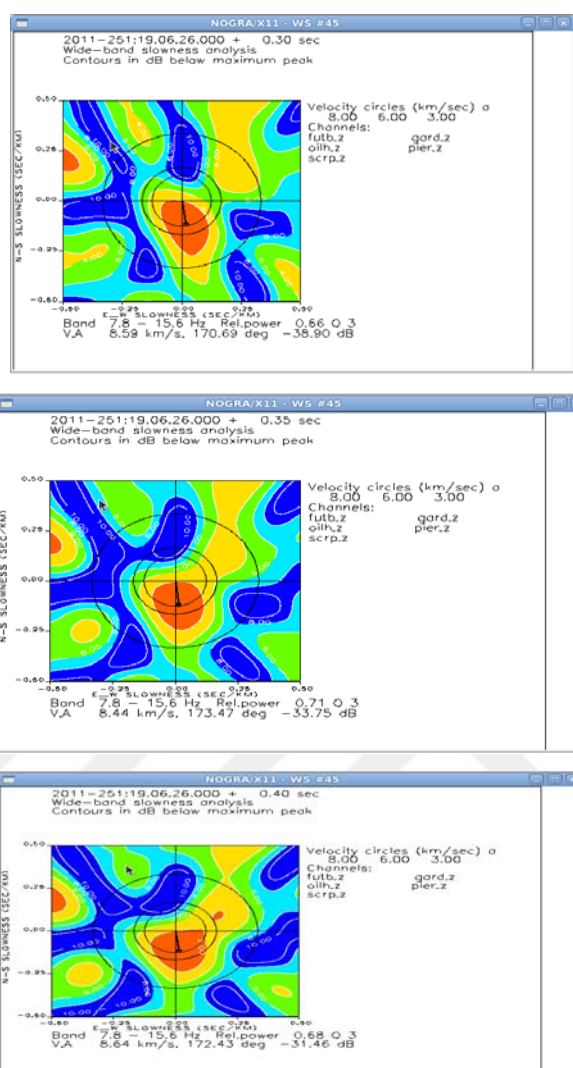
Figure F7. FK plots obtained using different window lengths (300 ms, 350 ms and 400 ms), respectively.

FK analysis technique has been applied as Kvaerna and Doornbos (1986) have proposed. It is called as wide band or broadband FK analysis. The method depends on integrating over a wider frequency band rather than the single frequency wave number analysis. The reason is, side lobe positions in the space of the FK are frequency dependent. On the other hand, main lobe's position in terms of the different frequencies is always at the same location. Thus, amplitude distance between the main lobe and the side lobes increase if the FK results are summed up for the wide band frequencies (Schweitzer *et al.*, 2009), Figure F8.
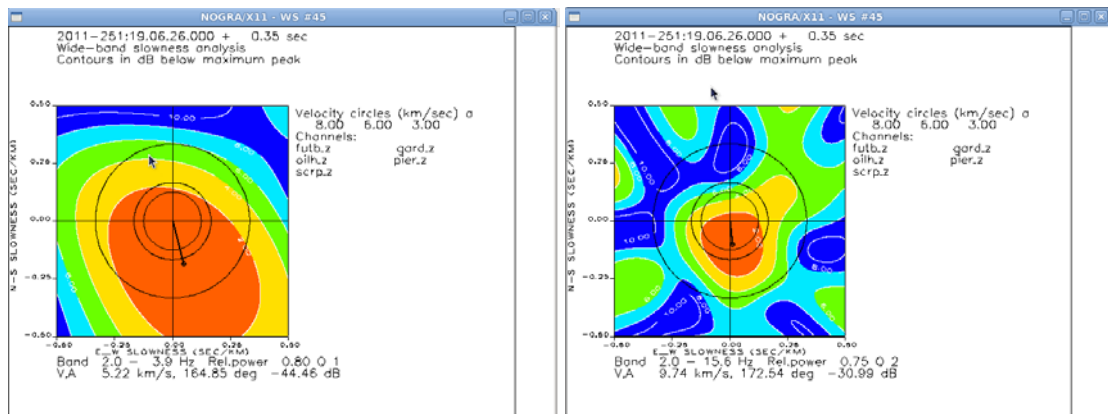
Figure F8. FK plots with different filters; 2-4 Hz and 2-16 Hz, respectively.

Figure F8 compares two different filter usages. The plot on the left hand side is an example of filtering at narrow band, between 2-4 Hz. On the other hand, the plot on the right is a demonstration of filtering at broader frequency range, 2-16 Hz. When filtering in narrow band, 2-4 Hz, the main lobe enlarges, relative power decreases and back azimuth and slowness values differ compared to filtering at broader frequency, 2-16 Hz, (Figure F8).
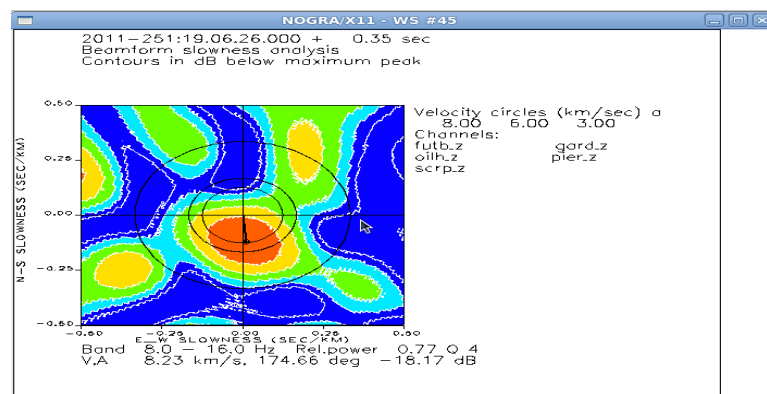

Figure F9. FK analysis in the time domain.

Generally, FK analysis and beamforming are both performed in the frequency domain for different slowness values. On the other hand, FK can also be performed in the time domain which needs longer calculation time. During the time domain FK analysis,

relative power increases more than the frequency domain analysis as it can be observed in Figure F9. If the FK analysis in the frequency domain, Figure F9 and FK analysis in the time domain, Figure F8, are compared, a slight increase in the relative power in the time domain can be observed.